



LANTHANIDE-BASED DIELECTRIC NANOPARTICLES FOR UPCONVERSION LUMINESCENCE

Elixir William Barrera Bello

Dipòsit Legal: T. 450-2013

ADVERTIMENT. L'accés als continguts d'aquesta tesi doctoral i la seva utilització ha de respectar els drets de la persona autora. Pot ser utilitzada per a consulta o estudi personal, així com en activitats o materials d'investigació i docència en els termes establerts a l'art. 32 del Text Refós de la Llei de Propietat Intel·lectual (RDL 1/1996). Per altres utilitzacions es requereix l'autorització prèvia i expressa de la persona autora. En qualsevol cas, en la utilització dels seus continguts caldrà indicar de forma clara el nom i cognoms de la persona autora i el títol de la tesi doctoral. No s'autoritza la seva reproducció o altres formes d'explotació efectuades amb finalitats de lucre ni la seva comunicació pública des d'un lloc aliè al servei TDX. Tampoc s'autoritza la presentació del seu contingut en una finestra o marc aliè a TDX (framing). Aquesta reserva de drets afecta tant als continguts de la tesi com als seus resums i índexs.

ADVERTENCIA. El acceso a los contenidos de esta tesis doctoral y su utilización debe respetar los derechos de la persona autora. Puede ser utilizada para consulta o estudio personal, así como en actividades o materiales de investigación y docencia en los términos establecidos en el art. 32 del Texto Refundido de la Ley de Propiedad Intelectual (RDL 1/1996). Para otros usos se requiere la autorización previa y expresa de la persona autora. En cualquier caso, en la utilización de sus contenidos se deberá indicar de forma clara el nombre y apellidos de la persona autora y el título de la tesis doctoral. No se autoriza su reproducción u otras formas de explotación efectuadas con fines lucrativos ni su comunicación pública desde un sitio ajeno al servicio TDR. Tampoco se autoriza la presentación de su contenido en una ventana o marco ajeno a TDR (framing). Esta reserva de derechos afecta tanto al contenido de la tesis como a sus resúmenes e índices.

WARNING. Access to the contents of this doctoral thesis and its use must respect the rights of the author. It can be used for reference or private study, as well as research and learning activities or materials in the terms established by the 32nd article of the Spanish Consolidated Copyright Act (RDL 1/1996). Express and previous authorization of the author is required for any other uses. In any case, when using its content, full name of the author and title of the thesis must be clearly indicated. Reproduction or other forms of for profit use or public communication from outside TDX service is not allowed. Presentation of its content in a window or frame external to TDX (framing) is not authorized either. These rights affect both the content of the thesis and its abstracts and indexes.

Lanthanide-based dielectric nanoparticles for upconversion luminescence

Elixir William Barrera Bello

Nowadays special attention has been given to materials capable of generating visible light by conversion of near infrared photons (upconversion) for save-energy technologies and reduction of photo-degradation caused by UV high energy photons. Nanoparticles using optically active trivalent lanthanide ions (Ln^{3+}) have shown great potential for use as upconverting luminescent materials in bio-analysis applications, improvement of solar cells efficiency, fight of counterfeit in printed documents and back-lighting in liquid crystal displays. However materials with nanometer dimensions may affect the luminescence dynamics of the Ln^{3+} ion modifying the emission lifetime, quantum yield, and concentration quenching.

This thesis discusses the synthesis and upconversion emission of lanthanide doped nanostructures with Lu_2O_3 and $\text{KLu}(\text{WO}_4)_2$ as host because they possess high chemical stability; they offer favorable incorporation of Ln^{3+} ions and high absorption and emission cross sections. Three kinds of nanostructures are discussed: nanocrystals, nanorods and core-shell particles. Er^{3+} , Ho^{3+} and Tm^{3+} are used as emitting ions and Yb^{3+} as sensitizer. Luminescence dynamics of these ions into these nanostructures and the possibility of white light emission in KLuW nanocrystals are discussed.

Elixir William Barrera Bello

Lanthanide-based dielectric nanoparticles for upconversion luminescence

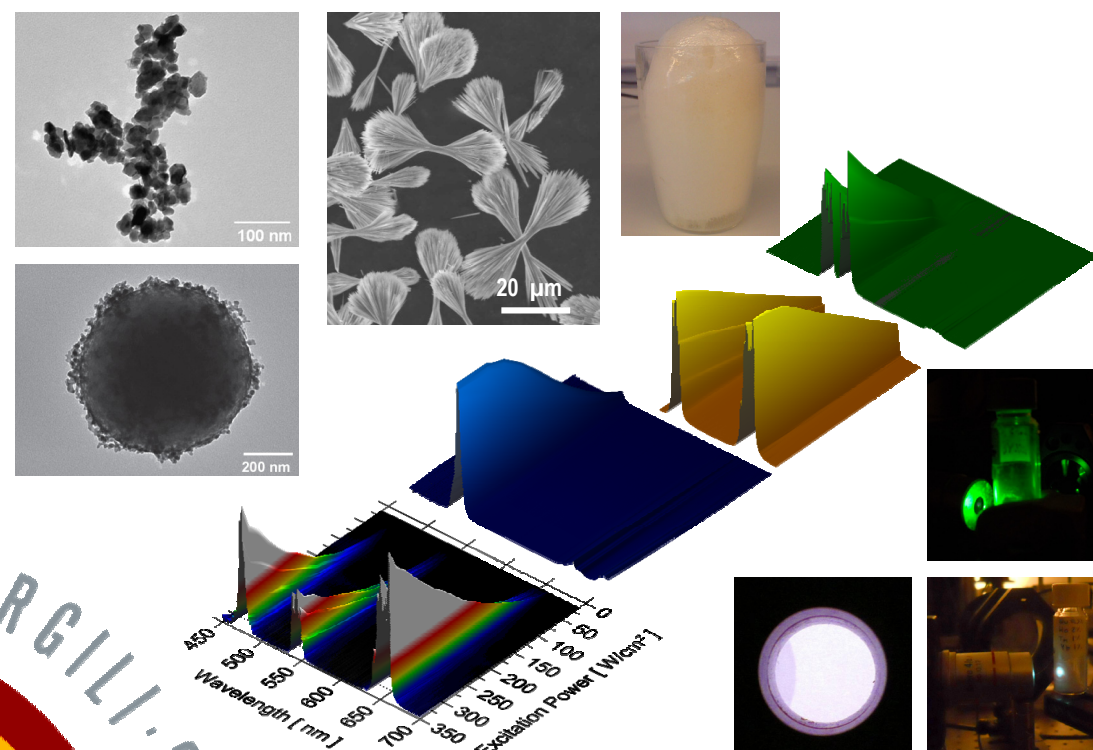


UNIVERSITAT
ROVIRA I VIRGILI

Lanthanide-based dielectric nanoparticles for upconversion luminescence

Elixir William Barrera Bello

Doctoral Thesis



Supervised by:
Dr. Maria Cinta Pujol Baiges and
Prof. Dr. Concepción Cascales Sedano

Tarragona, 2013



UNIVERSITAT ROVIRA I VIRGILI
LANTHANIDE-BASED DIELECTRIC NANOPARTICLES FOR UPCONVERSION LUMINESCENCE
Elixir William Barrera Bello
Dipòsit Legal: T. 450-2013

Elixir William Barrera Bello

**LANTHANIDE-BASED DIELECTRIC NANOPARTICLES FOR
UPCONVERSION LUMINESCENCE**

DOCTORAL THESIS

Supervised by:

Dr. Maria Cinta Pujol Baiges
Dr. Concepción Cascales Sedano

Department of Physical Chemistry and Inorganic
Group of Physics and Crystallography of Materials and Nanomaterials
(FiCMA-FiCNA)

Doctorate program in
Electronic Engineering, Automation and communications



UNIVERSITAT
ROVIRA I VIRGILI
Tarragona
2013

UNIVERSITAT ROVIRA I VIRGILI
LANTHANIDE-BASED DIELECTRIC NANOPARTICLES FOR UPCONVERSION LUMINESCENCE
Elixir William Barrera Bello
Dipòsit Legal: T. 450-2013



UNIVERSITAT
ROVIRA I VIRGILI

DEPARTAMENT DE QUÍMICA FÍSICA
I INORGÀNICA

Campus Sescelades
Marcel·lí Domingo, s/n
43007 Tarragona
Tel. +34 977 55 81 37
Fax +34 977 55 95 63
www.quimica.urv.es

FAIG CONSTAR que aquest treball, titulat “**Lanthanide-based dielectric nanoparticles for upconversion luminescence**”, que presenta **Elixir William Barrera Bello** per l’obtenció del títol de Doctor, ha estat realitzat sota la meva direcció al Departament de Química Física i Inorgànica d’aquesta universitat i que apleix els requeriments per poder optar a Menció Europea.

Tarragona, 14 de desembre de 2012.

Dra. Maria Cinta Pujol Baiges
Directora

Dra. Concepción Cascales Sedano
Codirectora

UNIVERSITAT ROVIRA I VIRGILI
LANTHANIDE-BASED DIELECTRIC NANOPARTICLES FOR UPCONVERSION LUMINESCENCE
Elixir William Barrera Bello
Dipòsit Legal: T. 450-2013

Lanthanide-based dielectric nanoparticles for upconversion luminescence

Elixir William Barrera Bello

Abstract

Nowadays special attention has been given to materials capable of generating visible light by conversion of near infrared photons (upconversion) for save-energy technologies and reduction of photo-degradation caused by UV high energy photons. Nanoparticles using optically active trivalent lanthanide ions (Ln^{3+}) have shown great potential for use as upconverting luminescent materials in bio-analysis applications, improvement of solar cells efficiency, fight of counterfeit in printed documents and back-lighting in liquid crystal displays. However materials with nanometer dimensions may affect the luminescence dynamics of the Ln^{3+} ion modifying the emission lifetime, quantum yield, and concentration quenching.

This thesis discusses the synthesis and upconversion emission of lanthanide doped inorganic nanocrystalline cubic $Ia\bar{3}$ Lu_2O_3 and monoclinic $C2/c$ $\text{KLu}(\text{WO}_4)_2$ (KLuW) materials as host. Three kinds of nanostructures were produced by modified Pechini method and low hydrothermal technique: nanocrystals, nanorods and core-shell particles. $\text{Tm}:\text{Lu}_2\text{O}_3$ nanocrystals show no dependence of the crystallite size and low increment of the linear thermal expansion coefficient supporting the use of Lu_2O_3 as a host for Tm^{3+} ions in $\text{Tm}:\text{Lu}_2\text{O}_3$ ceramic lasers made from nanocrystalline precursors. The presence of contaminant functional groups adsorbed on the surface of the nanostructures modifies the red-to-green optical emission of in $\text{Er}, \text{Yb}:\text{Lu}_2\text{O}_3$ nanorods ($90 \text{ nm} \times 45 \mu\text{m}$). $\text{Ln}:\text{Yb}:\text{KLuW}$ nanocrystals with $\sim 100 \text{ nm}$ were produced as green ($\text{Ln}=\text{Er}$), yellow ($\text{Ln}=\text{Ho}$) and blue ($\text{Ln}=\text{Tm}$) upconverting emitters with high color purity. For $\text{Er}:\text{Yb}:\text{KLuW}$ nanocrystals, quantum yield of $\sim 0.2 \%$ was obtained with $30\text{-}150 \text{ W/cm}^2$ power density excitation. A model for calculating the optimal proportion to obtain light with chromaticity near to the white point was proposed from the physical mixture of $\text{Ln}, \text{Yb}:\text{KLuW}$ ($\text{Ln} = \text{Er}, \text{Ho}, \text{Tm}$) prepared nanocrystals and contrasted with the corresponding mixture of upconverting KLuW nanocrystals. White light emission was produced for the $0.25\text{-}1.00 \%$ Ho doped 1% Tm , 1% $\text{Yb}:\text{KLuW}$ nanocrystals with $14\text{-}354 \text{ W/cm}^2$ excitation power. Eu^{3+} doping in $\text{Ho}:\text{Tm}:\text{Yb}:\text{KLuW}$ reduces the QYs in one magnitude order, quenching on upconversion visible emissions.

Keywords:

Lanthanide, nanoparticle, upconversion, luminescence, spectroscopy, nanocrystal, nanorod, core-shell.

Preface

The Ph.D. investigation contained in this thesis has been carried out at Group of Physics and Crystallography of Materials and Nanomaterials (FiCMA-FiCNA) in the Department of Physical Chemistry and Inorganic at Rovira i Virgili University and was advised by Dr. Maria Cinta Pujol (Rovira i Virgili University) and Prof. Dr. Concepción Cascales Sedano (ICMM-CSIC).

Within the development of this investigation, we have collaborated actively with the following groups: Prof. Carlos Zaldo at ICMM-CSIC (Madrid-Spain); Prof. Marco Bettinelli and Prof. Adolfo Speghini in Solid State Chemistry Lab at University of Verona (Verona-Italy); Fabian Rotermund in Division of Energy Systems Research at Ajou University (Suwon- Korea).

This project was possible thanks to financial support from Generalitat de Catalunya under projects 2009SGR235 and FP7-SPA-2010-263044. By Ministerio de Educación y Ciencia (MEC) of the Spanish Government under projects MAT2008-06729-C02/NAN, MAT2008-04046-E/MAT, TEC2010-21574-C02-02, MAT2011-29255-C02-02 and the project PI09/90527; and EU project CLEAN SPACE (FP7-SPACE-2010-1-GA-263044).

I would like to thank also personal financial support of the commissioner for Universities and Research from Department of Innovation, Universities and Enterprise of Generalitat de Catalunya and the European Social Fund under grants 2009FI-00148, 2010FI-B00834, 2011FI-B100097, 2011 BE1-00836 and 2012FI-B200136. The support of the COST Action CM1006 (EUFEN: European F-Element Network) by the STSM-CM1006-050512-017263 grant is gratefully acknowledged

Elixir William Barrera Bello
Tarragona, 2013

UNIVERSITAT ROVIRA I VIRGILI
LANTHANIDE-BASED DIELECTRIC NANOPARTICLES FOR UPCONVERSION LUMINESCENCE
Elixir William Barrera Bello
Dipòsit Legal: T. 450-2013

Acknowledgements

I express my sincere gratitude to Prof. Francesc Díaz for giving me the opportunity to join the FiCMA-FiCNA group and develop this doctoral thesis and for all his support for exposing our results in different conferences. I would like to thank especially Magdalena Aguiló for teaching me the basics of symmetry, crystallography, nucleation and crystal growth. Also for her advice, and support in different grant applications.

I am grateful to my thesis directors, Dr. Cinta Pujol and Prof. Dr. Concepción Cascales for their support, guidance and encouragement throughout my doctoral thesis. My sincere thanks to Cinta, for his enthusiasm, patience, open-minded discussions and friendship. I am grateful for the opportunity to work with. I owe my deepest gratitude to Dr. Concepción Cascales, for forcing the best of me through her advices, discussions and assertive corrections in spectroscopy. I extend my sincere thanks to Prof Carlos Zaldo, CSIC, Madrid for measuring and discussion of lifetimes in Tm-doped nanocrystals, and for serving in my thesis committee.

I also want to thank the other senior members of the FiCMA-FiCNA group: Dr. Joan Carvajal, Dr. Xavier Mateos, Dr. Jaume Massons, and Dr. Rosa Solé and for their support during my stay in this research group and discussion of papers and results.

I would like to thank the support of technician staff in FiCMA-FiCNA lab: to Agustí Montero (furnace, hydraulic press, thermocouple and sensor repairing), Nicolette van der Bakker (cutting, polishing, labeling, finding) and especially to Laura Escorihuela for her friendship and willingness of support my work during these years.

I would like to thank all my FiCMA-FiCNA colleagues. We started out as lab mates and along the way became friends sharing lunches, coffees, birthdays, etc.: Isabel Parreu, Montserrat Galceran, Western Bolaños, Venkatesan Jambunathan, Martha Segura, Raj Kumar, Maria Méndez, Jaume Cugat, Muhammad Usman Qadri, Oleksandr Bilosouv, Muhammad Ali Butt, Carla Berrospe, Oleksandr Savchuk, Elena Perez, Mina Moeini, Airan Rodenas, José Maria Serres, Marc Medina and Josué Mena.

I am grateful to Prof. Marco Bettinelli for the privilege of work in the Solid State Chemistry Lab at University of Verona, I owe my deep appreciation to him for show me a new vision of trends of lanthanide research and for his advice. I also thank his hospitality as organizer during the 8th International conference on f-elements in Udine. I thank Prof. Adolfo Speghini for his patience in the emission measurements, for his willingness to help me with the lab facilities, for his motivation during my stay in Verona, and for serving in my thesis committee. Besides, I would like to thank to the staff of Solid State Chemistry Lab at University of Verona: Dr. Fabio Piccinelli, Dr. Marco Pedroni, Mattia Trevisani, Irene Xochilt, Agata Lazarowska, Erika Viviani and Dr. Patricia Haro. I thank to Valentina Allodi in Department of Computer Science at University of Verona for emission and excitation measurements with spectrofluorimeter.

I thank people on Serveis Científico-Tècnics of the University of Barcelona, Dr. Xavier Llovet for EPMA measurements, and Dr. Portillo for HRTEM characterization. In Servei de Recursos Científics i Tècnics at Rovira i Virgili University, I express my gratitude to the microscopy chief

Dr. Mercè Moncusí and all the staff: Lukas Vojkuvka, Mariana Stefanova, Nuria Argany and Rita Marimon. Thanks for all their support when I was operating RAMAN, FTIR, ESEM, and TEM microscopes. I thank to Dr. Francesc Gispert for all the reliable, precise and always on time X-Ray diffraction measurements. I would like to express my gratitude to the administrative staff: Yolanda Albero and Silvia Duran (Secretary of Department of Inorganic Chemistry), Anna Benages (Human Resources) and Zoe Magi (Research Management).

During this time in Tarragona I have met special friends that provided me a lot of good memories and I would like remember them: Raúl Pérez, Isabel Chaparro, Sergi Ollé, Nohora Martinez, Gabriela Fauth, Marcelo Vieira, Ximena Castaño Laura Borel, Juan Pablo Galeano. I would like to thank my colombian friends and colleagues at URV Sescelades: Said Pertuz, Yanine Arrieta, Maryluz Moreno, Edwin Pinto and Julian Cristiano.

I will aspire to thank especially my star friend Ligia Guerrero, with whom I have shared this long and arduous way to complete our respective doctorates. Thanks for all the flat meetings, trips, Barcelona events, wake-up calls and uncountable coffees and cinema times. Thank you for your support, patience and understanding during these years.

I thank to other members of the Chemistry Faculty: Dr. Antonio Rodriguez to let me assist to Molecular Spectroscopy lectures during 2009-10 and 2010-11 courses, Dr. Josefina Gavaldà, Dominica Bratkowska, Carolina Blanco, Tatiana Sanchez and Raquel Rivas for their support and chats during hall meetings. I want to thanks all the hospitality and friendship from my colombian colleagues Yolima Arias (University of Valencia), Adriana Figueroa, Oscar Fajardo and Marcela Bonilla (University of Zaragoza).

I am grateful because I had the opportunity to live with good friends in the different places during this years: Maria Castella (Catalonia), Jessica Paredes and Carlo Corrales (Peru), Isabel Mena and Roberto Carrion (Ecuador), Raffaella Fassoli (Italy), Flavio Fratton (Italy), Javier Ruiz (Catalonia) and Mina Moeini (Iran). Especially I remember Geovanna Garcia and her daughter Valerie Johnson (Chile-Germany) for their friendship, enthusiasm and support.

I thank my dear parents Gilberto Barrera and Amalia Bello. I have missed you but no more than you to me. It was your hard work and your innumerable sacrifices that let me reach the doctoral studies. I could always count on your support and prayers from the distance with love. I thank my dear sister, Elizabeth Barrera, for being a strength and inspirational source, for supported me in many ways during our long Skype and phone calls. I thank my brother Tomas Barrera and Laura Carreño for their support and unforgettable visits in Tarragona and Verona. To all the rest of my family, thanks for their support throughout these years. I feel heartbroken writing these last lines in memorial of my loved aunt Marleny Bello. She passed during the writing of this thesis. Thank you for your joy, love and support.

*To my father and mother
Gilberto Barrera and Amalia Bello
with great love*

UNIVERSITAT ROVIRA I VIRGILI
LANTHANIDE-BASED DIELECTRIC NANOPARTICLES FOR UPCONVERSION LUMINESCENCE
Elixir William Barrera Bello
Dipòsit Legal: T. 450-2013

Publication in journals

This doctoral thesis is partially based on the work contained in the following papers, referred to by roman numerals in the text:

I. E. W. Barrera, M. C. Pujol, C. Cascales, J. J. Carvajal, X. Mateos, M. Aguiló, and F. Díaz, *Synthesis and structural characterization of Tm:Lu₂O₃ nanocrystals. An approach towards new laser ceramics* **Optical Materials** 33 722–727 (2011).

II. E. W. Barrera, C. Cascales, M. C. Pujol, K. H. Park, S. B. Choi, F. Rotermund, J. J. Carvajal, X. Mateos, M. Aguiló, F. Díaz *Synthesis of Tm:Lu₂O₃ nanocrystals for phosphor blue applications* **Physics Procedia** 8 142-150 (2010).

III. E. W. Barrera, M. C. Pujol, C. Cascales, C. Zaldo, K. H. Park, S. B. Choi, F. Rotermund, J. J. Carvajal, X. Mateos, M. Aguiló, and F. Díaz, *Spectroscopic characterization of sol-gel synthesized Tm:Lu₂O₃ nanocrystals* **Applied Physics B: Lasers and Optics**, 106 409-417 (2012).

IV. E. W. Barrera, M. C. Pujol, F. Díaz, S. B. Choi, F. Rotermund, K. H. Park, M. S. Jeong, C. Cascales *Emission properties of hydrothermal Yb³⁺, Er³⁺ and Yb³⁺, Tm³⁺-codoped Lu₂O₃ nanorods: upconversion, cathodoluminescence and assessment of waveguide behavior* **Nanotechnology** 22 075205 (2011).

V. E. W. Barrera, C. Cascales, M. C. Pujol, J. Carvajal, X. Mateos, M. Aguiló, F. Díaz. *White Upconversion Luminescence in nanocrystalline (Ho,Tm,Yb):KLuW phosphor*, **Physica Status Solidi C** 8 2676–2679 (2011).

VI. E. W. Barrera, M. C. Pujol, F. Diaz, S. B. Choi, F. Rotermund, C. Cascales. *Hydrothermal trivalent lanthanide doped Lu₂O₃ nanorods: Evaluation of the influence of the surface in optical emission properties* **Optical Materials** 34 399–403 (2011).

VII. E. W. Barrera, M. C. Pujol, C. Cascales, J. J. Carvajal, X. Mateos, M. Aguiló, and F. Díaz, *Synthesis and characterization of core-shell SiO₂@(Er³⁺, Yb³⁺):Lu₂O₃* **Optical Materials** 34 355–359 (2011).

UNIVERSITAT ROVIRA I VIRGILI
LANTHANIDE-BASED DIELECTRIC NANOPARTICLES FOR UPCONVERSION LUMINESCENCE
Elixir William Barrera Bello
Dipòsit Legal: T. 450-2013

List of acronyms

1D	one-dimensional
2D	two-dimensional
α	fraction of absorbed light
α_A	absorption coefficient
α_L	linear thermal expansion coefficient
σ_A	absorption cross section
a	lattice parameter (cubic)
CCD	charge-coupled device
CA'	chelating agent
CA	citric acid
C_G	gold-to-sesquioxide mass ratio
CIE	Commission Internationale de l'Éclairage
C_S	silica-to-sesquioxide mass ratio
CL	cathodoluminescence
CW	continuous-wave
d	interplanar distance
D	crystallite size
DTA	differential thermal analysis
EDAX	energy dispersive X-ray
EDTA	ethylenediaminetetraacetic acid
EG	ethylene glycol
EPMA	electron probe micro-analysis
E_{REF}	Excitation intensity not absorbed by the reference
E_S	Excitation intensity not absorbed by the sample
ESA	excited-state absorption
ET	energy transfer
ETU	energy-transfer upconversion
F_{ATT}	correction factor due to attenuators
FTIR	Fourier transform infrared
FWHM	full-width at half-maximum
HRTEM	High-resolution transmission electron microscopy
I_0	excitation intensity
I_{UC}	upconversion emission intensity
JCPDS	Joint Committee on Powder Diffraction Standards
k_B	Boltzmann constant
KLuW	KLu(WO ₄) ₂
λ_{EMI}	Emission wavelength
λ_{EXC}	Excitation wavelength

<i>M</i>	measured spectrum
Ln	lanthanide
Ln-UCNPS	lanthanide-based upconverting nanoparticles
<i>n</i>	Slope in the log-log graph of intensity-versus-power curves
NC	Nanocrystal
NIR	Near infrared
<i>n_f</i>	Refractive index
OD	Optical density
PL	photoluminescence
PMT	photomultiplier
<i>QY</i>	Quantum yield
<i>R</i>	Instrumental function
<i>R_B</i>	Ideal gas constant
RT	Room temperature
SAED	small angle electron diffraction
SEM	scanning electron microscopy
SNOM	scanning near-field optical microscopy
TEM	transmission electron microscopy
TMES	trimethylethoxysilane
UC	upconversion
UV	ultraviolet
VIS	visible
<i>W</i>	calibration spectrum
<i>x_e</i>	stoichiometric subscript calculated from EPMA results
XRPD	X-ray powder diffraction
YAG	Y ₃ Al ₅ O ₁₂

Table of Contents

Chapter 1

Introduction

1.1 Nanotechnology.....	3
1.2 Lanthanide spectroscopy	4
1.3 Luminescent of lanthanide ions in an inorganic host	7
1.4 Lanthanide doped nanoparticles	8
1.5 Upconverting nanoparticles.....	9
1.6 Applications of upconverting nanoparticles	12
1.6.1 Biological applications	12
1.6.2 Cancer therapy.....	12
1.6.3 Temperature nanosensors	12
1.6.4 Efficient solar cells	13
1.6.5 Security printing inks.....	13
1.6.6. Lighting devices.....	13
1.7 Upconversion processes	14
1.8 Host materials used in this thesis.....	15
1.8.1 Lutetium sesquioxides	15
1.8.2 Potassium lutetium double tungstates	17
1.9 Aims of this thesis	18
1.10 References	20

Chapter 2

Experimental Characterization Techniques

2.1. Introduction	29
2.2. X-ray powder diffraction (XRPD).....	30
2.3 Electron probe micro-analysis (EPMA)	33
2.4 Electron microscopy.....	35
2.4.1 Scanning electron microscopy (SEM)	35
2.4.2 Environmental scanning electron microscopy (ESEM).....	36
2.4.3 Transmission electron microscopy (TEM)	37
2.5 Differential thermal analysis (DTA).....	40
2.6 Optical spectroscopy	41
2.6.1 Optical absorption.....	41
2.6.2 Photoluminescence emission.....	43
2.6.3 Upconversion quantum yield	47
2.6.3 Photoluminescence decay	49
2.6.4 Cathodoluminescence	50
2.7 Scanning Near-Field Optical Microscopy (SNOM)	50
2.8 Raman and Fast Fourier infrared spectroscopy	52
2.7 References	54

Chapter 3

Synthesis and characterization of nanostructures

3.1. Introduction	59
3.2 Sol-gel Method	59
3.3 The modified Pechini Method	61
3.4 Tm ³⁺ doped Lu ₂ O ₃ nanocrystals	63
3.4.1 Differential thermal analysis and thermogravimetry	63
3.4.2 Crystal Lattice variation by Tm ³⁺ ion doping	63
3.4.3 Morphological characterization	64
3.4.4 Nanocrystalline grain growth as a function of temperature and time	66
3.4.5 Linear thermal expansion	67
3.5 Hydrothermal synthesis of sesquioxide Lu ₂ O ₃ nanorods	70
3.5.1 Introduction	70
3.5.2 Structural and morphological characterization	70
3.5.3 Gold decoration of Lu ₂ O ₃ nanorods by wetness impregnation	72
3.6 Synthesis of core-shell SiO ₂ @Ln ₂ O ₃ microstructures by modified Pechini method. Part I	75
3.6.1 Structural and morphological characterization	77
3.7 Synthesis of core-shell SiO ₂ @Ln ₂ O ₃ microstructures by modified Pechini method. Part II	79
3.7.1 Synthesis and morphological characterization	79
3.7.2 Functionalization with a silane coupling agent	84
3.8 Hydrothermal synthesis of core-shell SiO ₂ @Ln ₂ O ₃ microstructures	86
3.8.1 Lanthanide nitrates as precursors	88
3.8.2 Lanthanide chlorides as precursors	89
3.8.3 Effect of long isothermal annealing	89
3.9 Synthesis of lanthanide doped KLu(WO ₄) ₂ double tungstates nanocrystals	91
3.10 References	96

Chapter 4

Optical properties of doped sesquioxide nanostructures

4.1 Introduction	101
4.2 Spectroscopic properties of Tm ³⁺ in Lu ₂ O ₃ nanocrystals	101
4.2.1 Optical absorption	101
4.2.2 ³ H ₄ photoluminescence	104
4.2.3 ³ F ₄ photoluminescence	107
4.2.4 Discussion	109
4.3 Cathodoluminescence of Er ³⁺ in Yb:Lu ₂ O ₃ nanostructures	109
4.3.1 Effect of Yb ³⁺ concentration in Er,Yb:Lu ₂ O ₃ nanorods	109
4.3.2 Effect of Er ³⁺ concentration in Er,Yb:Lu ₂ O ₃ nanorods	110
4.3.3 SiO ₂ @Er:Yb:Lu ₂ O ₃ core-shell particles	111
4.3.4 Discussion	111
4.4 Cathodoluminescence of Tm ³⁺ in Lu ₂ O ₃ nanostructures	112
4.4.1 Effect of Yb ³⁺ in Tm,Yb:Lu ₂ O ₃ nanorods	112
4.4.2 Tm:Lu ₂ O ₃ nanocrystals	113
4.4.3 Discussion	114
4.5. Upconversion emission properties of Er ³⁺ in Er,Yb:Lu ₂ O ₃ nanostructures	114

4.5.1 Upconversion emission in Er,Yb:Lu ₂ O ₃ nanorods.....	114
4.5.2 Stokes emission in SiO ₂ @Er,Yb:Lu ₂ O ₃ core-shell particles.....	117
4.5.3 Upconversion emission in Er,Yb:Lu ₂ O ₃ nanoparticles.....	117
4.5.4 Discussion.....	117
4.6. Upconversion emission properties of Tm ³⁺ in Tm,Yb:Lu ₂ O ₃ nanostructures.....	119
4.6.1 Upconversion emission in Tm,Yb:Lu ₂ O ₃ nanorods.....	119
4.6.2. Upconversion emission in SiO ₂ @Tm,Yb:Lu ₂ O ₃ core-shell particles.....	120
4.6.3 Upconversion emission in Tm,Yb:Lu ₂ O ₃ nanoparticles.....	121
4.6.4 Discussion.....	122
4.7 Conclusions.....	122
4.8 References.....	124

Chapter 5

Yb³⁺ sensitized KLu(WO₄)₂ (KLuW) nanocrystals for white light generation

5.1 Introduction to CIE 1931 chromaticity theory.....	129
5.2 Ln, Yb:KLuW (Ln = Er, Ho, Tm) nanocrystals as red-green-blue emitters.....	131
5.2.1 Er,Yb:KLuW nanocrystals as green emitters.....	131
5.2.2 Ho,Yb:KLuW nanocrystals as yellow emitters.....	134
5.2.3 Tm,Yb:KLuW nanocrystals as blue emitters.....	137
5.2.4 Upconversion quantum yield.....	140
5.2.5 Chromaticity properties of upconversion emission.....	142
5.3 Physical mixture of Ho:Yb:KLuW and Tm:Yb:KLuW nanoparticles for white light generation.....	143
5.3.1 Proposed model.....	144
5.3.2 Upconversion emission.....	148
5.3.3 Upconversion quantum yield.....	150
5.3.4 Chromaticity.....	152
5.3.5 Stokes emission.....	152
5.4 Effect of Ho ³⁺ in Tm:Yb:KLuW nanocrystals.....	153
5.4.1 Upconversion emission and quantum yield.....	153
5.4.2 Chromaticity.....	155
5.4.3 Photoluminescence decay after 460 nm excitation.....	155
5.5 Effect of Tm ³⁺ in Ho:Yb:KLuW nanocrystals.....	157
5.5.1 Upconversion emission and quantum yield.....	157
5.5.2 Chromaticity.....	160
5.5.2 Photoluminescence decay after 460 nm excitation.....	160
5.6 Effect of Eu ³⁺ in Tm:Ho:Yb:KLuW nanocrystals.....	162
5.6.1 Upconversion spectra and quantum yield.....	162
5.6.2 Chromaticity.....	164
5.6.3. Stokes emission.....	164
5.6.4. Photoluminescence decay.....	166
5.6.5. Discussion.....	167
5.7 Conclusions.....	168
5.8 References.....	171

Chapter 6 Conclusions

6.1 Conclusions	175
-----------------------	-----

Chapter 7	
Printed Version Erratum.....	177

Chapter 1

Introduction

UNIVERSITAT ROVIRA I VIRGILI
LANTHANIDE-BASED DIELECTRIC NANOPARTICLES FOR UPCONVERSION LUMINESCENCE
Elixir William Barrera Bello
Dipòsit Legal: T. 450-2013

1.1 Nanotechnology

The start point of the technological possibilities at nanoscale can be traced back to 1959, when Richard Feynman gave a vision of the future of science in his speech titled “There’s Plenty of Room at the Bottom”, Feynman hypothesized that machine tools can build smaller and smaller machine tools until atoms and molecules can be manipulated like building blocks [1]. The first proof that atoms can be positioned by a manmade tool took place in 1989 when scientists at IBM manipulated 35 xenon atoms to form the letters IBM.

Nowadays, an important line of research is devoted to the nanoscience. Nanoscience is the study of phenomena on materials at atomic, molecular and macromolecular scales, where the properties can differ significantly from those at a larger scale. From technological application of nanoscience rises the nanotechnology, which includes the design, characterization, production and application of structures, devices and systems at nanometer scale. Figure 1.1 shows a schematic comparison of size particles in the nature.

The definition of nanoparticles differs depending upon the materials, fields and applications concerned. In many cases, the particles from 1 to 100 nm are generally called nanoparticles, but here they will be regarded as the particles smaller than those called conventionally “submicron particles”, and concretely less than the wavelength of visible light (its lowest limit is about 400 nm), which need to be treated differently from the submicron particles [2,3]. One nanometer is approximately the length of 10 hydrogen or 5 silicon atoms aligned in a line [4]. Materials in the micrometer scale mostly exhibit physical properties similar as that of bulk form; however, materials in the nanometer scale may exhibit physical properties distinctively different from that bulk [4].

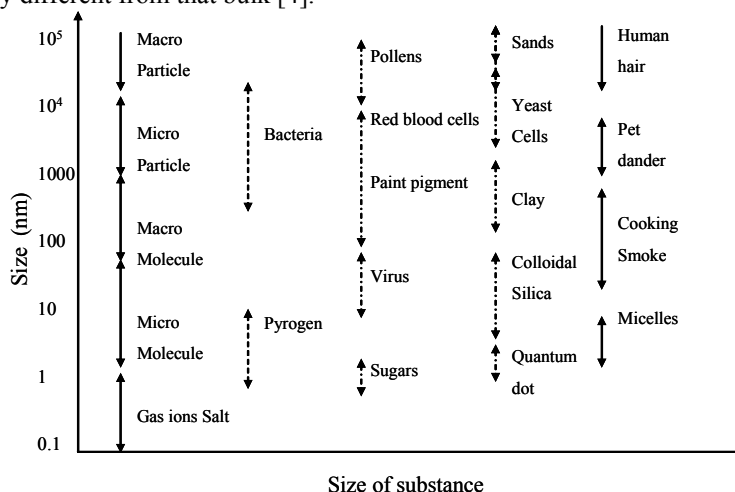


Figure 1.1. Examples of particles with their typical ranges of dimension.

As mentioned above, the chemical and physical properties of nanoscale particles are altered, providing new technological possibilities. These effects form when the mean size of crystalline grains does not exceed 100 nm, and are most evident when the grain size is

smaller than 10 nm. For example, metal crystals in the nanometer scale have a lower melting point than in bulk scale (the difference can be as large as 1000 K) and reduced lattice parameters, since the number of surface atoms or ions becomes a significant fraction of the total number of atoms or ions and the surface energy plays a significant role in the thermal stability [5]. Also, the change can be undesirable. Some ferroelectric nanoparticles can switch the polarization direction with thermal energy at room temperature, because transition temperature is size dependent, making them useless for data storage applications [6]. Nanoparticles can possess a large fraction of the atoms on their surface. A small nanoparticle of 1 nm diameter will have as much as 30% of its atoms on the surface, while a larger nanocrystal of 10 nm (approx. 1000 atoms) will have around 15% of its atoms on the surface [7]. Small enough nanoparticles can confine the electrons producing quantum confinement [8], appearing interesting properties as surface plasmon resonance in some metal particles [9], superparamagnetism in magnetic materials [10], and atom-like behavior in semiconductor quantum dots [11].

The use of nanotechnology has increased in many scientific disciplines, including electronics, stain-resistant clothing manufacture, and cosmetics [7]. The compression of nanoscale ceramic particles yields more flexible solid objects, apparently because of the multitude of grain boundaries that exist [12]. After further development of compression techniques, highly densified nonporous materials can be prepared, and these new materials may find uses replacing metals in many applications. Nanotechnology may especially hold the promise of significant improvements in human health in the field of potential medical applications, such as in drug delivery and development of fluorescent tags in bio-imaging and for cancer diagnosis and therapy [13,14].

1.2 Lanthanide spectroscopy

Lanthanide-activated luminescent materials are widely used for solid-state lasers, luminescent lamps, flat displays, optical fiber communication systems, and other photonic devices [15]. The lanthanides are the elements following lanthanum in the periodic table. In this range of elements the $4f$ shell is successively filled. Since the valence electrons are the same for all the ions, they all show very similar reactivity and coordination behavior.

Since luminescence of the trivalent lanthanide ions (Ln^{3+}) arises from transitions within the $4f$ shell and because this shell is shielded by filled $5s^2$ and $5p^6$ shells, electrons in the $4f$ orbitals have little participation in chemical bonding and the crystal field has almost no effect on the energy of the levels, i.e. the absorption and emissions of the ions are only slightly affected by the environment [15].

The alphanumeric designation next to each level is in accordance to the Russell-Saunders or LS coupling scheme. The labeling formula for each level in the LS coupling is $^{2s+1}L_J$; the s corresponds to the total spin multiplicity, L being the orbital angular momentum, and J representing total angular momentum. Figure 1.2 shows the energy levels of the $4f^N$ configurations. La^{3+} and Lu^{3+} are not shown because they have a completely empty and a completely filled $4f$ shell, respectively, and therefore have no optical transitions. Given the

above indicated weak influence of the crystalline neighborhood, this energy level diagram can be used for Ln^{3+} ions embedded in different host materials.

The selection rules for the different transitions are influenced by the symmetry of the environment. In a crystal site with inversion symmetry the electric dipole transitions are strictly forbidden [16]. However, when lanthanide is under the influence of a non-centrosymmetric crystal field, interactions allow the mixing of the higher energy configurations of opposite parity (like $4f^{N-1}5d$ [17]) into the $4f$ wavefunctions via the odd terms of the crystal field potential, relaxing the selection rules and the transition becomes partially allowed. This is called an induced (or forced) electric dipole transition [16].

Magnetic dipole transitions between the $4f^N$ states are not forbidden, but they are weak, and since the induced electric dipole transitions occur only as a consequence of a perturbation, both kinds of transitions have similar intensities in Ln^{3+} optical spectra.

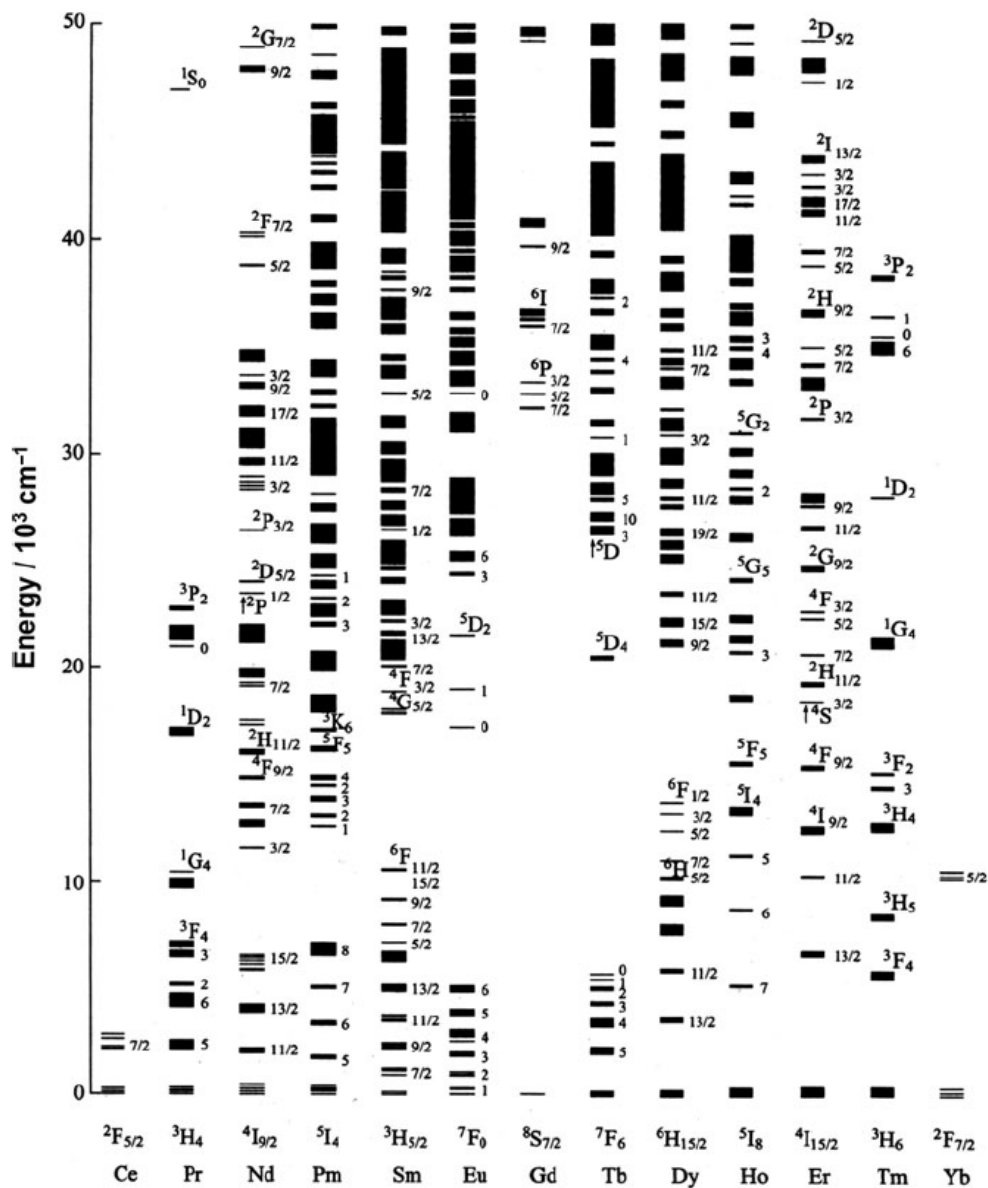


Figure 1.2. Energy level diagram for Ln³⁺ ions doped in a low-symmetry crystal, LaF₃ [18].

1.3 Luminescent of lanthanide ions in an inorganic host

Photoluminescence quantum yield is defined as the ratio of the number of emitted quanta to the number of absorbed quanta. In the absence of competing radiationless transitions its value is 1 (or 100%). The luminescence of lanthanide ions in inorganic hosts is generally characterized by high quantum yields and therefore long luminescence lifetimes [16]. There are, however, circumstances where the quantum yields of these inorganic materials are lowered by impurities such as hydroxyl groups. The other situation is that the separation between the energy levels of some lanthanide ions is so small that the vibrational energies of the inorganic host can also quench the luminescence by multi-phonon relaxation. In order to observe efficient lanthanide luminescence, materials with low phonon energies have to be used. Table 1.1 lists a summary of some of the commonly inorganic hosts.

Crystals are important for solid state laser applications [19]. Crystals were also important for the determination of the luminescence properties of lanthanide ions. In crystals, the Ln^{3+} ions can exist in a well-defined crystal sites. Thus, the specific characteristics of their optical spectra, mainly regarding the number of observed transitions for each multiplet, their relative intensity and the magnitude of the crystal field splitting, can provide important information about the crystalline environment of the Ln^{3+} in a given host. Glass hosts doped with Ln^{3+} are interesting materials for telecommunication where they can be integrated with un-doped optical glass fiber. In these glasses the Ln^{3+} do not have a fixed crystal site, which leads to inhomogeneous line broadening of all transitions which is advantageous for optical amplification purposes, as the useful photonic bandwidth is increased with respect to crystalline materials [20].

Table 1.1 Phonon energy extension of some inorganic host for luminescent lanthanide ions.

Material	Phonon energy [cm^{-1}]	Reference
Phosphate <i>g</i>	1200	[21]
Silica <i>g</i>	1100	[21]
Tellurite	750	[22]
Fluoride <i>g</i>	550	[21]
Chalcogenide <i>g</i>	350	[23]
LaPO ₄ <i>c</i>	1050	[21]
KLuW <i>c</i>	910	[24]
YAG <i>c</i>	860	[25]
YVO ₄ <i>c</i>	890	[26]
Lu ₂ O ₃ <i>c</i>	600	[91]
Y ₂ O ₃ <i>c</i>	600	[91]
NaYF ₄ <i>c</i>	550	[27]
LiYF ₄ <i>c</i>	560	[28]
LaF ₃ <i>c</i>	300	[29]
LaCl ₃ <i>c</i>	200	[21]

g glass *c* crystal

1.4 Lanthanide doped nanoparticles

Host materials with nanometer dimensions may affect the luminescence dynamics of the optically active lanthanide ion modifying the emission lifetime, quantum yield, and concentration quenching [30,31]. However the shift of electronic energy levels is not considered as a result of nano-confinement of electronic states. The quantum confinement of the energy level structure is not expected because the localized electronic states of the lanthanide ions [15].

According to crystal field theory, the electronic energy levels for lanthanide ions in nanoparticles may vary because of changes in the strength of local electrostatic field and site symmetry [30]. In nanoparticles, structure disordering and surface defects are inevitable, and emission lines in nanocrystalline materials show extra inhomogeneous broadening with regards to bulk crystals, especially due to the enormous increase in surface sites compared to bulk sites [32].

The symmetry of the lanthanide site can be modified in nanocrystalline materials. The change of lanthanide energy level structure in very small nanocrystals (1–10 nm) is due to a different local environment around the lanthanide ion that leads to symmetry modification. Decreasing the size of Eu doped YBO_3 nanoparticles lead to an increase of the $^5\text{D}_0 \rightarrow ^7\text{F}_2$ emission compared to other emission lines [33]. This effect was attributed to a lower symmetry around the Eu^{3+} ion. A similar effect was found for 14 nm Eu doped YVO_4 particles using selective-site spectroscopy [34]. In this technique excitation wavelength (narrow laser line) is slowly changed, scanning the absorption peak. Different Eu^{3+} sites with different site symmetries and luminescence lifetimes were found. The lower symmetry sites present lower lifetimes and they were attributed to sites on the nanoparticles surface. Nanofilms of $\text{Eu}:\text{Y}_2\text{O}_3$ with a thickness of 1 nm exhibit a completely different emission behavior from that of thick films (100–500 nm) [35], and also different photoluminescence properties have been observed for $\text{Eu}:\text{Gd}_2\text{O}_3$ in bulk and in 7 nm nanocrystals [36,37].

The environment around the lanthanide ion can change while the lanthanide ion is in the same crystal site inside the doped nanoparticles. It has been proved that non-solid medium surrounding the nanoparticles that changes the effective index of refraction of the media modifies the spontaneous emission of photons. Meltzer *et al* showed a dependence of refractive index and the luminescence lifetime of the Eu^{3+} ion in Y_2O_3 nanoparticles for different solvents [38]. This is originated from the change in the density of states for photons in the medium of reduced light velocity and the modification of the polarizability of the surrounding medium. A second mechanism influencing the spontaneous emission of photons is the size-dependent spontaneous emission rate due to interferences. Schniepp *et al* [39] have demonstrated a systematic change in the spontaneous emission rate of ions embedded in dielectric nanospheres by modifying the diameter and the dielectric surrounding.

Acoustic vibrations in nanoparticles possess a minimum size-quantized frequencies corresponding to the acoustic resonances of the particle. Usually below 20 nm size, density of phonon states becomes discrete and low frequency phonon modes are absent below a cutoff energy [15]. For this restriction on the phonon density of states in nanocrystals,

modifications of both luminescence lifetime and the efficiency of energy transfer are expected in comparison with bulk crystals [40]. Moreover, phonon assistance is also required in excitation via cross relaxation and upconversion in which energy mismatch in electronic energy levels is made up by lattice phonons.

Surface effects are expected in nanoparticles due to their inherently large surface area. In nanoparticles the surface can adsorb contaminants with high energy phonons favoring non-radiative relaxations [41]. It has been demonstrated that the quantum yield of doped insulating nanocrystals is usually lower than that of the bulk material as a result of energy transfer to the quenching centers at the surfaces as organic solvents, polymers or ligands [15]. It is expected that the quantum efficiency becomes solvent-independent shielding the lanthanide doped nanocrystal by covering with non-active optical material [42], since the lanthanide ions avoid contact with functional groups with high vibrational energy.

1.5 Upconverting nanoparticles

A great deal of attention has been given to the development of materials capable of generating short-wavelength radiation from long-wavelength pump sources as second-harmonic generation, simultaneous two-photon absorption, and upconversion [43]. Upconversion is a multi-step process where a near infrared (NIR) photon excites the ion from the ground-state to an intermediate state, which necessarily must possess a long lifetime, and from this a second NIR photon excites again the ion to a higher energy second excited state, from which a shorter wavelength emission is generated. In this way, with an appropriate choice of Ln^{3+} ion, visible emission can be achieved by NIR pumping. It is advantageous to excite at this wavelength range to avoid photo-degradation of the phosphor material caused by the high energy photons.

Yb^{3+} ion is used as sensitizer, transferring the absorbed energy to other lanthanide ions, because it has a broad absorption band [44] at 980 nm that can be pumped with low cost diode lasers, and it only shows one excited energy level in the electronic structure, reducing the non-radiative losses. The electronic energy level structure of Yb^{3+} is simple with only two levels: The ground state $^2F_{7/2}$ and the excited state $^2F_{5/2}$. The gap between these two levels is $\sim 10200 \text{ cm}^{-1}$ so, the non radiative emissions by multiphonon relaxation are strongly reduced. Some lanthanide ions are capable to emit upconversion luminescence because they possess particular ladder-like configuration of the electronic energy level. A second requirement is the presence of absorption bands around 980 nm. Er^{3+} , Ho^{3+} and Tm^{3+} feature this distribution and they are the most frequently used as emitting ions. Also other ions as, Dy [45], Tb [59], Pr [45] and Ce [58] have been reported for upconversion sensitized by Yb^{3+} .

Ln^{3+} doped upconverting nanoparticles (Ln-UCNPs) have shown great potential for use as luminescent materials. Upconversion process has been known since 1960 [46], and it was originally exploited for optical devices as IR quantum counters, temperature sensors and solid state lasers. From 1990, with the fast growth of nanoparticles research, new possibilities were opened for bioanalytical assays and luminescent imaging [47]. The

advantage of Ln-UCNPs is that the host shields the Ln³⁺ ion from the environment. The emission bands are narrow, they can be resolved easily and they possess a large anti-stokes shift relative to the excitation source, enabling the simultaneous use of multiple lanthanide probes to quantitatively detect several analytes without cross-interference [48]. Unlike quantum dots, Ln-UCNPs do not suffer from the photochemical destruction by the light exposure necessary to stimulate them into fluorescence (photo-bleaching), nor for fluorescence intermittency (blinking), and the emission wavelength is not size dependent.

The strategies for obtaining new upconverting nanoparticles not only involve the variation of the lanthanide ions, but also the variation of the host lattice, for example, the change from one having high phonon energies to one having low phonon energies can dramatically affect the competition between multiphonon and other radiative and nonradiative processes, and may lead to entirely different upconversion luminescence properties of a given ion. Also, the use of host materials with specific optical or magnetic properties may also influence the upconversion properties of a dopant ion through sensitization or perturbation by exchange interactions [43]. For practical application of UCNPs is required that Ln³⁺ can be incorporated into a host chemically stable and compatible with respect to the intended application. It is desired to synthesize small homogeneous UCNPs in size range of less than 50 nm with high upconversion efficiency. For this reason most studies focus on the systems containing Er or Tm in hosts with low phonon cutoff frequency, such as fluorides, in an effort to improve the efficiency by reducing the non-radiative relaxation rate from the metastable excited state [15]. Table 1.2 lists some selected examples of UCNPs. Multicolor emission can be reached by changing the host or the active lanthanide ion. The most frequently used hosts for upconversion are the fluorides and oxides, typically NaYF₄ and Y₂O₃. NaYF₄ possesses low phonon energy and the highest upconversion quantum yield (2-4 %) [49] and it is the most extended used material for bio-imaging applications due to absence of cytotoxicity in incubated cells. However, halide-based families are usually hygroscopic and show relatively poor chemical and photophysical stabilities compared with oxide matrices [42]. Also sub-20-nm hexagonal-phase NaYF₄ nanocrystals require air-sensitive, toxic organometallic precursors and hazardous coordinating solvents, which have become matters of substantial environmental concern [50].

The upconversion mechanisms in UCNPs can be more complicated than in the bulk crystals. In the case of Yb³⁺, Er³⁺ ions, a significant deviation from quadratic dependence on pumping power is observed in red and green emissions, which has been associated to changes in phonon modes and surface states [51]. Vetrone *et al* [52] report a significant enhancement of red upconverted emission between identically doped bulk and nanocrystalline Er,Yb:Y₂O₃ samples related to the concentration of Yb³⁺ ions. However the dramatic difference in the relative green-to-red ratios is much more pronounced in nanocrystals. A mechanism considering that nanocrystalline lattice adsorbs CO₂⁻³ and OH⁻ functional impurities on the surface has been proposed. These species have vibrational energies of 1500 and 3350 cm⁻¹, respectively and due to the large surface-to-volume ratio these high energy phonons interact with Er³⁺ ions creating a second population channel of the Er³⁺ ⁴F_{9/2} level, from which the red emission is radiated.

Table 1.2 Selected types of upconverting nanoparticles, typical excitation wavelengths (λ_{EXC}), emission peaks, diameters, and method of preparation.

Host lattice	Dopant ion	λ_{EXC} [nm]	Emission peaks [nm]	Diameter [nm]	Method of preparation	Reference
NaYF ₄	Yb, Er	980	518, 537, 652	33–166	Co-precipitation	[53,54]
	Yb, Tm	980	449, 474, 644, 693, 800	33		[55]
	Yb, Er, Tm	980	449, 474, 525, 545, 644, 693, 800	20	Solvothermal	[56]
	Yb, Ho, Tm	980	450, 475, 545, 650, 695	rods 110nm × 1 μ m	Hydrothermal	[57]
	Yb, Ho		541,647	100	[58]	
GdVO ₄	Yb, Tb	970	380, 413, 436, 488, 542, 584, 620	70		[59]
	Yb, Er	980	548–555	30–45		[60]
	Yb, Ho		645–665			
Lu ₂ O ₃	Yb, Tm		475,650			
	Yb, Er	980	525, 550, 650-690	rods 90nm × 45 μ m		[61]
Gd ₄ O ₃ F ₆	Yb, Tm		450-465, 470-490			
	Yb, Er, Tm	980	477, 523, 651-678, 800	50		[62]
	Yb, Er	980	510–530, 530–570, 635–675;	25–70	Ionothermal	[63]
	Yb, Tm		440–500, 630–670, 750–850			
NaYbF ₄	Yb, Ho	980	542, 645, 658	5–20	Thermal decomposition	[64]
	Ho	980	540, 650	20	Solvothermal	[65]
	Tm		476, 800			
CaF ₂	Er		520, 540, 655			
	Yb, Er	920	535-564, 638-685	11	Solvothermal	[66]
Gd ₄ O ₃ F ₆	Yb, Tm		635-667, 721-835			
	Yb, Er	980	521, 545, 659	~4	Thermal decomposition	[67]
BaTiO ₃	Yb, Er	980	523, 542, 662	~20	Sol–gel processing	[68]
	Yb, Tm		461, 478			
La ₂ O ₃	Yb, Er	976	240, 335, 350, 380, 409, 460, 475, 495,	~50	Combustion	[69]
			523, 548, 672			
Y ₂ O ₃	Yb, Er	978	520-579, 645-690	~20		[52]
Lu ₂ O ₃	Yb, Er, Tm	980	477/490, 540/565, 662	~40	Solvothermal	[70]

1.6 Applications of upconverting nanoparticles

1.6.1 Biological applications

Ln-UCNPs are suitable for bio-analysis applications because under NIR 980 nm excitation the absorption of biological matter, especially water is weak, reducing the background absorption, and the self-luminescence in other biological samples as proteins and nucleic acids [46]. The NIR excitation reduces the photo-damage and allow deep penetration [71], increasing the signal-to-noise ratio and thus improving detection. Ln-UCNPs have capability for multiple analyses by doping with different Ln³⁺ ions. Ln-UCNPs are easy internalized by many cells. Usually to increase the hydrophilicity, Ln-UCNPs are coated with a nanolayer of silica, and finally the surface is functionalized by covalent linkage of the adequate antibody using know conjugation methods [47]. Ln-UCNPs offer several advantages over organic dyes and fluorescent proteins in bio-imaging applications. Their very long luminescence lifetimes enable quantitative spatial determination of the intracellular concentration of an analyte through time-gating measurements.

1.6.2 Cancer therapy

Ln-UCNPs have been also applied for cancer photo dynamic therapy. Qian *et al* [72] report Er:Yb:NaYF₄ nanoparticles coated with a mesoporous-silica, where a photo-sensitizer (zinc phthalocyanine) was incorporated into this layer. The nanoparticles are injected into the blood stream, which stays into cells of whole body for several hours. After a certain period of time, nanoparticles leave the normal cells but remains in cancer cells for a longer time. Then, 980 nm excitation source is radiated on the affected part of body, that activates the photo-sensitizer remaining in cancer cells, and release the active singlet oxygen (¹O₂) that possibly kills the cancer cells [73].

1.6.3 Temperature nanosensors

Nanothermometry is a challenging topic, of great interest when temperature monitoring is required in integrated photonic devices to avoid deterioration and fatal failure [74]. Also temperature is known to be a critical parameter affecting living cell division rates, and hence the rate of tissue growth [75]. In these potential applications, thermal sensing must be achieved with the minimum perturbation of the thermal information. The temperature sensing techniques using luminescent nanoparticles analyze the spectral shift and band-shape [76] between energy levels with a separation of the order of some $k_B T$'s where $k_B T \sim 200 \text{ cm}^{-1}$ at room temperature. The most common technique is the so called fluorescence intensity ratio [77], and one of the most widely used trivalent lanthanide ion for thermal sensing is Er³⁺, because the energy gap between ⁴S_{3/2} and ²H_{11/2} energy levels fall into the 200-2000 cm⁻¹ range, so they are thermally coupled energy levels, and follow a Boltzmann like distribution, where the emitted intensities are proportional to the population of each emission level. Promising Er:Yb:Y₂O₃ nanoparticles have been reported for 400 – 800 K temperature sensing using the thermally coupled ⁴S_{3/2}, ²H_{11/2} energy levels, and for 20 – 300

K using the thermally coupled $^4F_{9/2}$ Stark levels [78]. Tm:Ho:Yb:Y₂O₃ nanoparticles using the intensity ratio between $^1G_4 \rightarrow ^3H_6$ and $^5F_3 \rightarrow ^3H_6$ transitions (i.e. I_{477nm}/I_{488nm}) were also reported as nano-thermometers at 300-584 K [79].

1.6.4 Efficient solar cells

Ln-based nanoparticles open new possibilities for the improvement of solar cells in the UV and in the near infrared spectral region. Semiconductor polymeric materials used for organic solar cells, as poly 3-hexylthiophene, extend their conversion spectral range if Eu:La₂O₃ nanoparticles are embedded. The Eu:La₂O₃ nanoparticles absorb the UV radiation at ~280 nm (due to O–Eu charge transfer band) and emit visible radiation (Eu³⁺ f-f transitions), that is efficiently absorbed by the semiconductor polymer [80]. In conventional solar cells, all the photons of the solar spectrum with energy lower than the solar cell energy gap are lost. The lost part, constituted by low energy near infrared photons from the solar spectrum, can be converted to high-energy photons, using the processes of upconversion in Yb³⁺ sensitized nanoparticles, which can then be utilized by the solar cell [81].

1.6.5 Security printing inks

Nowadays, security on printed documents is a key issue to maintain confidence. The fight against counterfeit and falsification demands an increment in security measurements and fake printing detection, not only for high-quality fake bank notes, but even for package in fake medications that put patient's lives at risk. Security printing inks based on Er:Yb:NaYF₄ and Tm:Yb:NaYF₄ nanoparticles has been reported by J Meruga *et al.*, for printing invisible quick-response (QR) codes on paper [82]. Once illuminated by the NIR light, the QR code become visible and it can be read by a smartphone in the conventional manner. The nanoparticles are both chemically and mechanically stable and they could withstand the stresses and strains of being placed on paper. Extension of this technology for printing on glass and flexible plastic films can include a wide variety of solid commercial goods [83].

1.6.6. Lighting devices

Ln-UCNPs are attracting attention for applications of VIS and NIR emitting phosphors. Upon excitation on the Yb³⁺ $^2F_{5/2}$ energy level, red, green and blue luminescence can be combined to obtain white light [84]. UC technology could be applied for backlighting in liquid crystal displays (LCDs) since currently the white-light sources have very broad emission spectra requiring that most of the light generated be filtered. The filtered emissions result in undesirable heating of the display and losses of energy [85]. Bright white light by UC has been obtained in Ln-UCNPs suspended in SiO₂ thin films, namely 5-6 nm LaF₃ nanoparticles co-doped with Yb-Eu, Yb-Er and Yb-Tm for red and green, red, and blue emission, respectively [86]. The possibility of a backlighting-type panel of white light using a UC-based white light emitter was demonstrated by J Milliez *et al* [85] through the mixture of 0.4% Tm, 20% Yb:KYF (blue) and 1% Er, 18% Yb:YF (red) microcrystalline powders.

The resulting mixture was dispersed in phosphorylated polymethyl-metacrylate (p-PMMA) serving as a passive polymeric binder and deposited on the edge of microscope slide.

1.7 Upconversion processes

Upconversion mechanisms involve some combination of absorption and non-radiative energy transfer (ET) steps. Absorption may come in two basic forms. Ground state absorption (GSA, Figure 1.3a) results in promotion of an ion from its ground state to an excited state. Excited-state absorption (ESA, Figure 1.3b) involves absorption of a photon by an excited ion, and results in promotion of that ion to a higher excited state.

Energy transfer may take a variety of forms. ET among levels of the same kind of ions is the basis for the common phenomenon of energy migration (Figure 1.3c). A similar process between unlike ions may lead to quenching or sensitization effects. ET among unlike levels may result in cross relaxation (CR), by which an ion is partially deactivated through ET to a ground-state neighbor, resulting in two ions in lower excited levels (Figure 1.3e). The reverse of cross-relaxation is also possible, in which a low-lying neighbor sacrificially donates its excitation energy to a neighboring excited ion, which is then promoted to a higher excited state. This process is referred to as energy-transfer upconversion, ETU (Figure 1.3f)

The predominant mechanisms of upconversion in Ln-UCNPs are: (1) GSA followed by ESA excited state absorption (GSA/ESA). (2) One that involves ETU following initial excitation of two ions by GSA energy transfer upconversion (GSA/ETU).

The GSA/ESA upconversion is inherently to a single optical center and this mechanism is relatively insensitive to concentration of the upconversion ion. The GSA/ETU is the most common upconversion mechanism [87]. The advantages offered by these types of upconversion processes are that they can be induced even by a low-power CW diode laser, without the need of an expensive high-power pulsed laser source.

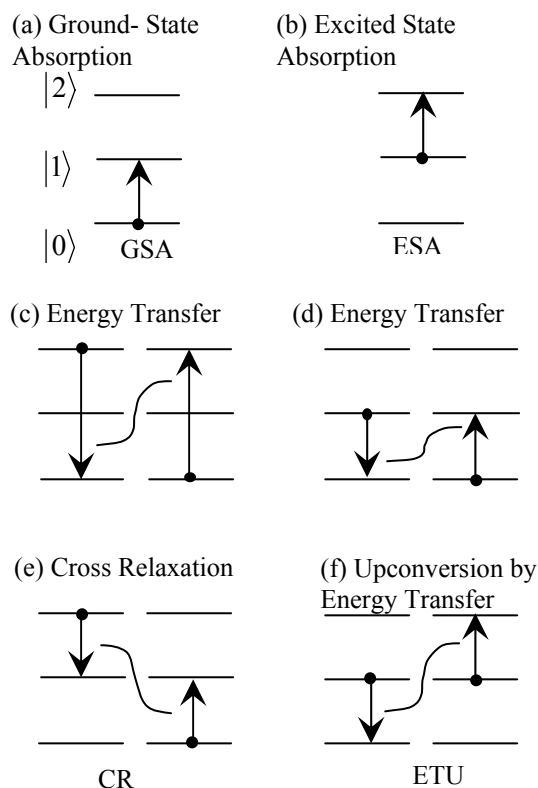


Figure 1.3. The basic energy transfer processes in upconversion mechanisms.

1.8 Host materials used in this thesis

1.8.1 Lutetium sesquioxides

The lanthanide sesquioxides (Ln_2O_3) are a group of compounds that are attractive from a technological and scientific viewpoint. Various applications of these compounds have been reported, specially for the sesquioxides with cubic bixbyite structure are isotropic and thus attractive for ceramic lasers [88]. Among the rare earth laser hosts, the sesquioxides Sc_2O_3 , Y_2O_3 , Gd_2O_3 , and Lu_2O_3 are known for their superior thermo-mechanical properties [89]. Their thermal conductivity considerably exceeds that of $\text{Y}_3\text{Al}_5\text{O}_{12}$ (YAG). So far the most efficient sesquioxide crystal laser has been $\text{Yb}:\text{Sc}_2\text{O}_3$, which possesses the largest ground-state splitting and emission cross section, and exhibits the highest thermal conductivity at low doping levels [7]. On the other hand, in lighting applications Eu -doped Y_2O_3 is still considered to be one of the best red downconverting oxide phosphors, mainly because of its excellent luminescence efficiency, color purity and stability [90].

The lutetium oxide, Lu_2O_3 , has been on focus recently due its potential applications in lasers, phosphors for lighting and displays, scintillators, etc. It has favorable properties, such

as high melting point, phase stability, low thermal expansion, and chemical stability. Furthermore, it possesses relative low phonon energy (about 393 cm^{-1}) [91], which is helpful for the enhancement of upconversion process. Lu_2O_3 nanoparticles have received special attention due to the enhanced intensity of emission detected for smaller size particles, and they can also be sintered in transparent ceramics [92].

The A form sesquioxide is hexagonal, with symmetry of the space group $P\bar{3}2/m$, with one formula per unit cell. The A-type structure has been found from La_2O_3 to Nd_2O_3 . The B form sesquioxide is a monoclinic distortion of the A form, possessing space group $C2/m$ with six formulas units per cell. The metal atoms in the B-type polymorph are seven and six coordinated [93, 94].

At room temperature, lanthanide oxides form the C-type, the most stable at all temperature for ordinary pressures [94]. The C-type structure, also know as bixbyite, is cubic with symmetry of the space group $Ia\bar{3}$. The unit cell contains 16 formula units, with 32 cations and 48 oxygen atoms per unit cell. The $Ia\bar{3}$ is related to a doubled-edge fluorite structure with one quarter of the oxygen sites vacant and regularly ordered, where the lanthanide ions are six-coordinated.

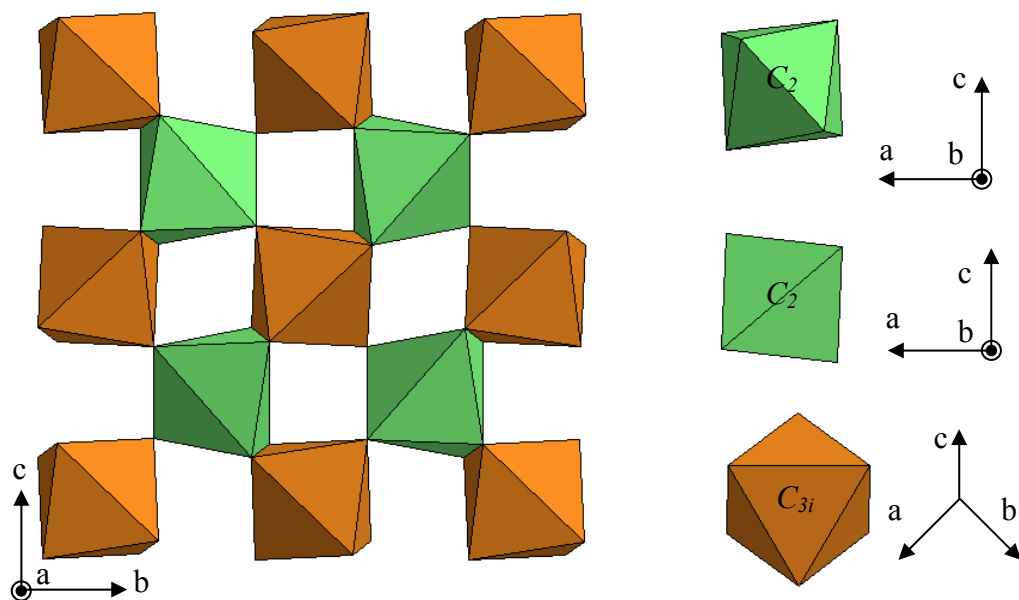


Figure 1.4. The cubic C-type Ln_2O_3 structure view parallel to $[1\ 0\ 0]$.

Twenty four of the lanthanide ions into the cell are on sites with two-fold rotational symmetry (C_2), and the eight remaining are on sites with three-fold rotatory inversion symmetry (C_{3i}) [94]. The oxygen coordination around the two lanthanide sites is shown in Figure 1.4. For the C_2 site, the oxygen falls almost on the corners of a cube with the

lanthanide at the center and with two missed oxygen atoms along a face diagonal. The two-fold axis is perpendicular to this diagonal face. One of the symmetry elements of the space group is the body-centered translation, so that there are two C_2 sites with the configuration pictured in Figure 1.4. There are six more sites with the same $[0\ 1\ 0]$ symmetry axis but with oxygen atoms missing along different face diagonals. Similarly there are eight sites with the twofold axis along $[1\ 0\ 0]$ and eight along $[0\ 0\ 1]$. For the C_{3i} sites the missing oxygen atoms are along $[1\ 1\ 1]$ directions. There are two lanthanide sites with the local symmetry axis along each of the four different $[1\ 1\ 1]$ directions [94].

1.8.2 Potassium lutetium double tungstates

In 1969, the structure of the low temperature monoclinic phases of $\text{KLu}(\text{WO}_4)_2$ (KLuW) was reported in the $I2/c$ space group [95,96]. Later, the structure was revised and refined in the $C2/c$ using powder samples [97,98] and single crystals [99,100]. The monoclinic double tungstates $\text{KLn}(\text{WO}_4)_2$ ($\text{Ln} = \text{Gd}, \text{Y}$ and Lu) are particularly interesting due to the high crystallographic anisotropy and high non-linear third-order coefficient [101]. Monoclinic KLuW host is a well-known material for laser applications [24] and more recently optical waveguide applications [102]. Along with the high Ln^{3+} doping admittance [99] specific main advantages of KLuW with regards to isostructural KYW and KGdW hosts are the higher optical absorption and emission cross sections as well as higher crystal field splitting for Ln^{3+} -doping ions [9]. Several properties of KLuW, like the maximum phonon energy ($\hbar\omega = 908\ \text{cm}^{-1}$) [24], thermal conductivity, hardness, optical transparency, and refractive index are very similar to those of the isostructural KYW [103].

The unit cell of KLuW contains 4 formula units. The Lu^{3+} ion in the unit cell is eightfold coordinated by oxygen atoms, forming a distorted square antiprism (Figure 1.5). These polyhedra form simple chains that extend in the $[101]$ direction. The Ln^{3+} ions are located in atomic sites with C_2 symmetry along the binary axes and substitution by dopant ions takes place only at this site. The W^{6+} ion is six coordinated by oxygen atoms. The WO_4^{2-} anions form a double chain along the c direction (Figure 1.5). The shorter distance Lu-Lu in the KLuW host, $5.98\ \text{\AA}$, is for adjacent cations in the same chain. For Lu-Lu located in different chains the minimum distance is $7.49\ \text{\AA}$.

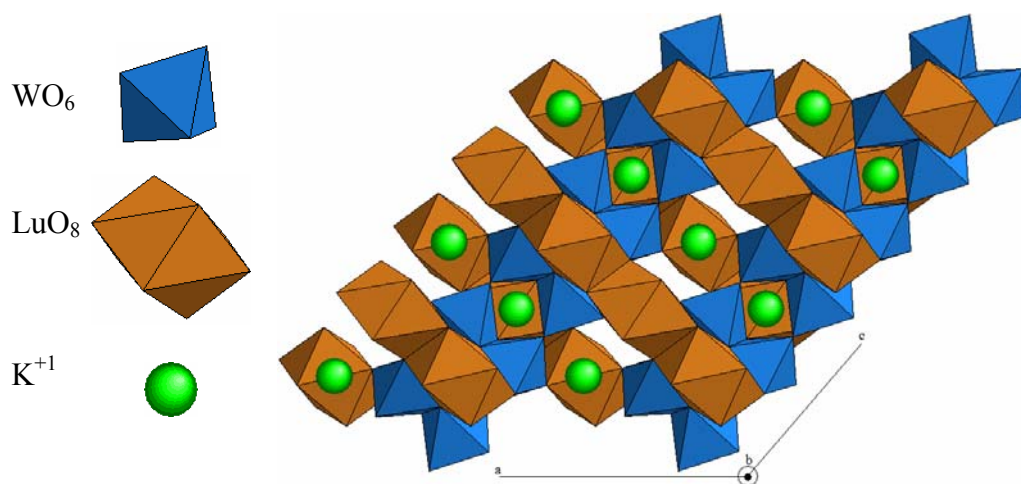


Figure 1.5. Projection parallel to [010] showing polyhedra chains along [101] and [001] for lutetium and tungsten ions, respectively.

1.9 Aims of this thesis

The aim of this work is the synthesis of nanostructures and the study of the luminescence of optically active Ln³⁺ embedded in Lu₂O₃ and KLuW nanostructures. Through the comparison with analog bulk crystals, the optical features associated to the nanoscale will be considered. The modified Pechini method has been used for producing Lu₂O₃ and KLu(WO₄)₂ nanoparticles as well as SiO₂@Lu₂O₃ core-shell structures, and Lu₂O₃ nanorods have been produced by a soft hydrothermal method in collaboration with the Instituto de Ciencia de Materiales de Madrid. Specifically we have focused on four kinds of lanthanide doped nanostructures produce by chemical routes:

- Tm:Lu₂O₃ nanocrystals as precursor for laser ceramics.
- Ln:Yb:Lu₂O₃ nanorods for upconversion emission.
- SiO₂@Ln:Yb:Lu₂O₃ core-shell particles for study surfaces effects on upconversion emission.
- Ln:Yb:KLu(WO₄)₂ nanocrystals for white light generation.

As a requirement for producing transparent ceramic materials with free-porous structures, the production of highly crystalline Tm:Lu₂O₃ nanoparticles with narrow size distribution is a first step for sintering below melting point at low or high pressure [104]. The Tm³⁺ ion has a large optical absorption around 785–810 nm, which is suitable for commercially available laser diodes, as AlGaAs laser diode operating at 800 nm, to produce laser emission at 1.9 μm. Although Ho³⁺ lacks a strong absorption for diode pumping at 800 nm, it can be sensitized in this region with Tm³⁺ codoping [105] or Tm lasers using a pumping cascade scheme [106], emitting around 2.1 μm. Around 1.9 μm, there is a local maximum of water

absorption in the eye safe region, generating many applications of this emission, such as surgery and other medical laser applications [107].

It was foreseeable that crystalline 1D nanostructures can be applied in optoelectronics and luminescence applications [108]. Also, 1D crystalline nanostructures can play an important role as functional building units for the fabrication of nanodevices based on 2D or 3D ordered structures [61]. As one important phosphor material with analogous structure of Y_2O_3 , more and more attentions have been paid to fabricate Lu_2O_3 -based low dimensional nanostructures [108], for the favorable incorporation of the highest concentrations of Ln, with absorption and emission cross sections larger than the more usual Y_2O_3 host [109]. In this work, we use a low-temperature hydrothermal method for preparation of Ln:Yb: Lu_2O_3 (Ln= Er, Tm) nanorods and describe their upconversion and cathodoluminescence behavior. These nanorods can avoid photo-bleaching due to their high chemical stability [110] and possess potential applications in biological imaging, as well as photodynamic therapy, as the analog Y_2O_3 [111]

The modified Pechini method has been used by the Jun Li *et al* for depositing active layers on the surface of SiO_2 spheres to obtain core-shell particles [112] after several deposition cycles. The most part of reported SiO_2 core-shell particles are focused on the optical properties of Eu^{3+} ions in view of their high absorption and emission properties [15]. Sometimes Tb^{3+} is also included because Tb^{3+} sensitizes Eu^{3+} [113,114] and also serve as a green emitter [115]. However, upconversion emission in core-shell particles has not been explored. In this work, we study the synthesis procedure for depositing Lu_2O_3 layers doped with Er^{3+} and Yb^{3+} on SiO_2 microspheres. Er^{3+} was chosen because it shows a high upconversion quantum yield when it is sensitized with Yb^{3+} . Core-shell particles can be useful to study surface modifications on the lanthanide luminescence or for the synthesis of lanthanide-doped hollow spheres [15].

Currently there is a great interest to tailor new Ln-doped white light emitting materials at the nanoscale for the construction of more complex devices such as solid-state multicolor three dimensional displays and back light in LCDs. Through appropriate choice of Ln^{3+} ions, red-green-blue emissions can be achieved simultaneously by NIR pumping to obtain the desired white light. In this way, we have characterized the power dependence of the upconversion emission of Ln:Yb:KLuW (Ln = Er, Ho, Tm) nanocrystals, and the possibility to tune the chromaticity by mixture of Tm:Yb:KLuW and Ho:Yb:KLuW nanocrystals. Also, we have studied the generation of red-green-blue emission in Tm:Ho:Yb:KLuW nanocrystals, as well as the effect of the variation of Tm^{3+} and Ho^{3+} concentration and of the doping with Eu^{3+} in the latter materials.

1.10 References

- [1] J. C. Miller, R. Serrato, J. M. Represas-Cardenas, and G. Kundahl, *The handbook of Nanotechnology*, John Wiley & Sons, Inc. (2005).
- [2] M Hosokawa, K. Nogi, M Naito, T Yokoyama *Nanoparticle Technology Handbook 2nd Edition* Elsevier B.V. Amsterdam (2007).
- [3] B. Bhushan, *Handbook of nanotechnology*, Springer, (2004).
- [4] G. Cao *Nanostructures and Nanomaterials*, World Scientific Publishing Company.
- [5] I. Hrivnak, *Nanocrystalline Materials*, Cambridge International Science Publishing, (1995).
- [6] A. Gruverman, A. Kholkin *Nanoscale ferroelectrics: processing, characterization and future trends* **Rep. Prog. Phys.** 69 2443–2474 (2006)
- [7] C. N. R. Rao, A. Müller, A. K. Cheetham *The Chemistry of Nanomaterials: Synthesis, Properties and Applications*. Wiley-VCH Verlag GmbH & Co Weinheim, (2004).
- [8] G. Binnig, H. Rohrer, Ch. Gerber, E. Weibel, *Surface Studies by Scanning Tunneling Microscopy*, Vol. 49, No 1, (1982).
- [9] R.B. Wehrspohn, H.-S. Kitzerow, K. Busch *Nanophotonic materials: photonic crystals, plasmonics, and metamaterials* Wiley-VCH, Weinheim (2008).
- [10] A. P. Guimarães, *Principles of Nanomagnetism*, Springer-Verlag Berlin-Heidelberg (2009).
- [11] P. P. Edwards, R. L. Johnston, C. N. R. Rao, *Metal Clusters in Chemistry*, Wiley-VCH, Weinheim (1999).
- [12] R. P. Andres, R. S. Averback, W. L. Brown, L. E. Brus, W. A. Goddard, A. Kaldor, S. G. Louie, M. Moscovits, P. S. Peercy, S. J. Riley, R. W. Siegel, F. Spaepen, Y. Wang *Research opportunities on clusters and cluster-assembled materials—A Department of Energy, Council on Materials Science Panel Report* **J. Mater. Res.** 4 704 (1989).
- [13] I. Brigger, C. Dubernet, P. Couvreur *Nanoparticles in cancer therapy and diagnosis* **Adv. Drug. Deliver. Rev.** 54 631–651 (2002).
- [14] X. Michaley, F. F. Pinaud, L. A. Bentolila, J. M. Tsay, S. Doose, J. J. Li, G. Sundaresa, A. M. Wu, S. S. Gamhir, S. Weiss *Quantum Dots for Live Cells, in Vivo Imaging, and Diagnostics* **Science** 307 538-544 (2005).
- [15] G. Liu, X. Chen *Spectroscopic properties of lanthanides in nanomaterials in Handbook on the physics and chemistry of rare earths vol. 37* edited by K. A. Gschneider, Jr., J.-C. G. Bünzli and V. K. Pecharsky Elsevier B. V. Amsterdam (2007).
- [16] J.-C. G. Bünzli, S. V. Eliseeva, *Basics of lanthanide photophysics* In *Lanthanide Luminescence: Photophysical, Analytical and Biological Aspects*; P. Hänninen, H. Härmä, Eds.; Springer-Verlag, Berlin, (2010).
- [17] M. C. Pujol *Obtenció i caracterització de cristalls monocíclics de $KGd(WO_4)_2$ substituïts amb lantànids* Ph.D. Dissertation. Universitat Rovira i Virgili, Spain (2000).
- [18] W. T Carnall, G. L. Goodman, K. Rajnak, R. S. Rana *A systematic analysis of the spectra of Lanthanides doped into single crystal LaF_3* . **J Chem. Phys.** 90, 3443–3457 (1989).
- [19] M. J. Weber *Handbook of lasers*, CRC Press LLC (2001).
- [20] M. H. V. Werts *Making sense of lanthanide luminescence* **Science Progress** 88, 101–131 (2005).
- [21] K. Soga, W. Wang, R. E. Riman, J. B. Brown, K. R. Mikeska *Luminescent properties of nanostructured Dy^{3+} - and Tm^{3+} -doped lanthanum chloride prepared by reactive*

- atmosphere processing of sol-gel derived lanthanum hydroxide* **J. Appl. Phys.** 93, 2946 (2003).
- [22] E. R. Taylor, L. Na Ng, N. P. Sessions, H. Buerger *Spectroscopy of Tm³⁺-doped tellurite glasses for 1470 nm fiber amplifier* **Appl. Phys.** 92, 112-117 (2002).
- [23] R. S. Deol, J. Wang, G. Wylangowski, J. A. Medeiros Neto, B. N. Samson, R. I. Laming, W. S. Brocklesby, D. N. Payne, A. Jha, M. Poulain, S. Otero, S. Surinach, M. D. Baro, *Low phonon-energy glasses for efficient 1.3 μm optical fiber amplifiers* **Electron. Lett.** 29, 237 (1993)
- [24] V. Petrov, M. C. Pujol, X. Mateos, O. Silvestre, S. Rivier, M. Aguiló, R. M. Sole, J. Liu, U. Griebner, F. Diaz, *Growth and properties of KLu(WO₄)₂ and novel ytterbium and thulium lasers based on this monoclinic crystalline host* **Laser & Photon. Rev.** 1, 179-212 (2007).
- [25] J. P. Horrell, S. P. S. Porto, I. F. Chang, S.S. Mitra, R. P. Bauman *Optical Phonons of Yttrium Aluminum Garnet* **Phys. Rev.** 173 851 (1968).
- [26] A. A. Kaminskii, K. Ueda, H. J. Eichler, Y. Kuwano, H. Kouta, S. N. Bagaev, T. H. Chyba, J. C. Barnes, G. M.A. Gad, T. Murai, J. Lu *Tetragonal vanadates YVO₄ and GdVO₄ – new efficient χ⁽³⁾-materials for Raman lasers* **Optics Commun.** 194 201-206 (2001).
- [27] J. F. Suyver, J. Grimm, M. K. van Veen, D. Biner, K. W. Krämer, H. U. Güdel *Upconversion spectroscopy and properties of NaYF₄ doped with Er³⁺, Tm³⁺ and/or Yb³⁺* **J. Lumin.** 117 1-12 (2006).
- [28] B. M. Walsh, N. P. Barnes, B. Di Bartolo *Branching ratios, cross sections, and radiative lifetimes of rare earth ions in solids: Application to Tm³⁺ and Ho³⁺ ions in LiYF₄* **J. Appl. Phys.** 83, 2772 (1998).
- [29] M. J. Weber *Probabilities for Radiative and Nonradiative Decay of Er³⁺ in LaF₃* **Phys. Rev.**, 157, 262 – 272 (1967).
- [30] B. M. Tissue, *Synthesis and Luminescence of Lanthanide Ions in Nanoscale Insulating Hosts* **Chem. Mater.** 10, 2837 (2008).
- [31] R. N. Bhargava, *Doped nanocrystalline materials - Physics and applications* **J. Lumin.** 70, 85 (1996).
- [32] D. K. Williams, B. Bihari, B. M. Tissue, J. M. McHale, *Preparation and Fluorescence Spectroscopy of Bulk Monoclinic Eu³⁺:Y₂O₃ and Comparison to Eu³⁺:Y₂O₃ Nanocrystals* **J. Phys. Chem. B** 102, 916 (1998).
- [33] Z. Wei, L. Sun, C. Liao, X. Jiang, C. Yan *Size dependence of luminescent properties for hexagonal YBO₃:Eu nanocrystals in the vacuum ultraviolet region* **J. Appl. Phys.** 93, 9783 (2003).
- [34] C. H. Yan, L. D. Sun, C. S. Liao, Y. X. Zhang, Y. Q. Lu, S. H. Huang, S. Z. Lü, *Eu³⁺ ion as fluorescent probe for detecting the surface effect in nanocrystals* **Appl. Phys. Lett.** 82, 3511 (2003).
- [35] S. Bar, G. Huber, J. Gonzalo, A. Perea, A. Climent, F. Paszti, *Europium-doped sesquioxide thin films grown on sapphire by PLD* . **Mater. Sci. Eng. B** 105, 30 (2003).
- [36] B. Mercier, C. Dujardin, G. Ledoux, C. Louis, O. Tillement, P. Perriat, *Observation of the gap blue shift on Gd₂O₃:Eu³⁺ nanoparticles* **J. Appl. Phys.** 96, 650 (2004).
- [37] C. Louis, R. Bazzi, M. A. Flores, W. Zheng, K. Lebbou, O. Tillement, B. Mercier, C. Dujardin, P. Perriat *Synthesis and characterization of Gd₂O₃:Eu³⁺ phosphor nanoparticles by a sol-lyophilization technique* **J. Solid State Chem.** 173 335–341 (2003).

- [38] R. S. Meltzer, S. P. Feofilov, B. Tissue, and H. B. Yuan, *Dependence of fluorescence lifetimes of $Y_2O_3:Eu^{3+}$ nanoparticles on the surrounding medium* **Phys. Rev. B** 60, R14012-R14015 (1999).
- [39] H. Schniepp, V. Sandoghdar *Spontaneous Emission of Europium Ions Embedded in Dielectric Nanospheres* **Phys. Rev. Lett.** 89, 257403 (2002).
- [40] X. Y. Chen, H. Z. Zhuang, G. K. Liu, S. Li, R.S. Niedbala *Confinement on energy transfer between luminescent centers in nanocrystals* **J. Appl. Phys.** 94, 5559 (2003).
- [41] F. Esteban-Betegón, C. Zaldo, C. Cascales *Hydrothermal Tm^{3+} - Lu_2O_3 Nanorods with Highly Efficient $2\ \mu m$ Emission* **Inorg. Chem.** 50 1836 (2011).
- [42] R. Calderón-Villajos, C. Zaldo, C. Cascales *Enhanced upconversion multicolor and white light luminescence in SiO_2 -coated lanthanide-doped $GdVO_4$ hydrothermal nanocrystals* **Nanotechnology** 23 505205 (2012).
- [43] D. R. Gamelin, H. U. Güdel, *Upconversion processes in transition metal and rare earth metal systems* **Top. Curr. Chem.** 214 1 (2001).
- [44] L. D. DeLoach, S. A. Payne, L. L. Chase, L. K. Smith, W. L. Kway, W. F. Krupke. *Evaluation of absorption and emission properties of Yb^{3+} doped crystals for laser applications.* **IEEE Journal of Quantum Electronics** 29, 1179 (1993).
- [45] X. Yu, M. Li, M. Xie, L. Chen, Y. Li, Q. Wang *Dopant-controlled synthesis of water-soluble hexagonal $NaYF_4$ nanorods with efficient upconversion fluorescence for multicolor bioimaging* **Nano. Res.** 3 51-60 (2010).
- [46] H. S Mader, P. Kele, S. M Saleh and O. S Wolfbeis *Upconverting luminescent nanoparticles for use in bioconjugation and bioimaging* **Curr. Opin. Chem. Biol.** 14:582–596 (2010).
- [47] S.V. Eliseeva, J.-C.G. Bünzli *Lanthanide luminescence for functional materials and bio-sciences* **Chem. Soc. Rev.** 39 189–227 (2010).
- [48] A. Thibon, V. C. Pierre *Principles of responsive lanthanide-based luminescent probes for cellular imaging* **Anal. Bioanal. Chem.** 394 107–120 (2009).
- [49] R. H. Page, K. I. Schaffers, P. A. Waide, J. B. Tassano, S. A. Payne, W. F. Krupke, W. K. Bischel *Upconversion-pumped luminescence efficiency of rare-earth-doped hosts sensitized with trivalent ytterbium* **J. Opt. Soc. Am. B**, 15 996-1008 (1998).
- [50] F. Wang, Y. Han, C. S. Lim, Y. Lu, J. Wang, J. Xu, H. Chen, C. Zhang, M. Hong X. Liu *Simultaneous phase and size control of upconversion nanocrystals through lanthanide doping* **Nature Letters** 463 1061-1065 (2010).
- [51] W. Wang, M. Wu, G. K. Liu. *Analysis of Upconversion Fluorescence Dynamics in $NaYF_4$ Codoped with Er^{3+} and Yb^{3+}* **Spectrosc. Lett.** 40 259-269 (2007).
- [52] F. Vetrono, J. C. Boyer, J. A. Capobianco, A. Speghini and M. Bettinelli *Significance of Yb^{3+} concentration on the upconversion mechanisms in codoped $Y_2O_3:Er^{3+}$, Yb^{3+} nanocrystals* **J. Appl. Phys.** 96 661 (2004).
- [53] G. Yi, H. Lu, S. Zhao, Y. Ge, W. Yang, D. Chen, L. -H. Guo *Synthesis, characterization, and biological application of size-controlled nanocrystalline $NaYF_4:Yb$, Er infrared-to-visible upconversion phosphors* **Nano Lett.** 4 2191-9196 (2004).
- [54] L Wang, R Yan, Z Huo, L Wang, J Zeng, J Bao, X Wang, Q Peng, Y Li *Fluorescence resonant energy transfer biosensor based on upconversion luminescent nanoparticles.* **Angew. Chem. Int. Ed.** 44 6054-6057 (2005).
- [55] Y. Wei, F. Lu, X. Zhang, D. Chen *Synthesis and characterization of efficient near-infrared upconversion Yb and Tm codoped $NaYF_4$ nanocrystal reporter.* **J. Alloys Compd.** 427333-340 (2007).

- [56] F. Wang, X. G. Liu *Upconversion multicolor fine-tuning: visible to near-infrared emission from lanthanide-doped NaYF₄ nanoparticles*. **J Am. Chem. Soc.** 130 5642-5643 (2008).
- [57] L. W. Yang, H. L. Han, Y. Y. Zhang, J. X. Zhong: *White emission by frequency up-conversion in Yb³⁺-Ho³⁺-Tm³⁺ triply doped hexagonal NaYF₄ nanorods*. **J Phys. Chem. C**, 113 18995-18999 (2009).
- [58] G. Chen, H. Liu, G. Somesfalean, H. Liang, Z. Zhang *Upconversion emission tuning from green to red in Yb³⁺/Ho³⁺-codoped NaYF₄ nanocrystals by tridoping with Ce³⁺ ions*. **Nanotechnology** 20 385704 (2009).
- [59] H. J. Liang, G. Y. Chen, L. Li, Y. Liu, F. Qin, Z. Zhang *Upconversion luminescence in Yb³⁺/Tb³⁺-codoped monodispersed NaYF₄ nanocrystals* **Optics Commun**, 282 3028-3031 (2009).
- [60] R. Calderón-Villajos, C. Zaldo, C. Cascales *Enhanced upconversion multicolor and white light luminescence in SiO₂-coated lanthanide-doped GdVO₄ hydrothermal nanocrystals* **Nanotechnology** 23 505205 (2012).
- [61] E. W. Barrera, M. C. Pujol, F. Díaz, S. B. Choi, F. Rotermund, K. H. Park, M. S. Jeong, C. Cascales *Emission properties of hydrothermal Yb³⁺, Er³⁺ and Yb³⁺, Tm³⁺-codoped Lu₂O₃ nanorods: upconversion, cathodoluminescence and assessment of waveguide behavior* **Nanotechnology** 22 075205 (2011).
- [62] T. Passuello, F. Piccinelli, M. Pedroni, M. Bettinelli, F. Mangiarini, R. Naccache, F. Vetrone, J.A. Capobianco, A. Speghini *White light upconversion of nanocrystalline Er/Tm/Yb doped tetragonal Gd₄O₃F₆* **Opt. Mater.** 33 643–646 (2011).
- [63] X. Liu, J. Zhao, Y. Sun, K. Song, Y. Yu, C. Du, K. Xianggui, H. Zhang *Ionothermal synthesis of hexagonal phase NaYF₄:Yb³⁺,Er³⁺/Tm³⁺ upconversion nanophosphors*. **Chem. Commun.** 6628-6630 (2009).
- [64] J. Shan, X. Qin, N. Yao, Y. Ju *Synthesis of monodisperse hexagonal NaYF₄:Yb, Ln (Ln = Er, Ho and Tm) upconversion nanocrystals in TOPO*. **Nanotechnology**, 18 445607 (2007).
- [65] O. Ehlert, R. Thomann, M. Darbandi, T. Nann *A four-color colloidal multiplexing nanoparticle system*. **ACS Nano**, 2 120-124 (2008).
- [66] N.-N. Dong, M. Pedroni, F. Piccinelli, G. Conti, A. Sbarbati, J. E. Ramírez-Hernández, L. Martínez Maestro, M. C. Iglesias-de la Cruz, F. Sanz-Rodríguez, A. Juarranz, F. Chen, F. Vetrone, J. A. Capobianco, J. García Solé, M. Bettinelli, D. Jaque, A. Speghini *NIR-to-NIR Two-Photon Excited CaF₂: Tm³⁺,Yb³⁺ Nanoparticles: Multifunctional Nanoprobes for Highly Penetrating Fluorescence Bio-Imaging* **ACS Nano** 5 8665–8671 (2011).
- [67] Y.-P. Du, Y.-W. Zhang, L.-D. Sun, C.-H. Yan: *Luminescent monodisperse nanocrystals of lanthanide oxyfluorides synthesized from trifluoroacetate precursors in high-boiling solvents*. **J Phys. Chem. C**, 112 405-415 (2008).
- [68] Y. Liu, W. A. Pisarski, S. Zeng, C. Xu, Q. Yang: *Tri-color upconversion luminescence of rare earth doped BaTiO₃ nanocrystals and lowered color separation*. **Opt. Express** 17 9089-9098 (2009).
- [69] S. K. Singh, A. K. Singh, D. Kumar, O. Prakash, S. B. Rai: *Efficient UV-visible up-conversion emission in Er³⁺/Yb³⁺ co-doped La₂O₃ nano-crystalline phosphor*. **Appl. Phys. B** 98 173-179 (2010).
- [70] J. Yang, C. Zhang, C. Peng, C. Li, L. Wang, R. Chai, J. Lin *Controllable red, green, blue (RGB) and bright white upconversion luminescence of Lu₂O₃:Yb³⁺/Er³⁺/Tm³⁺ nanocrystals through single laser excitation at 980 nm*. **Chem. Eur. J** 15 4649-4655 (2009).

- [71] D. K. Chatterjee, R. A. Jalil, Y. Zhang *Upconversion fluorescence imaging of cells and small animals using lanthanide doped nanocrystals*. **Biomaterials** 29 937-943 (2008).
- [72] H. S. Qian, H. C. Guo, P. C. -L. Ho, R. Mahendran, Y. Zhang *Mesoporous-silica-coated up-conversion fluorescent nanoparticles for photodynamic therapy* **Small** 5 2285-2290 (2009).
- [73] B. A. Lindig, M. A. J. Rodgers, A. P. Schaap, *Determination of the lifetime of singlet oxygen in water-d₂ using 9,10-anthracenedipropionic acid, a water-soluble probe* **J. Am. Chem. Soc.** 102 5590-5593 (1980).
- [74] E. Saidi, N. Babinet, L. Lalouat, J. Lesueur, L. Aigouy, S. Volz, J. Labeguerie-Egea, and M. Mortier *Tuning Temperature and Size of Hot Spots and Hot-Spot Arrays* **Small** 7, 259 (2011).
- [75] F. Tardieu, M. Reymond, P. Hamard, C. Granier, and B. Muller *Turgor, Cell Growth and Leaf Development* **J. Exp. Bot.** 51, 1505 (2000).
- [76] P. Haro-González, L. Martínez Maestro, M. Trevisani, S. Polizzi, D. Jaque, J. Garcia Sole, and M. Bettinelli *Evaluation of rare earth doped silica sub-micrometric spheres as optically controlled temperature sensors* **J. Appl. Phys.** 112, 054702 (2012).
- [77] S. A. Wade, S. F. Collins, G. W. Baxter *Fluorescence intensity ratio technique for optical fiber point temperature sensing* **J. Appl. Phys.** 94, 4743 (2003).
- [78] L. Liu, Y. Wang, X. Zhang, K. Yang, Y. Bai, C. Huang, Y. Song *Optical thermometry through green and red upconversion emissions in Er³⁺/Yb³⁺/Li⁺:ZrO₂ nanocrystals* **Opt. Commun.** 284 1876-1879 (2011).
- [79] A. Pandey, V. K. Rai *Colour emission tunability in Ho³⁺-Tm³⁺-Yb³⁺ co-doped Y₂O₃ upconverted phosphor* **Appl. Phys. B** 109 611-616 (2012).
- [80] M. Méndez, Y. Cesteros, L.F. Marsal, E. Martínez-Ferrero, P. Salagre, P. Formentín, J. Pallarès, M. Aguiló, F. Díaz, J.J. Carvajal *Polymer composite P3HT:Eu³⁺ doped La₂O₃ nanoparticles as a down-converter material to improve the solar spectrum energy* **Opt. Mater.** 33 1120 (2011).
- [81] R. Chai, H. Lian, Z. Hou, C. Zhang, C. Peng, J. Lin *Preparation and Characterization of Upconversion Luminescent NaYF₄:Yb³⁺, Er³⁺ (Tm³⁺)/PMMA Bulk Transparent Nanocomposites Through In Situ Photopolymerization* **J. Phys. Chem. C** 114 610 (2010).
- [82] J. M Meruga, W. M Cross, P. S. May, Q. Luu, G. A. Crawford, J. J. Kellar *Security printing of covert quick response codes using upconverting nanoparticle inks* **Nanotechnology** 23 395201 (2012).
- [83] W. J. Kim, M. Nyk, P. N Prasad *Color-coded multilayer photopatterned microstructures using lanthanide (III) ion co-doped NaYF₄ nanoparticles with upconversion luminescence for possible applications in security* **Nanotechnology** 20 185301 (2009).
- [84] B. Dong, H. Song, R. Qin, X. Bai, S. Lu, X. Ren, G. Pan, H. Zhang, F. Wang, L. Fan *Upconversion White Light Devices: Ln³⁺-Tridoped NaYF₄ Nanoparticles and PVP Modified Films* **J. Nanosci. Nanotechnol.** 8, 3921-3925 (2008).
- [85] J. Milliez, A. Rapaport, M. Bass, A. Cassanho, H. P. Jenssen, *High-Brightness White-Light Source Based on Up-Conversion Phosphors* **J. Display Technol.** 2 307-311 (2006).
- [86] Sri Sivakumar, Frank C. J. M van Veggel, M. Raudsepp *Bright White Light through Up-Conversion of a Single NIR Source from Sol-Gel-Derived Thin Film Made with Ln³⁺-Doped LaF₃ Nanoparticles* **J. Am. Chem. Soc.** 127 12464-12465 (2005).
- [87] P. N. Prasad *Nanophotonics*, John Wiley & Sons, Inc. (2004).
- [88] C. P. Poole Jr., F. J. Owens, *Introduction to nanotechnology*, Ed Wiley-Interscience, (2003).

- [89] V. Petrov, K. Petermann, U. Griebner, V. Peters, J. Liu, M. Rico, P. Klopp, G. Hüber *Continuous-wave and mode-locked lasers based on cubic sesquioxide crystalline hosts* in *Laser source and system Technology for defense and security II*, G. L. Wood, M. A. Dubinskii Eds. **Proc. of SPIE** 6216 62160H-1 (2006).
- [90] J. H. Gwak, S. H. Park, J. E. Jang, S.J. Lee, J. E. Jung, J.M. Kim, Y. W. Jin, N. S. Lee, W. K. Yi, V. A. Vorobyov *Synthesis and modification of red oxide phosphors for low voltage excitation* **J. Vac. Sci. Technol. B** 18, 1101 (2000).
- [91] L. Laversenne, Y. Guyot, C. Goutaudier, M. Th. Cohen-Adad, G. Boulon *Optimization of spectroscopic properties of Yb³⁺-doped refractory sesquioxides: cubic Y₂O₃, Lu₂O₃ and monoclinic Gd₂O₃* **Opt. Mater.** 16 475-483 (2001).
- [92] E. Zych, D. Hreniak, W. Strek, L. Kepinski, K. Domagala, *Sintering Properties of Urea-Derived Lu₂O₃-Based Phosphors* **J Alloys Compd**, 341 (1-2) 391-394 (2002).
- [93] G. Cao, *Nanostructures and Nanomaterials*, World Scientific Publishing Co Pte. Ltd. London (2004).
- [94] G. Adachi, N. Imanaka, *The Binary Rare Earth Oxides*, **Chem. Rev.** 98, 1479-1514 (1998).
- [95] P. V. Klevtsov, L. P. Kozeeva, *Synthesis and X-ray and thermal studies of potassium rare-earth tungstates, KLn(WO₄)₂, Ln = rare-earth element*, **Sov. Phys. - Dokl.** 14, 185-187 (1969) [transl. from Dokl. Akad. Nauk SSSR 185, 571-574 (1969)].
- [96] P. V. Klevtsov, L. P. Kozeeva, R. F. Kletsova, **Izv. Akad. SSSR Ser. Neorg. Mater.** 4, 1147-1151 (1968).
- [97] L. I. Yudanova, O.G. Potapova, A.A. Pavlyuk, *Phase diagram of the system KLu(WO₄)₂-KNd(WO₄)₂ and growth of KLu(WO₄)₂ single crystals*, **Inorg. Mater.** 23, 1657-1660 (1987) [transl. from Izv. Akad. Nauk SSSR, Neorganicheskie Materialy 23, 1884-1887 (1987)].
- [98] P. V. Klevtsov, L. P. Kozeeva, L. Yu. Kharchenko, *Study of the crystallization and polymorphism of double potassium and trivalent metal tungstates, KR(WO₄)₂*, **Sov. Phys. Crystallogr.** 20, 732-735 (1975) [transl. from Kristallografiya 20, 1210-1215 (1975)].
- [99] M. C. Pujol, X. Mateos, A. Aznar, X. Solans, S. Surinach, J. Massons F. Diaz, M. Aguiló, **J. Appl. Cryst.** 39, 230-236 (2006).
- [100] J. Zhang, J. Wang, K. Wang, W. Yu, H. Zhang, Z. Wang, X. Wang, M. Ba, *Growth and structure of monoclinic KLu(WO₄)₂ crystals*, **J. Cryst. Growth** 292, 373-376 (2006).
- [101] A. A. Kaminskii *Modern developments in the physics of crystalline laser materials* **Phys Status Solidi A** 200 215-296 (2003).
- [102] W. Bolaños, J. J. Carvajal, X. Mateos, M. Aguiló, F. Díaz *Exploring Waveguiding properties of heavily doped Yb³⁺KLu(WO₄)₂ epitaxial layers* **IEEE Photonics Journal**, 2, 482-489 (2010).
- [103] A. A. Kaminskii, K. Ueda, H. E. Eichler, J. Findeisen, S. N. Bagaev, F.A. Kuznetsov, A. A. Pavlyuk, G. Boulon, F. Bourgeois, *Monoclinic tungstates KDy(WO₄)₂ and KLu(WO₄)₂: New $\chi^{(3)}$ -active crystals for laser Raman shifters*, **Jpn. J. Appl. Phys.** 37, L923-L926 (1998).
- [104] A. Ikesue, Y. Lin Aung, *Ceramic laser materials*, **Nat. Photon.** 2, 721 (2008).
- [105] A. Brenier, L. C. Courrol, C. Pedrini, C. Madej, and G. Boulon *Yb³⁺ and Tm³⁺ ions as sensitizers for the Ho³⁺ infrared emission in Gd₃Ga₅O₁₂ garnet and up-conversion energy losses* **Phys. Rev. B** 49, 881-887 (1994).
- [106] B. Yao, Y. Wang, Y. Ju, and W. He *Performance of AO Q-switched Tm, Ho:GdVO₄ laser pumped by a 794nm laser diode* **Opt. Express** 13, 5157-5162 (2005).

- [107] P. Cérny, H. Jelinkova, *Developing Thulium Lasers for Depth-selective Scalpels* (SPIE Newsroom, 2006). doi:10.1117/2.1200607.0281
- [108] H. J. Qiu, Y. Shi, J. J. Xie, J. Xie, L. L. Zhang, F. F. Xu *Hydrothermal route to Eu doped LuO(OH) and Lu₂O₃ nanorods* **Sci. China Technol. Sci.** 53 1576-1582 (2010).
- [109] L. Fornasiero, *Nd³⁺ - und Tm³⁺ - dotierte Sesquioxides* Ph.D. Dissertation. Universität Hamburg, Hamburg, (1999).
- [110] A. -W. Xu, Y-P. Fang, L.-P. You, H.-Q. Liu *A Simple Method to Synthesize Dy(OH)₃ and Dy₂O₃ Nanotubes* **J. Am. Chem. Soc.** 125 1494-1495 (2003).
- [111] T. Andelman, S. Gordonov, G. Busto, P. V. Moghe, R. E. *Riman Synthesis and Cytotoxicity of Y₂O₃ Nanoparticles of Various Morphologies* **Nanoscale Res Lett** 5 263-273 (2010).
- [112] J. Lin, M. Yu, C. Lin, X. Liu *Multiform Oxide Optical Materials via the Versatile Pechini-Type Sol-Gel Process: Synthesis and Characteristics* **J Phys. Chem. C**, 111, 5835-5845 (2007).
- [113] M. Bettinelli, C. D. Flint, *Non-resonant energy transfer between Tb³⁺ and Eu³⁺ in the cubic hexachloroelpasolite crystals Cs₂sNaTb_{1-x}Eu_xCl₆ (x = 0.01-0.15)* **J Phys. Condens. Matter** 2, 8417-8426 (1990).
- [114] B. C. Joshi, *Enhanced Eu³⁺ emission by non-radiative energy transfer from Tb³⁺ in zinc phosphate glass* **J. Non-Cryst. Solids** 180, 217-220 (1995).
- [115] J. R. DiMaio, B. Kokuoz, J. Ballato *White light emissions through down-conversion of rare-earth doped LaF₃ nanoparticles* **Opt. Express**, 14 11412 (2006).

Chapter 2

Experimental Characterization Techniques

2.1. Introduction

The emergence of nanoscale science and technology has increased the challenges facing the characterization methods. The structure of materials with nanoscale features has been a long standing theme in materials science. Typical characterization problems include determining the morphology and composition of single phase regions, information that includes both the elemental concentrations derived from spectrometry and the crystallographic parameters derived from diffraction patterns.

The structural study of nanomaterials is always a high priority, because the physical properties of materials depend very much on their structure. The structural study, start with the investigation of the crystallography of single nanoparticles or grains. The quality of these materials can be assessed by the size of the crystallites, single phase material or preferred orientation to continue further studies of the electrical, magnetic and optical properties of materials. The final stage of structural study is the morphology of the nanoparticles and the tendency to form two-dimensional structures or to the close packing order [1].

Some of the techniques for characterization and analysis of nanomaterials are briefly described below:

X-ray Powder Diffraction (XRPD)

Although XRD has been useful for crystalline powders for several decades, modern improvements in electronics, computer and X-ray sources have allowed it to become an indispensable tool for identifying nanocrystalline phases as well crystal size. Luminescent materials should be highly crystalline and with few lattice defects to achieve high light output.

Scanning Electron Microscopy (SEM)

Besides, there have been great technical advances in electron microscopes during the last 30 years (mostly in automation and electronics), but all instruments are built around an electron column, which produces a stable electron beam; controls beam current, beam size and beam shape; and rasters the beam for SEM work [2]. The electron beam excitation has provided an important tool because of the powerful combination of high resolution morphological imaging through transmission and scanning electron microscopy and the elemental analysis possible by associated x-ray and electron spectrometries.

Electron probe micro-analysis (EPMA)

EPMA is a traditional method of elemental composition and it was adopted in the study of nanoscale materials [1]. Electron probe micro-analysis is based on interaction of high-energy electrons with electrons on core atomic levels of sample, and the spectrometry of the emitted X-rays. Registration and control of low concentrations of elements (on the level of parts per million, or parts per billion) is crucial on nano-structured luminescent materials to determine the effect of active ions concentration on luminescence and to reduce impurities as possible.

Transmission Electron Microscopy (TEM)

Imaging and crystallographic studies with nanometer scale resolution have been performed for more than 40 years with the transmission electron microscope [3]. Nanoparticle sizes and shapes are easily imaged. It is possible to image heavy atoms in some cases by high resolution TEM. Sample preparation is crucial, and usually involves placing very dilute particle suspensions onto carbon coated-copper grids.

Differential Thermal Analysis (DTA)

Heating nano-structured materials can lead to crystal growth, melting or crystal phase changes (exo or endothermic). By use of DTA, these transformations can be monitored, which can be helpful in characterization.

Optical spectroscopy

Optical spectroscopy (absorption, luminescence, reflection) analyzes the frequency and intensity of these emerging beams as a function of the frequency and intensity of the incident beam. Optical spectroscopy also provides an excellent tool with which to obtain information on the electronic structure of absorbing/emitting centers (atoms, ions, defects, etc.), their lattice locations, and their environments by analyzing the emerging light [4].

Raman and Fast Fourier Infrared spectroscopy

An excellent technique for chemical analysis is the Fast Fourier Infrared spectroscopy (FTIR), which is based upon the registration of characteristic spectra of molecular vibrations in the materials. Raman spectroscopy is based on the registration of vibration spectra excited by a powerful laser in the visible spectral range. Raman spectral shift between the main excitation line and coupled vibration frequencies is the characteristic parameter for the recognition of molecular vibrations.

2.2. X-ray powder diffraction (XRPD)

In 1912, German physicist Max Von Laue suggested with great insight that if the wavelength of X-rays is order of the interatomic distance (about 1 Å), the crystals could be a diffraction lattice for them whose wavelength is comparable with the lattice parameter. In that way, X-rays give information about the structure of crystalline materials. The interference within individual atoms affects the amplitude of the outgoing wave and scattering has a constructive interference in specific directions. However the intensity integrated in all directions remains constant due to energy conservation.

Figure 2.1 illustrates the reflection of X-rays by the atomic planes. Constructive interference or reflection is obtained when the path of the wave scattered of the lower of the two planes is longer by an integer number of wavelengths λ than that of the wave scattered of the upper plane. It is established in the Bragg equation,

$$n\lambda = 2d_{hkl} \sin \theta \quad (2.1)$$

And gives the permitted angles of reflection θ , in terms of the wavelength λ of the radiation used and the spacing of the reflecting planes d , n is an integer, analogous to the order of diffraction from a grating, so that $n\lambda$ is the path difference between waves scattered from adjacent lattice planes with equivalent indices.

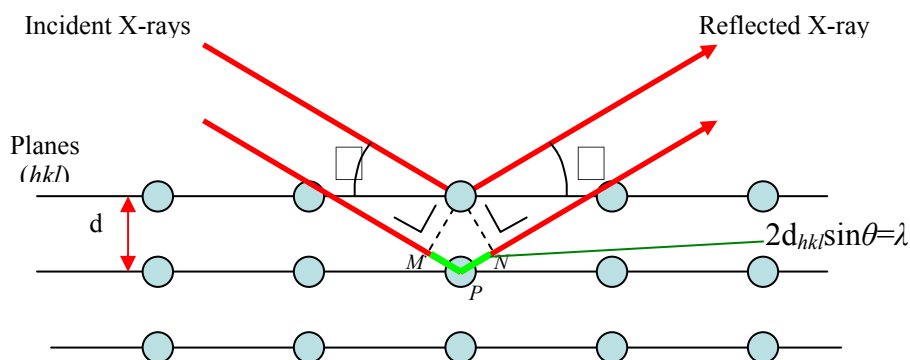


Figure 2.1. Geometric diagram showing the reflection of X-rays by two planes.

When X-rays reach an atom, the electric field interact with all electrons, which then emit an almost spherical wave with the same wavelength as the incident radiation by a elastic interaction. The amplitude of this wave, f is called atom form factor [5] and it depends on the number of electrons in the atom, so f is proportional to the atomic number. Detection limit is influenced by this effect. Light elements, e.g. carbon are poor scatterers but heavy elements are good scatterers.

Different crystalline materials show specific positions and intensities of the diffraction lines in XRPD patterns. This is explained by the interaction of waves scattered by different atoms in different positions within the unit cell, given by the structure factor $F(hkl)$ [5],

$$F(hkl) = \sum_n f_n (\cos \Phi_n + i \sin \Phi_n), \quad (2.2)$$

The summation goes over all n atoms in the unit cell and the f_n are the atom form factors of these n atoms. The phase Φ_n is given by

$$\Phi_n = 2\pi(hx_n + ky_n + lz_n) \quad (2.3)$$

where x_n , y_n , and z_n are the fractional coordinates of atom n within the unit cell and h , k and l are the Miller indices of the respective set of lattice planes giving rise to the reflection.

Each crystalline solid has its unique characteristic XRPD pattern which may be used as a "fingerprint" for its identification. Once the material has been identified, X-ray crystallography may be used to identify the crystal structure and by Rietveld refinement to determine the unit cell parameters.

In our work we obtain other specific results from XRPD: Determination of crystallite size from analysis of peak broadening, recognition of amorphous materials in partially crystalline mixtures, identification of multiple phases in microcrystalline mixtures and thermal expansion coefficient in crystal structures using in-situ heating stage equipment.

XRPD patterns were collected using a Siemens D-5000 powder diffractometer was used with Bragg-Brentano para-focusing geometry with $\theta - \theta$ configuration, using a Cu source with $\lambda_{K\alpha 1} = 1.540560 \text{ \AA}$ and $\lambda_{K\alpha 2} = 1.544390$, available at the Servei de Recursos Científics of the Rovira i Virgili University (Figure 2.2). In this system, the source, the sample and the detector occupy three consecutive positions on a circumference. This configuration guarantees the same Bragg conditions for a large area of the sample. The positions of the source and the detector vary in a synchronous way, always maintaining a symmetrical position, while the sample is always fixed. The measured was carried out in step-scanning mode and the 2θ angles ranged between 5 to 70 degrees. The X-ray patterns were recorded using a step size = 0.02° , step time = 16 s. Identification of the phases was carried by comparison with the compiled diffraction patterns by the Joint Committee for Powder Diffraction Standards (JCPDS) [6]. Lattice parameters were calculated using the software FullProf [7] based on Rietveld method [8].

For thermal expansion measurements by XRPD, a high temperature chamber Anton-Paar HTK10 was coupled to the diffractometer. XRPD patterns were recorded at $2\theta = 10-70^\circ$, step size = 0.03° , step time = 5 s, at temperatures of 298 K and intervals of 100 K up to 1273 K. The samples were placed and heated on a platinum support.

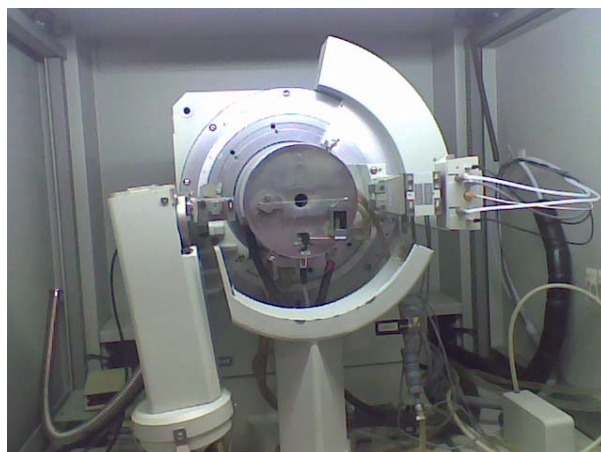


Figure 2.2. Siemens D-5000 powder diffractometer.

Apart from the crystalline phase determination, crystallite size of a nanocrystalline material can be calculated from the XRPD patterns. From the half-width of the X-ray refined pattern, the crystallite size was estimated by applying the Scherrer formula [9],

$$D = \frac{K\lambda}{B \cos \theta_B} \quad (2.4)$$

Where B the FWHM (Full width at half maximum) is measured in radians of 2θ , λ is the diffractometer wavelength, θ_B is the Bragg angle of the peak and K is a constant equal to $2(\ln 2 / \pi)^{\frac{1}{2}} \approx 0.9$, for D taken as the volume-averaged crystallite dimension perpendicular to the hkl diffraction plane [5].

2.3 Electron probe micro-analysis (EPMA)

Electron probe microanalysis (EPMA) is an elemental analysis technique to determine the concentration of the any atom into the material. The physical basis for X-ray spectrometric analysis under electron bombardment is illustrated in Figure 2.3 [10]. The sample is bombarded with a focused beam of accelerated electrons. The initial interaction is an inner shell ionization event created by inelastic scattering of the energetic electron beam with a bound inner shell electron. In this inelastic event, the electron beam transfers an amount of energy at least equal to the binding energy of the atomic electron, which is then ejected from the atom, leaving a vacancy in the shell. After the primary ionization of a K-shell, the excited atom resides in the excited state for a few picoseconds and then undergoes electron transitions between the L and K shells to lower its energy back toward ground state, emitting an X-ray photon [11].

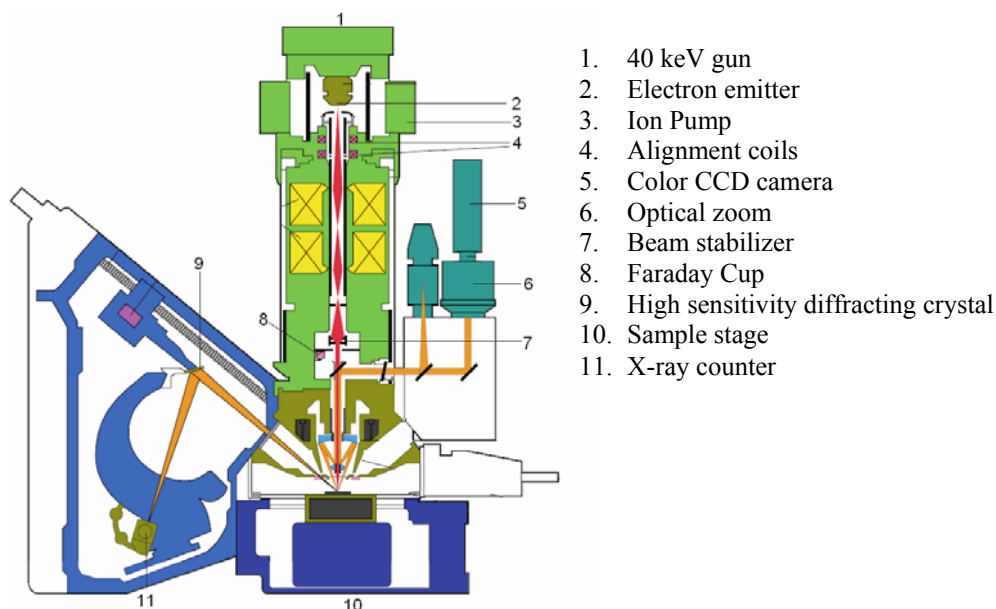


Figure 2.3. Scheme of the Cameca SX 100 electron probe micro analyzer.

Because the energy levels of the atomic shells are sharply defined and specific to each element, the transition of an electron from one shell to another produces a sharply defined difference in energy that manifests as the energy of the x-ray photon, making it characteristic of the particular atom species. As a result of the transition process, the vacancy moves out to an outer atomic shell, where the transition process can repeat (for high atomic number atom), resulting in a family of characteristic X-ray photons. These X-rays are detected at particular wavelengths associated at one element and their intensities are measured to determine concentrations using a wavelength dispersive spectrometer (WDS). Table 2.1 list the diffracting crystals and standards used to calculate the chemical composition of the samples by comparing the X-ray intensity of the sample respect to the standard using the formula:

$$\frac{I_S}{I_R} = F_C \frac{C_S}{C_R} \quad (2.5)$$

Where I_S is the X-ray intensity emitted by the sample, I_R the X-ray emitted by the reference. C_S and C_R are the concentrations of the atom in the sample and in the reference material, respectively; and F_C is the correction factor.

All the samples were prepared in the same way by uniaxial pressing of the nanocrystalline ceramic powder to produce a pellet. The pellet is broken and only a small piece of the pellet is putted in a furnace and annealed at 1073 K for 2h in such a way by the sintering of the nanocrystals a bulk piece is obtained. The sample is putted into a cylindrical mould, where a resin (Recapoli 2196 styrene and phthalic anhydride) and a catalyst (X-8 Methyl ethylketone peroxide) was added, and let it for curing at room temperature for 24 h. Flat surfaces

of the final embedded-sample cylinder are polished with sand paper grade 1000 and then the sample side is polished with a diamond powder of 3 and 1 μm in a Struers DAP 7-polisher until optical quality is reached.

Table 2.1. EPMA measurement conditions, diffracting crystals and standard references.

Element	Line	Time [s]	Diffracting Crystal	Standard
K	K_{α}	10	PET ^a	KLuW ^e
W	M_{α}	10	TAP ^b	KLuW
O	K_{α}	10	PC1 ^c	KLuW
Lu	L_{α}	30	LIF ^d	KLuW
Er	L_{α}	60	LIF	REE4 ^f
Tm	L_{α}	60	LIF	REE1 ^g
Ho	L_{β}	60	LIF	REE4
Yb	L_{α}	60	LIF	REE2 ^h

a Pentaery thritol

b Thallium phthalate acid

c W/Si multilayered pseudo-crystal

d Lithium fluoride

e Potassium lutetium tungstate oxide

f SiO₂, Al₂O₃, CaO, Dy₂O₃, Er₂O₃, Ho₂O₃ artificial glass [12]

g SiO₂, Al₂O₃, CaO, Eu₂O₃, Gd₂O₃, Tb₂O₃, Tm₂O₃ artificial glass [12]

h SiO₂, Al₂O₃, CaO, Nd₂O₃, Sm₂O₃, Yb₂O₃, Lu₂O₃ artificial glass [12]

The EPMA analysis was carried out in Cameca SX 50 microprobe analyzer operating in wavelength dispersive mode available at the Servei de Recursos Científic-Tècnics of the Universitat de Barcelona. By using different analyzing crystals, the wavelength range covered 1-24 Å. This mean that *K* lines for elements with atomic number *Z* between 9 and 35, *L* lines for elements *Z* less than 83 and all *M* lines can be recorded.

2.4 Electron microscopy

2.4.1 Scanning electron microscopy (SEM)

The scanning electron microscope is an instrument that produces a largely magnified image by using electrons instead of light to form an image. Figure 2.4 shows a schematic image of SEM. In SEM an electron are emitted by a tungsten or LaB₃ filament and accelerated in the range between 1 to 30 kV. The electron beam is collimated by electromagnetic condenser lens through a column. In the interaction of electron beam and sample, X-rays, backscattered electrons, Auger electrons and secondary electrons are emitted by the sample.

The deflection coils produce the displacement of the electron beam for scanning a specific surface area. The principal method of image construction is the secondary electrons detection, which are detected by a scintillation counter and amplified by the photo-multiplier

tube to obtain the signal output. The correlation of the scanning and the signal output of the counter, form an image with great lighting and contrast showing the topography.

The signal obtained from the secondary electrons comes from the surface region due only these electrons have probability to escape from material. The SEM resolution is currently limited around 25 Å or 300000 magnifications [13]. Characteristic X-rays are emitted when the electron beam removes an inner shell electron from the sample, causing a higher energy electron to fill the shell and release energy. These characteristic X-rays are used to identify the composition and measure the abundance of elements in the sample. For this reason, SEM used to be coupled to an energy dispersive X-ray spectrometer (EDAX). In this work a JEOL JSM 6400 SEM from the Servei de Recursos Científics i Tècnics of the Universitat Rovira i Virgili was used.

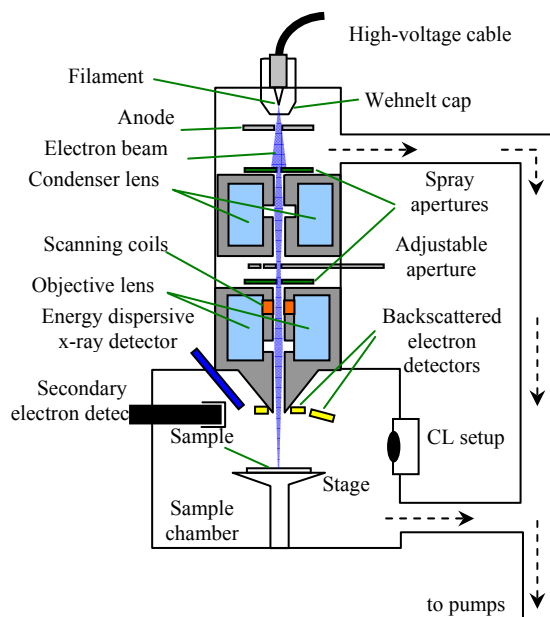


Figure 2.4. Scanning electron microscope schematic overview

2.4.2 Environmental scanning electron microscopy (ESEM)

The environmental scanning electron microscope has capabilities to study the morphology of insulating samples including ceramics, plastics, biological materials, fibers and gas releaser samples, without previously preparation unlike conventional vacuum SEM. Real time phenomena could be seen in ESEM, e .g. chemical reactions, dissolutions, crystallizations.

The conventional SEM require high vacuum (10^{-5} mTorr) into sample chamber to prevent dispersion of primary and secondary electrons, whereas ESEM can operate in poor vacuum (above 10 Torr). ESEM uses an Environmental Secondary Detector (ESD) which can works

in non-vacuum environment instead of the Everhart-Thornley (ET) detector used in SEM. By applying a positive potential of a few hundred volts to the detector, the secondary electrons are attracted to the detector, where they collide with gas molecules, releasing electrons and positive ions. The electrons reach the detector amplifying the signal, and the positive ions created during the gas ionization are attracted by the sample and they suppress charging effects on the sample surface, thus, no conductive coating of the sample is necessary. Though the ESEM could exam a wide range of materials avoiding the coating process, it has a disadvantage: the secondary electrons are dispersed by water molecules reaching the detector. The signal noise is increased but the image resolution and contrast is lowered.

FEI QUANTA 600 environmental scanning electron microscope from the Servei de Recursos Científics i Tècnics of the Universitat Rovira i Virgili (Figure 2.5), was used to obtain morphological images in this work.



Figure 2.5. Environmental scanning electron microscope FEI QUANTA 600.

2.4.3 Transmission electron microscopy (TEM)

The transmission electron microscope works similarly as an optical analogue to the conventional light microscope. Electron wavelength allows higher magnification and better resolutions. Figure 2.6 shows a schematic of the transmission electron microscope. The electrons are accelerated under a potential of up 100 keV or higher. The electron beam is focused by several electromagnetic lenses on a single, spot or element at a very thin sample, and detecting those transmitted through it hitting the phosphor screen on the other side. After interaction of electrons with the sample one is able to obtain a map of the local densities with lighter and darker areas, as well as diffraction information when there are ordered structures such as crystals. Sample preparation is crucial, and usually involves placing very dilute particle suspensions onto carbon-coated copper grids. Another useful technique is imbedding the particle in a solid organic polymer, slicing very thin sections, and passing the electron beam through the section [14].

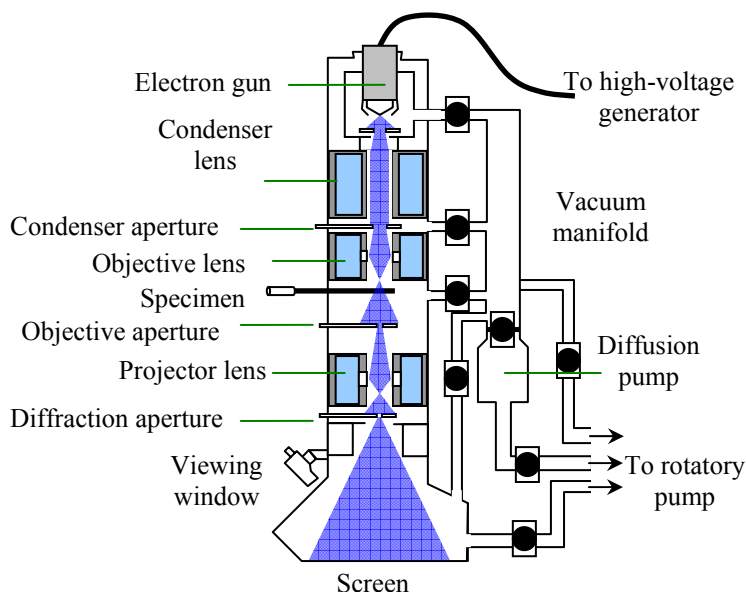


Figure 2.6. Schematic of a Transmission Electron Microscope.

Transmission electron microscopy (TEM) was performed with a JEOL JEM-1011 microscope operating at 100 kV equipped with a CCD camera available at the Servei de Recursos Científics i Tècnics of Universitat Rovira i Virgili (Figure 2.7). We putted 0.2 mg of nanocrystalline powder and 1 ml ethanol in a glass vial and sonicated for 10 minutes. One drop of the resulting suspension was dropped on an amorphous carbon film (HD200 Fomvar/Carbon) supported on a 200 mesh copper grid. Automatic particle size histograms were calculated on micrographs showing dispersed particles with high contrast (dark) respect to the carbon film (bright background). In the case of agglomerated particles, the profile of each particle was draw using the geometry tools of iTEM software.



Figure 2.7. Transmission electron microscope JEOL JEM-1011.

The high resolution transmission electron microscope (HRTEM) allows the visualization of the atomic planes and lattice imperfections of materials with a resolution in the 0.1 nm range [14]. Depending on the imaging conditions, it is possible to image heavy atoms in some cases, one or more sets of lattice planes of certain zone axis orientation, and nanoparticles sizes and shapes are easily imaged.

Fast Fourier transform Fourier processing was used to reveal the periodic contents of HRTEM images. A fast Fourier transform is a special algorithm for quickly calculating a Fourier transform based on (appropriately sized) regions of interest placed on an image. The result of a Fourier transform on a real image is a complex image that is Hermitian in nature. This means that the image is symmetrical around the center (with symmetric points being complex conjugates of one another). The resulting transform represents the source image in the reciprocal space.

A JEOL JEM 2010F HRTEM operating at 200 keV with a Schottky field emission electron source was used (Figure 2.8). It is equipped with Electron Energy Loss Spectroscopy (EELS), a Gatan imaging filter (GIF) and a Z-STEM unit with a high-angle annular detector, which is available at the Servei de Recurs Científic-Tècnic of the Universitat de Barcelona. The samples are prepared using the same methodology as TEM, and the copper grids match for both microscopes. Digital Micrograph[®] software was used for Fast Fourier transform Fourier processing of HRTEM images.



Figure 2.8. High resolution transmission electron microscope JEOL JEM 2010F.

2.5 Differential thermal analysis (DTA)

The thermal analysis includes many techniques where a thermodynamic property is measured into a controlled atmosphere as the temperature is changed. Usually the atmosphere is artificial air (artificial air: 79% nitrogen and 21% oxygen) or an inert atmosphere with argon. Among thermal analysis techniques, the thermo-gravimetric analysis (TG) allows determining the thermal stability of the sample. The TG is based on the measure of mass changes as the temperature changes. This variation could be result of weight loss or weight profit. Commonly, the TG analysis is carried out simultaneously with differential thermal analysis (DTA) or differential scanning calorimetry (DSC) techniques. In the DTA, the changes in temperature difference between the sample and an inert reference material, (a material which physical and chemical properties not change in the range of the interested temperatures) are recorded under identical conditions. Changes in the sample such as oxidation, decomposition, melting, crystallization or phase transition, which lead to endothermic or exothermic process in the sample, can be detected.

In this work, the combination of DTA-TG analysis was used, and thermal behavior with the weight loss of the sample was measured simultaneously using a SDT 2960 analysis module from TA instruments at the FicMA group. The equipment is showed in Figure 2.9. Calcinated Al_2O_3 powder was used as reference material, since it does not show any phase transition or chemical reaction in the range from 300 K to 1473 K. The samples were heated at a rate of 10 K / min, from room temperature to 1473 K and then cooled at the same rate by using synthetic air as purge gas with 90 cm^3/min flow rate.



Figure 2.9. Simultaneous Differential Thermal Analysis Module SDT 2960 and gas flow controller (left). Platinum cups on the balance arms.

2.6 Optical spectroscopy

2.6.1 Optical absorption

When the electromagnetic radiation (such as ultraviolet, visible and infrared light) reaches a thin transparent sample, a fraction of this radiation is absorbed, transmitted and finally a small percentage (~10%) is reflected. This effect is produced by electrons, ions or molecules in the sample. The Beer-Lambert law is an empirical relationship that relates the absorption of light to the properties of the material through which the light is traveling:

$$I = I_0 e^{-\alpha_A(\lambda)d} \quad (2.6)$$

Where I_0 is the incident light intensity of the emerge radiation, I is the transmitted light intensity d is the thickness of the sample and $\alpha_A(\lambda)$ is the absorption coefficient. Experimentally, we measure the optical density OD (or absorbance) using a spectrophotometer.

$$OD = \log_{10} \left(\frac{I_0}{I(\lambda)} \right) \quad (2.7)$$

From the OD, the absorption coefficient can be calculated:

$$\alpha_A = \frac{OD}{d \cdot \log_{10}(e)} \quad (2.8)$$

The optical density is a function of the thickness and dimensionless, and the absorption coefficient has inverse distance units, usually cm^{-1} . The characteristic absorption of an active ion, e.g. Tm^{3+} or Yb^{3+} , is defined by the absorption cross section (σ_A):

$$\sigma_A(\lambda) = \frac{\alpha_A(\lambda)}{[Ln^{3+}]} \quad (2.9)$$

In Figure 2.10, the diagram of a typical spectrophotometer is shown. The optical absorption was measured using Varian Cary 500 Scan spectrophotometer at FicMA-FicNA lab. The experimental spectra range is from 175 nm to 3300 nm and can measure optical densities from 0 to 10. This spectrophotometer has two monochromators with 1200 lines/mm grating for the UV/VIS region and 300 lines/mm in the NIR region. The optical sources used were deuterium lamp and a quartz halogen lamp in the zone of visible and infrared. The detectors were a photomultiplier (PMT) in UV/VIS region (175–850 nm) and a lead sulfide in the IR regime (850–3300 nm).

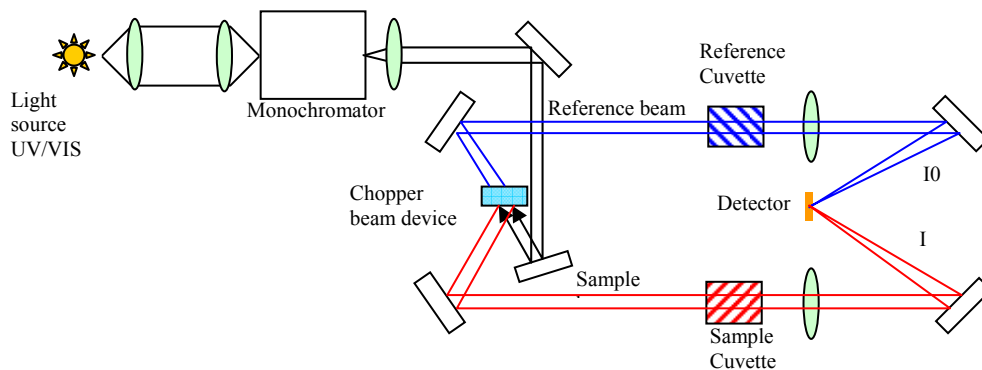


Figure 2.10. Diagram of the components of a typical spectrophotometer.

For low temperature measurements (6 K) of optical absorption, an Oxford Instruments cryostat (SU 12) with a Leybold RDK-6-320 Helium closed circuit and a Leybold LTC 60 temperature controller have been used. The cryostat uses a mechanical vacuum pump to reach 10^{-3} mbar and a turbo-molecular pump to reach 10^{-5} mbar. Figure 2.11 show a picture of Cary spectrophotometer and the setup for low temperature measurements.

For the sample preparation, KBr (0.090 g) and as-produced nanocrystalline powder (0.010g) were mixed together in an agate mortar and then pressed uniaxially in a cylindrical mold under 20 tons to obtain a semi-transparent thin pellet sample. No sample was used as absorption reference.

The spectral resolution depends on the spectral band width (SBW) and the Energy Level (EL). The SBW controls the amount of light reaching the detector and EL is adjusted in response to the amount of light striking the detector to maintain a constant signal level. To be more specific, when you increase the SBW, the spectrophotometer will decrease EL to make the detector less sensitive. When you narrow down the SBW, only a small amount of light will reach the detector and the spectrophotometer will increase EL to make the detector more sensitive to the lower light level.

In the UV/VIS region, SBW is normally used to control EL (a good starting value is SBW = 2 nm). In the NIR region the reverse is true, EL controls SBW ($1 < EL < 3$, this provides the best signal-to-noise ratio). Due to the inherent differences between the two types of detector, the different methods of control ensure the widest dynamic range in each region.

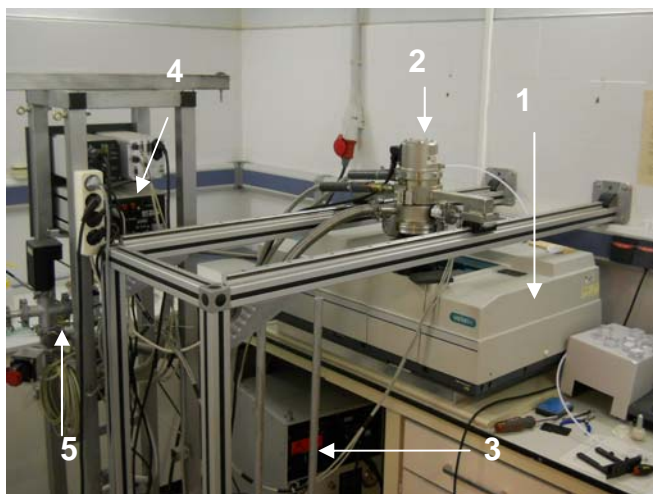


Figure 2.11. Cary 500 spectrophotometer setup (1), cryostat (2), helium cooling system (3), temperature and vacuum controllers (4) and turbo-molecular pump (5).

2.6.2 Photoluminescence emission

Luminescence or optical emission is the result of a spontaneous emission of photons after an electron relaxes from an excited or higher energy level to a lower energy level. This de-excitation process is called luminescence. The electron is excited by some form of energy, (photons, electrons, heat, chemical reaction, etc). In the case of photons, it is called photoluminescence (PL).

Luminescence spectra are often measured using compact commercial equipment called spectrofluorimeters. The sample is excited with a lamp, which is followed by the excitation monochromator for fixing excitation wavelength. The emitted light is collected by a focusing lens and analyzed by means of the emission monochromator, followed by a suitable detector connected to a computer. Two kinds of spectra can be registered:

- (i) Emission spectra, the excitation wavelength is fixed and the emitted light intensity is measured at different wavelengths.
- (ii) Excitation spectra, the emission monochromator is fixed at any emission wavelength while the excitation wavelength is scanned in a certain spectral range.

For a rigid two-level system, the absorption and emission spectra lay at the same energy, in accordance with the energy levels diagram of Figure 2.12a. In general, emission spectrum is shifted to lower energies relative to the absorption spectrum. This shift is called a Stokes shift [4]. Assuming that neighboring ions follow a harmonic motion, the two energy levels of Figure 2.12a become parabolas with different equilibrium positions for the ground (Q_0) and excited states (Q_0') as shown in Figure 2.12b. The Stokes shift avoids a strong overlap between the absorption and emission bands, reducing the reabsorbed light.

It is also possible to obtain luminescence at photon energies higher than the absorbed photon energy. This is called anti-Stokes or upconversion luminescence [4], and it occurs for multilevel systems, as in the example shown in Figure 2.13. Two photons of frequency ν_{abs} are sequentially absorbed from the ground state 0 and then from the first excited state 1, thus promoting an electron to the excited state 3. Then, the electron decays nonradiatively to state 2, from which the anti-Stokes luminescence $2 \rightarrow 1$ is produced. In that way, $\nu_{abs} < \nu_{emi}$ (the anti-Stokes shift).

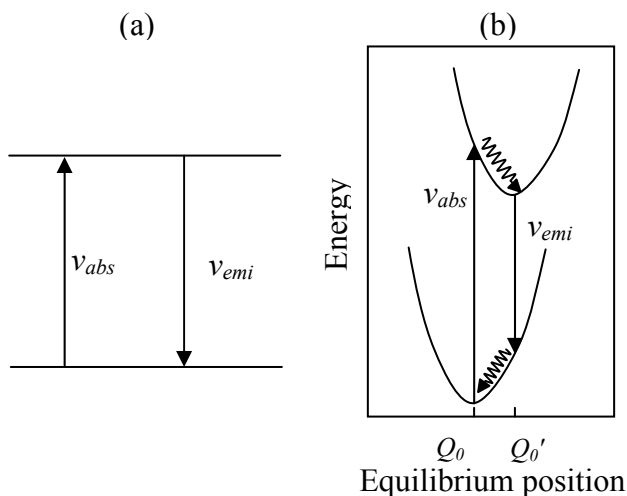


Figure 2.12. (a) The absorption and emission energies for a two-level system (rigid lattice). (b) The absorption and emission energies showing the Stokes shift (vibrating lattice).

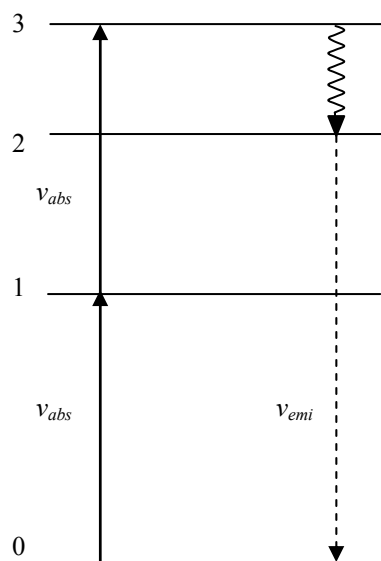


Figure 2.13. Four energy level system producing anti-Stokes luminescence.

Upconversion luminescence (I_{UC}) is a nonlinear process and the intensity of I_{UC} depends on higher powers of the excitation intensity I_0 .

$$I_{UC} \propto I_0^n \quad (2.10)$$

where the exponent n denotes the number of photons involved in the upconversion process [15].

Upconversion photoluminescence for papers IV, V and VII was recorded in FiCMA-FiCNA optical lab, using the setup shown in Figure 2.14. From as produced nanocrystalline powder, pellet samples were produced by uniaxial pressing at 20 ton. Samples were excited by a 980 nm Ti:Sapphire laser Coherent (model – Mira 900-P) pumped by a second harmonic Nd:GdVO₄ solid state laser. For detection, the emission was collected normal to the incident beam and was collected by a Jobin-Yvon Spex HR460 double monochromator with a focal length of 460 mm. An 1800 g/mm groove density grating for a spectral range of 450-850 nm was used. The detector used was a Hamamatsu PMTR928 sensible to visible radiation. Laser beam was chopped at 30 Hz by a rotating helix. The detector was connected to the lock-in amplifier (EG&G DSP-7265) and the chopper signal was used as external reference to increase the signal-to-noise ratio of data acquisition.

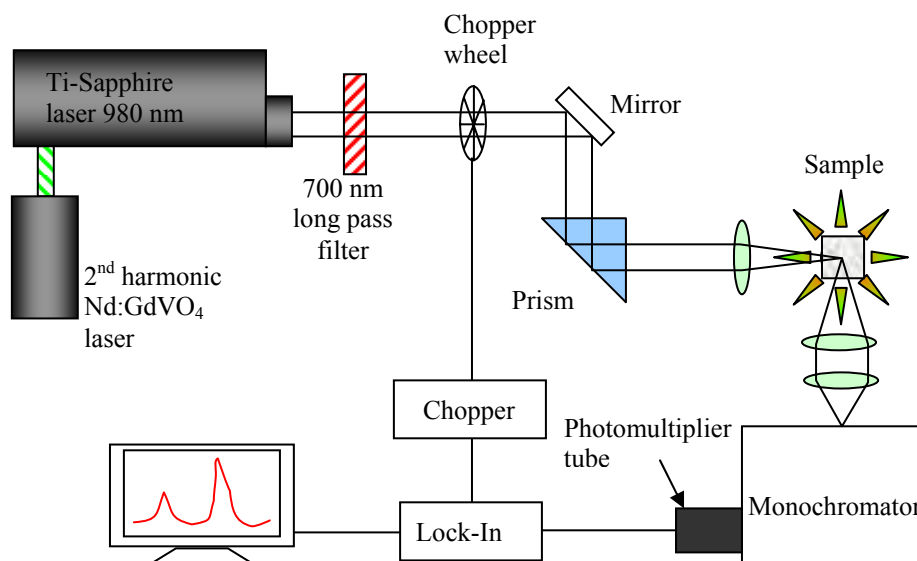


Figure 2.14. Scheme of the upconversion PL setup used in FiCMA-FiCNA optical lab.

Upconversion PL characterization as a function of excitation power density for KLuW nanocrystals was recorded in Solid State Chemistry Lab at University of Verona, using the setup shown in Figure 2.15. The upconversion PL spectra were obtained after CW excitation at 980 nm with a MDL III980 diode laser. Laser was focused on samples, with a spot size ~0.5 mm. 900 nm short pass filter was used for filtering the excitation pumping. Upconversion radiation was collected normal to the incident beam by achromatic lens and launched to an optical fiber connected to a HR460 Jobin Ivon monochromator. Spectrum

One CCD2000 detector operating at 251 K with 0.05 mm slit aperture. The upconversion PL spectrum is collected by combination of partial measurements as indicated in Figure 2.15. Wavelength calibration was carried using the Ne^{1+} and Hg^{1+} visible emission lines [16] from fluorescent lamps and wavelength corrections were calculated for the different monochromator positions. To allow intensities comparison, spectra were collected under identical conditions for all samples. For correcting the influence of monochromator, optic fiber and detector, the spectrum of a calibrated xenon lamp was collected and the instrumental function R was calculated as $R = M / W$, where M is the spectrum measured with the setup and W is the calibration spectrum. The M , W and R are presented in Figure 2.16. To obtain the corrected spectrum L from a measured spectrum E , is necessary to apply the following rule $L = E / R$.

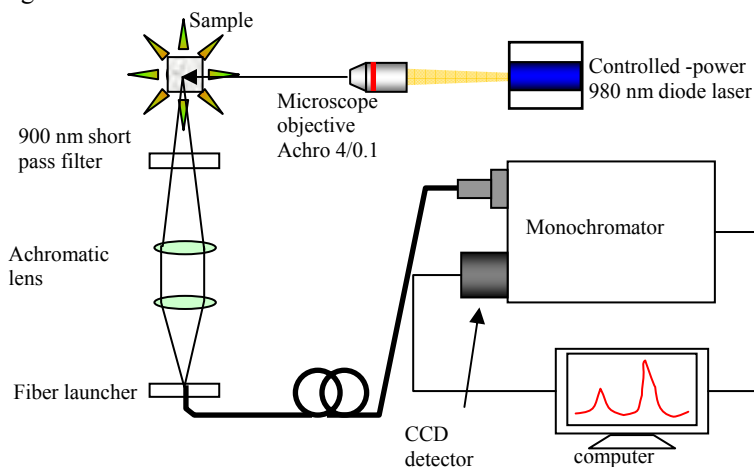


Figure 2.15. Scheme of the upconversion PL measurements versus excitation power density.

Table 2.2. Wavelength correction functions for the different monochromator steps used for spectra collection at Solid State Chemistry Lab at University of Verona.

Monochromator position [nm]	CCD spectral range [nm]	Wavelength correction [nm]
500	410 - 590	$11.194 + 0.992 \cdot \lambda_{\text{exp}}$
570	480 - 660	$15.592 + 0.984 \cdot \lambda_{\text{exp}}$
650	560 - 740	$10.773 + 0.994 \cdot \lambda_{\text{exp}}$
800	710 - 890	$-28.077 + 1.034 \cdot \lambda_{\text{exp}}$
950	860 - 940	$-27.187 + 1.034 \cdot \lambda_{\text{exp}}$
1030	940 - 1120	$15.739 + 0.991 \cdot \lambda_{\text{exp}}$

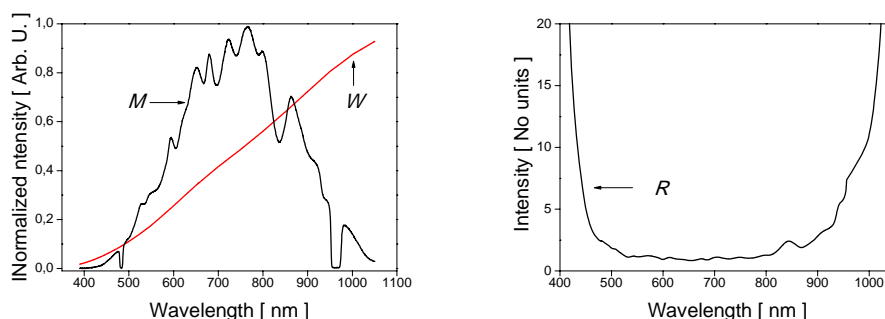


Figure 2.16. Spectrum measured M and calibration spectrum W of Xenon lamp (left). Calculated instrumental response function R (right).

2.6.3 Upconversion quantum yield

Upconversion quantum yield (QY) measurements were carried out following the technique proposed by Boyer *et al* [17] as shown in Figure 2.17. Powder samples were held on 1.5 mL borosilicate bottom flat vials. Sample vials were shaken slightly to compact the powder and they were positioning so that their flat bottom faced inside a Labsphere 4GPS-020-SL integrating sphere of 2 inches diameter (Figure 2.18). Samples were excited with a 200 μm core diameter fiber-coupled 975 nm InGaAs laser diode S50-980-2 Apollo Instruments. The laser from the fiber tip was collimated with a spot size of ~ 3 mm. One baffle was employed to ensure that no scattered excitation light or emissions would be collected before multiple scattering inside the sphere. Signal was collected using an Avantes S2000 fiber spectrometer. A neutral filter of 1 % transmittance was used to measure the excitation intensity and a 300-800 nm filter was used to collect the emission of the samples. All the spectroscopic data collected were corrected for the spectral response of the integrating sphere, spectrometer and the 300-900 nm filter. A vial filled with undoped KLuW nanocrystalline powder was employed as reference in order to mimic sample scattering. One magnitude order reduction of the obtained quantum yield values was applied after a final comparison with 3% Er: 20 % Yb:NaYF₄ microcrystalline powder with a reported quantum yield of 3-4 in the 10-100 W/cm² power density range [17][18].

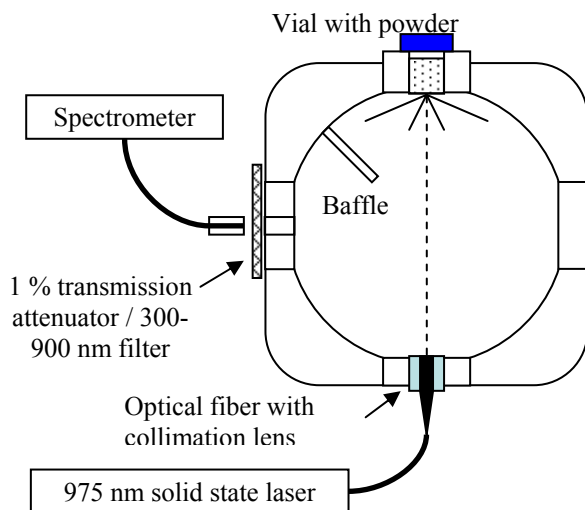


Figure 2.17. Schematic of the quantum yield measurement setup

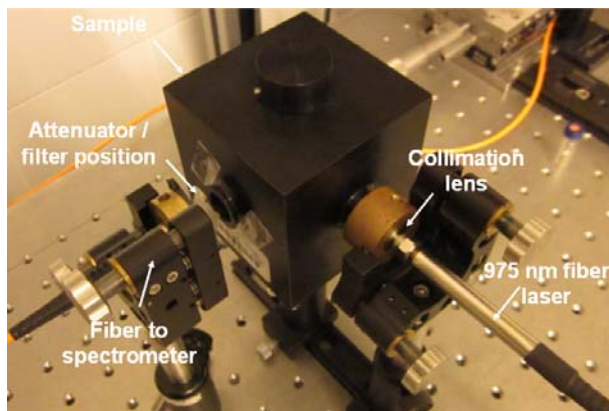


Figure 2.18. Experimental setup of the integrating sphere for quantum yield measurements.

2.6.3 Photoluminescence decay

When a given material is excited by a pulse of light with an adequate wavelength, this incident radiation is absorbed by optical centers, which are excited to higher energy states. Once the excitation pulse has expired, the centers relax to lower energy states through the emission of photons (radiative) and phonons (non-radiative). The time evolution of the emitted intensity provides valuable information about the nature of the physical phenomena involved.

For the measurement of timescales ranging from several milliseconds down to hundreds of picoseconds, the combination of an adequate detector together with a digital oscilloscope constitutes the simplest experimental setup, to monitor the time evolution of the optical signal, with timescales typically larger than hundreds of picoseconds [4]. One of the main advantages of this experimental setup is that modern digital oscilloscopes allow for very large integration times, and so the continuous averaging of repetitive signals leads to high signal-to-noise ratios.

For PL spectra at 460 nm excitation a Quanta Systems pulsed dye laser was used. The signal was 90° collected respect to the laser pumping by an achromatic lens and launched to an optical fiber connected to the HR460 Jobin Ivon monochromator using a photomultiplier as detector and connected to a Lecroy LT342 oscilloscope for data acquisition of decay measurements. This setup is available in Solid State Chemistry Lab at University of Verona

PL lifetimes at 980 nm excitation in Paper V was measured with an optical parametric oscillator from Oportek (Model-Vibrant HE 355 II+UV) with pulse duration of around 6 ns and a repetition frequency of 10 Hz. The signal was collected using a Hamamatsu R928 photomultiplier connected to a Tektronix TDS 714L oscilloscope for decay time measurements. Figure 2.19 shows the scheme of the PL equipment at the FICMA-FICNA laboratories.

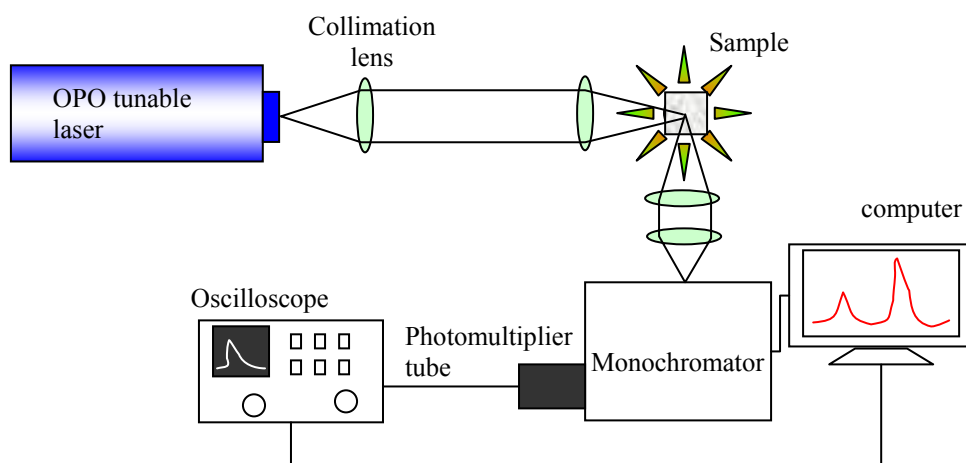


Figure 2.19. Scheme of the system used in the PL decay measurements at 980 nm excitation.

Tm^{3+} photoluminescence (PL) in the NIR region was characterized at the Instituto de Ciencia de Materiales (ICMM) of the Consejo Superior de Investigaciones Científicas (CSIC), Madrid, Spain. The samples were excited at 300 K with a Quanta-Ray MOPO-HF optical parametric oscillator. This tunable laser system provides optical pulses shorter than 5 ns from 730 to 1750 nm. Pulse energy at $\lambda = 800$ nm was ≈ 32 mJ. Fluorescence was dispersed by a single-grating SPEX spectrometer ($f = 34$ cm) and measured by a Hamamatsu H9170-75 InP/InGaAs cooled PMT working at 213 K sensitive in the 950–1700 nm range with a rise time of 0.9 ns, or by an InAs Hamamatsu photovoltaic detector cooled with liquid nitrogen and sensitive in the 1500–3100 nm range with a rise time of 0.1 ms. The electrical signals were recorded with a Tektronix TDS-520 500-MHz oscilloscope for lifetime measurements. A long-wavelength pass filter with a cutting edge at 1000 nm was used to remove background excitation light.

2.6.4 Cathodoluminescence

Luminescence can also be produced under excitation with an electron beam, and in this case it is called Cathodoluminescence (CL). This technique is conventionally used to investigate some characteristics of specimens, such as trace impurities and lattice defects, as well as to investigate crystal distortion [4]. CL analyses (luminescence emission after irradiation with the primary electrons) can be carried out simultaneously with SEM.

2.7 Scanning Near-Field Optical Microscopy (SNOM)

An optical microscope is limited by the so-called Rayleigh diffraction limit, which means that the dimensions of a focusing spot are always about half size of the wavelength used.

$$d > \frac{\lambda}{2\sin\theta} \quad (2.11)$$

where d = the distance between the two objects (resolution), λ = the wavelength of the incident light, and θ = the angle through which the light is collected. According to this equation, the best resolution achievable with optical light is about 200 nm. This treatment only considers the light diffracted into the far-field that propagates without any restrictions. It is possible to use other microscopic techniques such as scanning probe microscopy or electron microscopy, but the information obtained by visible light is a valuable tool in scientific studies. With the introduction of scanning near-field optical microscopy (SNOM), this limitation no longer exists, and optical resolution of < 50 nm can be achieved.

SNOM makes use of evanescent or non propagating fields that exist only near the surface of the object. These fields carry the high frequency spatial information about the object and have intensities that drop off exponentially with distance from the object. Because of this, the detector must be placed very close to the sample in the near field zone, typically a few nanometers. As a result, near field microscopy remains primarily a surface inspection technique. The detector is then rastered across the sample using a piezoelectric stage. The scanning can either be done at a constant height or with regulated height by using a feedback mechanism [19]. A diagram of the SNOM optics is presented in Figure 2.20.

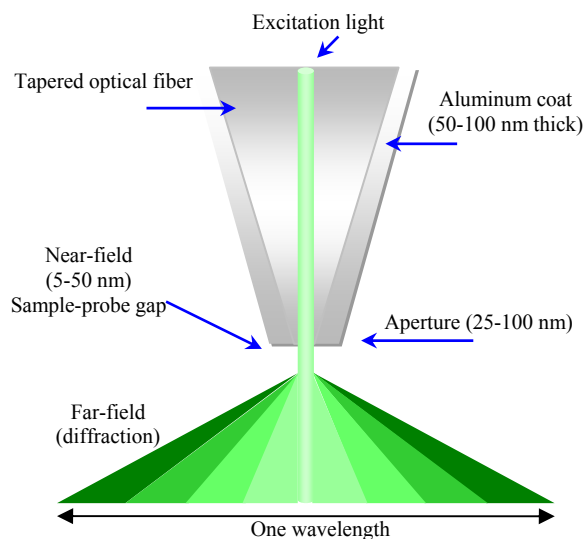


Figure 2.20. Diagram of near-field optics indicating near-field and far-field region.

There are four possible modes of operation with SNOM, depicted in Figure 2.21:

- *Transmission mode imaging.* The sample is illuminated through the probe, and the light passing through the sample is collected and detected.
- *Reflection mode imaging.* The sample is illuminated through the probe, and the light reflected from the sample surface is collected and detected.
- *Collection mode imaging.* The sample is illuminated with a macroscopic light source from the top or bottom, and the probe is used to collect the light from the sample surface.
- *Illumination/collection mode imaging.* The probe is used for both the illumination of the sample and for the collection of the reflected signal.

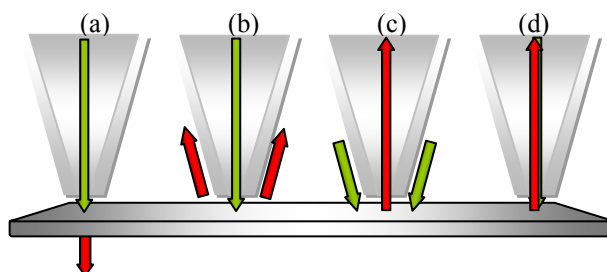


Figure 2.21 Aperture modes of SNOM operation: transmission (a), reflection (b), collection (c) and illumination-collection (d).

Detecting the collected light can be achieved with a wide variety of instruments: an Avalanche Photo Diode (APD), PMT, a CCD, or a spectrometer. The signal obtained by these detectors is then used to create an SNOM image of the surface. SNOM characterization was carried out on doped sesquioxide Lu_2O_3 nanorods in transmission mode and experimental setup is described in paper IV.

2.8 Raman and Fast Fourier infrared spectroscopy

Several fundamental issues underlying Raman utility are illustrated in Figure 2.22. When monochromatic light of energy $h\nu_0$ encounters matter (gas, solid, or liquid), there is a small probability that it will be scattered at the same frequency. If the object in question (e.g., a molecule) is much smaller than the wavelength of the light, the scattering is Rayleigh scattering, as shown in Figure 2.22. The “virtual state” is not necessarily a true quantum state of the molecule but can be considered a very short lived distortion of the electron cloud caused by the oscillating electric field of the light [20].

Blue light is more efficiently scattered than red, and Rayleigh scattering is responsible for the blue sky. The electron cloud of the molecule is also perturbed by vibrations (vibration mode or phonon), and it is possible for the optical and vibrational oscillations to interact, leading to Raman scattering. Raman scattering is shown in Figure 2.22 in which the scattered photon is lower in energy by an amount equal to a vibrational transition, $h\nu_1$.

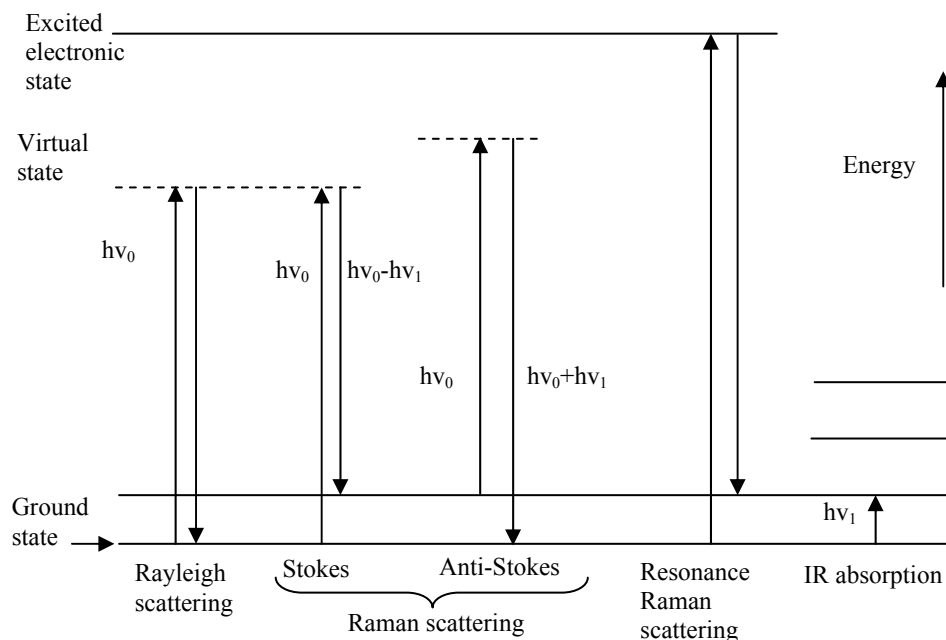


Figure 2.22 Spectroscopic transitions underlying several types of vibrational spectroscopy. ν_0 indicates laser frequency.

A Raman spectrum consists of scattered intensity plotted vs. energy. Each peak corresponds to a given Raman shift from the incident light energy $h\nu_0$. If the crystal happens to be in an excited vibrational state when an incident photon is scattered, the photon may gain energy when scattered, leading to anti-Stokes Raman scattering. The Stokes and anti-Stokes Raman peaks are symmetrically positioned about the Rayleigh peak, but their intensities are very different.

Infrared absorption, often called Fourier transform infrared (FTIR) or mid-IR absorption, also depends on vibrations, as shown in Figure 2.22. Although Raman spectroscopy probes vibrational transitions indirectly by light scattering, the Raman shift has the same energy range as FTIR absorption, and in many cases, the same energies are observed. The selection rules for Raman scattering and FTIR are different, but the chemical information is similar. A fundamental difference between absorption and Raman scattering is the probability to occur, with absorption usually being a more probable event. The first major impediment to using Raman spectroscopy is the weakness of the effect, with Raman scattering being roughly 10^{-10} as likely as the corresponding mid-IR absorption in typical experimental situations [20].

A second problem with Raman spectroscopy is another competitive effect, fluorescence. The visible light typically used for Raman spectroscopy often excites fluorescence of the sample or of impurities. Fluorescence is not a scattering process, and fluorescence emission from most liquids and solids does not have the vibrational fine structure observed in Raman spectra [20]. However luminescence of $\text{SiO}_2@Yb,Er:Lu_2O_3$ nanostructures in paper VII was measured using a Raman microscope that excites the luminescence of Er^{3+} at 514 nm and 633 nm.

Micro-Raman system Renishaw confocal InVia spectrometer equipped with a FTIR accessory and a CCD camera as a detector. The provided lasers were 514 nm Argon laser and a 633 nm He-Ne laser, was used to analyze. The radiation was focused by long working distance microscopic objective 50X. This equipment is available at the Servei de Recursos Científic-Tècnics of the Universitat Rovira i Virgili.

2.7 References

- [1] A. Nabok *Organic and inorganic nanostructures*. Artech House Inc, Norwood, MA (2005).
- [2] J. I. Goldstein, D. E. Newbury, D. C. Joy, C. E. Lyman, P. Echlin, E. Lifshin, L. Sawye, and J. Michael, *Scanning Electron Microscopy and X-ray microanalysis*, 3rd edition, Kluwer Academic Plenum Press, New York, (2003).
- [3] D. B. Williams, and C. B. Carter, *Transmission Electron Microscopy* Plenum Press, New York, (1996).
- [4] J. García Solé, L. E. Bausá, D. Jaque. *An introduction to the optical spectroscopy of inorganic solids*, John Wiley & Sons Ltd, (2005).
- [5] B. D. Cullity S. R. Stock, *Elements of X-ray diffraction, third edition* Prentice hall New Jersey, (2001).
- [6] JCPDS-ICDD, *Joint committee for powder diffraction standards, International Center of Diffraction Data* (1997).
- [7] J. J. Carvajal, *Introduction to the program FULLPROF: Refinement of crystal and magnetic structures from powder and single crystal data*, Institut Laue-Langevin, Grenoble Cedex 9, France (2006).
- [8] H. M. Rietveld, *A profile refinement method for nuclear and magnetic structures*, **J. Appl. Cryst.**, 2, 65, (1969).
- [9] A. L. Patterson, *The Scherrer Formula for X-Ray Particle Size Determination*, **Phys. Rev.**, 56, 978 (1939).
- [10] Cameca Scientific Instruments, *SX 100 Universal EPMA Synopsis*, <http://www.cameca.com>, (2012).
- [11] N. Yao, Z. L. Wang, *Handbook of microscopy for nanotechnology*, Kluwer Academic Publishers (2005).
- [12] M. J. Drake, D. F. Weill, *New rare earth element standards for electron microprobe analysis*. **Chem. Geolog.** 10, 179-181 (1972).
- [13] Advanced Research Systems *Scanning Electron Microscopy*. <http://advressys.com> (2012).
- [14] K. J. Klabunde, *Introduction to Nanotechnology in Nanoscale materials in chemistry*. K. J. Klabunde, eds. John Wiley & Sons, Inc. (2001)
- [15] D. R. Gamelin, H. U. Güdel, *Upconversion Processes in Transition Metal and Rare Earth Metal Systems* **Top. Curr. Chem.** 214 1 (2001).
- [16] Y. Ralchenko, A. E. Kramida, J. Reader, NIST ASD Team. *NIST Atomic Spectra Database*. <http://physics.nist.gov/asd>. National Institute of Standards and Technology, Gaithersburg, MD. (2011).
- [17] J. -C. Boyer, F. C. J. M. van Veggel *Absolute quantum yield measurements of colloidal NaYF₄: Er³⁺, Yb³⁺ upconverting nanoparticles* **Nanoscale** 2, 1417, (2010).
- [18] R. H. Page, K. I. Schaffers, P. A. Waide, J. B. Tassano, S. A. Payne, W. F. Krupke, W. K. Bischel *Upconversion-pumped luminescence efficiency of rare-earth-doped hosts sensitized with trivalent ytterbium* **J. Opt. Soc. Am. B** 15 996 (1998).
- [19] Olympus America Inc. *Near-Field Scanning Optical Microscopy*. <http://www.olympusmicro.com> (2012).

[20] R. L. McCreery, *Raman spectroscopy for chemical analysis* John Wiley & Sons, Inc. USA (2000).

UNIVERSITAT ROVIRA I VIRGILI
LANTHANIDE-BASED DIELECTRIC NANOPARTICLES FOR UPCONVERSION LUMINESCENCE
Elixir William Barrera Bello
Dipòsit Legal: T. 450-2013

Chapter 3

Synthesis and characterization of nanostructures

3.1. Introduction

The challenge for the research community in nanoparticles chemistry is the confinement of chemical reactions on nanometer length scale to produce chemical products that are of nanometer dimensions (generally in the range of 1-100 nm) [1]. The ongoing challenge for the research community is to continue to devise and perfect methodologies that can produce cost-effectively and reliably the desired nanoparticles with the desired particle size, particle size distribution, purity, and uniformity in terms both composition and structure [2]. Given the fact that properties of the nanoparticles are size-dependent, it is significant to be able to synthesize nanoparticles of precise dimensions with minimal size-distributions.

3.2 Sol-gel Method

The sol-gel process is a wet-chemical method that allows high-purity, high-homogeneity nanoscale materials to be synthesized at lower temperatures compared to competing high-temperature methods. Materials can be produced in forms such as particles, films and bulks. This method is especially suited for the synthesis and preparation of ultrafine lanthanide oxide particles at low temperatures. Two main routes and chemical classes of precursors are used for sol-gel processing [2]:

1. The inorganic route (“colloidal route”), which uses metal salts in aqueous solution (chloride, oxychloride, nitrate) as raw materials. These are generally less costly and easier to handle than the metal-organic route, but their reactions are more difficult to control and the surfactant that is required by the process might interfere later in downstream manufacturing and end use.
2. The metal-organic route (alkoxide route) in organic solvents. This route typically employs metal alkoxides $M(OR)_z$ as the starting materials, where M is Si, Ti, Zr, Al, Sn, or Ce; OR is an alkoxy group, and z is the valence or the oxidation state of the metal. Metal alkoxides are preferred due to their commercial availability. They are available for nearly all elements. The selection of appropriate OR groups allows to fine-tune the properties. Other precursors are metal diketonates and metal carboxylates. A large range of mixed-metal nanoparticles can be produced in mild conditions, often at room temperature by mixing metal alkoxides (or oxoalkoxides) and other precursors.

Sol-gel process consists of the following five steps: (1) Sol formation, (2) gelling, (3) shape forming, (4) drying and (5) densification.

After mixing the reactants, the organic or inorganic precursors undergo two chemical reactions: hydrolysis and condensation or polymerization, typically with an acid or base as a catalyst, to form small solid particles or clusters in a liquid (either organic or aqueous solvent). The resulting solid particles or clusters are so small (1 to 1000 nm) that gravitational forces are negligible and interactions are dominated by van der Waals, coulombic, and esteric forces. These sols – colloidal suspensions of oxide particles – are stabilized by either an electric double layer or by esteric repulsion, and even a combination of both. Over time, the colloidal particles link together by further condensation and a

dimensional network occurs. As gel generation proceeds, the viscosity of the solution increases dramatically.

The sol-gel can then be formed into three different shapes: thin film, fiber, and bulk. Thin (100 nm or so) uniform and crack-free films can readily be formed on various materials by dipping, spinning, or spray coating techniques. An overview of the capabilities of sol-gel is shown in Figure 3.1. Drying the gel simply by evaporating the interstitial liquid gives rise to capillary forces that lead to the shrinkage of the gel, and to the formation of cracks as a result of the differential stresses generated in the drying gel. The resulting dried gel is known as a *xerogel*. When the wet gel is dried in a condition that no capillary forces exist in the supercritical fluid regime, the pore and network structure of the gel should be maintained even after drying. The resulting gel is called *aerogel* in this case.

The sol-gel synthesis of some lanthanide oxides has been reported for the first time in 1971 [3]. For the preparation of such oxides, rare earth isopropoxide, acetylacetonate, and nitrate are used as the precursors. Using this method, Sc_2O_3 [4], La_2O_3 [5], CeO_2 [5], Gd_2O_3 [5], Dy_2O_3 [3], Er_2O_3 [3] and Yb_2O_3 [3] nanoparticles have been synthesized.

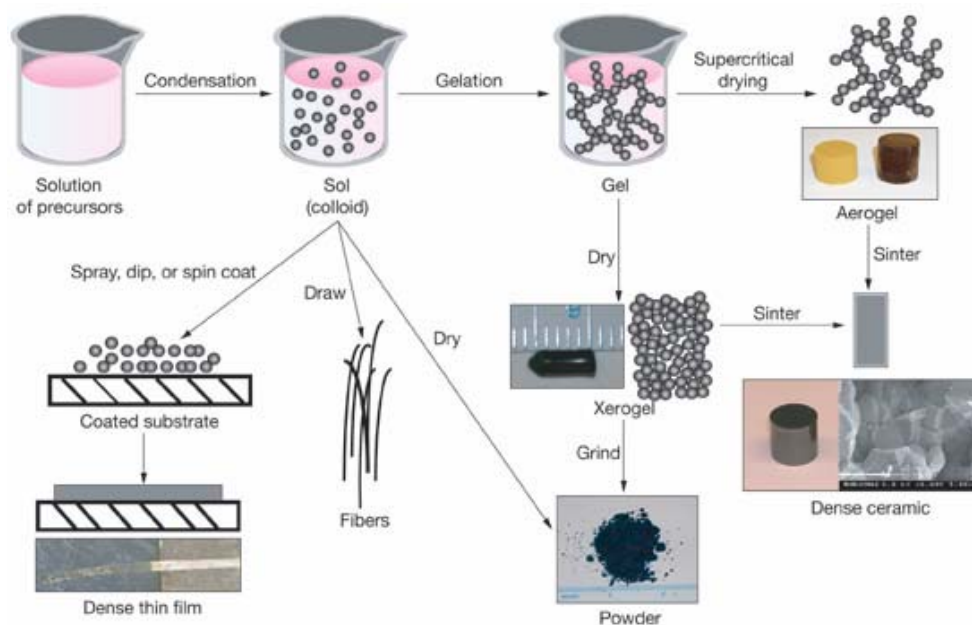


Figure 3.1. Overview of the sol-gel technology synthesis.

3.3 The modified Pechini Method

The modified Pechini method follows the sol-gel inorganic route and use organic acids for chelate metal ions in solution. The Pechini method is a useful technique for preparation of highly dispersed metal oxides [6], with homogeneous mixing of the starting materials at the molecular level gel, low synthetic temperature, good control of stoichiometry, fine particle size and uniform morphology.

Originally this method uses the ability of certain alpha-hydroxycarboxylic acids, e.g. citric acid, to form polybasic acid chelates with titanium, zirconium and niobium [7]. The technique is based on the stable formation of metal-citrate complexes uniformly dispersed into a mixed solvent of ethylene glycol (EG) and water [9]. These chelates can undergo polyesterification when heated in a polyhydroxyl alcohol to form a polymeric network which contains cations uniformly distributed throughout. By the evaporation of the water solvent from the aqueous solution of the metal salt and organic acid, a polymeric complex gel is obtained and fine particles are produced by pyrolysis. For this reason this method is also called the polymer combustion synthesis. Besides citric acid, a variety of organic acids are used as the chelating agents such as ethylenediaminetetraacetic acid (EDTA) [8], tartaric acid, malonic acid, oxalic acid and acetic acid [9]. Nanosize Y_2O_3 [9], [10] and CeO_2 [11] have been prepared at low temperatures by pyrolysis of the complex polymer gel.

Modified Pechini method is described in detail below, and a flow chart of the synthesis process is presented in Figure 3.2. The following process was outlined from $Yb:Lu_2O_3$ and $KTiOPO_4$ syntheses developed by Galceran *et al* [12], [13] in FiCMA-FiCNA lab.

1. In a Pyrex beaker containing around 10 ml of nitric acid (65%) and 10 ml of distilled water, the metal oxide precursors were added. The beaker was heated at 423 K under strong magnetic stirring until metal nitrates (viscous mass) were produced. For checking that metal nitrates were synthesized and knowing that nitrates are water soluble, 50 ml of distilled water were added and a clear solution was obtained.

2. The chelating agent (CA') was added to the nitrate precipitates in a specific molar ratio (C_M) to prepare metal- CA' complexes. The molar ratio C_M was defined as:

$$C_M \equiv \frac{[CA']}{[METAL]} \quad (3.1)$$

The nitrates were dissolved with CA in a molar ratio $C_M = 1$.

3. The solution was put in a 50 ml capacity quartz crucible beak and heated to 353 K for 4 h. The stirring velocity was reduced to avoid splashing.

4. The esterification agent, in our case EG, is added to produce a polymeric network. The molar ratio C_E was defined as:

$$C_E \equiv \frac{[CA']}{[EG]} \quad (3.2)$$

Chapter 3: Synthesis and characterization of nanostructures

which describes the degree of esterification between the chelating agent and the ethylene glycol. EG was added with a molar ratio to organic acid of $C_E = 2$.

5. The quartz crucible is placed inside a sand bath on a hot magnetic plate heated at 423 K for 15 h, to release remaining water by evaporation, and the esterification starts producing a viscous bubbly mass that forms the polymer gel upon cooling.

6. The quartz crucible is removed from sand bath and placed immediately into an oven (preheated to 573 K) to char the resin for 3 h. After charring, a black fragile foam is obtained. It is necessary to grind this foam [14].

7. Final annealing in the temperature range from 973 to 1073 K is carried out, in order to release carbon dioxide and other subproducts and obtain the desired phase transition. The annealing time is controlled to allow only crystal growth at nanometer scale.

8. The as-produced nanocrystalline powder is kept inside clear glass vials, especially for UC and PL measurements.

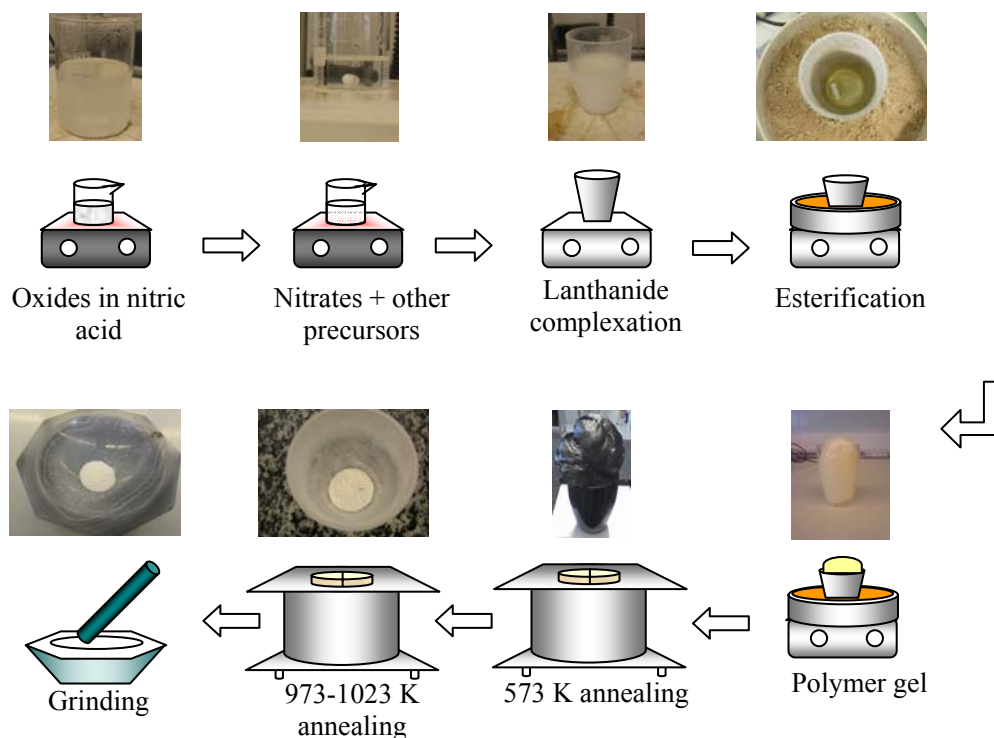


Figure 3.2. Flow chart for the nanocrystals preparation using the modified Pechini method.

3.4 Tm³⁺ doped Lu₂O₃ nanocrystals

A modified Pechini method following the previously described process was used to prepare the Tm-doped Lu₂O₃ nanocrystals with 0.5, 5, 8 and 15 %* of Tm³⁺. Used precursors are listed in paper I. These oxides were dissolved in nitric acid (65%) to form nitrate salts after water evaporation. The chelating agent was EDTA. The polymer gel was dried in a muffle preheated at 573 K to obtain the precursor powder. Sesquioxide nanocrystals were then obtained at 1073 K for 2 h.

3.4.1 Differential thermal analysis and thermogravimetry

Figure 3.3 shows the DTA-TG measurements of the precursor powder of Tm:Lu₂O₃ nanocrystals in the temperature range from 300 to 1200 K. In the temperature range of 300–550 K the dehydration of the powder causes a weight loss of about 3%. The strong exothermic peak at 700 K is attributed to the decomposition of the polyester formed by the esterification of ethylene glycol and EDTA, and it is associated to the releasing of CO₂, H₂O and NO₂. The interval from 750 to 900 K corresponds to the transformation of the amorphous phase into the crystalline cubic structure. The temperature of the decomposition peak and the final weight loss are not affected by the Tm³⁺ content.

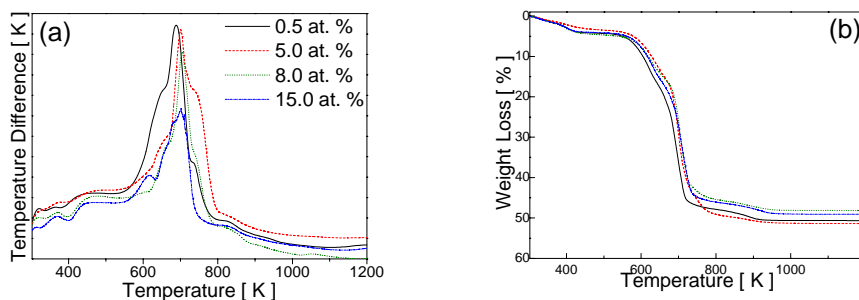


Figure 3.3. DTA (left) and weight loss (right) curve of the precursor powders of Tm:Lu₂O₃ nanocrystals.

3.4.2 Crystal Lattice variation by Tm³⁺ ion doping

In all cases, XRPD patterns of the obtained nanocrystals correspond to the pure cubic phase, with space group $Ia\bar{3}$ as can be seen from the comparison with Bragg peaks of Lu₂O₃ in the JCPDS File 43-1021. For each composition the lattice parameter was refined using the FULLPROF program [15] based on the Rietveld method [16]. The crystallite size, D , was estimated using the Scherrer's equation. Table 3.1 lists the refined a parameters, D values, and Tm³⁺ contents, x_e from EPMA measurements for all prepared Tm:Lu₂O₃ samples.

* Symbol % refers to atomic percent, in the case of elemental concentration description in the text.

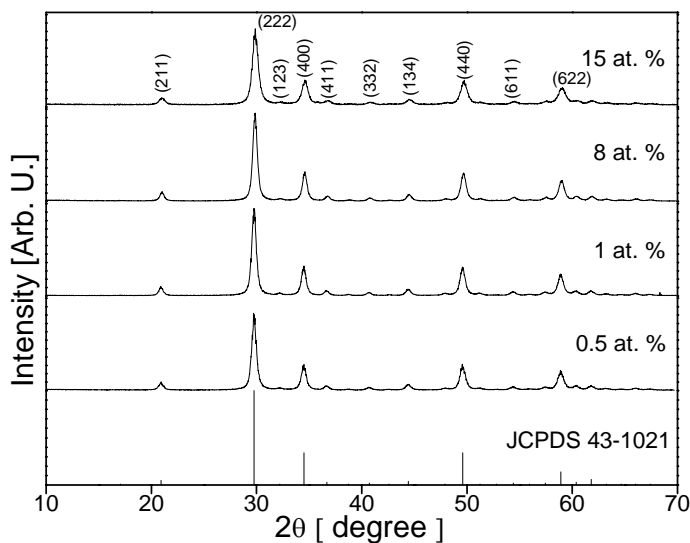


Figure 3.4. XRPD patterns of Tm:Lu₂O₃ nanocrystals for different Tm³⁺ doping at room temperature.

Table 3.1. Stoichiometry, unit cell parameters and average crystallite size of the Tm:Lu₂O₃ nanocrystals at 293 K.

[at. %]	Tm ³⁺ concentration			<i>a</i> [Å]	<i>V</i> [Å ³]	<i>D</i> [nm]
	<i>x</i> [†]	<i>x_e</i> [‡]	[10 ²⁰ at/cm ³]			
0	-	-	-	10.3900(1) ^a	1121.6(1)	-
0.5	0.010	0.009(8)	1(1)	10.3915(8)	1124.3(2)	15.7
5	0.100	0.101(4)	14.4(6)	10.3984(7)	1124.6(3)	17.2
8	0.160	0.15(2)	21(3)	10.4028(7)	1125.8(2)	16.9
15	0.300	0.287(7)	41(3)	10.4111(7)	1128.5(2)	16.8

[†] calculated

[‡] EPMA

^a See reference [17].

3.4.3 Morphological characterization

TEM images of the prepared Tm:Lu₂O₃ nanocrystals are shown in Figure 3.5. These nanocrystals have polygonal shape and their size distribution is narrow, with mean particle size of 17–23 nm, similar to that estimated from XRPD for the crystallite size. TEM images show that agglomeration by attractive interactions between the nanocrystals is producing bigger particles. ESEM images displayed in Paper I Figure 3, show agglomeration of nanocrystals, and from size distribution histograms in Figure 5 of paper II the calculated size of these agglomerated particles is in the range of 100-300 nm.

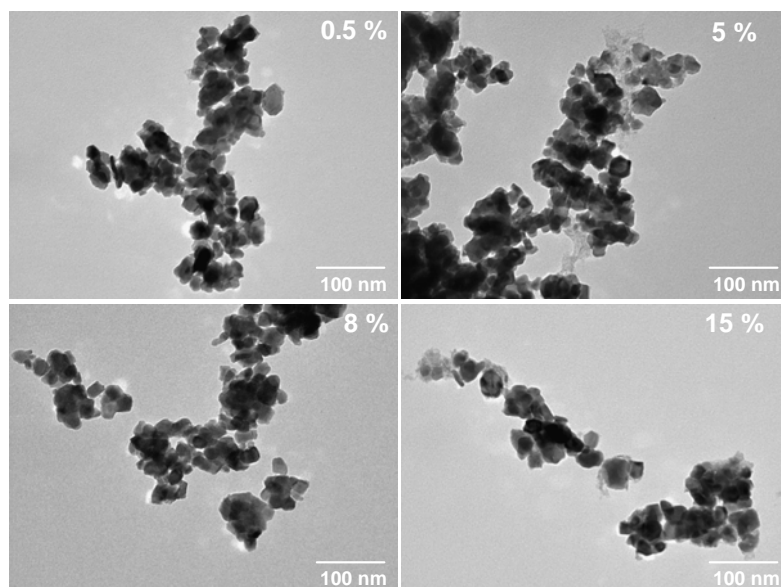


Figure 3.5. TEM micrographs of sol-gel prepared Tm:Lu₂O₃ nanocrystals for different % of Tm³⁺.

Figure 3.6 shows the selected area electron diffraction (SAED) of a single Tm:Lu₂O₃ NC. The electron diffraction pattern shows the presence of equivalent reflections corresponding to (2 2 2) planes.

Lattice fringes with no detectable defects indicate that the synthesized materials are composed by single-crystal nanoparticles. In Figure 3.7 distances between fringes equal to 5.2 Å and 3.7 Å were observed which correspond to the (2 0 0) and (2 2 0) crystallographic planes of the cubic sesquioxide Lu₂O₃ structure, respectively. The simulated SAED pattern by Fast-Fourier transform of the micrograph shows the presence of these reflexions.

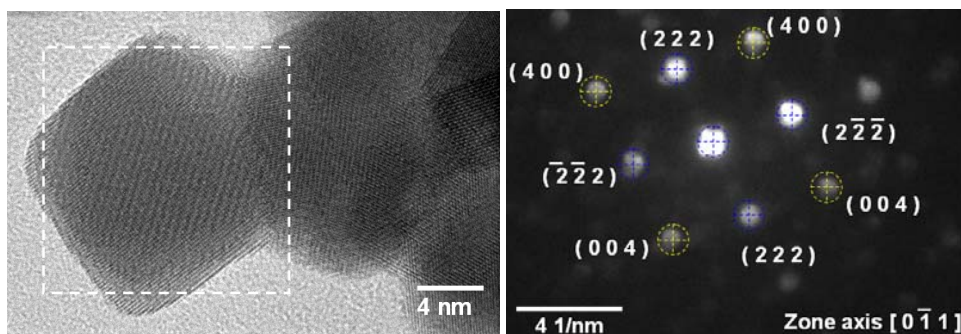


Figure 3.6. HRTEM image of one 5 % Tm:Lu₂O₃ nanocrystal (left). SAED pattern obtained (right).

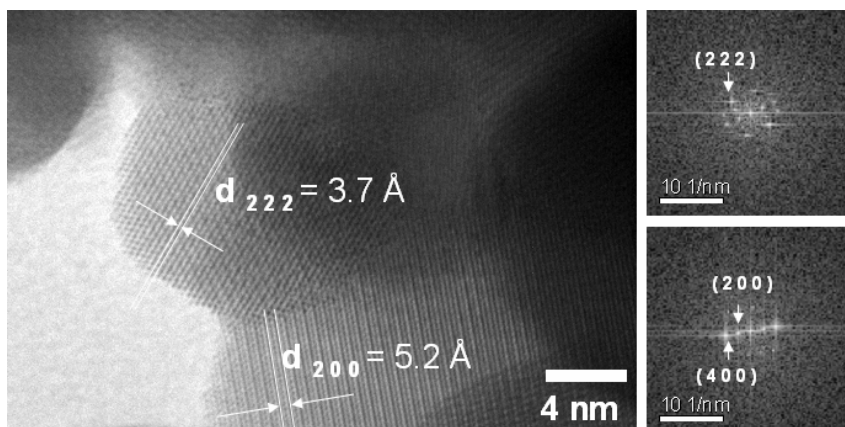


Figure 3.7. HRTEM image of 5 % Tm:Lu₂O₃ nanocrystals and FFT patterns.

3.4.4 Nanocrystalline grain growth as a function of temperature and time

The peak broadening analysis on the diffraction peak (2 2 2) was used to evaluate changes in the size of the crystallite, in relation with temperature and time during isothermal sintering processes. Figure 3.8 shows the grain growth during the heat-treatment; this grain growth is very slow or almost nonexistent below 900 K, but above 900 K grain growth develops quickly, increasing the crystallite size. It can also be deduced from Figure 3.8, that the grain growth rate does not depend on the Tm³⁺ concentration. With heating, it is expected that the as-crystallized Tm:Lu₂O₃ nanocrystals can grow by activated atomic diffusion processes at certain temperatures. The Ostwald ripening mechanism describes this process that is due to the merging of the smaller particles into larger ones, and results on potential energy differences between small and large particles. This process can occur through solid state diffusion, so the larger particles grow at the expense of the smaller ones.

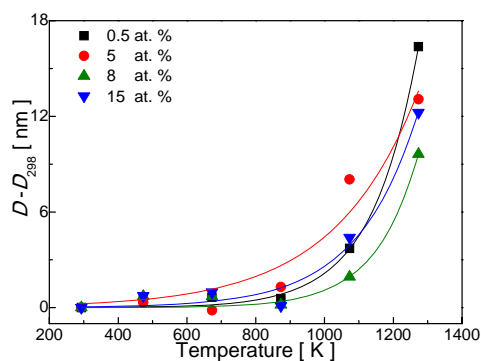


Figure 3.8. Thermal dependence of the crystallite size of Tm:Lu₂O₃ nanocrystals obtained from XRD patterns at different temperatures.

The evolution of the crystallite size with time during isothermal sintering processes was studied for 8 % Tm:Lu₂O₃ nanocrystals and it is presented in Figure 3.9. Crystal growth was found to follow the empirical relation [18]:

$$D_t^n - D_{298K}^n = Kt \quad (3.3)$$

where D_{298K} is the initial crystallite size, D_t the crystal size at time t , and K is a time-independent constant that follows the Arrhenius equation,

$$K = K_{298K} \cdot e^{-\frac{Q}{R_B T}} \quad (3.4)$$

in which K_{298K} is a constant, Q is the activation energy for grain growth, R_B is the gas constant, and T is temperature. At 723 K and 873 K the grain growth is almost stopped, but for 1267 K which is higher than the synthesis temperature (1073 K) the grain growth is reactivated.

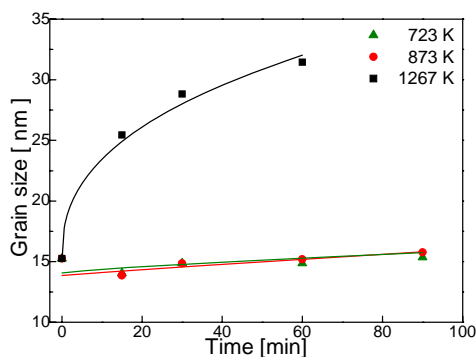


Figure 3.9. Crystallite size of 8 % Tm:Lu₂O₃ nanocrystals at different times of the final annealing heat step.

3.4.5 Linear thermal expansion

The expression for the linear thermal expansion coefficient α_L at constant pressure P , is given by

$$\alpha_L = \frac{1}{a_0} \left(\frac{da(T)}{dT} \right)_P, \quad (3.5)$$

Where a_0 is the cell parameter at room temperature, $a(T)$ the cell parameter at temperature T . From the XRPD patterns measured at 293, 493, 693, 893, 1093 and 1293 K we obtain the cell parameter as a function of the temperature $a(T)$ for every Tm³⁺ doping concentration. We can rewrite Eq. (3.5) and the finally function α_L becomes

$$\alpha_L = \frac{d}{dT} \left(\frac{a - a_0}{a_0} \right)_P \quad (3.6)$$

Where $(a(T) - a_0)/a_0$ is the relative change of cell parameter at temperature T with respect to the cell parameter at room temperature.

Table 3.2, Table 3.3 and Table 3.4 list the unit cell parameter a , crystallite size and the fraction of expansion $(a - a_0)/a_0$, respectively. Figure 3.11 plot the α_L values obtained for Tm:Lu₂O₃ nanocrystals with different Tm³⁺ concentrations. In line with previous values for bulk single crystals measured by the dilatometric technique, ($6.8 \times 10^{-6} \text{ K}^{-1}$ for Tm₂O₃ and $5.9 \times 10^{-6} \text{ K}^{-1}$ for Lu₂O₃ [19]), we observed an increase of this parameter for the nanocrystals with increasing Tm³⁺ content. The effect of the change of α due to the nano size has not been studied extensively in literature, and it is generally expected an increase of this property with the decrease of the grain size [20]. To elucidate if in the current case this increase can be related to the nano size, an evaluation of α for commercial Lu₂O₃ was performed, which yielded a value of $\alpha_L = 7.0 \times 10^{-6} \text{ K}^{-1}$. From results summarized in Table 3.2, it seems that the nano size of prepared materials has no effect on α values. On the other hand, the introduction of Tm³⁺ in the Lu₂O₃ structure of nanocrystals produces the expected slight increase of this coefficient.

Table 3.2. Unit cell parameters as function of temperature and Tm³⁺ doping.

Tm ³⁺ concentration		temperature [K]				
[%]	x_e	473	673	873	1073	1273
		cell parameter a [Å]				
0	-	10.3900(1) [†]	10.3915(8)	10.3984(7)	10.4028(7)	10.4111(7)
0.5	0.009(8)	10.414(2)	10.432(2)	10.446(2)	10.459(2)	10.474(1)
5	0.101(4)	10.407(1)	10.419(1)	10.434(1)	10.4486(6)	10.468(6)
8	0.15(2)	10.411(2)	10.426(2)	10.444(2)	10.459(2)	10.476(2)
15	0.287(7)	10.4217(9)	10.437(1)	10.454(1)	10.468(1)	10.485(1)

Table 3.3. Scherrer crystallite size D calculated from (2 2 2) reflection as function of temperature for different Tm³⁺ doping.

Tm ³⁺ concentration		Temperature [K]				
[%]	x_e	473	673	873	1073	1273
		D [nm]				
0.5	0.009(8)	15	15	15	18	31
5	0.101(4)	14	15	16	23	29
8	0.15(2)	15	15	15	17	25
15	0.287(7)	19	19	19	24	30

[†] Ref. [17]

Table 3.4. Relative expansion of cell parameter as function of temperature, for different Tm^{3+} doping.

Tm ³⁺ concentration [%] x_e		Temperature [K]				
		473	673	873	1073	1273
		$100 \cdot (a - a_0) / a_0$				
0.5	0.009(8)	0.125	0.298	0.433	0.558	0.702
5	0.101(4)	0.144	0.260	0.404	0.545	0.731
8	0.15(2)	0.096	0.240	0.413	0.558	0.721
15	0.287(7)	0.111	0.258	0.422	0.556	0.719

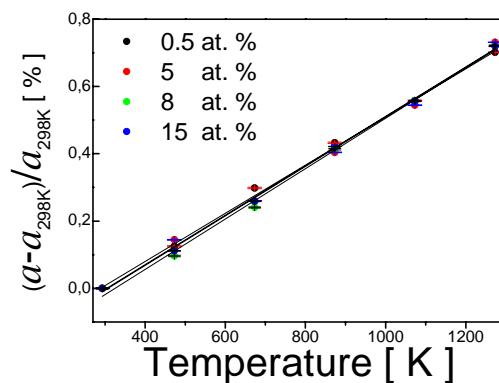


Figure 3.10. Relative thermal evolution of the cell parameter for Tm:Lu₂O₃ nanocrystals

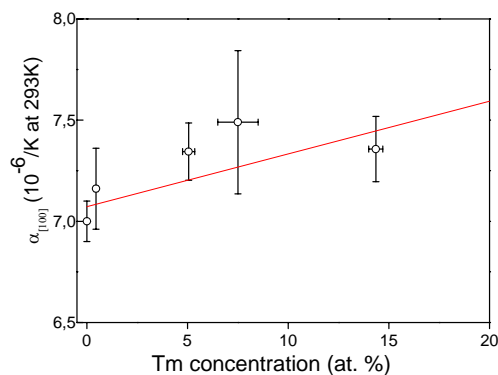


Figure 3.11. Linear thermal expansion coefficients for Tm:Lu₂O₃ nanocrystals in the range of 298 K - 1273 K.

3.5 Hydrothermal synthesis of sesquioxide Lu_2O_3 nanorods

3.5.1 Introduction

The hydrothermal technique not only helps in processing monodispersed and highly homogeneous nanoparticles, but also acts as one of the most attractive techniques for processing nano-hybrid and nanocomposite materials [21]. Hydrothermal processing can be defined as any heterogeneous reaction in the presence of aqueous solvents or mineralizers under high pressure and temperature conditions to dissolve and recrystallize (recover) materials that are relatively insoluble under ordinary conditions [22].

In a soft hydrothermal process, a sealable Teflon-lined container is used to keep water and reactants inside and a stainless steel vessel is used for keep the container hermetically sealed. After sealing, the container is kept at high temperatures inside an oven (373-773 K). The pressure of the container depends on the level of filling of the water. Hydrothermal technique provides supercritical conditions that can lead to unique morphologies of the products. The method is simple, economical and robust. Different experimental parameters as reagents, pH and additives can be modified to control the morphology of the products.

In the most cases, hydrothermal reactions at low temperatures, typically below 473 K, and autogenic pressures, produce materials having well defined morphologies with the required phase after reactor extraction, as reported in tetragonal double tungstates [23] and tetragonal vanadates [24], with no need of further annealing.

However, concerning the preparation of Lu_2O_3 sesquioxides, the hydrothermal reaction of corresponding starting chlorides provides a precursor, either the hexagonal hydroxide, the oxyhydroxide or other chlorate-related phases, which must be subsequently annealed during a short time to yield the cubic phase. The hydrothermal precursor and the derived sesquioxide have basically the same morphology, although the development of pores in the latter is due to the release of internal bubbles of water and/or hydroxyl as well as other anionic groups during the final annealing.

3.5.2 Structural and morphological characterization

The sets of samples prepared by the hydrothermal technique are listed in Table 3.5. The corresponding stoichiometric molar amounts of the starting sesquioxides were dissolved under heating with agitation in a dilute HCl solution (10 ml distilled water and 5 ml 38 wt% HCl). After complete evaporation, 20 ml of distilled water was added to form a clear solution, and the pH was adjusted to 7 and 10 with dilute NH_4OH . In each case the white suspension was subsequently heated during 24 h to 458 K in Teflon-lined autoclaves of 75 ml capacity. The product obtained in the hydrothermal reaction was separated by centrifugation and washed with distilled water several times, dried and then annealed at 1073 K for 30 min.

Table 3.5. Sets of Yb and Er or Tm co-doped Lu₂O₃ samples produced by hydrothermal technique.

Yb	Er	Tm	Lu	Yb	Er	Tm
	[%]		2-x-y-z	x	y	z
2	2	-	1.920	0.040	0.040	-
2	5	-	1.860	0.040	0.100	-
2	7.5	-	1.810	0.040	0.150	-
6	2	-	1.840	0.120	0.040	-
6	5	-	1.780	0.120	0.100	-
6	7.5	-	1.730	0.120	0.150	-
10	2	-	1.760	0.200	0.040	-
10	5	-	1.700	0.200	0.100	-
10	7.5	-	1.650	0.200	0.150	-
12.5	2	-	1.710	0.250	0.040	-
12.5	5	-	1.650	0.250	0.100	-
12.5	7.5	-	1.600	0.250	0.150	-
15	2	-	1.660	0.300	0.040	-
15	5	-	1.600	0.300	0.100	-
15	7.5	-	1.550	0.300	0.150	-
2	-	2	1.920	0.040	-	0.040
6	-	2	1.840	0.120	-	0.040
10	-	2	1.760	0.200	-	0.040

The described preparations have yielded in all cases the pure cubic $Ia\bar{3}$ phase. A mean particle size of ~ 25 nm is calculated from FWHM of broadened Bragg peaks by using the Debye–Scherrer formula. Figure 2 in paper IV shows the XRPD patterns of Yb³⁺, Ln³⁺ (Er³⁺, Tm³⁺) codoped Lu₂O₃ samples prepared at pH = 7. Figure 4 in paper IV show a panel of representative SEM and TEM images of cubic sesquioxides 2 % Ln Yb:Lu₂O₃ prepared at pH = 7. The morphology can be described as consisting of rods of ~ 45 μ m in length and ~ 90 nm of diameter, which are gathered to form microsized bunches tied in the middle. These rods are not homogeneous but porous and they are made up of pseudo-hexagon-shaped highly crystalline nanoparticles with size (circular section) of ~ 20 nm consistent with results from the XRPD analysis.

SEM and TEM images of 2 % Ln Yb:Lu₂O₃ prepared in an alkaline pH = 10 medium are displayed at Figure 5 in paper IV showing nanorods having diameters of ~ 20 nm considerably thinner than previous nanorods prepared at pH = 7. Nanorods from this preparative route appear, in general, to be assembled side by side.

3.5.3 Gold decoration of Lu_2O_3 nanorods by wetness impregnation

Gold nanoparticles show optical properties that could potentially be exploited in luminescent materials [25]. The optical properties of Au NPs are associated to the strong surface plasmon resonance (SPR), which is due to collective oscillations of electrons on the particle surface. The resonant frequency of SPR is highly dependent on particle size, shape, material, and environment [26]. Enhancement of infrared-to-green up-conversion process in Er^{3+} -doped glasses containing silver NPs has been investigated experimentally [27] and attributed to the increased local field in the proximity of the NPs, however no theoretical model was reported.

In the first set of synthesis experiments, 80 ± 10 nm in diameter gold spherical nanoparticles capped with the citrate group, with gold concentration of $300 \mu\text{g/mL}$ and SPR wavelength at 538 nm were used. For the second set, 6 ± 2 nm in diameter gold spherical nanoparticles capped with the citrate group, with gold concentration of $328 \mu\text{g/mL}$ and a SPR wavelength at 520 nm were used. The mass ratio C_G was defined as:

$$C_G \equiv \frac{m_{\text{Au}}}{m_{\text{Ln}_2\text{O}_3}} \quad (3.7)$$

Optimal results were obtained for gold to sesquioxide mass ratio of $C_G = 0.3$ without agglomeration of gold nanoparticles.

The gold decoration was carried by wetness impregnation. In that way, 1 mL of gold aqueous solution was centrifuged and the slurry precipitate was diluted in 5 mL of ethanol. The sesquioxide nanorod powder (previously produced by hydrothermal technique as described before), was added and the suspension was stirred at room temperature. Then, the solid was separated by centrifugation, washed three times with ethanol and centrifugation cycles between each washing. The samples were dried in air at 373 K for 2 h, and finally aged at 573 K for 1 h. Further experimental details are listed in Table 3.6.

Figure 3.12 and Figure 3.13 show TEM micrographs of gold nanoparticles on the surface and inside the pores of 2% Er Yb: Lu_2O_3 nanorods. The origin of this morphology for co-doped Yb^{3+} , $\text{Er}^{3+}/\text{Tm}^{3+}$ - Lu_2O_3 has been studied in paper IV [28]. Gold nanoparticles (~ 5 nm) were uniformly dispersed and linked to the most external porous surface of the nanorods or inside the porous structure. Despite the uniform distribution of gold nanoparticles, low coverage density was obtained.

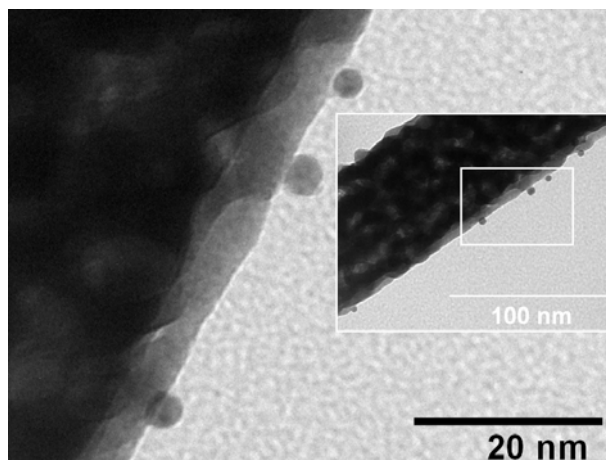


Figure 3.12. TEM image showing gold nanoparticles on the surface of Lu₂O₃ nanorods.

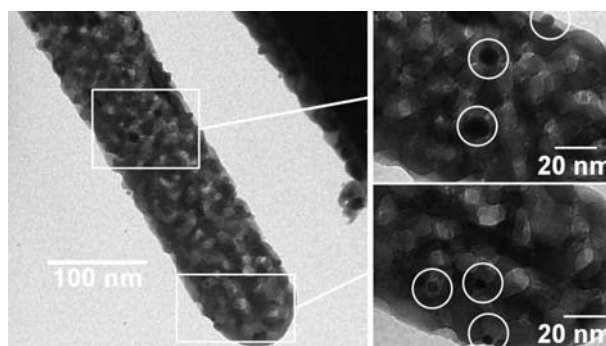


Figure 3.13. TEM image showing gold nanoparticles inside the pores of Lu₂O₃ nanorods.

Table 3.6. Experimental parameters for gold decoration of sesquioxide Lu₂O₃ nanorods (NRs).

Yb	Er	Tm	Lu	Yb	Er	Tm	Ln ₂ O ₃	Au	Au	Au	C _G	Solution	Annealing	TEM		Remarks
														Gold	Morphology	
	[%]			y	x	z	[mg]	[μL]	[mg]	[nm]			[K-h]			
4	0.5	2.5	1.860	0.080	0.010	0.050	50	50	0	82±10	-	-	373-10	No	Spindle group of NRs	-
4	0.5	2.5	1.860	0.080	0.010	0.050	50	50	0	82±10	-	EtOH	573-3	Few	Spindle group of NRs	-
10	0.75	0	1.785	0.200	0.015	0.000	20	500	0.02	82±10	-	NH ₄ OH	373-10	No	NRs agglomerates	Gold dissolution pH=11
10	0.75	0	1.785	0.200	0.015	0.000	1	1000	0.03	82±10	3.0	Acetone	373-10	Some	NRs and some gold	pink powder
10	0.75	0	1.785	0.200	0.015	0.000	1	1000	0.03	82±10	3.0	H ₂ O	373-10	Yes	NRs and gold separated	white and dark points
10	0.75	0	1.785	0.200	0.015	0.000	1	1000	0.03	82±10	3.0	EtOH	373-10	Yes	Bonded Au or next to NRs	pink powder
10	0.75	0	1.785	0.200	0.015	0.000	100	10000	0.3	82±10	0.3	EtOH	573-1	Yes	Bonded Au to NRs	-
2	2	0	1.920	0.040	0.040	0.000	100	1000	0.33	6±2	0.3	EtOH	573-1	Yes	Bonded Au to NRs	-
6	2	0	1.840	0.120	0.040	0.000	100	1000	0.33	6±2	0.3	EtOH	573-1	Yes	Bonded Au to NRs	-
10	2	0	1.760	0.200	0.040	0.000	100	1000	0.33	6±2	0.3	EtOH	573-1	Yes	Bonded Au to NRs	-
12.5	2	0	1.710	0.250	0.040	0.000	100	1000	0.33	6±2	0.3	EtOH	573-1	Yes	Bonded Au to NRs	-
15	2	0	1.660	0.300	0.040	0.000	100	1000	0.33	6±2	0.3	EtOH	573-1	Yes	Bonded Au to NRs	-
2	0	2	1.920	0.040	0.000	0.040	100	1000	0.33	6±2	0.3	EtOH	573-1	Yes	Bonded Au to NRs	-
6	0	2	1.840	0.120	0.000	0.040	100	1000	0.33	6±2	0.3	EtOH	573-1	Yes	Bonded Au to NRs	-
10	0	2	1.760	0.200	0.000	0.040	100	1000	0.33	6±2	0.3	EtOH	573-1	Yes	Bonded Au to NRs	-

3.6 Synthesis of core-shell $\text{SiO}_2@ \text{Ln}_2\text{O}_3$ microstructures by modified Pechini method. Part I

In a first study, a series of synthesis was carried using the modified Pechini method with EDTA as chelation agent, ethylene glycol (EG) as the esterification agent and a Tm^{3+} doping fixed to 5 %. It is necessary to define the sesquioxide to silica mass ratio as:

$$C_s \equiv \frac{m_{\text{Ln}_2\text{O}_3}}{m_{\text{SiO}_2}} \quad (3.8)$$

Silica spheres (Alpha Aesar, 100 nm in diameter) were added after EG under ultrasonic stirring to disperse the spheres. Further experimental details are listed in Table 3.7.

Aqueous ammonia NH_4OH was added in some experiments to increase the solubility of EDTA generating a clear solution. Solubility of EDTA is 0.05 g/100 ml at 293 K. In this way, NH_4OH was added to enhance the solubility of EDTA in water. It was observed that the annealing at 573 K is inconvenient due to the rapid formation of a white fume of ammonium nitrate (NH_4NO_3) that spreads part of material out of the crucible. For NH_4OH addition it is necessary to carry out the annealing using a slow temperature ramp until 573 K.

Table 3.7. Experimental parameters in the synthesis of SiO₂@Ln₂O₃ core-shell microstructures by modified Pechini.

Tm:Lu ₂ O ₃ [%]	Salt ^a	NH ₄ OH	C _M	C _E	C _S	Anneal. 1 [K-h]	Anneal. 2 [K-h]	TEM Morphology			XRPD
								SC ^b	IP ^c	Agglom ^d	Phase
5	nit	yes	1	0.5	3.4	573-3	-	full	nps	high	Lu ₂ O ₃
5	nit	yes	1	0.5	3.4	573-1	-	-	-	-	NH ₄ NO ₃
5	nit	-	1	0.5	0.2	573-3	973-2	full	no	partial	Lu ₂ O ₃ SiO ₂
5	nit	-	1	0.5	0.2	573-3 ^e	973-2 ^f	no	no	partial	SiO ₂
5	nit	-	1	0.5	4.0	573-3	973-2	partial	no	high	Lu ₂ O ₃
5	nit	-	1	0.5	6.7	573-3	973-2	partial	mps	high	-
5	nit	-	1	0.5	6.7	573-3	973-2	no	mps	high	Lu ₂ O ₃
5	nit	-	1	0.5	6.7	-	973-2 ^g	no	ps	high	Lu ₂ O ₃
5	nit	-	1	0.5	6.7	573-3	973-2	no	ps	high	-
5	nit	yes	1	0.5	1.3	573-3 ^e	973-2	no	mps	high	-
0	-	yes	-	0.5	-	573-3 ^e	973-2	partial	-	high	-
0	-	-	-	0.5	-	573-3	973-2	no	-	high	-

^a nit = nitrates

^b SC = shell cover

^c IP = Dispersed Lu₂O₃ particles: nps/mps/ps/no = particles with < 100 nm / 100 nm- 100µm / larger than 100 µm / not observed

^d Agglom = agglomeration between SiO₂ spheres and Lu₂O₃ nanoparticles

^e Starting from 463 K with a ramp of 130 K/h

^f Starting from 573 K with a ramp of 105 K/h

^g Starting from 293 K with a ramp of 25 K/h

3.6.1 Structural and morphological characterization

Figure 3.14 shows the effect of different C_S values on the morphology of the final product. Only for a low value of $C_S = 0.2$, sesquioxide nanoparticles get bonded to the silica spheres but no complete layer formation was observed. For higher C_S values, individual particles of sesquioxide tend to agglomerate forming micro sized particles. Figure 3.15 shows the XRPD patterns of Tm^{3+} doped Lu_2O_3 samples with $C_S = 0.2$. The comparison with the XRPD pattern of amorphous silica, 5 % $\text{Tm}:\text{Lu}_2\text{O}_3$ nanocrystalline powder and the JCPDS card, verify that deposited nanoparticles correspond to the cubic $Ia\bar{3}$ phase of lutetium oxide.

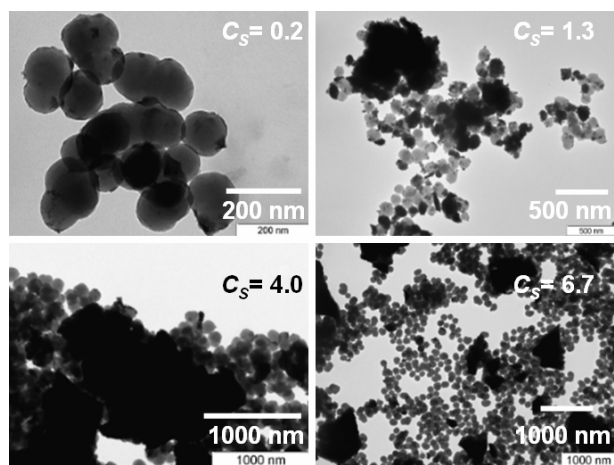


Figure 3.14. TEM micrographs for different values of sesquioxide/silica mass ratio.

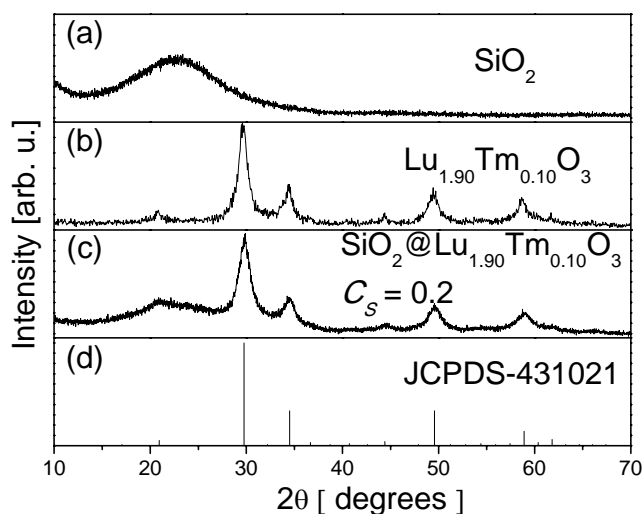


Figure 3.15. X-ray powder diffractions patterns of amorphous silica (a), 5% $\text{Tm}:\text{Lu}_2\text{O}_3$ nanocrystals (b), silica spheres with $C_S=0.2$ (c), and the JCPDS card 43-1021 for Lu_2O_3 (d).

The formation a dark layer was observed in experiments with blank spheres when aqueous ammonia was added. In this way, Figure 3.16a shows blank samples of SiO_2 nanospheres produced without doped Lu_2O_3 sesquioxide addition, and the formation of a darker layer when NH_4OH was used to process the above blank sample can be viewed in Figure 3.16b. Erosion of the surfaces and sintering of spheres was also observed in Figure 3.16b. Erosion of the surface could explain this layer formation by segregation of silica from other spheres. Also it was observed that 100 nm silica spheres get deformed and sintered during calcination at 973 K.

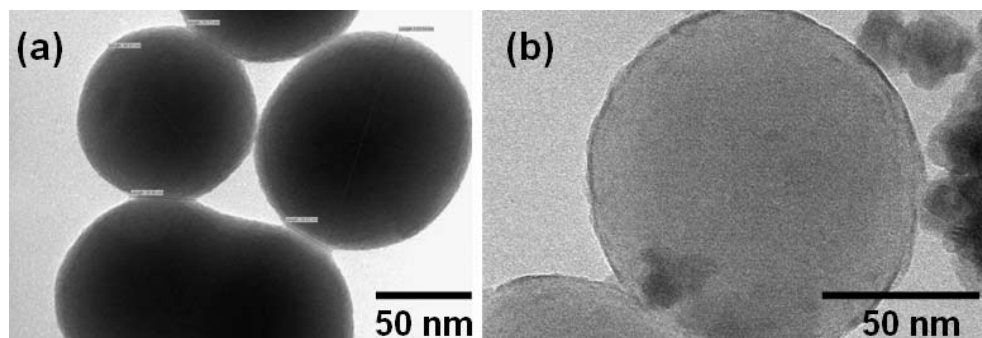


Figure 3.16. TEM micrographs of blank samples after annealing at 973 K for 2 h. (a) normal solution. (b) With the addition of NH_4OH .

In general, no layer deposition was obtained in these series of experiments due to the independent growth of the sesquioxide forming aggregates. NH_4OH was used to increase the solubility of EDTA but segregation of SiO_2 was observed in the form of a dark amorphous layer deposition over other spheres as previously discussed. Temperatures above 873 K are necessary to obtain the sesquioxide phase, but undesirable sintering of 100 nm silica spheres was observed at this temperature.

3.7 Synthesis of core-shell $\text{SiO}_2@ \text{Ln}_2\text{O}_3$ microstructures by modified Pechini method. Part II

3.7.1 Synthesis and morphological characterization

Centrifugation process and ethanol washing were included in the synthesis process to warrant that excess of material for desired layer coating is removed. Table 3.8 lists the experimental parameters of the preparation, as well as structural and morphological characterization results of the core-shell $\text{SiO}_2@ \text{Ln}_2\text{O}_3$ microstructures fabricated by the Pechini method. Silica spheres with a larger diameter (327 ± 44 nm) were chosen to avoid the deformation and sintering process during annealing. The syntheses follow the Pechini method in which the modification consists in the incorporation of the amorphous silica spheres to the solution after addition of EG (paper VII). Aqueous ammonia, NH_4OH , was used to control the pH value. Ammonia solution enhances the production of silanol groups (Si-O) on the surface of the silica [29], where the esterified chelates of lanthanide ions will be bonded. The solution was left with magnetic stirring during 24 h. After that, the silica spheres were extracted by centrifugation at 6000 rpm for 30 min and washed with ethanol twice. The slurry was putted in a platinum crucible and heated at 373 K for 1 h in order to remove water, after that an annealing process at 573 K for 1 h was carried out to eliminate the organic compounds and finally a second annealing at 1073 K for 2 h to obtain a white color powder.

Table 3.8. Experimental parameters of SiO₂@Ln₂O₃ core-shell microstructures by modified Pechini method with centrifugation.

Sample	Salt ^a	pH	Base	C _M	C _E	Ln ₂ O ₃ [mmol]	EtOH	C _S	SiO ₂ [g]	Anneal.1 [K-h]	Anneal.2 [K-h]	Anneal.3 [K-h]	SC ^b	TEM		XRPD Phase	Observations
														IP ^c	Agglom. ^d		
M1	chlor	<1	-	0.5	2	1.26	yes	1.0	0.5036	373-1	573-1	-	no shells	nps + mps	high	-	step 1 of 2
M1	chlor	<1	-	0.5	2	1.26	yes	1.0	0.5036	373-1	573-1	873-2	spots	nps	low	SiO ₂ +(222)Lu ₂ O ₃	step 2 of 2
M1	chlor	<1	-	0.5	2	2.52	yes	26.7	0.0374	-	573-1.5	1073-3.5	spots	no	partial	-	-
M1	chlor	<1	NH ₄ OH	0.5	2	2.52	yes	26.7	0.0374	373-1	573-1	1073-18	spots	nps	high	-	long calcination
M1	chlor	7	NH ₄ OH	0.5	2	2.52	yes	26.7	0.0374	373-1	573-1	1073-2	partial	no	low	-	paper VII
M1	chlor	11	NH ₄ OH	0.5	2	2.52	yes	26.7	0.0374	373-1	573-1	1073-2	necklace nps	no	low	-	paper VII
M1	nit	<1	NH ₄ OH	0.5	2	2.52	yes	26.7	0.0374	373-1	573-3	-	-	-	-	-	not centrifuged
M1	nit	7	NH ₄ OH	0.5	2	2.52	no	26.7	0.0374	373-1	573-2	1073-2	partial	no	low	SiO ₂ +Lu ₂ O ₃	paper VII
M1	nit	11	NH ₄ OH	0.5	2	2.52	no	26.7	0.0374	373-1	573-2	1073-2	partial	no	low	SiO ₂ +Lu ₂ O ₃	paper VII
M1	chlor	7	NH ₄ OH	0.5	2	2.52	yes	<26.7	0.0374	1293-2	573-1	1073-2	necklace nps	no	low	SiO ₂ +Lu ₂ O ₃	green and red emission
M1	chlor	11	NH ₄ OH	0.5	2	2.52	yes	<26.7	0.0374	1293-2	573-1	1073-2	-	-	-	SiO ₂ +Lu ₂ O ₃	green and red emission
M1	nit	7	NH ₄ OH	0.5	2	2.52	yes	4.2	0.0800	-	573-1	1073-1	necklace	no	low	-	step 1 of 3
M1	nit	7	NH ₄ OH	0.5	2	2.52	yes	6.3	0.0800	-	573-1	1073-1	necklace	no	partial	-	step 2 of 3
M1	nit	7	NH ₄ OH	0.5	2	2.52	yes	12.4	0.0800	-	573-1	1073-1	necklace	no	high	-	step 3 of 3
M1	nit	7	NH ₄ OH	0.5	2	2.52	yes	4.2	0.0800	293-12	573-3	1073-2	partial	mps	low	-	H ₂ O washed
M1	nit	7	NH ₄ OH	0.5	2	2.52	yes	4.2	0.0800	-	573-1	1073-2	spots, shells	mps	high	-	-
M2	nit	<1	-	0.5	2	1.26	yes	5.0	0.1000	-	573-3	1073-1	large spots necklace	nps	low	-	TMES
M2	nit	7	NH ₄ OH	0.5	2	1.26	yes	2.5	0.2000	-	573-2	1073-1	large spots necklace	nps	low	-	TMES
M2	nit	11	NH ₄ OH	0.5	2	1.26	yes	2.5	0.2000	-	573-2	1073-1	thin shells necklace	nps	low	SiO ₂ +Lu ₂ O ₃	TMES
M3	nit	<1	-	0.5	2	1.26	no	2.5	0.2000	-	573-1	1073-1	small spots necklace	nps	low	-	HSO+TMES
M3	nit	7	NH ₄ OH	0.5	2	1.26	no	2.5	0.2000	-	573-1	1073-1	spots necklace	nps	low	SiO ₂ +Lu ₂ O ₃	HSO+TMES
M4	nit	<1	-	0.5	2	1.26	no	2.5	0.2000	-	573-1	1073-1	spots necklace	nps	low	-	HSO

Sample*	Salt	pH	Base	C_M	C_E	Ln ₂ O ₃	EtOH	C_S	SiO ₂	Anneal. 1	Anneal. 2	Anneal. 3	TEM			XRD	Observations
						[mmol]			[g]	[K-h]	[K-h]	[K-h]	SC ^b	IP ^c	Agglom. ^d	Phase	
M4	nit	7	NH ₄ OH	0.5	2	1.26	no	2.5	0.2000	-	573-1	1073-1	spot	nps	low	SiO ₂ +Lu ₂ O ₃	HSO
M5	nit	<1	-	-	-	1.26	no	2.5	0.2000	-	573-1	1073-1	thick shells	nps	low	-	HSO, TMES, hydrophobic
M5	nit	7	-	0.5	2	1.26	no	1.3	0.4000	-	573-1	1073-1	spots	no	high	SiO ₂	HSO+TMES
M6	nit	<1	-	-	-	1.26	no	1.3	0.4000	-	573-2	1073-1	spots	nps	low	-	HSO, no H ₂ O washed
M6	nit	<1	-	-	-	1.26	no	1.3	0.4000	373-1	573-2	1073-1	large spots	no	low	SiO ₂ +other	HSO, no H ₂ O washed
M7	nit	7	NH ₄ OH	0.5	2	1.26	no	5.0	0.1000	373-1	573-2	1073-1	-	-	-	-	-
M8	nit	7	NH ₄ OH	0.5	2	1.26	no	5.0	0.1000	373-1	573-2	1073-1	thick shells	no	low	-	-

* M1 = Lu_{1.84}Yb_{0.12}Er_{0.03}O₃
 M2 = Lu_{1.76}Yb_{0.20}Tm_{0.04}O₃
 M3 = Lu_{1.80}Yb_{0.16}Tm_{0.04}O₃
 M4 = Lu_{1.88}Yb_{0.08}Tm_{0.04}O₃
 M5 = Lu_{1.92}Yb_{0.04}Tm_{0.04}O₃
 M6 = Lu_{1.84}Yb_{0.12}Tm_{0.04}O₃
 M7 = Lu_{1.92}Yb_{0.08}O₃
 M8 = Lu_{1.889}Yb_{0.110}Tm_{0.001}O₃

^a nit / chlor = nitrates / chlorides

^b SC = shell cover

^c IP = Dispersed Lu₂O₃ particles: nps/mps/ps/no =
 particles with < 100 nm / 100 nm- 100µm / larger than 100 µm / not observed.

^d Agglomeration between SiO₂ spheres and Lu₂O₃ nanoparticles.

† TMES = Trimethyletoxysilane treatment of SiO₂ spheres

‡ HSO = 50 v % H₂O₂ + 50 v % H₂SO₄ treatment of SiO₂ spheres

Figure 3.17 shows the XRPD patterns of $\text{SiO}_2@(\text{2 \% Er, 6 \% Yb})\text{:Lu}_2\text{O}_3$ particles. SiO_2 pattern shows a broad band centered at $2\theta = 22^\circ$ corresponding to the amorphous phase. All the diffraction lines are indexed as the cubic Lu_2O_3 with space group $Ia\bar{3}$ (JCPDS File 43-1021). By using the Scherrer equation the mean crystallite size of the phosphor shell calculated from the analysis of FWHM of the XRPD peaks is approximately 5 nm.

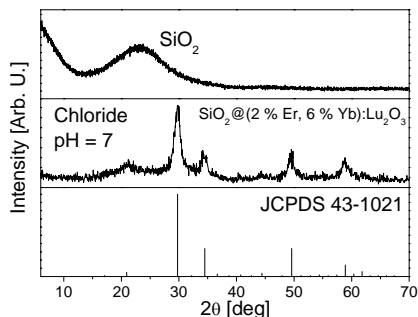


Figure 3.17. XRPD of $\text{SiO}_2@(\text{2 \% Er, 6 \% Yb})\text{:Lu}_2\text{O}_3$ microstructures sample

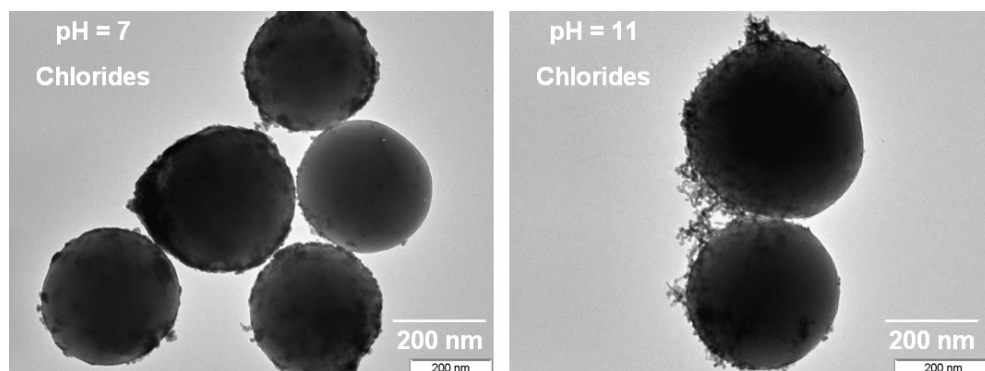


Figure 3.18. TEM image showing a core-shell particles obtained from chloride precursor with pH = 7 (left) and pH = 11 (right).

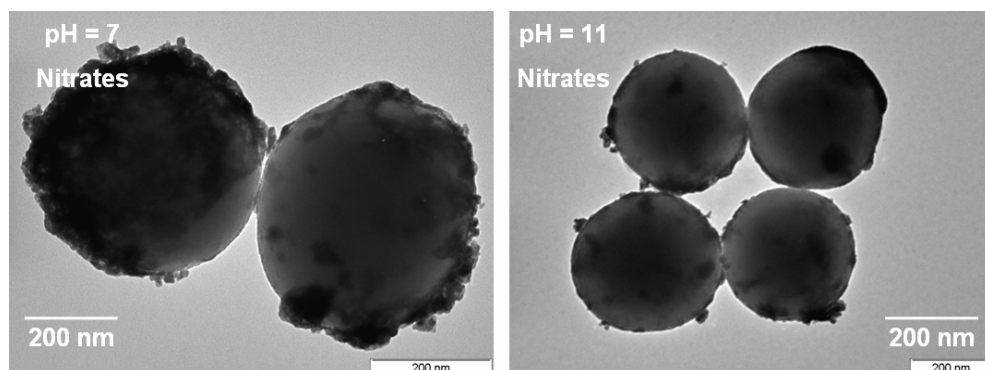


Figure 3.19. TEM image showing a core-shell structure obtained from nitrate precursors with pH = 7 (left) and pH = 11 (right).

Figure 3.18 and Figure 3.19 show the effect of the pH and the starting precursor in the morphology of the deposited sesquioxide layers. The difference between the resulting particles is due to the precursors and pH value used during the synthesis, however for pH values below 6, previous experiments did not show the formation of complete layers (shells) for both kinds of precursors. For pH = 7, shells composed by nanocrystals were obtained. Figure 3.20 shows one silica sphere partially coated by a sesquioxide polycrystalline layer of some nm of thickness. For higher pH values sesquioxide nanocrystals grow forming short necklace structures bonded on the surface of the spheres, as shown in Figure 3.21.

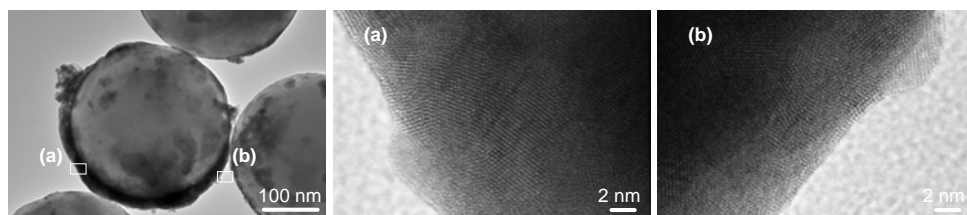


Figure 3.20. HRTEM micrographs of a $\text{SiO}_2@(\text{2 \% Er, 6 \% Yb})\text{:Lu}_2\text{O}_3$ sphere produced from nitrates at pH=7. The regions (a) and (b) show non-porous nanocrystalline domains.

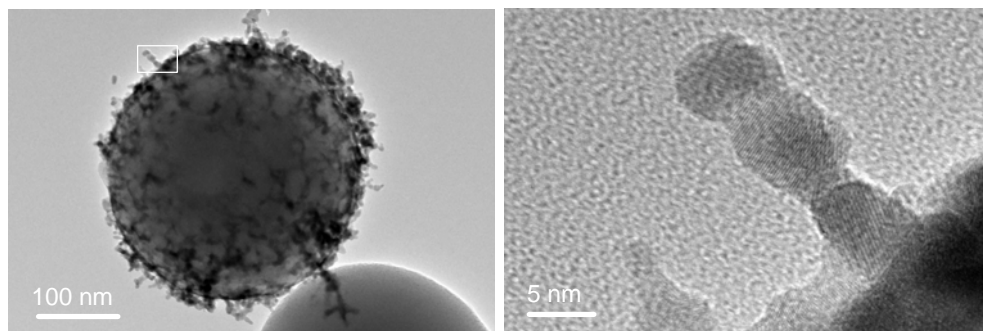


Figure 3.21. HRTEM image of one isolated coated $\text{SiO}_2@(\text{2 \% Er, 6 \% Yb})\text{:Lu}_2\text{O}_3$ produced from chlorides at pH = 11 (left). Necklace structure composed by 3 nanocrystals (right).

Experiments attempting the coating of silica spheres through two or three cycles (Figure 3.22) of the above processing were also carried out, but unsatisfactory results were obtained due to the agglomeration of the spheres by the independent sesquioxide growth onto others nanocrystals.

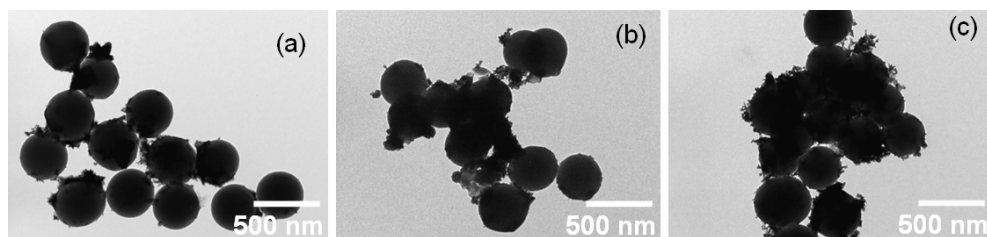


Figure 3.22. Collection of TEM images showing the morphology of silica spheres after one (a), two (b) and three (c) coating cycles.

Figure 3.23. shows a SEM image of core-shell particles, where sesquioxide growth is not occurring on the surfaces of the spheres producing partial shell. Some sesquioxide to silica mass ratios, C_s , do not limit the sesquioxide growth to the spheres surfaces, and a direct control of surface functionalization of silica spheres is necessary to limit the sesquioxide growth to the surface and get full covered spheres.

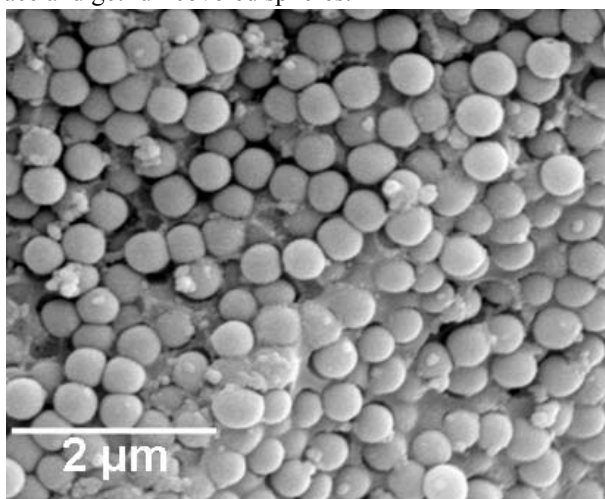


Figure 3.23. SEM images of $\text{SiO}_2@(\text{2 \% Er, 6 \% Yb})\text{:Lu}_2\text{O}_3$ sample.

3.7.2 Functionalization with a silane coupling agent

Silane coupling agents are effective for improving the adhesion at the interface between the organic and inorganic materials, and have been frequently utilized to enhance the strength and performance of glass-fiber reinforced plastics [30]. Silane coupling agents are organosilicone compounds having two functional groups with different reactivity. One of the two functional groups reacts with the organic materials and the other reacts with inorganic materials. Their general structure is Y-R-Si(X)_3 , where Y denotes a functional group that links with organic materials, e.g. vinyl, epoxy, amino group and so on. X is a functional group that undergoes hydrolysis by water or moisture to form silanol. This silanol links with inorganic materials. Representative examples of X include chlorine, alkoxy, and acetoxy group.

One can form covalent bonds between an organic functional group and a substrate through an intermediary functional silane, called a coupling agent. Coupling agents are used in solid state synthesis, for example as antimicrobial agents and as organic surface coatings. In most cases the substrate is pretreated with the silane-coupling agent, but integral blending accomplished by simple mixing of all the reactants at once, particularly for coatings and fabrication of composites, is frequently used [31].

In the case of glass and silicon dioxide substrates, the X group reacts with OH groups on the substrate eliminating a low molecular weight compound, so that the silicon in the organosilane forms a strong chemical bond with the substrate and the alkyl group causes the surface to be hydrophobic [21].

For functionalization of SiO₂ spheres we use the trimethylethoxysilane C₅H₁₄OSi (TMES), purchased from Gelest Inc. TMES has shown reaction with silica in water-rich ethanol medium (water/ethanol 25/75 v/v) [32]. TMES schematic formula is shown in Figure 3.24. The silane derivative may be described by the general formula RSiX₃, where R is an ethoxyl group, that links with the SiO₂ and X designates the proprietary hydrolysable methyl group attached to silicon that links the citric acid lanthanide complex

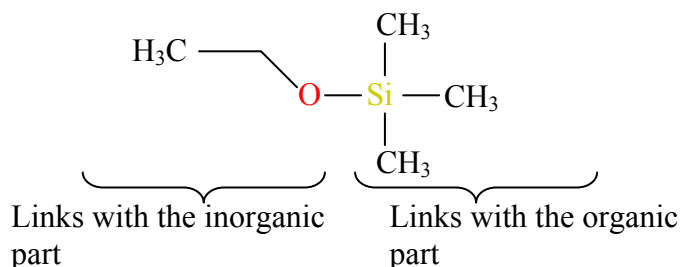


Figure 3.24. Scheme of trimethylethoxysilane molecule.

The first step was to increase the hydroxyl concentration (-OH) on the surface silica spheres with a piranha solution [33] as follow: immersing the spheres in a 1:1 mixture of 50% aqueous sulfuric acid : 30% hydrogen peroxide for 30 minutes followed by rinses in distilled water and ethanol and then air drying.

Two grams of silica powder was dispersed in 20 mL of water, ethanol (50/50 v/v) solution. Then 4 mL of TMES was added and the reaction mixture was stirred at ambient temperature for 2 h. The modified silica particles were then separated by centrifugation and washed with ethanol. This procedure was repeated three times. Silica spheres shown hydrophobicity verifying the functionalization with TMES.

In the same way the nitrates were dissolved in water/ethanol (50/50 v/v) solution and silica spheres were added and the modified Pechini method was completed as describe in previous section. No enhancement of deposition of sesquioxide on the surface was observed respect

to the activation of the silica surfaces with NH_4OH . It was verified by the presence of sesquioxide nanoparticles agglomeration and partially coated silica spheres.

3.8 Hydrothermal synthesis of core-shell $\text{SiO}_2@ \text{Ln}_2\text{O}_3$ microstructures

The corresponding stoichiometric molar amounts of the starting sesquioxides were dissolved under heating with stirring in HNO_3 or HCl solutions to produce the nitrate and chloride precursors. Citric acid was added as the chelation agent with a molar ratio of CA to metal cations $C_M = 1$. Citric acid was used to avoid independent growth of sesquioxide nanostructures with special morphologies. Amorphous silica spheres (Alpha Aesar, 100 nm in diameter) were added and the pH value was adjusted using diluted KOH or diluted NH_4OH . Further details of the experiment parameter are listed in Table 3.9.

Table 3.9. Experimental parameters of the synthesis SiO₂@Ln₂O₃ core-shell microstructures by hydrothermal technique.

Sample [†]	Salt ^a	pH	Base	C _M	C _S	Ln ₂ O ₃	SiO ₂	Anneal. 1	Anneal 2	TEM			XRPD	Observations
						[mmol]	[g]	[K-h]	[K-h]	SC ^b	IP ^c	Agglom. ^d	Phase	
H1	nit	7.5	KOH	1	0.46	0.75	0.6691	-	-	-	-	-	SiO ₂ +amorph.Lu ₂ O ₃	step 1 of 2
H1	nit	7.5	KOH	1	0.46	0.75	0.6691	873-1/2	-	none	no	high	SiO ₂ +amorph.Lu ₂ O ₃	step 2 of 2
H1	nit	12	KOH	1	0.46	0.75	0.6691	-	-	-	-	-	SiO ₂ +amorph.Lu ₂ O ₃	step 1 of 2
H1	nit	12	KOH	1	0.46	0.75	0.6691	873-1/2	-	-	-	-	SiO ₂ +amorph.Lu ₂ O ₃	step 2 of 2
H1	nit	12	KOH	1	0.46	0.75	0.6691	-	-	-	-	-	SiO ₂ +amorph.Lu ₂ O ₃	step 1 of 2
H1	nit	12	KOH	1	0.46	0.75	0.6691	873-1/2	-	-	-	-	SiO ₂ +amorph.Lu ₂ O ₃	step 2 of 2
H1	nit	7.4	NH ₄ OH	1	0.46	0.75	0.6691	-	-	-	-	-	SiO ₂ +amorph.Lu ₂ O ₃	step 1 of 3
H1	nit	7.4	NH ₄ OH	1	0.46	0.75	0.6691	873-1/2	-	-	-	-	SiO ₂ +amorph.Lu ₂ O ₃	step 2 of 3
H1	nit	7.4	NH ₄ OH	1	0.46	0.75	0.6691	1073-1/2	-	none	no	high	SiO ₂ +amorph.Lu ₂ O ₃	step 3 of 3
H1	chlor	7	NH ₄ OH	1	0.46	0.75	0.6494	1073-1/2	-	none	no	high	SiO ₂ + .Lu ₂ O ₃	-
H2	chlor	7	NH ₄ OH	1	1.27	1	0.2987	1073-1/2	-	partial	nps,mps	low	SiO ₂ + .Lu ₂ O ₃	amorphous shell (SAED)
H2	nit	7.3	NH ₄ OH	1	1.27	1	0.2987	-	-	-	-	-	SiO ₂ +amorph.Lu ₂ O ₃	step 1 of 3
H2	nit	7.3	NH ₄ OH	1	1.27	1	0.2987	873-1/2	-	-	-	-	SiO ₂ +amorph.Lu ₂ O ₃	step 2 of 3
H2	nit	7.3	NH ₄ OH	1	1.27	1	0.2987	1073-1/2	-	partial	no	low	SiO ₂ +amorph.Lu ₂ O ₃	step 3 of 3
Blank	-	7	KOH	-	-	-	-	873-1/2	-	none	-	low	-	deformed spheres
Blank	-	7	KOH	-	-	-	-	873-1/2	-	partial	-	low	-	necks of sintering
Blank	-	9	NH ₄ OH	-	-	-	-	873-1/2	-	none	-	low	-	deform spheres,porous surface
Blank	-	9	NH ₄ OH	-	-	-	-	873-1/2	-	none	-	low	-	deform spheres,porous surface
H3	nit	7	KOH	1	3.02	-	0.1992	873-3/4	1073-96	none	no	high	-	few spheres observed
H3	nit	12	NH ₄ OH	1	3.02	-	0.1992	873-3/4	1013-3/4 , 1073-96	none	nps	low	-	deform spheres,porous surface
H3	nit	14	KOH	1	3.02	-	0.1992	873-3/4	1013-3/4 , 1073-96	partial	no	low	-	deform spheres,porous surface
H3	nit	7	NH ₄ OH	1	3.02	-	0.1992	873-3/4	1013-3/4 , 1073-96	none	nps	low	-	deform spheres,porous surface

[†] H1 = Lu_{1.98}Yb_{0.02}O₃

H2 = Lu_{1.905}Yb_{0.08}Er_{0.01}Tm_{0.05}O₃

H3 = Lu_{1.96}Yb_{0.04}O₃

^a nit / chlor = nitrates / chlorides

^b SC = shell cover

^c IP =Dispersed Lu₂O₃ particles: nps/mps/ps/no = particles with < 100 nm / 100 nm- 100µm / larger than 100 µm / not observed

^d Agglom = agglomeration between SiO₂ spheres and Lu₂O₃ nanoparticles

3.8.1 Lanthanide nitrates as precursors

Figure 3.25 shows the XRPD patterns of a sample in which KOH base was used to adjust the pH value to 7.5. It shows a superposition of one amorphous phase and one crystalline phase. Two peaks could be distinguished: The peak at 22° corresponding to amorphous silica and the 29.8° peak in the same position of the highest diffraction line (2 2 2) of cubic phase of Lu_2O_3 . Independent of the type of precursor, this behavior was observed for all samples which pH value was adjusted with KOH. TEM image in Figure 3.25 shows segregation of silica due to KOH attack.

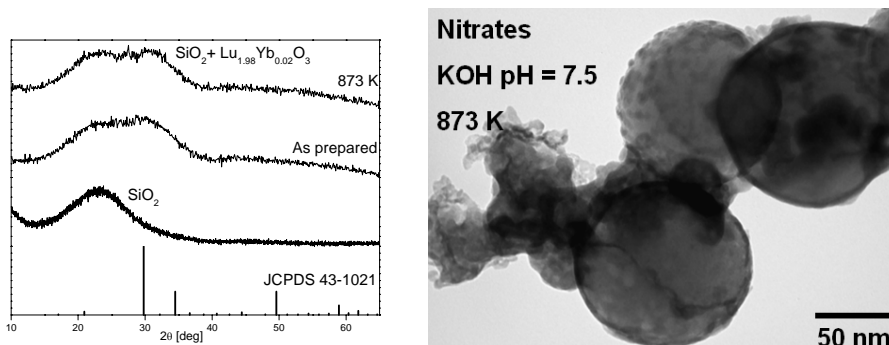


Figure 3.25. XRPD pattern of sample treated with KOH at pH = 7.5 and comparison with SiO_2 and JCPDS card 43-1021 (left). Segregation of silica observed by TEM (right).

A similar superposition of amorphous-crystalline phases was also observed when NH_4OH was used, instead of KOH, to adjust the pH value to 7.5, see the Figure 3.26. Calcination at higher temperature was carried out, but it did not produce enhancement of the crystallinity of the sesquioxide phase. The corresponding TEM micrograph in Figure 3.26 shows the segregation of silica due to NH_4OH in the hydrothermal process. The segregation of SiO_2 could reduce the sesquioxide crystallization, producing an amorphous mix of oxides. Blank samples (no sesquioxide added), showed similar erosion as this shown in Figure 3.25 and Figure 3.26 when KOH was used to control the pH in the hydrothermal process. It is clear that KOH attack strongly the spheres in the hydrothermal process producing SiO_2 segregation.

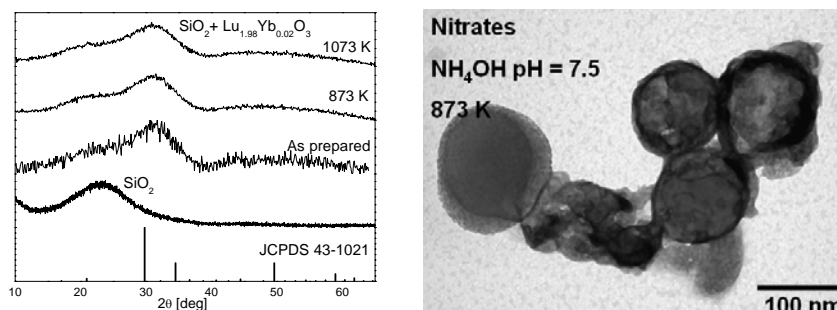


Figure 3.26. XRPD pattern of sample treated with NH_4OH at pH = 7.5, and comparison with SiO_2 and JCPDS card 43-1021 (left). TEM micrograph showing SiO_2 segregation (right).

3.8.2 Lanthanide chlorides as precursors

For lanthanide chlorides used as precursors and pH = 7 with NH_4OH addition, the XRPD pattern of $\text{SiO}_2 + \text{Lu}_{1.905}\text{Yb}_{0.08}\text{Er}_{0.01}\text{Tm}_{0.05}\text{O}_3$ in Figure 3.27 shows diffractions lines corresponding to the $Ia\bar{3}$ cubic phase of Lu_2O_3 and also an amorphous background. From comparison with SiO_2 patterns, it is clear that amorphous background in the XRPD pattern corresponds to SiO_2 . High resolution TEM images and FFT analysis in Figure 3.28 revealed the growth of individual sesquioxide nanocrystals mixed with silica spheres coated by an amorphous dark layer that can be constituted of segregated SiO_2 from other spheres.

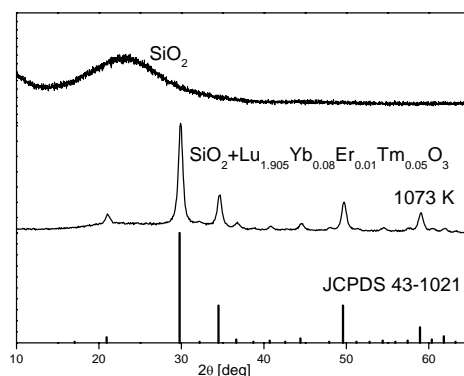


Figure 3.27. XRPD pattern of silica spheres sample $\text{SiO}_2 + \text{Lu}_{1.905}\text{Yb}_{0.08}\text{Er}_{0.01}\text{Tm}_{0.05}\text{O}_3$

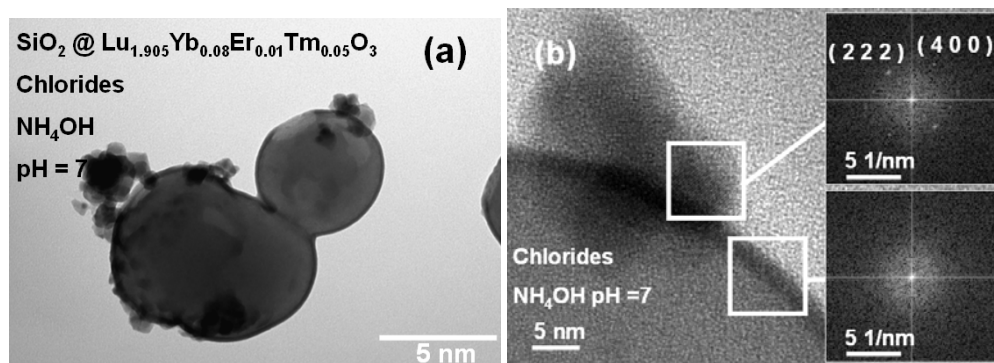


Figure 3.28. (a) HRTEM micrograph of silica spheres and sesquioxide nanocrystals. (b) FFT analysis of two regions on the surface.

3.8.3 Effect of long isothermal annealing

To discard a lack of time for the crystal growth of the sesquioxide phase as showed in Figure 3.25 and Figure 3.26, a long annealing process at 1073 K for 4 days was carried out for $\text{SiO}_2@ \text{Lu}_{1.96}\text{Yb}_{0.04}\text{O}_3$ samples. Samples synthesized with pH = 7 using KOH and NH_4OH show high agglomeration and SiO_2 segregation. However, the surface coating of some silica spheres by sesquioxide crystalline material was observed. HRTEM micrographs

and electron diffraction patterns in Figure 3.29 and Figure 3.30 show that the highly crystalline deposited material corresponds to the sesquioxide $Ia\bar{3}$ cubic phase. For samples treated at pH = 12-14, no crystallinity was observed on the surfaces of the silica spheres.

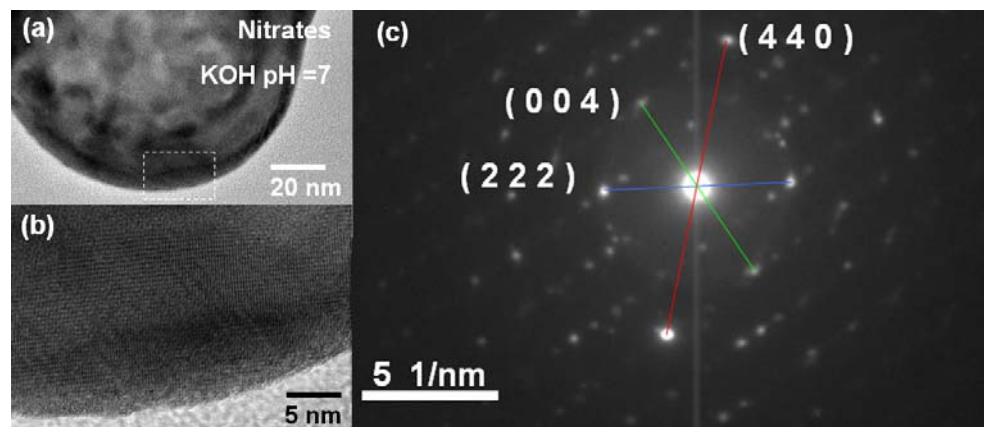


Figure 3.29. HRTEM images of $\text{SiO}_2@Lu_{1.96}Yb_{0.04}O_3$ sphere surface after annealing at 1073 K for 4 days (a). Lattice fringes on the surface (b) and SAED pattern (c).

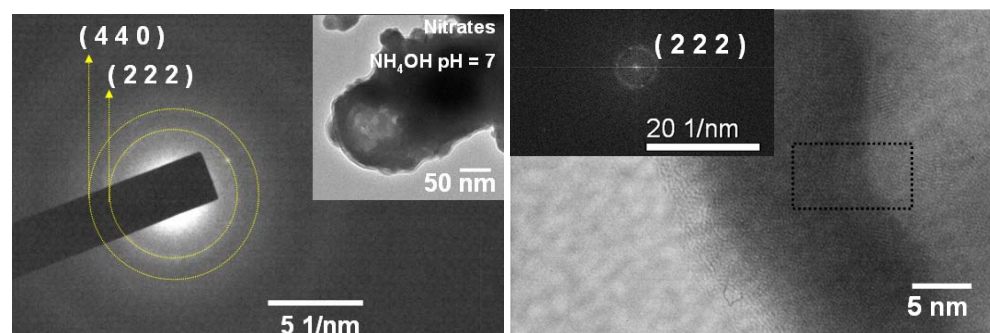


Figure 3.30. Electron diffraction image of one $\text{SiO}_2@Lu_{1.96}Yb_{0.04}O_3$ sphere after annealing at 1073 K for 4 days (left). FFT pattern of the sphere surface (right).

3.9 Synthesis of lanthanide doped $\text{KLu}(\text{WO}_4)_2$ double tungstates nanocrystals

For the preparation of potassium lutetium double tungstates $\text{KLu}(\text{WO}_4)_2$ (hereafter KLuW) doped with active lanthanide ions, the modified Pechini method follows the procedure described previously. We have used citric acid (CA) (or EDTA in some cases) as the chelation agent ($C_M = 1$) and ethylene glycol (EG) as the esterification agent ($C_E = 0.5$), and two precursor salts: the potassium carbonate (K_2CO_3) and ammonium paratungstate ($5(\text{NH}_4)_2\text{O}_{12}\text{WO}_3 \cdot n\text{H}_2\text{O}$), or ammonium tungstate ($(\text{NH}_4)_2\text{WO}_4$). These precursors are added to the as produced lanthanide nitrates in aqueous solution. Table 3.10 summarized the experimental parameters and structural and morphological results for the different atomic contents of the doping active ions.

The citric acid was used because is completely soluble in water, allowing to check the complete dissolution of precursors in the aqueous solution, especially the ammonium tungstates that possesses a partial solubility in water (1.5-30 g/100mL). Also citric acid polymerization is easier than that of EDTA and allows obtaining a good polymer gel at 423 K.

The monoclinic $C2/c$ phase of the KLuW double tungstate was obtained above 1023 K as shown in Figure 3.31 in comparison with the KLuW single crystal and with the JCPDS 54-1204 card. For higher temperature an enhancement of the crystallinity is observed. XRPD patterns for isothermal annealing at 1023 K are shown in Figure 3.32. The monoclinic $C2/c$ phase was obtained from a short holding time of 15 minutes, but the pure single phase was obtained only after 1 h of thermal treatment with the total release of decomposition products.

A second crystalline phase was observed which is characterized by diffraction lines observed in the XRPD patterns at $2\theta = 10.3^\circ$, below 973 K. However this was also observed in some samples after the final annealing at 1023 K for 2 h. After comparison with the JCPDS database, we conclude this line is not associated with any precursor used. This peak has been associated with decomposition products that remain in the final powder, as explained below. In the step 6 of the Pechini process described in section 3.3, after grinding the calcinated foam, the precursor powder form a column of 2-3 cm height into the quartz crucible. If this material column is shortened, reducing the amount of precursor powder or using a crucible with larger diameter, after annealing at 1023 K for 2 h, no extra peaks are observed in the XRPD patterns. Special care must be taken to avoid high columns of precursor powder that produce a large pathway for the decomposition products.

Table 3.10. Experimental parameters of the synthesis of doped KLuW nanocrystals.

Active Ion [at. %]				Chelating Agent	APT [†] with HNO ₃	Solution Color ^a	C _M	C _E	Anneal. 0 [K-h]	Anneal. 1 [K-h]	Anneal. 2 [K-h]	TEM		XRPD Phase	Observations
Eu	Ho	Tm	Yb									size [nm]	Agglom. ^b		
-	0.5	1	1	EDTA	yes	Y	1	0.5	-	473-3	973-5	50-100	low	KLuW [‡]	33mL NH ₄ OH
-	0.5	1	1	EDTA	yes	Y	1	0.5	-	473-3	973-5	-	-	KLuW [‡]	33mL NH ₄ OH
-	0.5	1	1	EDTA	yes	Y	1	0.5	-	473-3	-	-	-	Amorphous	33mL NH ₄ OH
-	0.5	1	1	EDTA	yes	Y	1	0.5	-	573-3	973-5	*	high	KLuW	33mL NH ₄ OH
-	0.5	1	1	CA	yes	Y	1	0.5	-	573-3	873-2	-	-	KLuW [‡]	-
-	0.5	1	1	CA	yes	Y	1	0.5	-	573-3	923-2	-	-	KLuW + other	-
-	0.5	1	1	CA	yes	Y	1	0.5	-	573-3	973-2	100	low	KLuW	paper V
-	0.5	1	1	CA	yes	Y	1	0.5	-	573-3	1023-2	40- 80 *	low	KLuW	paper V
-	0.5	1	1	CA	yes	Y	1	0.5	-	573-3	1023-5	50- 250 *	-	KLuW	paper V
-	0.5	1	1	CA	yes	Y	1	0.5	-	573-3	1023-1/12	-	-	KLuW [‡]	-
-	0.5	1	1	CA	yes	Y	1	0.5	-	573-3	1023-1/4	-	-	KLuW [‡]	-
-	0.5	1	1	CA	yes	Y	1	0.5	-	573-3	1023-1/2	50 - 80 *	low	KLuW [‡]	-
-	0.5	1	1	CA	yes	Y	1	0.5	-	573-3	1023-1	40 - 80 *	low	KLuW	paper V
-	1.5	1	1	CA	yes	Y	1	0.5	-	573-3	1023-2	-	-	KLuW [‡]	-
-	2	1	1	CA	no	W	1	0.5	-	573-3	1023-2	100	low	KLuW	-
0.5	2	1	1	CA	no	W	1	0.5	-	573-3	973-2	100	low	KLuW	-
1	2	1	1	CA	yes	Y	1	0.5	-	573-3	973-2	100	low	KLuW [‡]	-
1.5	2	1	1	CA	no	W	1	0.5	423-20	-	973-2	100	low	KLuW [‡]	gray powder
2	2	1	1	CA	no	W	1	0.5	423-20	-	973-2	100	low	KLuW	-
	2	0.75	1	CA	no	W	1	0.5	423-20	-	1023-2	100	low	KLuW	-
	2	0.25	1	CA	no	W	1	0.5	423-20	573-3	1023-2	100	low	KLuW	-

Continued on next page.

Continued from previous page

Active Ion [%]				Chelating Agent	AT† with HNO ₃	Solution Color	C _M	C _E	Anneal. 0	Anneal. 1	Anneal. 2	TEM		XRPD Phase	Observations
Er	Ho	Tm	Yb									size [nm]	Agglom. ^a		
1	-	-	10	CA	no	SC	1	0.5	423-39	573-3	1023-2	100	low	KLuW	-
-	-	1	10	CA	no	SC	1	0.5	423-39	573-3	1023-2	100	low	KLuW	-
-	1	-	10	CA	no	SC	1	0.5	423-39	573-3	1023-2	100	low	KLuW	-

† APT = Ammonium paratungstate

AT = Ammonium tungstate

EDTA = ethylenediaminetetraacetic acid

CA = Citric acid

^a Y = yellow W = White SC = semi-clear

* Other microparticles were observed.

^b Agglom = Observed agglomeration.

‡ One extra peak at 2θ ~ 10°

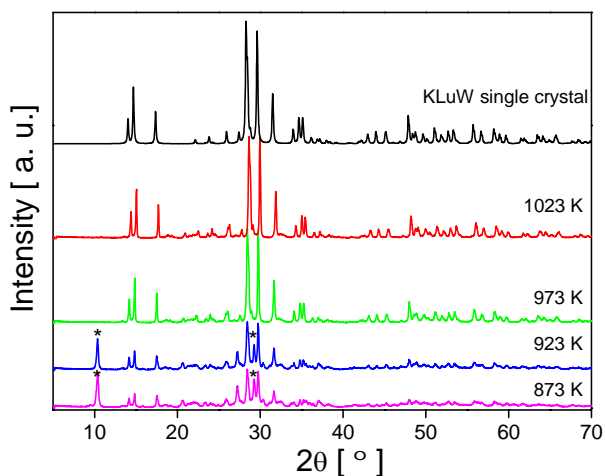


Figure 3.31. XRPD patterns for doped 1 % Tm, 0.5 % Ho, 1 % Yb:KLuW nanocrystals at room temperature after several annealing temperatures for 2 h. Peaks non indexed as corresponding to the monoclinic $C2/c$ phase are indicated with *.

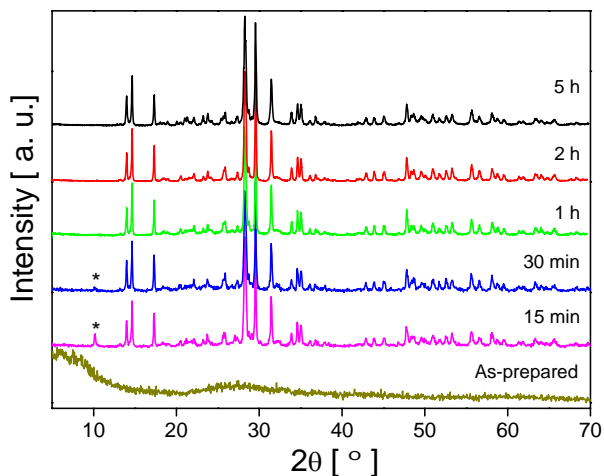


Figure 3.32. Evolution of XRPD patterns for 1 % Tm, 0.5 % Ho, 1 % Yb:KLuW nanocrystals after different times of thermal treatment at 1023 K. Peaks non indexed as corresponding to the monoclinic $C2/c$ phase are indicated with *.

Figure 3.33 shows that the crystallite size D at 1023 K calculated from the $(\bar{2}22)$ reflexion at $2\theta = 29.571^\circ$. Crystallite size follows the empiric relation indicated in Eq. 3.3, reaching a maximum size ~ 47 nm for 2 h. Optimal fitting was obtained for $n = 2$ indicating a normal grain growth [34]. For longer annealing times, agglomeration was increased as observed in Figure 3.34 and Figure 3.35. The morphology of Ln-doped KLuW nanocrystals is characterized for polygonal and faceted shapes with a particle size around 100 nm for samples prepared at 1023 K for 2 h. The particle size histograms were fitted to the log-normal function.

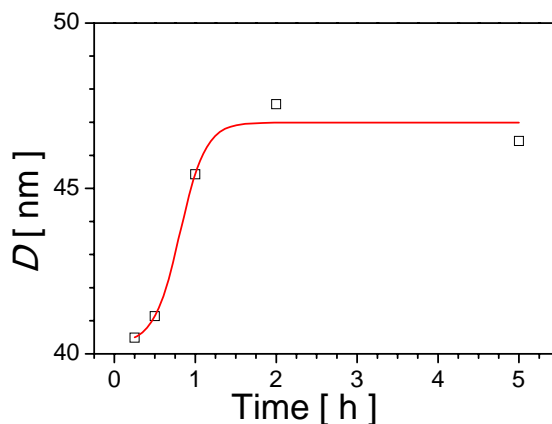


Figure 3.33. Crystallite size of 1 % Tm, 0.5 % Ho, 1 % Yb:KLuW nanocrystals vs time for different annealing time at 1023 K. The line is a guide for the eye.



Figure 3.34. TEM micrographs for a 1 % Tm, 0.5 % Ho, 1 % Yb:KLuW nanocrystals after isothermal annealing at 1023 K.

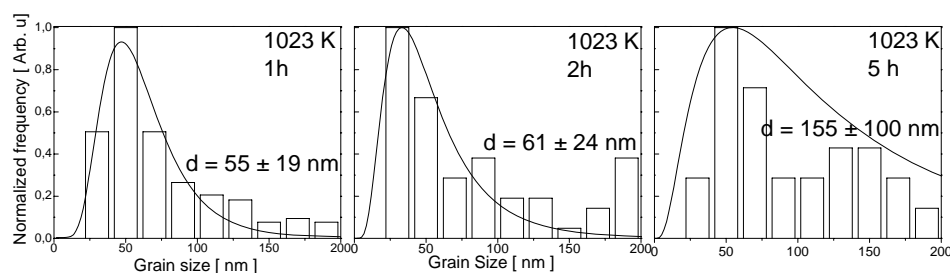


Figure 3.35. Calculated grain size histograms from TEM micrographs in Figure 3.34.

3.10 References

- [1] P. N. Prasad *Nanophotonics*, John Wiley & Sons, Inc. (2004).
- [2] L. Theodore, *Nanotechnology: Basic Calculations for Engineers and Scientist*, John Wiley & Sons, Inc. (2006).
- [3] K. S. Mazdiyasi, L.M. Brown, *Influence of Dynamic Calcination on Crystallite Growth of Submicron Rare-Earth Oxide* **J. Am Ceram. Soc.**, 54, 479 (1971).
- [4] D. Grosso and P.A. Sermon, *Scandium oxide nanoparticles produced from sol-gel chemistry*, **J. Mater. Chem.**, 10, 359 (2000).
- [5] F. Imoto, T. Nanataki, S. Kaneko, *Preparation and characterization of fine rare earth oxide powders through alkoxide processes*, **Ceram. Trans.**, 1, 204 (1988).
- [6] Y. Xu, X. Ming Chen, Y. Jun Wu, *Preparation of $Ba_{6-3x}Nd_{8+2x}Ti_{18}O_{54}$ via Ethylenediaminetetraacetic Acid Precursor*, **J. Am Ceram. Soc.**, 83, 11, 2893 (2000).
- [7] M. P. Pechini, *Method of Preparing Lead and Alkaline Earth Titanates and Niobates and coating method using the same to form a capacitor*. **US Patent Specification 3330697** (1967).
- [8] T. Zhang, T. F. Zhou, T. Qian, X. G. Li, *Particle size effects on interplay between charge ordering and magnetic properties in nanosized $La_{0.25}Ca_{0.75}MnO_3$* , **Phys. Rev. B** 76, 174415 (2007).
- [9] S. Roy, W. Sigmund, and F. Aldinger, *Nanostructured yttria powders via gel combustion*, **J. Mater. Res.**, 14, 1524 (1999).
- [10] A. Dupont, C. Parent, B. Le Garrec, and J. M. Heintz, *Size and morphology control of Y_2O_3 nanopowders via a sol-gel route*, **J. Solid State Chem.**, 171, 152 (2003).
- [11] X. Dong, G. Hong, D. Yu, and D. Yu, *Synthesis and properties of cerium oxide nanometer powders by pyrolysis of amorphous citrate*, **J. Mater. Sci. Technol.**, 13, 113 (1997).
- [12] M. Galceran, M. C. Pujol, M. Aguiló, F. Díaz, *Sol-gel modified Pechini method for obtaining nanocrystalline $KRE(WO_4)_2$ ($RE = Gd$ and Yb)* **J. Sol-Gel Sci. Techn.** 42, 79 (2007).
- [13] M. Galceran, M. C. Pujol, M. Aguiló, F. Díaz, *Synthesis and characterization of nanocrystalline $Yb:Lu_2O_3$ by modified Pechini method*, **Mat. Sci. Eng. B** 146, 7 (2008).
- [14] Y. Xu, W. Peng, S. Wang, X. Xiang, P. Lu, *Synthesis of $SrAl_2O_4$ and $SrAl_{12}O_{19}$ via ethylenediaminetetraacetic acid precursor*, **Mater. Chem. Phys.** 98 51 (2006).
- [15] J. Rodriguez-Carvajal, *Reference Guide for the Computer Program FullProf*. Laboratoire León Brillouin. CEA-CNRS.Saclay, France. 2000.
- [16] H. M. Rietveld, *A profile refinement method for nuclear and magnetic structures*, **J. Appl. Cryst.** 2 65 (1969).
- [17] A. Ikesue, Y. Lin Aung, *Ceramic laser materials*, **Nat. Photon.** 2, 721 (2008).
- [18] H.V. Atkinson, *Overview no. 65: Theories of normal grain growth in pure single phase systems* **Acta. Metall.** 3, 469 (1988).
- [19] S. Stecura, W.J. Campbell, *Thermal expansion and phase inversion of rare-earth oxides*, US Dept. of the Interior, Bureau of Mines, Washington, (1961).
- [20] K. Lu M. L. Sui, *Thermal expansion behaviors in nanocrystalline materials with a wide grain size range* **Acta metall. mater.** 43, 3325 (1995).

- [21] K. Byrappa, T. Adschiri *Hydrothermal technology for nanotechnology* **Prog. Cryst. Growth. Ch.** 53, 117, (2007).
- [22] K. Byrappa, M. Yoshimura, *Handbook of Hydrothermal Technology*, Noyes Publications, New Jersey, USA, (2001).
- [23] F. Esteban-Betegón, C. Zaldo, C. Cascales *Hydrothermal Yb³⁺-Doped NaGd(WO₄)₂ Nano- and Micrometer-Sized Crystals with Preserved Photoluminescence Properties* **Chem. Mater.**, 22, 2315 (2010).
- [24] R. Calderón-Villajos, C. Zaldo, C. Cascales, *Micro and nano-sized architectures in hydrothermal Tm³⁺-doped GdVO₄: chemical insights towards preservation of the emission efficiency* **CrystEngComm** 14, 2756 (2012).
- [25] R. Esteban, M. Laroche, J.J. Greffet, *Influence of metallic nanoparticles on upconversion processes* **J. Appl. Phys.** 105 033107-10 (2009).
- [26] E. S. Shibu, K. Kimura, T. Pradeep *Gold nanoparticle superlattices: novel surface enhanced Raman scattering active substrates* **Chem. Mater.** 21 3773-3781 (2009).
- [27] L. R. P. Kassab, F. A. Bomfim, J. R. Martinelli, N. U. Wetter, J. J. Neto, C. B. de Araújo, *Energy transfer and frequency upconversion in Yb³⁺-Er³⁺-doped PbO-GeO₂ glass containing silver nanoparticles*, **Appl. Phys. B** 94 239-242 (2009).
- [28] E. W. Barrera, M. C. Pujol, F. Díaz, S. B. Choi, F. Rotermund, K. H. Park, M. S. Jeong, C. Cascales, *Emission properties of hydrothermal Yb³⁺, Er³⁺ and Yb³⁺, Tm³⁺-codoped Lu₂O₃ nanorods: upconversion, cathodoluminescence and assessment of waveguide behavior*, **Nanotechnology** 22 075205 (2011).
- [29] V. G. Pol, D. N. Srivastava, O. Palchik, V. Palchik, M. A. Slifkin, A. M. Weiss, A. Gedanken, *Sonochemical Deposition of Silver Nanoparticles* **Langmuir**, 18, 8, 3357 (2002).
- [30] B. Arkles, *Silane Coupling agents: Connecting across boundaries* Gelest, Inc. (2006)
- [31] B. Arkles, *Silicon, Germanium & Tin Compounds, Metal alkoxides, Metal Diketonates, Silicone: A Survey of Properties and Chemistry* Gelest, (1998).
- [32] S. de Monredon-Senani, C. Bonhomme, F. Ribot, F. Babonneau *Covalent grafting of organoalkoxysilanes on silica surfaces in water-rich medium as evidenced by ²⁹Si NMR*, **J Sol-Gel Sci Technol** 50 152 (2009).
- [33] K. Shirai, Y. Yoshida, Y. Nakayama, M. Fujitani, H. Shintani, K. Wakasa, M. Okazaki, J. Snauwaert, B. Van Meerbeek. *Assessment of decontamination methods as pretreatment of silanization of composite glass fillers.* **J Biomed Mater Res.** 53 204 (2000).
- [34] J.E. Burke, D. Turnbull, *Recrystallization and grain growth* **Prog. Metal Phys.** 2 220 (1952).

UNIVERSITAT ROVIRA I VIRGILI
LANTHANIDE-BASED DIELECTRIC NANOPARTICLES FOR UPCONVERSION LUMINESCENCE
Elixir William Barrera Bello
Dipòsit Legal: T. 450-2013

Chapter 4

Optical properties of doped sesquioxide nanostructures

In this chapter we present results from luminescence characterization of lanthanide doped sesquioxide nanostructures. We first present the photoluminescence of Tm^{3+} in Lu_2O_3 nanoparticles, and their possibility to be used as precursors of transparent ceramic laser materials. After, a study the cathodoluminescence in terms of relative intensity dependence with active ions concentration is explained. The dependence of upconversion emission of $\text{Ln}, \text{Yb}:\text{Lu}_2\text{O}_3$ ($\text{Ln} = \text{Er}, \text{Tm}$) nanostructures with the excitation power is presented showing similarities among different nanostructures. The last part of each section is devoted to the discussion of results.

Cathodoluminescence measurements were carried out at Ajou University in Suwon-Republic of Korea. Upconversion measurements in nanorods were carried out also at Ajou University and at FiCMA-FiCNA optics laboratory of the Rovira i Virgili University, Tarragona, Spain. Nanoparticles and core-shell particles were characterized at the Servei de Recursos Científics of the Rovira i Virgili University (Stokes emission) and the Solid State Chemistry Laboratory at University of Verona, Italy (upconversion measurements).

4.1 Introduction

It is usually assumed that Ln^{3+} ions are incorporated randomly in the C_2 and C_{3i} sites in the cubic c-type structure of the Lu_2O_3 sesquioxide, with symmetry of the space group $Ia\bar{3}$. This assumption is supported by X-ray powder diffraction and magnetic susceptibility measurements in bulk $\text{Eu}:\text{Y}_2\text{O}_3$ [1], and by Mössbauer measurements in $\text{Eu}:\text{Lu}_2\text{O}_3$ in bulk and 10-20 nm nanocrystals [2]. The spectroscopic features observed for Ln^{3+} in the Lu_2O_3 host are mostly related to the electric dipole transitions of ions in the C_2 site, since the inversion centre of the C_{3i} site only allows magnetic dipole transitions. The non-centrosymmetric C_2 sites mix wave functions with different parity, and electric dipole transitions are partially allowed. In C_{3i} sites where the parity does not change due to its inversion center, the electric dipole transitions are forbidden.

4.2 Spectroscopic properties of Tm^{3+} in Lu_2O_3 nanocrystals

4.2.1 Optical absorption

Tm^{3+} optical absorption spectra at 6 K are presented in Figure 4.1, and those corresponding to room temperature appear in the Paper III Figure 4. Stark energy levels of Tm^{3+} in Lu_2O_3 nanocrystals have been determined from the above spectra, and they are listed in Table 4.1. Their values are consistent with those already reported for Tm^{3+} in Lu_2O_3 single crystals [3]. It indicates that size reduction does not modify the average energy of the electronic levels but it enlarges the optical line widths. This broadening of the spectral lines is possibly originated by the local disorder around the optically active ions produced by oxygen vacancies and structural or surface defects [4].

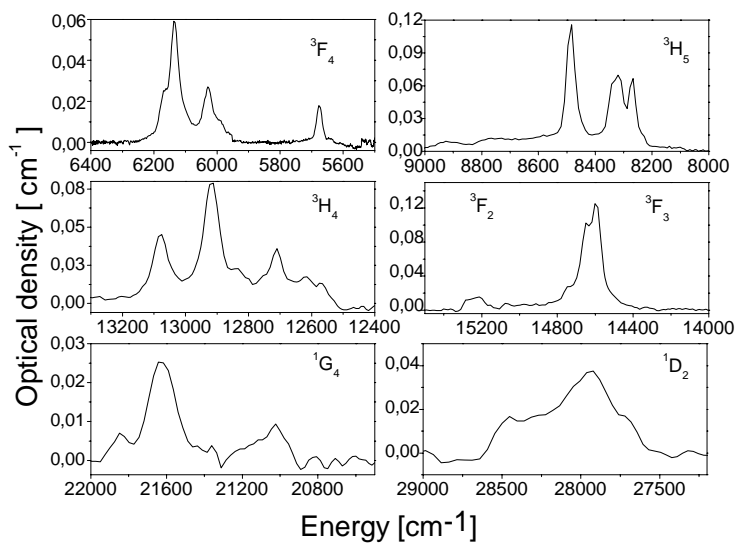


Figure 4.1. Low temperature (6 K) optical absorption of 15 % Tm:Lu₂O₃ nanocrystals.

Table 4.1 Comparison of the experimental Stark energy levels, E_{exp} in cm^{-1} , of Tm^{3+} ions occupying C_2 sites in Lu_2O_3 nanocrystals and in the single crystal.

$2s+1L_J$	Nanocrystals	Bulk single crystal	$2s+1L_J$	Nanocrystals	Bulk single crystal	
3F_4	-	5613	3F_3	-	14558	
	5678	5680		14600	14592	
	5990	6033		14650	14688	
	6029	6045		-	14695	
	6135	6127		14757	14760	
	6168	6141		-	14841	
	-	6174		-	14922	
	-	6223		3F_2	-	15029
	8227	8232			15070	15080
	8266	8267			15210	15213
-	8282	15276	15272			
-	8303	-	15390			
3H_5	8318	8318	1G_4	21017	-	
	8340	8340		21619	-	
	-	8475		21842	-	
	8483	8487	1D_2	27711	-	
	-	8578		27935	-	
	-	8785		28267	-	
	-	8938		28455	-	
	-	-		-	-	
12568	12562	3H_4	-	-		
12617	-		-	-		
12710	12710		-	-		
12800	-		-	-		
12833	12831		-	-		
12915	12915		-	-		
-	12936		-	-		
13078	13080		-	-		
-	13140		-	-		
-	13254		-	-		
-	12484	-	-			

4.2.2 3H_4 photoluminescence

The $^3H_6 \rightarrow ^3H_4$ transition of the Tm:Lu₂O₃ nanocrystals was measured by monitoring the emission intensity at 1559 nm, see the Figure 4.2. As in single crystals, nanocrystals show the strongest absorption of Tm³⁺ corresponding to the hypersensitive $^3H_4 \leftarrow ^3H_6$ electronic transition at around 800 nm.

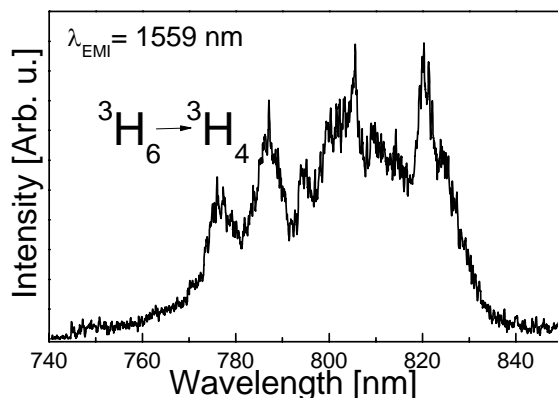


Figure 4.2. Room temperature excitation spectrum ($\lambda_{\text{EMI}} = 1559$ nm) of the 3H_4 multiplet of 5 % Tm:Lu₂O₃ nanoparticles

Figure 4.3 shows the 300 K photoluminescence associated with the $^3H_4 \rightarrow ^3F_4$ ($\lambda \approx 1350$ -1600 nm) transition, which is obtained exciting close to the maximum of the above $^3H_6 \rightarrow ^3H_4$ transition ($\lambda_{\text{EXC}} \sim 800$ nm). The spectrum shows the large crystal field splitting characteristic of sesquioxides, with the three most intense peaks at 1559, 1534 and 1437 nm. All collected optical transitions for 5 % Tm:Lu₂O₃ nanocrystals display splittings very similar to those reported for 4 % Tm:Lu₂O₃ single crystal [3], indicating that in the prepared sesquioxide, Tm³⁺ is actually incorporated at the same crystal site(s) as in single crystals.

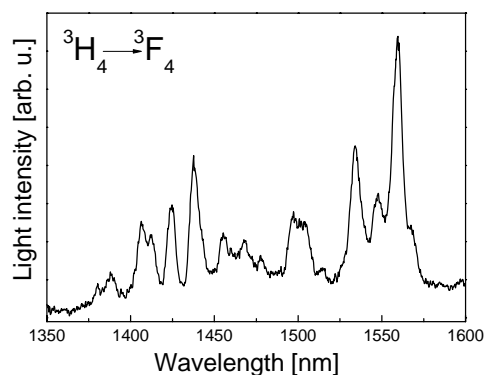


Figure 4.3. Room temperature $^3H_4 \rightarrow ^3F_4$ photoluminescence of 5 % Tm:Lu₂O₃ nanocrystals excited at $\lambda_{\text{EXC}} = 800$ nm.

Radiative lifetime of Ln-doped nanoparticles may be affected by the refractive index of the surrounding media [5]. As a preliminary methodological procedure, we assess the validity of the results obtained by measuring the $^3\text{H}_4$ lifetime of $\text{Tm}^{3+}:\text{Lu}_2\text{O}_3$ nanocrystals in air ($n_{rf} = 1$) and dispersed in liquids with different refractive indices, namely ethylene glycol (EG) with $n_{rf} = 1.52$ and fluorolube (FL) with $n_{rf} = 1.94$. The refractive index of undoped Lu_2O_3 sesquioxides at 800 nm and 300 K is about 1.92 [3].

After short pulse excitation at 800 nm, the photoluminescence intensity decays at the wavelengths of the three most intense peaks of the $^3\text{H}_4 \rightarrow ^3\text{F}_4$ emission were similar. None of the decays observed was exponential. This is illustrated in Figure 4.4 for the lowest Thulium composition, i.e. 0.5 % $\text{Tm}:\text{Lu}_2\text{O}_3$, for which non radiative Tm-Tm losses are negligible [6]. The complex time dependency of the fluorescence intensity of Tm^{3+} in these nanocrystals is different to the exponential behavior documented in Lu_2O_3 single crystals with low enough Tm^{3+} concentration [7]. The fast component of the decay was related with quenching of fluorescence by OH- attached groups. This effect is observable in the nanocrystalline samples due to their high ratio of surface ions in relation with ions in the body of the nanocrystals.

The measured decays have been described by two exponential terms, the shortest is ascribed to the emission of Tm^{3+} ions on the surface of the nanocrystals and the longest to Tm^{3+} ions in the body of the nanocrystals. The long-lived lifetime was first calculated from the tail of the $\text{Ln}(I/I_0)$ vs. time representations as shown in Figure 4.4a, which in principle should approach the lifetime value measured in $\text{Tm}:\text{Lu}_2\text{O}_3$ single crystals. Later we fitted the intensity decay, $I(t)$, to the curve $I(t) = I_1 e^{-t/\tau_1} + I_2 e^{-t/\tau_2}$, where $I_1 + I_2 = 1$. In this fit, the previously calculated lifetime was used as an initial value to achieve convergence, but in the final refinement step this was also left to vary freely. This procedure systematically produced good fits of the experimental intensity decays, as shown in Figure 4.4b for 0.5 % $\text{Tm}:\text{Lu}_2\text{O}_3$ nanocrystals.

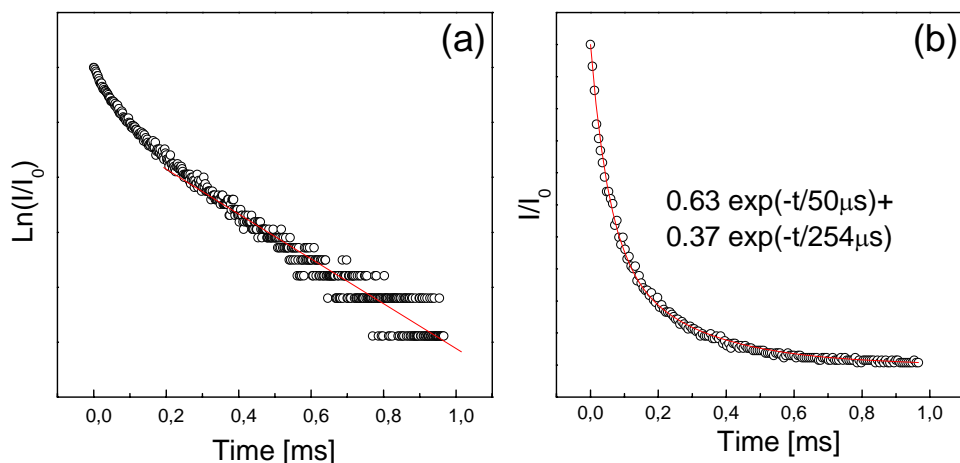


Figure 4.4. Room temperature decay curve of the ${}^3\text{H}_4$ multiplet of Tm^{3+} in 0.5 % $\text{Tm}:\text{Lu}_2\text{O}_3$ nanocrystals in air. $\lambda_{\text{EXC}}= 800$ nm, $\lambda_{\text{EMI}}= 1558$ nm. The open circles are the experimental results, and the lines are (a) a linear fit of the tail of the $\text{Ln}(I/I_0)$ vs t dependency, and (b) a fit with two exponential decays of the (I/I_0) vs t dependency.

Table 4.2 lists the decay time results of the $\text{Tm}:\text{Lu}_2\text{O}_3$ nanocrystals. The most significant features of these results are the following:

a) Photoluminescence decay is independent of the surrounding media; this indicates that the crystal size of the presently used nanocrystal is above the threshold to produce modifications of the radiative lifetime.

b) The analysis of the photoluminescence decay kinetics of ${}^3\text{H}_4 \rightarrow {}^3\text{F}_4$ emission with two exponential regimes yields good results for Tm^{3+} concentration of up to 8 %.

c) Both the fast and slow decay components decrease as Tm^{3+} concentration increases. The increment in the Tm^{3+} content produces two effects: (1) it reduces the mean distance between ions of Tm^{3+} and makes the energy migration by self-resonant energy transfers (${}^3\text{H}_4, {}^3\text{H}_6 \rightarrow {}^3\text{H}_6, {}^3\text{H}_4$) and cross-relaxation (${}^3\text{H}_4, {}^3\text{H}_6 \rightarrow {}^3\text{F}_4, {}^3\text{F}_4$) more probable, and (2) the transfer rate becomes not homogeneous due to statistical distribution of different Tm-Tm distances leading to non-exponential photoluminescence curves [8].

The long-lived value obtained for 0.5 % Tm in nanocrystals is similar to the experimental value of 300 μs obtained at 300 K in 0.2 % $\text{Tm}:\text{Lu}_2\text{O}_3$ single crystal. Both values are clearly shorter than the ${}^3\text{H}_4$ radiative value expected for Tm^{3+} in Lu_2O_3 , i.e. 690 μs [3].

Table 4.2. Decay time (τ) and intensities (I) of the $^3\text{H}_4$ de-excitation (at 300 K) of $\text{Lu}_{2-x}\text{Tm}_x\text{O}_3$ nanocrystals prepared by the sol-gel method. $\lambda_{\text{EXC}}= 800$ nm, $\lambda_{\text{EMI}}= 1558$ nm, x_c determined by electron probe micro-analysis (EPMA).

Tm^{3+}		Air ($n_{rf}=1$)				EG ($n_{rf}=1.52$)				FL ($n_{rf}=1.94$)			
[%]	x_c	I_1	τ_1 [μs]	I_2	τ_2 [μs]	I_1	τ_1 [μs]	I_2	τ_2 [μs]	I_1	τ_1 [μs]	I_2	τ_2 [μs]
0.5	0.009(8)	0.63	50	0.37	254	0.79	110	0.21	340	0.77	13	0.23	340
5	0.101(4)	0.75	0.9	0.25	5.1	0.78	0.7	0.22	4.1	0.74	0.8	0.26	4.5
8	0.15(2)	0.85	0.4	0.15	3.1	0.72	0.6	0.18	2.1	0.76	0.4	0.24	2.2
15	0.287(7)	-	-	1	0.3	-	-	-	-	0.65	0.04	0.35	0.2

4.2.3 $^3\text{F}_4$ photoluminescence

In comparison to the multiplet $^3\text{H}_4$, the lifetime of the $^3\text{F}_4$ multiplet was more difficult to observe because of the relatively weak photoluminescence intensity at 1950 nm and the lower response of the InAs photovoltaic detector used. However, decay signals could be observed using a $\times 10$ amplifier.

After $^3\text{H}_4$ optical excitation, Tm^{3+} interacts with near enough neighboring Tm^{3+} ions in the $^3\text{H}_6$ ground state to reach two ions at the intermediate $^3\text{F}_4$ excited multiplet by cross-relaxation process (see Figure 4.5), increasing in this way the electronic population in the emitting level for the two microns (≈ 1950 nm) $^3\text{F}_4 \rightarrow ^3\text{H}_6$ transition, and at the same time reducing the photon energy transferred as heat to the host. Because $^3\text{F}_4$ photoluminescence is excited through the $^3\text{H}_4$ multiplet, fluorescence intensity initially grows corresponding to the electron population growth of the $^3\text{F}_4$ multiplet, in the way indicated by the diagram in Figure 4.6. To remove this contribution, we have ignored decay signals for times shorter than twice the decay time of $^3\text{H}_4$. The remaining decay curve was analyzed in a similar manner to that described for the analysis of $^3\text{H}_4$ decays.

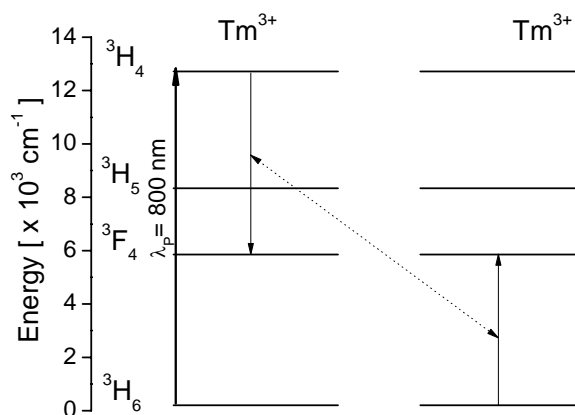


Figure 4.5. Energy cross-relaxation between Tm^{3+} ions.

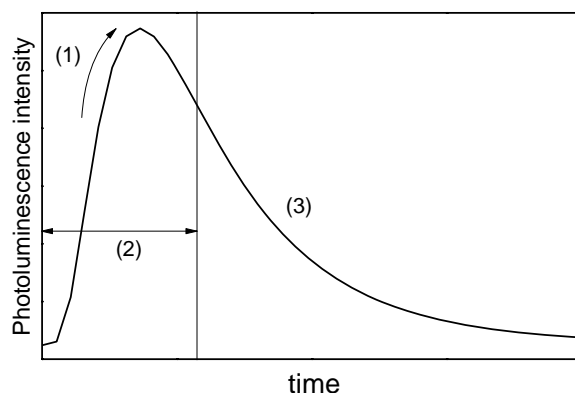


Figure 4.6. Schematic graph of the 3F_4 photoluminescence decay after $\lambda_{\text{EXC}}=800$ nm excitation. Population of 3F_4 via cross relaxation (1), discarded decay time width is twice the long-lived decay of 3H_4 multiplet (2), fitting region (3).

The decay of the 3F_4 multiplet in 0.5 % Tm:Lu₂O₃ nanocrystals was fitted with two exponentials. The long-lived value, $\tau_2=2.21$ ms, that we associate with Tm³⁺ ions in the body of nanocrystals, is something shorter than the corresponding value found in bulk single crystals, $\tau=3.38$ ms [7], but both measured values are considerably lower than the calculated 3F_4 radiative value $\tau=5.22$ ms [3]. Although Tm-Tm interactions can be nearly ignored for such low Tm³⁺ concentration, the likely origin of these reductions is a non-radiative probability of intra-ionic upconversion giving rise to strong temperature dependence, which decreases the lifetime measured at room temperature with regards to its value at 10 K [9].

The measured 3F_4 lifetime systematically decreased as the Tm concentration increased, see the Table 4.3. At higher Tm concentrations, the decay occurs too fast and the signal intensity becomes so weak that the reliable analysis of the decays was not possible, as for 15 % Tm:Lu₂O₃ samples.

Table 4.3. Decay time (τ) of 3F_4 de-excitation (at 300 K) of Lu_{2-x}Tm_xO₃ nanocrystals prepared by the sol-gel method. $\lambda_{\text{EXC}}=800$ nm, $\lambda_{\text{EMI}}=1950$ nm.

Tm ³⁺		Decay time [μ s]	
[%]	x_e	τ_1	τ_2
0.5	0.009(8)	870	2210
5	0.101(4)	-	29
8	0.15(2)	-	10
15	0.287(7)	-	-

4.2.4 Discussion

Optical absorption measurements at low temperature allow listing the Stark energy levels of Tm^{3+} in the C_2 sites in Lu_2O_3 . The comparison with those reported for Lu_2O_3 single crystals [3] indicates that size reduction does not modify the average energy of the electronic levels. We have suggested that oxygen vacancies, structural or surface defects can probably produce the line enlargement of the spectral lines.

The photoluminescence intensity decays of emission from $^3\text{H}_4$ and $^3\text{F}_4$ energy levels exhibit non-exponential dynamics even at very low Tm concentration. No influence of the refractive index of the medium on the measured lifetimes was found for the long-lived component of the calculated lifetime.

The photoluminescence decay shows two components, one fast component that decays about five times faster than the long lived one. The fast component of the decay is related to quenching of the fluorescence of Tm^{3+} ions at the surface of the nanoparticles by near surface defects and attached species with high energy phonons. This effect is observable in the nanocrystalline samples due to their high ratio of surface ions to ions in the body of the nanocrystals.

The long component is affected by concentration quenching due to Tm–Tm interactions of Tm^{3+} ions in the body of the nanocrystals, including energy migration by fast diffusion, similarly to that observed in single crystals. For the lowest doped nanocrystals (0.5 % Tm: Lu_2O_3), the $^3\text{H}_4$ was similar to the experimental value of 300 μs obtained at 300 K in 0.2 % Tm: Lu_2O_3 single crystal [3]. On the other hand, the $^3\text{F}_4$ decay shows a lifetime something shorter than the corresponding value found in bulk single crystals, probably originated by a temperature-dependent intra-ionic upconversion which can decrease the measured lifetime with regards to its value at 10 K.

4.3 Cathodoluminescence of Er^{3+} in $\text{Yb}:\text{Lu}_2\text{O}_3$ nanostructures

4.3.1 Effect of Yb^{3+} concentration in $\text{Er},\text{Yb}:\text{Lu}_2\text{O}_3$ nanorods

Cathodoluminescence spectra of 2, 6, 10, 12.5 and 15 % Yb in 2 % $\text{Er}:\text{Lu}_2\text{O}_3$ at room temperature are shown in the Paper IV Figure 13. The broad background emission centered in the 360 nm spectral region results from non-lanthanide defect centers in the host, mainly transitions involving oxygen vacancies [10, 11]. The sharp observed lines arise from the intra-shell $4f^{11}$ transitions of the Er^{3+} configuration, and have been assigned on the basis of previously determined energy levels of Er^{3+} in Lu_2O_3 single crystals [12]. UV bands are observed, with an important contribution corresponding to the $^2\text{H}_{9/2} \rightarrow ^4\text{I}_{15/2}$ transition centered at ~ 410 nm. The intensity ratio between red and green emissions $I_{\text{RED}}/I_{\text{GREEN}}$ and also between UV and green emissions $I_{\text{UV}}/I_{\text{GREEN}}$ evolve getting higher with increasing Yb^{3+} content. This behavior is shown in Figure 4.7, where the highest limit of $I_{\text{RED}}/I_{\text{GREEN}}$ ratio was reached for the sample with 12.5 % Yb^{3+} .

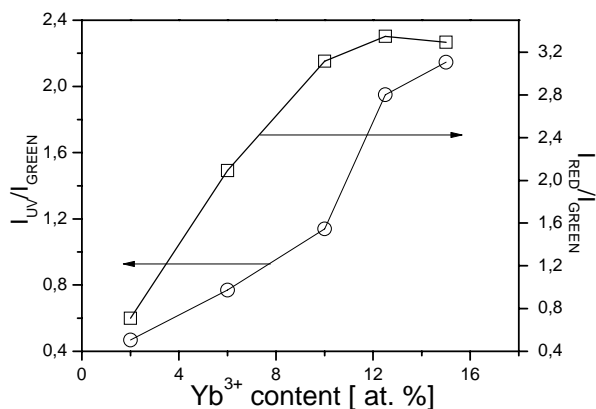


Figure 4.7. Intensity ratio of UV to green (circles) and red to green (squares) cathodoluminescence bands for Yb³⁺-doped 2 % Er:Lu₂O₃ nanorods.

4.3.2 Effect of Er³⁺ concentration in Er,Yb:Lu₂O₃ nanorods

Cathodoluminescence spectra of 2, 5 and 7.5 % Er³⁺ in 10 % Yb:Lu₂O₃ is presented in the Paper IV Figure 14. A broad background emission in the 300–500 nm associated to defect centers in the host was observed. The sharp lines of Er³⁺ corresponding to UV and visible emissions were identified. Figure 4.8 shows that relative intensity I_{UV}/I_{GREEN} is almost constant. As Er³⁺ increases, red emission is almost constant and green emission is shortened, so I_{RED}/I_{GREEN} ratio increases as Er³⁺ content increases.

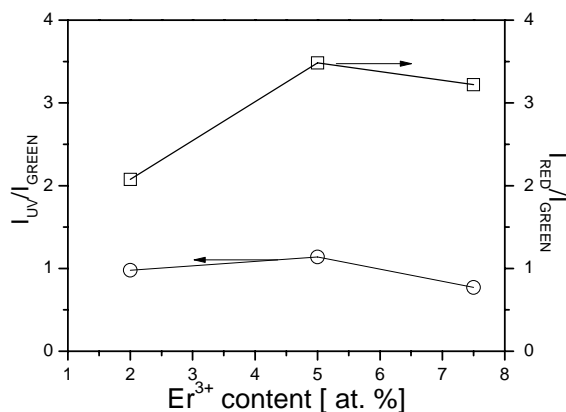


Figure 4.8. Intensity ratio of UV to green (circles) and red to green (squares) cathodoluminescence bands for Er³⁺-doped 10 % Yb:Lu₂O₃.

4.3.3 $\text{SiO}_2@(\text{Er}:\text{Yb}:\text{Lu}_2\text{O}_3)$ core-shell particles

The cathodoluminescence spectra of $\text{SiO}_2@(\text{2 \% Er, 6 \% Yb}):\text{Lu}_2\text{O}_3$ particles are constituted by a superposition of wide bands and sharp lines, as shown in Figure 4.9. The sharp lines arise from the intra-shell $4f^{11}$ transitions of the Er^{3+} configuration. Two emission bands were observed for silica spheres nanoparticles in the blue and red spectral regions, originated by structural defects in the amorphous silica spheres. These bands have been reported in cathodoluminescence measurements on films [13] and silica nanoparticles [14]. The main emission band at $\sim 450 \text{ nm}^*$ is attributed to an oxygen vacancy ($\equiv \text{Si}-\text{Si} \equiv$) and to intrinsic oxygen defect center ($\equiv \text{Si}-\text{O}-\text{Si}-\text{O}-\text{Si} \equiv$) [15]. The blue light emitting center is corresponding to the defect resulting from the dehydroxylation reaction of a pair of silanol groups ($-\text{Si}-\text{OH}$) on the surface of silica by heat treatment [15]. The other luminescence band at $\sim 650 \text{ nm}^\dagger$ is considered as originated from non-bridging oxygen hole center ($=\text{Si}-\text{O}^\uparrow$) [16].

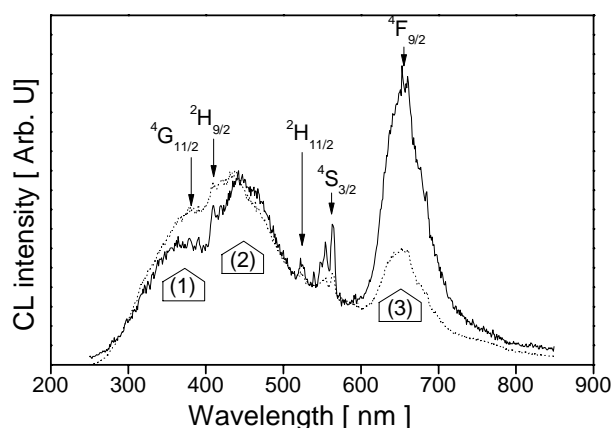


Figure 4.9. Cathodoluminescence spectra of $\text{SiO}_2@(\text{2 \% Er, 6 \% Yb}):\text{Lu}_2\text{O}_3$ particles prepared with $\text{pH} = 7$ (dot line) and $\text{pH} = 11$ (solid line). Er^{3+} transitions to the ground state $^4\text{I}_{15/2}$ are labeled with its corresponding excited state. Wide bands correspond to oxygen vacancies in Lu_2O_3 (1) and SiO_2 (2), (3).

4.3.4 Discussion

The broad background emission centered $\sim 360 \text{ nm}$ was observed in the same spectral region for all $\text{Er, Yb}:\text{Lu}_2\text{O}_3$ nanorods. For the core-shell SiO_2 sample a similar broad background was observed in spite of a different synthesis process. The study of the effect of different active ions and nanostructures could clarify if the origin of this broad band is produced by doping ions or by structural defects of the host produced in the synthesis process.

* Corresponding to 2.75 eV

† Corresponding to 1.91 eV

All the observed cathodoluminescence transitions are indicated in the Er^{3+} energy level diagram in Figure 4.10. The transitions are linear decays from high lying excited multiplets, and the optically active centers involved are those in the body of nanorods. The intensity of the red ${}^4\text{F}_{9/2} \rightarrow {}^4\text{I}_{15/2}$ transition increases proportionally to the Yb^{3+} content. As the Er^{3+} increases the intensity of observed green ${}^2\text{H}_{11/2}, {}^4\text{S}_{3/2} \rightarrow {}^4\text{I}_{15/2}$ transitions is somewhat lowered. The intensities of UV ${}^4\text{G}_{11/2} \rightarrow {}^4\text{I}_{15/2}$ and ${}^2\text{H}_{9/2} \rightarrow {}^4\text{I}_{15/2}$ transitions are proportional to the Er^{3+} or Yb^{3+} content. However, the UV ${}^2\text{P}_{3/2} \rightarrow {}^4\text{I}_{15/2}$ transition was only observed for the lowest Er^{3+} content, see the cathodoluminescence spectra for nanorods with compositions 2 % Er, 2 % $\text{Yb}:\text{Lu}_2\text{O}_3$, Figure 13e, and 2 % Er, 10 % $\text{Yb}:\text{Lu}_2\text{O}_3$, in Paper IV Figures 13c and 14c.

The Er^{3+} emissions were identified in the core-shell particles, but an intensity analysis is difficult because the two broad emissions originated by oxygen vacancies in SiO_2 have ~ 100 nm bandwidth and stronger intensities than Er^{3+} transitions.

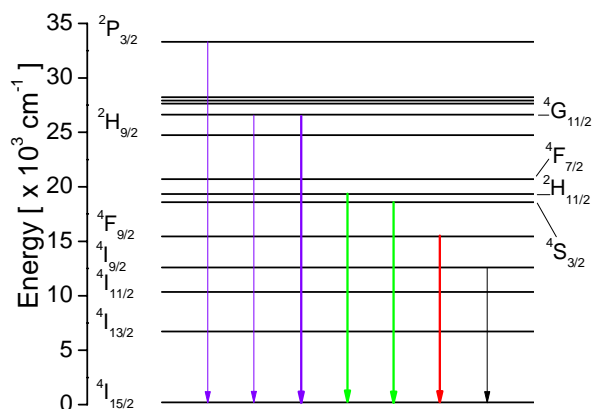


Figure 4.10. Cathodoluminescence transitions observed in $\text{Er}, \text{Yb}:\text{Lu}_2\text{O}_3$ nanorods at 15 kV and probe current 20 nA.

4.4 Cathodoluminescence of Tm^{3+} in Lu_2O_3 nanostructures

4.4.1 Effect of Yb^{3+} in $\text{Tm}, \text{Yb}:\text{Lu}_2\text{O}_3$ nanorods

Room temperature cathodoluminescence spectra of 2, 6, 10 % Yb^{3+} in 2 % $\text{Tm}:\text{Lu}_2\text{O}_3$ nanorods in the 200–900 nm range are shown in the Paper IV, Figure 17. The sharp observed lines arise from the intra-shell $4f^{12}$ transitions of the Tm^{3+} configuration, and have been assigned taking into account the crystal field energy levels scheme of Tm^{3+} in the Lu_2O_3 sesquioxide host [12]. Also in these spectra is observed the broad background emission in the 300–500 nm spectral range, with the same origin as indicated for Yb, $\text{Er}:\text{Lu}_2\text{O}_3$ nanorods. Superimposed on the broad background have been observed UV bands at ~ 380 – 390 nm attributed to the ${}^1\text{D}_2 \rightarrow {}^3\text{H}_6$, the very intense deep-blue emission at 450–470 nm corresponding to the ${}^1\text{D}_2 \rightarrow {}^3\text{F}_4$, which is the dominant band in these spectra, while the blue emission ${}^1\text{G}_4 \rightarrow {}^3\text{H}_6$ and other red (${}^1\text{D}_2 \rightarrow {}^3\text{H}_4$, ${}^1\text{G}_4 \rightarrow {}^3\text{F}_4$) and NIR (${}^1\text{D}_2 \rightarrow {}^3\text{F}_{2,3}$, ${}^1\text{G}_4 \rightarrow {}^3\text{H}_5$, ${}^3\text{H}_4 \rightarrow {}^3\text{H}_6$) transitions are very weak. Figure 4.11 shows a scheme summarizing all the

observed transitions. Furthermore, the intensity ratios between deep-blue and blue emissions, and also between deep blue and UV emissions, increase with the Yb^{3+} content, see Figure 4.12.

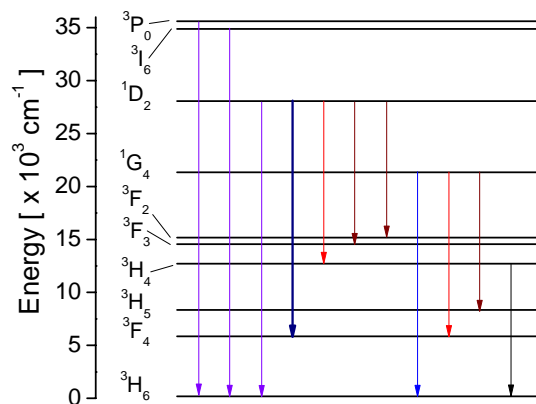


Figure 4.11. Cathodoluminescence transitions observed in $\text{Tm,Yb:Lu}_2\text{O}_3$ nanorods.

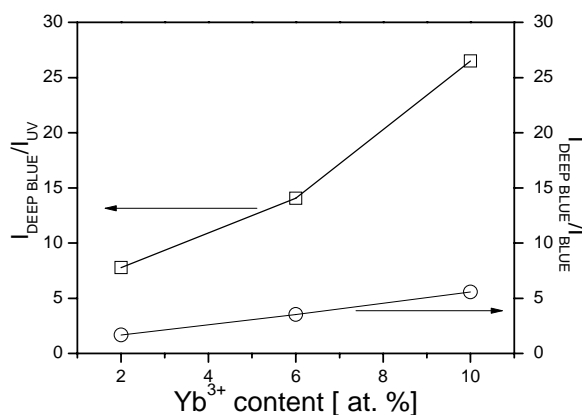


Figure 4.12. Intensity ratio of deep-blue to UV (squares) and deep-blue to blue (circles) cathodoluminescence emission bands.

4.4.2 $\text{Tm:Lu}_2\text{O}_3$ nanocrystals

Paper III, Figure 7 shows the cathodoluminescence spectrum for the $\text{Lu}_{1.713}\text{Tm}_{0.287(7)}\text{O}_3$ (15 % Tm) nanocrystals at room temperature indicating the identified Tm^{3+} electronic transitions. Residual peaks at 598 nm and 728 nm are second-order diffraction harmonics of ultraviolet 299 nm and 364 nm emissions inside the spectrometer. The broad background emission was attributed to radiative recombination at defect centers [5].

4.4.3 Discussion

For Tm:Lu₂O₃ nanocrystals the width of the broad background was shortened with regards to that observed for Er,Y:Lu₂O₃ nanorods, with a maximum intensity located at ~460 nm, indicating that ¹D₂→³H₆ emission could be quenched partially by defect states [5]. In the case of nanorods the broad background emission reaches at maximum in a different position at ~360 nm. We propose that the broad background emission is originated by defect centers created after the synthesis processes.

4.5. Upconversion emission properties of Er³⁺ in Er,Yb:Lu₂O₃ nanostructures

4.5.1 Upconversion emission in Er,Yb:Lu₂O₃ nanorods

The room temperature upconversion (UC) spectra in the range 350–700 nm for 2, 6, 10, 12.5, 15 % Yb³⁺ in 2 % Er:Lu₂O₃ nanorods under excitation into the ²F_{5/2} state of Yb³⁺ ($\lambda_{\text{EXC}} = 980$ nm) are shown in the Paper IV Figure 7. Figure 4.13 shows a scheme of the observed UC emissions at room temperature and the proposed UC mechanisms are explained in this section below. Figure 4.14 (a) and (b) show the UC spectra collected under different power excitations (up to ~425 mW) for Er,Yb:Lu₂O₃ nanorods with two compositions. The green emissions centered at 525 and 550 nm are attributed to ²H_{11/2}→⁴I_{15/2} and ⁴S_{3/2}→⁴I_{15/2} transitions, respectively. The red emission is observed at 650–690 nm, which corresponds to the ⁴F_{9/2}→⁴I_{15/2} transition. Additionally, the very weak UV emission that can be seen at 405–420 nm is attributed to ²H_{9/2}→⁴I_{15/2}. Splitting of these optical transitions are comparable to those reported for Er³⁺ doped bulk single crystal [12], indicating that in all cases the crystal sites for Er³⁺ is kept in the prepared nanorods. In Figure 4.14 it is observed that UC emission spectra were collected in the high energy pump regime. The red ⁴F_{9/2}→⁴I_{15/2} emission profile was divided in two power regimes due to the profile modification and to the quenching observed at 150–180 mW. In the high pumping regime part the excess of energy is transferred to the host increasing the temperature. As the temperature increases some phonons with energy $k_B T$ (~200 cm⁻¹ at room temperature) can produce thermalization between close energy levels. Thermalization of ⁴S_{3/2} and ²H_{11/2} was observed showing that for these close levels (~750 cm⁻¹) the ²H_{11/2} is more populated producing a major emission intensity respect ⁴S_{3/2} as the pump power increases. The blue ⁴G_{11/2}→⁴I_{15/2} emission is only observed for pumping power higher than 200 mW.

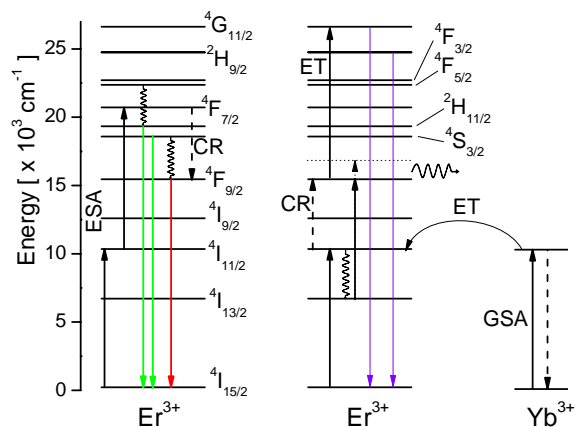


Figure 4.13. Scheme of energy levels of Er^{3+} and Yb^{3+} in Lu_2O_3 and the cross-relaxation process (CR) for populating $^4\text{F}_{9/2}$ in Yb^{3+} , $\text{Er}^{3+}:\text{Lu}_2\text{O}_3$ nanorods after pumping at $\lambda_{\text{EXC}} = 980$ nm.

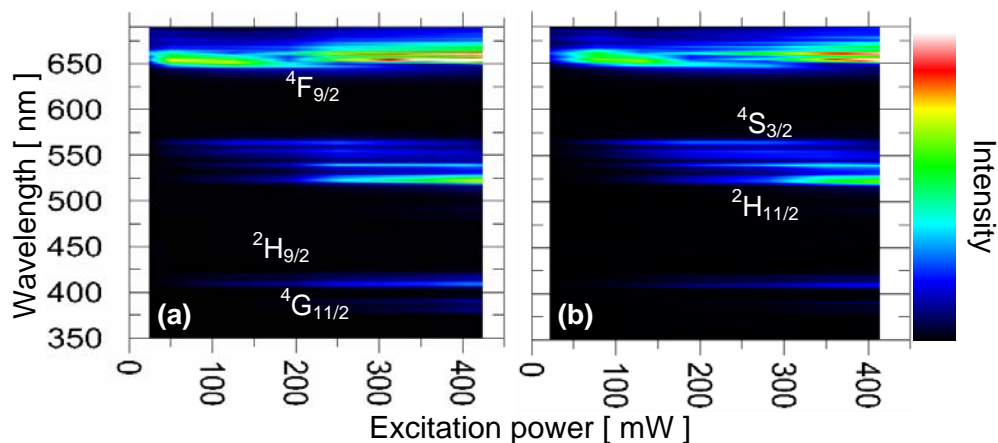


Figure 4.14. Power dependence of the upconversion emission spectra in doped Lu_2O_3 nanorods with (a) 2 % Er, 15 % Yb and (b) 7.5 % Er, 10 % Yb. All transitions are from the indicated states to the ground $^4\text{I}_{15/2}$ multiplet.

The evolution of the relative intensities of green and red UC emissions with the Yb^{3+} content is presented in Figure 4.15. As the Yb^{3+} concentration increases, a strong development of red $^4\text{F}_{9/2} \rightarrow ^4\text{I}_{15/2}$ emission with regard to the green bands $^4\text{S}_{3/2} \rightarrow ^4\text{I}_{15/2}$ and $^2\text{H}_{11/2} \rightarrow ^4\text{I}_{15/2}$ is produced, with the green emission bands vanishing beyond 10 % Yb^{3+} . The effect of the Er^{3+} content on 10 % $\text{Yb}:\text{Lu}_2\text{O}_3$ nanorods is shown in Paper IV Figure 8. For this high Yb^{3+} content, the UC spectra show only—the red $^4\text{F}_{9/2} \rightarrow ^4\text{I}_{15/2}$ emission, and no appreciable differences were observed as the Er^{3+} content is modified.

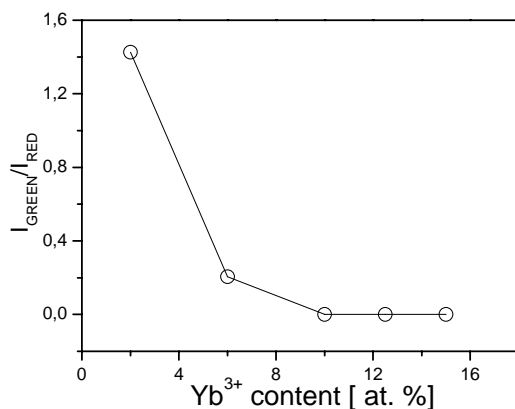


Figure 4.15. Intensity ratio of green to red UC emission bands for Yb³⁺ doped 2 % Er:Lu₂O₃.

UC intensities versus the excitation power for Er³⁺ red, green and blue emissions are presented in log-log plots in Paper IV, Figures 11 and 12. Here we resume the calculated slopes in Table 4.4 and Table 4.5. Severely reduced slopes were obtained for the ⁴F_{9/2}→⁴I_{15/2}, ⁴S_{3/2}→⁴I_{15/2}, ²H_{11/2}→⁴I_{15/2} and ²H_{9/2}→⁴I_{15/2} visible UC emissions in Er,Yb:Lu₂O₃ nanorods. As Yb³⁺ or Er³⁺ content increases slopes decrease, with one exception regarding green emissions where slopes decrease as Er³⁺ concentration decreases.

Table 4.4. Measured slope values for Yb³⁺ doped 2 % Er:Lu₂O₃ nanorods.

[%]	² H _{9/2} → ⁴ I _{15/2}	² H _{11/2} → ⁴ I _{15/2}	⁴ S _{3/2} → ⁴ I _{15/2}	⁴ F _{9/2} → ⁴ I _{15/2} [†]	⁴ F _{9/2} → ⁴ I _{15/2} [‡]
10	1.4	1.3	1.8	1.0	1.1
12.5	1.4	1.2	1.9	0.6	1.2
15	1.0	0.9	1.6	0.4	0.8

[†] 20-150 mW excitation.

[‡] 180-350 mW excitation.

Table 4.5. Measured slope values for Er³⁺ doped 10 % Yb:Lu₂O₃ nanorods

[%]	² H _{9/2} → ⁴ I _{15/2}	² H _{11/2} → ⁴ I _{15/2}	⁴ S _{3/2} → ⁴ I _{15/2}	⁴ F _{9/2} → ⁴ I _{15/2} [†]	⁴ F _{9/2} → ⁴ I _{15/2} [‡]
2	1.4	1.3	1.8	1.0	1.1
5	1.3	1.0	1.7	0.4	0.9
7.5	1.2	1.2	1.9	0.5	0.9

[†] 20-150 mW excitation.

[‡] 180-350 mW excitation.

4.5.2 Stokes emission in $\text{SiO}_2@Er, Yb:Lu_2O_3$ core-shell particles

No UC emission was observed for the $\text{SiO}_2@(2\% \text{ Er}, 6\% \text{ Yb}):Lu_2O_3$ core-shell particles pumping at 980 nm with 1 W excitation power. Instead, the Er^{3+} Stokes emission was characterized by laser excitation using a Raman spectrometer. Stokes emission spectra in the range of 520–570 nm and 640–700 nm under excitation with $\lambda_{\text{exc}} = 514$ nm and $\lambda_{\text{exc}} = 633$ nm are shown in Figure 4.16. The broad background was associated to the Raman bands of vibrational modes in silica. Emission spectra exhibit lines with splittings similar to 2 % Er 6 % Yb Lu_2O_3 nanocrystals under the same conditions. However, the green and red emissions are not comparable because they were collected under different excitation wavelength from different laser sources.

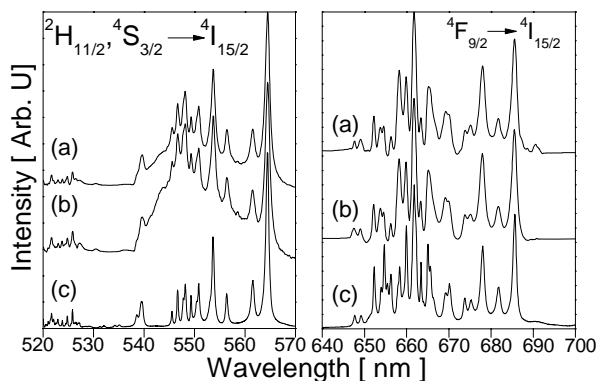


Figure 4.16. Room emission spectra showing the Er^{3+} green ${}^2\text{H}_{11/2}, {}^4\text{S}_{3/2} \rightarrow {}^4\text{I}_{15/2}$ (left) and red ${}^4\text{F}_{9/2} \rightarrow {}^4\text{I}_{15/2}$ transitions (right) for core-shell particles processed at pH = 7 (a); pH = 11 (b); and nanocrystals (c).

4.5.3 Upconversion emission in $Er, Yb:Lu_2O_3$ nanoparticles

UC photoluminescence spectra were collected in nanocrystalline powder 2 % Er 6 % Yb Lu_2O_3 , obtained from the precursor solution afterwards used to produce $\text{SiO}_2@(2\% \text{ Er}, 6\% \text{ Yb}):Lu_2O_3$ core-shell particles. The UC spectra are showed in the Paper VII, Figure 9. The red ${}^4\text{F}_{9/2} \rightarrow {}^4\text{I}_{15/2}$ emission is one order of magnitude stronger than the green ${}^4\text{S}_{3/2} \rightarrow {}^4\text{I}_{15/2}$ emission in. The graph of the emission intensity versus excitation power yields a slope of 0.68 for the red emission. This value is lower than the expected ~ 1 in the high power limit [18] indicating a saturation of the UC emission.

4.5.4 Discussion

As indicated in chapter 3, it is usually assumed the proportionality between the UC visible emission to an n th power of the IR excitation intensity, $I_{UC} \propto (I_0)^n$, where the integer n represents the number of photons required to populate the visible states per upconverted photon emitted from them. In the logarithmic representation, the expression become linear and n is corresponds to the slope. In the high power regime this linearity between the slope

and the number of photons is not fulfilled and it is necessary to modify the interpretation of the slope. Güdel group have studied the dependence of UC intensity on pump power and gave a theoretical model considering the competition between linear decay and upconversion processes for the depletion of the intermediate excited states, for ions capable of energy transfer UC by the acceptor itself [17] or by sensitization [18], concluding that a realistic UC system will exhibit a intensity-versus-power dependence which is less than $(I_0)^n$. In the high power limit, the power dependence reduces to $(I_0)^1$ for only acceptors or by sensitization with donors, regardless of the number of UC steps involved in the excitation process of the emitting level. For our system the slopes for the emission of Er^{3+} $^2\text{H}_{9/2}$, $^2\text{H}_{11/2}$, and $^4\text{F}_{9/2}$ energy levels have values that can be approximated to 1. We point that the energy transfers from Yb^{3+} are the main UC mechanism at high-power pumping due to large absorption cross section of Yb^{3+} [19]. However the ESA processes of Er^{3+} ions can not be dismissed. We can conclude that the severely reduced slopes for the $^4\text{F}_{9/2} \rightarrow ^4\text{I}_{15/2}$, $^2\text{H}_{11/2} \rightarrow ^4\text{I}_{15/2}$ and $^2\text{H}_{9/2} \rightarrow ^4\text{I}_{15/2}$ visible UC emissions observed in $\text{Er,Yb:Lu}_2\text{O}_3$ nanorods and nanoparticles point to larger UC rates for depletion for intermediate excited states. Slopes of the Er^{3+} $^4\text{S}_{3/2} \rightarrow ^4\text{I}_{15/2}$ green emission are in all cases closer to 2 than to 1. In this case the intermediate excited level is $^4\text{I}_{11/2}$. Non-radiative relaxation of $^4\text{I}_{11/2}$ to $^4\text{I}_{13/2}$, by high energy phonons from surface, reduces the importance of the UC decreases, leading the slope of this green emission to be ~ 2

Although we have described the origin of the slope for Er^{3+} $^2\text{H}_{9/2}$, $^2\text{H}_{11/2}$, and $^4\text{F}_{9/2}$ energy levels in terms of the high power limit, we need more information to describe the UC mechanism, so we will refer to literature to complete this description. Slopes of ~ 2 have been reported for the UC photoluminescence intensity of Er^{3+} $^4\text{F}_{9/2} \rightarrow ^4\text{I}_{15/2}$, $^2\text{H}_{11/2} \rightarrow ^4\text{I}_{15/2}$ and $^4\text{S}_{3/2} \rightarrow ^4\text{I}_{15/2}$ for $\text{Er,Yb:Y}_2\text{O}_3$ nanocrystals [19, 21, 22] and bulk [19] and slopes of nearly 3 for $^4\text{S}_{3/2} \rightarrow ^4\text{I}_{15/2}$ in highly Yb^{3+} -doped samples [21] where UV emissions of Er^{3+} have been observed as well. Following this result we show in Figure 4.13 that green and red emission are emitted after two successive near-resonant transfers of energy from Yb^{3+} to Er^{3+} , leading Er^{3+} to the intermediate $^4\text{I}_{11/2}$ state and then to $^4\text{F}_{7/2}$. The lower emitting levels $^2\text{H}_{11/2}$ and $^4\text{S}_{3/2}$ (green), and then $^4\text{F}_{9/2}$ (red) will be populated by multiphonon relaxation from $^4\text{F}_{7/2}$ level. On this basis, the expected slopes values for the low power regime are ~ 2 . The expected Er^{3+} emission would be predominantly green, as the red-emitting $^4\text{F}_{9/2}$ is populated by non-radiative decay from $^4\text{S}_{3/2}$. However, the low intensity of the green emission and its gradual decrease with regards to the red emission for higher Yb^{3+} contents points to an increase in the efficiency of the ion-pair cross-relaxation (CR) process ($^4\text{F}_{7/2}$, $^4\text{I}_{11/2}$) \rightarrow ($^4\text{F}_{9/2}$, $^4\text{F}_{9/2}$) that directly populates $^4\text{F}_{9/2}$ bypassing $^2\text{H}_{11/2}$ and $^4\text{S}_{3/2}$ [20]. This process fully explains the observed emphasized red emission following NIR excitation in both bulk crystals [21] and polycrystalline ceramic powders [20], does not account for the larger intensity differences in the red emission between bulk and nanocrystalline size regimes [22]. In that way, another mechanism also populating $^4\text{F}_{9/2}$ and favored by the specific characteristics of prepared $\text{Yb,Er:Lu}_2\text{O}_3$ nanostructures must be additionally operative under NIR excitation. A proposed process [21] indicates that after initial energy transfer from Yb^{3+} in $^2\text{F}_{5/2}$, Er^{3+} in $^4\text{I}_{11/2}$ non-radiatively decays to $^4\text{I}_{13/2}$, the energy gap between both states being $\sim 3600 \text{ cm}^{-1}$. This relaxation process can be very effective given the previously indicated availability of large phonons at ~ 1400 , ~ 1530 , ~ 1630 and $\sim 3440 \text{ cm}^{-1}$ from adsorbed CO_2 and/or H_2O

species [19], which can easily cover the gap. Next, another energy transfer from Yb^{3+} in $^2\text{F}_{5/2}$ will populate Er^{3+} $^4\text{F}_{9/2}$ through the non-resonant $^4\text{I}_{13/2} \rightarrow ^4\text{F}_{9/2}$ transition, and the excess energy ($\sim 1600 \text{ cm}^{-1}$) was also dissipated through phonons of the lattice. The full phonon-assisted process is clearly dependent on the Yb^{3+} concentration, since an increase in the latter results in a corresponding increase in red enhancement. The vanishing of green Er^{3+} emission in heavily Yb^{3+} -doped sesquioxide nanocrystalline materials has been explained by activation of the ion-pair cross-relaxation (CR) process ($^4\text{F}_{7/2}, ^4\text{I}_{11/2} \rightarrow ^4\text{F}_{9/2}, ^4\text{F}_{9/2}$) and two photon to a three-photon process for populating $^4\text{S}_{3/2}$ when electrons in $^4\text{I}_{11/2}$ energy level non-radiatively decays to $^4\text{I}_{13/2}$ energy level.

4.6. Upconversion emission properties of Tm^{3+} in $\text{Tm,Yb:Lu}_2\text{O}_3$ nanostructures

4.6.1 Upconversion emission in $\text{Tm,Yb:Lu}_2\text{O}_3$ nanorods

The room temperature UC spectra in the range 330–700 nm for 2, 6, 10 % Yb in 2 % $\text{Tm:Lu}_2\text{O}_3$ nanorods under excitation at $\lambda_{\text{EXC}} = 980 \text{ nm}$ are shown in Paper IV Figure 15. The energy level diagram of Tm^{3+} and Yb^{3+} indicating the observed emissions is presented in Figure 4.17. The observed deep-blue emission at $\sim 450\text{--}465 \text{ nm}$ is attributed to $^1\text{D}_2 \rightarrow ^3\text{F}_4$, and the very intense blue emission observed at $\sim 470\text{--}490 \text{ nm}$ is ascribed to the $^1\text{G}_4 \rightarrow ^3\text{H}_6$ transition. Additionally, the very weak green emission centered at $\sim 529 \text{ nm}$ can be assigned to the $^1\text{D}_2 \rightarrow ^3\text{H}_5$ transition. Figure 4.18 shows the intensity ratio of blue-to-deep blue emissions, where a clear development of the dominant $^1\text{G}_4 \rightarrow ^3\text{H}_6$ transition with regard to $^1\text{D}_2 \rightarrow ^3\text{F}_4$ results when the Yb^{3+} content increases. The dominant peak at $\sim 800 \text{ nm}$ accounting for the $^3\text{H}_4 \rightarrow ^3\text{H}_6$ transition does not appear because a 700 nm short pass filter was used during UC emission measurements. The $^1\text{G}_4 \rightarrow ^3\text{F}_4$ red emission at $\sim 650 \text{ nm}$, which although weak is usually seen in $\text{Yb}^{3+}, \text{Tm}^{3+}:\text{Lu}_2\text{O}_3$ nanoparticles [23,24], is absent in the current $\text{Yb}^{3+}, \text{Tm}^{3+}:\text{Lu}_2\text{O}_3$ nanorods. The population of Tm^{3+} $^3\text{H}_4, ^1\text{G}_4$ and $^1\text{D}_2$ excited states is accomplished by sequential two-, three- and four-photon energy transfer processes from excited Yb^{3+} $^2\text{F}_{5/2}$ to Tm^{3+} , respectively.

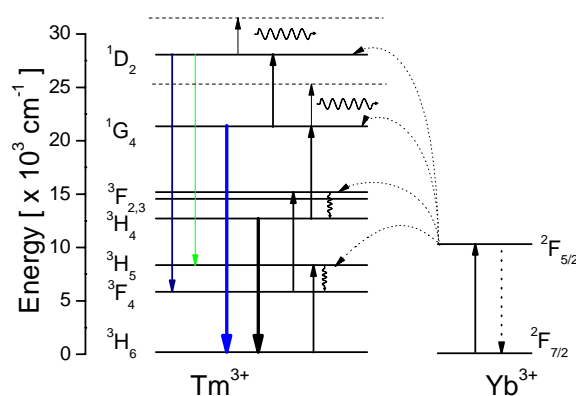


Figure 4.17. Scheme of energy levels for Tm^{3+} and Yb^{3+} configurations in Lu_2O_3 , and energy transfers proposed for observed UC emission.

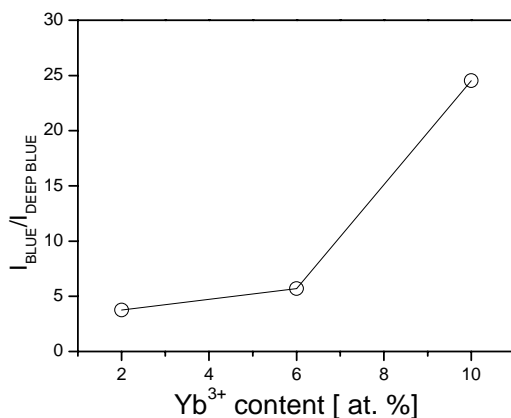


Figure 4.18. Intensity ratio of blue to deep-blue upconversion bands.

4.6.2. Upconversion emission in $\text{SiO}_2@\text{Tm,Yb:Lu}_2\text{O}_3$ core-shell particles

The evolution of UC spectra with the pump power in the range 450–800 nm for $\text{SiO}_2@\text{Tm,Yb:Lu}_2\text{O}_3$ ($\text{Lu}_{1.889}\text{Yb}_{0.110}\text{Tm}_{0.001}\text{O}_3$) core-shell particles under excitation at $\lambda_{\text{EXC}} = 980$ nm is shown in Figure 4.19. The blue $^1\text{G}_4 \rightarrow ^3\text{H}_6$ transition is observed at ~450–490 nm. The $^1\text{G}_4 \rightarrow ^3\text{F}_4$ red emission was observed with relative low intensity and the broad $^3\text{H}_4 \rightarrow ^3\text{H}_6$ emission is also observed. Figure 4.20 shows the dependence of integrated intensities of each emission band with the excitation power. The calculated slope value is ~2 for $^3\text{H}_4 \rightarrow ^3\text{H}_6$ emission indicating a two photon upconversion process. The blue and red emission radiated from $^1\text{G}_4$ level have similar slope values ~2, however a value ~3 was expected for the first one.

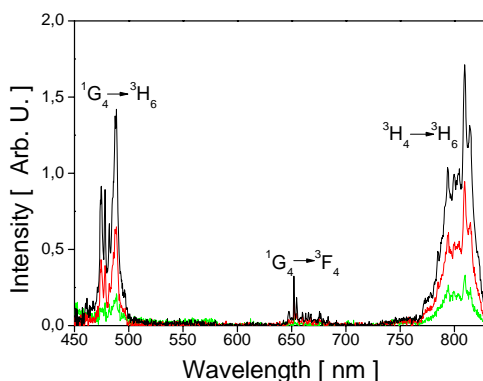


Figure 4.19. Upconversion emission spectra for $\text{SiO}_2@\text{Lu}_{1.889}\text{Yb}_{0.110}\text{Tm}_{0.001}\text{O}_3$ core-shell particles at 150, 250 and 350 W/cm^2 .

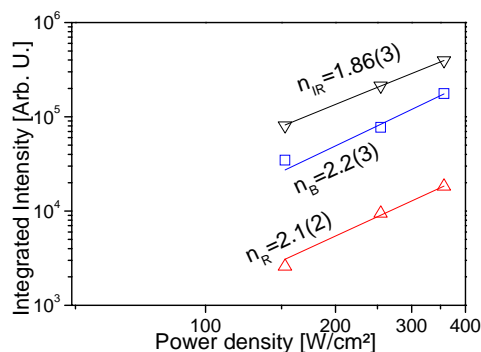


Figure 4.20. Integrated intensities of emission bands as a function of the excitation power density for $\text{SiO}_2@Lu_{1.889}Yb_{0.110}Tm_{0.001}O_3$ core-shell particles.

4.6.3 Upconversion emission in $Tm, Yb:Lu_2O_3$ nanoparticles

$Tm, Yb:Lu_2O_3$ nanoparticles ($Lu_{1.889}Yb_{0.110}Tm_{0.001}O_3$) have been produced from the starting solution for production of $\text{SiO}_2@Tm, Yb:Lu_2O_3$ core-shell particles. The UC spectra profiles for different excitation power densities for $Tm, Yb:Lu_2O_3$ nanoparticles are shown in Figure 4.21. The weak green emission observed in the range 540-550 nm was attributed to $^1D_2 \rightarrow ^3H_5$ transition. The intensity versus excitation power dependence is presented in Figure 4.22. Slope values of 1.5-1.7 were calculated for the visible emissions, and for the NIR $^3H_4 \rightarrow ^3H_6$ emission a value of 1.35(3) was obtained.

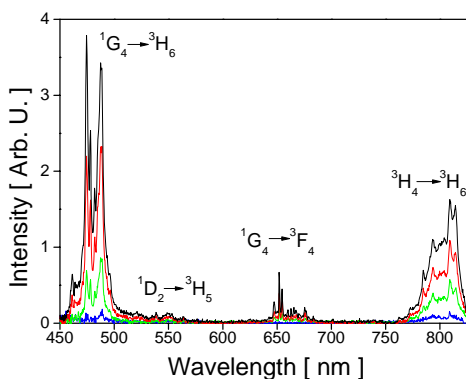


Figure 4.21 Upconversion emission spectra in $Lu_{1.889}Yb_{0.110}Tm_{0.001}O_3$ nanoparticles under excitation power densities of 50, 150, 250 and 350 W/cm^2 .

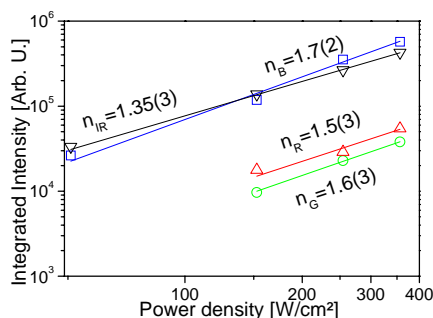


Figure 4.22. Integrated intensities of emission bands as a function of excitation power density for $\text{Lu}_{1.889}\text{Yb}_{0.110}\text{Tm}_{0.001}\text{O}_3$ nanoparticles.

4.6.4 Discussion

In the low excitation power limit, a slope of ~ 3 is expected regarding the number of energy transfer from Yb^{3+} to Tm^{3+} to reach the $^1\text{G}_4$ level [17]. In the other hand, in the high power region a value of 1 is expected regardless the number of energy transfers [18]. Then, we suggest that slopes of $^1\text{D}_2 \rightarrow ^3\text{F}_4$, $^1\text{G}_4 \rightarrow ^3\text{H}_6$ and $^1\text{G}_4 \rightarrow ^3\text{F}_4$ transitions, with values of ~ 2 , lay into an intermediate region between the low and high power regions in similar case as the examples reported by Pollnau *et al* [17]. For $\text{Tm}^{3+} ^3\text{H}_4 \rightarrow ^3\text{H}_6$ emission, the slope of 1.86(3) is associated to a two photon process.

The mechanism involved in the UC visible emissions of $\text{Tm,Yb:Lu}_2\text{O}_3$ sesquioxide nanostructures is shown in Figure 4.17. For the population of the $^1\text{G}_4$ level, a series of a non resonant phonon-assisted energy transfer processes are suggested. The Tm^{3+} ion is excited from the ground state $^3\text{H}_6$ to the $^3\text{F}_4$ level by the ET process from the $\text{Yb}^{3+} ^2\text{F}_{5/2}$ level, then a second ET process leads Tm^{3+} above the $^3\text{F}_{2,3}$ level, and by multiphonon relaxation $\text{Tm}^{3+} ^3\text{H}_4$ level is reached. A third ET process leads Tm^{3+} to the $^1\text{G}_4$, from which multiphonon relaxations mainly to $^3\text{H}_6$ and in some extent to $^3\text{F}_4$ produce the predominant blue and the weak red emissions, respectively. The weak $^1\text{D}_2 \rightarrow ^3\text{F}_4$ transition is produced by a low probability process, when electrons in excited $^1\text{G}_4$ level reach the $^1\text{D}_2$ energy level by a four ET from $\text{Yb}^{3+} ^2\text{F}_{5/2}$ level.

4.7 Conclusions

Stark energy levels of Tm^{3+} in Lu_2O_3 nanoparticles were assigned by comparison with those reported data for Lu_2O_3 single crystals, showing no modification of their average energy, but with some linewidth enlargement, possibly originated by a local disorder around the optically active ions. As in single crystals, in the current nanocrystals one of the strongest absorptions of Tm^{3+} corresponds to the $^3\text{H}_6 \rightarrow ^3\text{H}_4$ transition at 796 nm. This transition can be used for pumping $\text{Tm:Lu}_2\text{O}_3$ ceramic lasers made from nanocrystal precursors. The operation efficiency of such lasers relies on a large lifetime of the $^3\text{F}_4$ excited level; however, the accumulation of surface defects in nanocrystals may lead to a significant reduction of the lifetime and correspondingly, of the photoluminescence yield. The

photoluminescence intensity decays of emission from $^3\text{H}_4$ and $^3\text{F}_4$ energy levels exhibit non-exponential dynamics due to inhomogeneous transfer rate between Tm^{3+} ions as the Tm^{3+} content increases. OH- attached groups affect the fast component of the decay, and the long lived and Tm-Tm interactions in the body of the nanocrystals were associated to the long lived component. Increasing the Tm^{3+} concentration further reduces the lifetime due to Tm-Tm interactions as energy migration ($^3\text{H}_4, ^3\text{H}_6 \rightarrow ^3\text{H}_6, ^3\text{H}_4$) and cross relaxation ($^3\text{H}_4, ^3\text{H}_6 \rightarrow ^3\text{F}_4, ^3\text{F}_4$) similarly to that observed in single crystals.

Cathodoluminescence spectra of Er,Yb:Lu₂O₃ nanorods show that as the Yb³⁺ concentration increases the red $^4\text{F}_{9/2} \rightarrow ^4\text{I}_{15/2}$ emission increases, while as Er³⁺ concentration increases the green $^2\text{H}_{11/2} \rightarrow ^4\text{I}_{15/2}$ and $^4\text{S}_{3/2} \rightarrow ^4\text{I}_{15/2}$ transitions slightly decrease. The intensities of UV $^4\text{G}_{11/2} \rightarrow ^4\text{I}_{15/2}$ and $^2\text{H}_{9/2} \rightarrow ^4\text{I}_{15/2}$ transitions are proportional to the Er³⁺ or Yb³⁺ content. The broad background emission observed in nanorods (~360 nm) and nanoparticles (~460 nm) are originated by structural defect in the host during synthesis process. Er³⁺ visible emission were overlapped with the broad band emission at 450 and 650 nm in SiO₂@Er,Yb:Lu₂O₃ particles. The broad bands are originated by oxygen vacancies in the amorphous SiO₂ spheres.

UC photoluminescence spectra of Er,Yb:Lu₂O₃ nanostructures show that an increment in the Yb³⁺ concentration increases the red to green emission ratio, explained in terms of energy transfer from Yb³⁺ to Er³⁺ and the Er³⁺- Er³⁺ cross-relaxation (CR) process ($^4\text{F}_{7/2}, ^4\text{I}_{11/2} \rightarrow ^4\text{F}_{9/2}, ^4\text{F}_{9/2}$), and UC becomes efficient. UC visible emissions intensity versus excitation power in Er,Yb:Lu₂O₃ nanorods and nanoparticles reflect the high energy pumping conditions that generate Er³⁺ $^4\text{F}_{9/2} \rightarrow ^4\text{I}_{15/2}$, $^2\text{H}_{11/2} \rightarrow ^4\text{I}_{15/2}$ and $^2\text{H}_{9/2} \rightarrow ^4\text{I}_{15/2}$ emissions following the proportionality $I_{VIS} \sim (I_0)^l$. We conclude that severely reduced slopes for the $^4\text{F}_{9/2} \rightarrow ^4\text{I}_{15/2}$, $^4\text{S}_{3/2} \rightarrow ^4\text{I}_{15/2}$, $^2\text{H}_{11/2} \rightarrow ^4\text{I}_{15/2}$ and $^2\text{H}_{9/2} \rightarrow ^4\text{I}_{15/2}$ visible UC emissions observed in Er,Yb:Lu₂O₃ nanorods and nanoparticles point to larger UC rates in for depletion for intermediate excited states. The two-photon $^4\text{S}_{3/2} \rightarrow ^4\text{I}_{15/2}$ green emission in Er,Yb:Lu₂O₃ nanorods present slopes closer to 2, because large $^4\text{I}_{11/2} \rightarrow ^4\text{I}_{13/2}$ non-radiative relaxation rate from the presence of phonons from adsorbed species as H₂O and CO₂, reducing the importance of the UC depletion and producing the extra enhancement of the red emission via the $^4\text{F}_{9/2} \leftarrow ^4\text{I}_{13/2}$ transition.

4.8 References

- [1] B. Antic, M. Mitric, D. Rodic, *Cation ordering in cubic and monoclinic (Y,Eu)₂O₃ : an x-ray powder diffraction and magnetic susceptibility study* **J. Phys.: Condens. Matt.** 9, 365 (1997).
- [2] G. Concas, G. Spano, M. Bettinelli, A. Speghini *Investigation of Eu³⁺ Site Occupancy in Cubic Y₂O₃ and Lu₂O₃ Nanocrystals* **Z. Naturforsch.** 58a, 551- 557 (2003).
- [3] L. Fornasiero, *Nd³⁺ - und Tm³⁺ - dotierte Sesquioxides* (Ph.D. Dissertation. Universität Hamburg, Hamburg, 1999).
- [4] H. Eilers, B.M. Tissue *Laser spectroscopy of nanocrystalline Eu₂O₃ and Eu³⁺:Y₂O₃* **Chem. Phys. Lett.** 251 74 (1990).
- [5] C. M. Donegá, E. Zych, A. Meijerink *Luminescence of Lu₂O₃:Tm nanoparticles* **Mat. Res. Soc. Symp. Proc.** 667, 1 (2001).
- [6] M. J. Weber *Radiative and Multiphonon Relaxation of Rare-Earth Ions in Y₂O₃* **Phys. Rev.** 171, 283-291 (1968).
- [7] P. Koopman *Effizienter Laserbetrieb von Tm³⁺:Lu₂O₃ bei 2 µm Wellenlänge* p41 (2008).
- [8] J. García Solé, L. E. Bausá, D. Jaque. *An introduction to the optical spectroscopy of inorganic solids*, John Wiley & Sons Ltd, (2005).
- [9] F. Cornacchia, D. Parisi, M. Tonelli, *Spectroscopy and Diode-Pumped Laser Experiments of LiLuF₄:Tm³⁺ Crystals* **IEEE J. Quantum Electron.** 44, 1076-1082 (2008).
- [10] H. D. Müller, J. Schneider, H. Lüth, R. Strümpfer *Cathodoluminescence study of erbium in La_{1-x}Er_xF₃ epitaxial layers on Si(111)* **Appl. Phys. Lett.** 57 2422 (1990).
- [11] E. Nogales, B. Méndez, J. Piqueras *Visible cathodoluminescence of Er ions in β-Ga₂O₃ nanowires and microwires* **Nanotechnology** 19 035713 (2008).
- [12] V. Peters *Spektroskopie und lasereigenschaften erbium-und praseodymdotierter hochschmelzender oxide* Master's Thesis Institute of Laser-Physics, University of Hamburg, Germany (1998).
- [13] M. Goldberg, H. -J. Fitting, A. Trukhin *Cathodoluminescence and cathodoelectroluminescence of amorphous SiO₂ films* **J. Non-Cryst. Solids** 220 69 (1997).
- [14] X. Yanga, K.-Y. Law, L. J. Brillson *Low energy cathodoluminescence spectroscopy of SiO₂ nanoparticles* **J. Vac. Sci. Technol.** A 15(3), (1997).
- [15] M. Jafarzadeh, I. A. Rahman, C. S. Sipaut *Optical properties of amorphous organo-modified silica nanoparticles produced via co-condensation method* **Ceram. Int.** 36 333 (2010).
- [16] S. Munekuni, T. Yamanaka, Y. Shimogaichi, R. Tohmon, Y. Ohki, K. Nagasawa, Y. Hama *Various types of non bridging oxygen hole center in high-purity silica glass* **J. Appl. Phys.** 68, 1 (1990).
- [17] M. Pollnau, D.R. Gamelin, S.R. Lüthi, H.U. Güdel, *Power dependence of upconversion luminescence in lanthanide and transition-metal-ion systems* **Phys. Rev. B** 61 3337 (2000).
- [18] J. F. Suyver, A. Aebischer, S. García-Revilla, P. Gerner, H. U. Güdel *Anomalous power dependence of sensitized upconversion luminescence* **Phys. Rev. B** 71, 125123 (2005).
- [19] F. Vetrone, J. -C. Boyer, J. A. Capobianco, A. Speghini, M. Bettinelli *Effect of Yb³⁺ Codoping on the Upconversion Emission in Nanocrystalline Y₂O₃:Er³⁺* **J. Phys. Chem. B** 107 1107 (2003).

- [20] J. P. Wittke, I. Ladany, P. N. Yocom *Y₂O₃:Yb:Er-New Red-Emitting Infrared-Excited Phosphor* **J. Appl. Phys.** 43, 595 (1972).
- [21] F. Vetrone, J. -C. Boyer, J. A. Capobianco, A. Speghini, M. Bettinelli *Significance of Yb³⁺ concentration on the upconversion mechanisms in codoped Y₂O₃:Er³⁺, Yb³⁺ nanocrystals* **J. Appl. Phys.** 96, 661 (2004)
- [22] L. Y, Zhang J, Zhang X, Luo Y, Ren X, Zhao H, Wang X, Sun L, Yan C *Near-Infrared to Visible Upconversion in Er³⁺ and Yb³⁺ Codoped Lu₂O₃ Nanocrystals: Enhanced Red Color Upconversion and Three-Photon Process in Green Color Upconversion* **J. Phys. Chem. C** 113 4413 (2009).
- [23] F. Wang, X. Liu *Recent advances in the chemistry of lanthanide-doped upconversion nanocrystals* **Chem. Soc. Rev.** 38 976 (2009).
- [24] L. An, J. Zhang, M. Liu, S. Wang *Upconversion luminescence of Tm³⁺ and Yb³⁺-codoped lutetium oxide nanopowders* **J. Alloys Compounds** 451 538 (2008).

Chapter 5
**Yb³⁺ sensitized KLu(WO₄)₂
(KLuW) nanocrystals for white
light generation**

In this chapter Yb³⁺-sensitized KLu(WO₄)₂ (hereafter KLuW) nanocrystals have been analyzed as possible candidates to produce white light by upconversion (UC) of near infrared (NIR) excitation light. We start introducing the basic principles of the chromaticity theory. Then, we studied the UC spectra of double doped Ln, Yb: KLuW (Ln= Er, Ho or Tm) nanocrystals, and by proposing an extension of the chromaticity theory in the 1931 Commission Internationale de l'Éclairage (CIE) framework, a prediction of a white light emitter by the physical mixture of them is carried out. After that we studied the effect of Ho³⁺ and Tm³⁺ in the Ho:Tm:Yb:KLuW nanocrystals, and finally the effect of Eu³⁺ on the Ho:Tm:Yb:KLuW sample with best chromaticity coordinates. Conclusions are presented in the last section.

Upconversion emission, Stokes emission and photoluminescence decay measurements were carried out at Solid State Chemistry Lab at University of Verona, Italy. Upconversion quantum yield measurements were carried out at optic lab at FiCMA-FiCNA group at Rovira i Virgili University in Tarragona, Spain.

5.1 Introduction to CIE 1931 chromaticity theory

A careful determination of the characteristics of the emitted light color is important for applications of luminescent materials phosphor. The CIE XYZ chromatic coordinates (x, y, z) can be calculated from the tristimulus ratios as follow [1]:

$$\begin{aligned} x &= \frac{X}{X+Y+Z} \\ y &= \frac{Y}{X+Y+Z} \\ z &= \frac{Z}{X+Y+Z} \end{aligned} \quad (5.1)$$

Where the tristimulus values (X, Y, Z) can be calculated by following integrations over the entire visible spectrum:

$$\begin{aligned} X &= \int \bar{r}(\lambda) s(\lambda) d\lambda \\ Y &= \int \bar{g}(\lambda) s(\lambda) d\lambda \\ Z &= \int \bar{b}(\lambda) s(\lambda) d\lambda \end{aligned} \quad (5.2)$$

where $s(\lambda)$ is the emission spectrum of interest. $\bar{r}(\lambda)$, $\bar{g}(\lambda)$ and $\bar{b}(\lambda)$ are normalized color matching functions that model the response of the photoreceptors in the human eye to monochromator blue, red and green radiators of equal radiant power [1]. The color matching functions are presented in Figure 5.1, and Figure 5.2 shows the CIE chromaticity diagram, where the chromaticity coordinates of a equi-energy radiator (CIE illuminat E) are $(x, y) = (1/3, 1/3)$. The color purity is defined as the ratio of the distance from the white

point (1/3, 1/3) to a given coordinate (x,y) and the distance from the white point to the boundary of the chromaticity diagram intersecting the coordinate (x,y) [2].

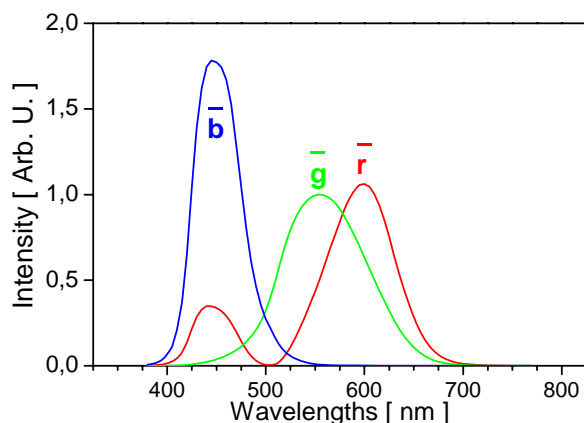


Figure 5.1. CIE 1931 Color Matching functions (2° observer). A 2° visual field represents a diameter of about 17 mm at a viewing distance of 0.5 m.

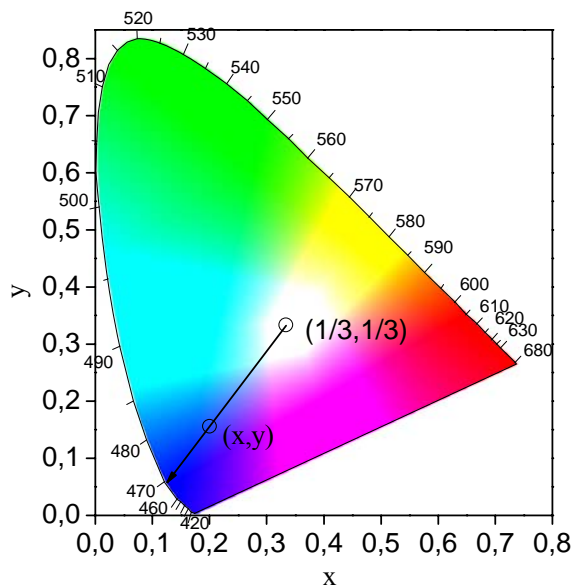


Figure 5.2. CIE 1931 chromaticity diagram.

5.2 Ln, Yb:KLuW (Ln = Er, Ho, Tm) nanocrystals as red-green-blue emitters.

5.2.1 Er, Yb:KLuW nanocrystals as green emitters

Figure 5.3 shows the 980 nm excited UC emission spectra in the range of 450-725 nm, of Yb, Er-doped nanocrystals. Emission bands are observed in the green region at 530-550 nm and in the red region at 660 nm corresponding to the Er³⁺ ²H_{11/2}, ⁴S_{3/2}→⁴I_{15/2} and ⁴F_{9/2}→⁴I_{15/2} transitions, respectively. The calculated *n* slopes for the relationship between visible emission intensity and NIR excitation intensity $I_{UC} \propto (I_0)^n$ [3] are presented in log-log graphs in the inset of Figure 5.3. A linear dependence was obtained in each case, with $n_R = 1.65 \pm 0.04$ and $n_G = 2.15 \pm 0.4$ for the red and green emissions, respectively. These emissions can be associated to two photon UC processes. The large I_{GREEN}/I_{RED} emission ratio in the UC spectra (~30) in comparison with the Er:Yb:Lu₂O₃ nanorods (~0.3) is explained by the different phonon energy of the hosts. For KLuW, the maximum phonon energy corresponds to $\hbar\omega_{max} = 908 \text{ cm}^{-1}$ [4], and in the case of Lu₂O₃ $\hbar\omega_{max} = 393 \text{ cm}^{-1}$ [5]. The larger phonon energy in KLuW deactivates the cross-relaxation mechanism (⁴F_{7/2}, ⁴I_{11/2}) → (⁴F_{9/2}, ⁴F_{9/2}) between Er-Er pairs observed in Lu₂O₃. The major contribution to the depopulation of ⁴F_{7/2} level is the multi-phonon decay to the ²H_{11/2} level through 1-2 phonons in KLuW, instead of the non-radiative decay to the red ⁴F_{9/2} emitter level.

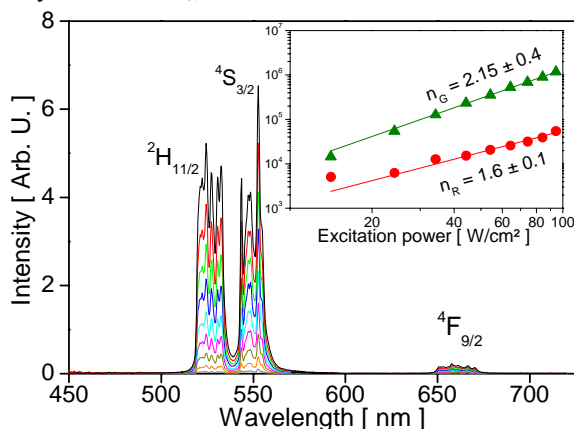


Figure 5.3. Upconversion spectra of 1 % Er, 10 % Yb:KLuW nanocrystals. Er³⁺ transitions to the ground state ⁴I_{15/2} are indicated by the corresponding excited state. Excitation power densities are in the 14-94 W/cm² range, with 10 W/cm² steps. The inset shows the dependence of the intensity with the excitation power and calculated slopes for green and red emissions.

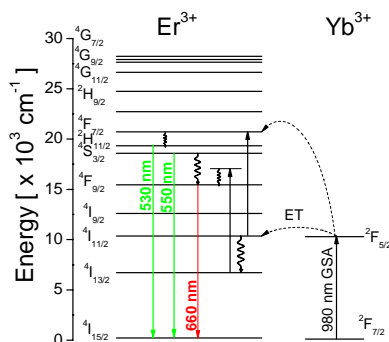


Figure 5.4. Upconversion mechanisms for 1 % Er, 10 % Yb:KLuW nanocrystals.

A scheme of the Er³⁺ energy level diagram as well as the electronic transitions involved in UC processes are shown in Figure 5.4. The population of ⁴F_{7/2} Er³⁺ proceeds through two successive near-resonant energy transfers (ET) from Yb³⁺ in ²F_{5/2} to Er³⁺, the first exciting Er³⁺ to the intermediate ⁴I_{11/2} state, and then to ⁴F_{7/2}, although UC processes through Er³⁺ ions can also play a role. The lower emitting levels ²H_{11/2} and ⁴S_{3/2} are populated by multiphonon relaxation from ⁴F_{7/2}. Radiative decays from ²H_{11/2} and ⁴S_{3/2} to the ⁴I_{15/2} ground state produce the intense 530 nm and 550 nm green emissions. Non-radiative decays from ²H_{11/2} and ⁴S_{3/2} multiplets populate the ⁴F_{9/2} state through 3-4 lattice phonons. The process is non-efficient, and the radiative ⁴F_{9/2}→⁴I_{15/2} red emission at 660 nm is considerably weaker than green bands. The red emission is not completely vanished because of the presence of defects and high energy phonons on the surface of nanocrystals (such as OH⁻ and CO₃²⁻), that deactivate the ⁴I_{11/2} level, leading electrons to the ⁴I_{13/2} level. Then, after a second ET from Yb³⁺, the Er³⁺ reaches the ⁴F_{9/2} level producing the ⁴F_{9/2}→⁴I_{15/2} red emission.

Figure 5.5 shows the Stokes emission of Yb, Er-doped nanocrystals under 460 nm excitation. Multiple non-radiative transitions populate sequentially the Er³⁺ ⁴F_{7/2}, ²H_{11/2}, ⁴S_{3/2}, ⁴F_{9/2}, and ⁴I_{9/2}, releasing phonons to the lattice, as shown in Figure 5.6, producing the radiative Er³⁺ visible transitions, ²H_{11/2}, ⁴S_{3/2}→⁴I_{15/2} (530-550 nm) and ⁴F_{9/2}→⁴I_{15/2} (660 nm), and also the NIR Er³⁺ ⁴I_{9/2}→⁴I_{15/2} transition at 850 nm, as well as the Yb³⁺ ⁴F_{5/2} → ²F_{7/2} transition at 980 nm. The Yb³⁺ ²F_{5/2}→²F_{7/2} transition is produced after an ET process from the Er³⁺ ⁴I_{9/2} that populates the Yb³⁺ ²F_{5/2} energy level releasing 2-3 phonons.

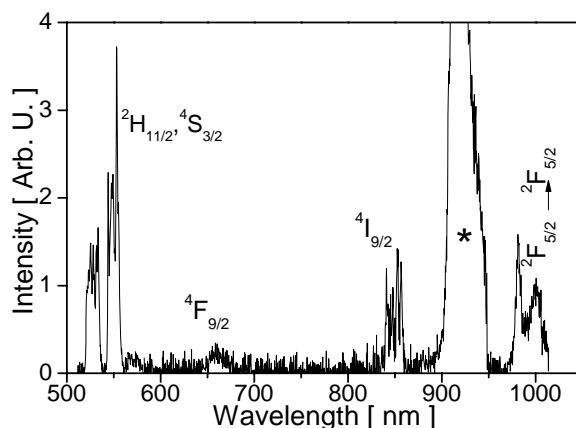


Figure 5.5. RT Stokes emission of 1 % Er, 10 % Yb:KLuW nanocrystals under 460 nm excitation. Er³⁺ transitions to ground state ⁴I_{15/2} are indicated by the excited state. The asterisk indicates the second order diffraction of partially transmitted laser pumping.

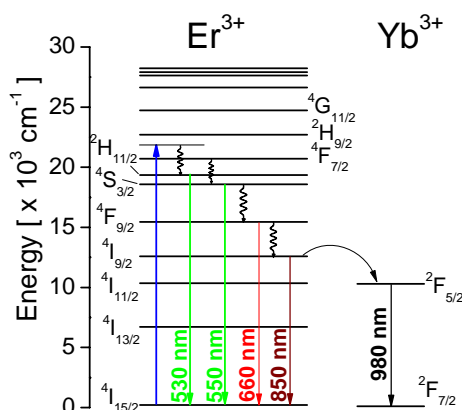


Figure 5.6 RT Stokes emission mechanisms for 1% Er, 10 % Yb:KLuW nanocrystals under 460 nm excitation.

The photoluminescence decay curves at 460 nm excitation are showed in Figure 5.7. The mean experimental decay times were evaluated by the general formula proposed by Inokuti and Hirayama [6]:

$$\tau = \frac{\int t \cdot I(t) dt}{\int I(t) dt} \quad (5.3)$$

Where $I(t)$ represents the luminescence intensity at time t . The background in $I(t)$ was subtracted and the integral range in Eq. (5.3) run over time until a convergence is reached. The convergence time is achieved when the excited energy level is exhausted and no more

luminescence can be detected. Table 5.1 summarizes the measured decay times. The initial fast decay observed after the transitions is produced by non-radiative relaxation of $^4F_{9/2}$ and $^4I_{9/2}$ levels involving surface phonons of OH⁻ and CO₃²⁻ bonds with vibrational energies of 3350 and 1500 cm⁻¹. Slow portion comes from more nearly isolated Er³⁺ ions [7].

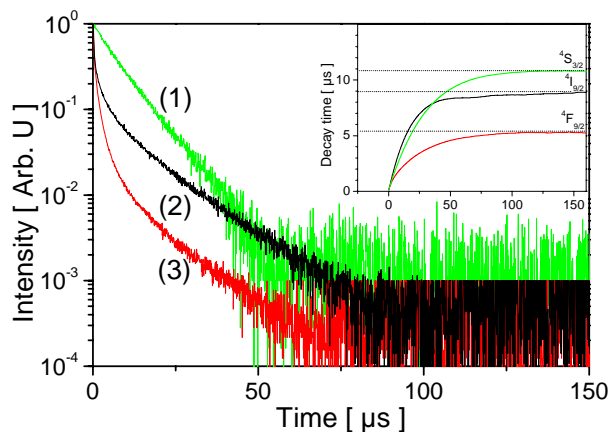


Figure 5.7 Photoluminescence decay of Er³⁺ $^4S_{3/2} \rightarrow ^4I_{15/2}$ (1), $^4I_{9/2} \rightarrow ^4I_{15/2}$ (2) and $^4F_{9/2} \rightarrow ^4I_{15/2}$ (3). The inset shows the convergence of τ value in Eq. 5.3.

Table 5.1. Measured decay lifetimes for 1 % Er³⁺, 10 % Yb³⁺ nanocrystals.

Er ³⁺ emitter state	λ_{EMI} [nm]	τ [± 1 μs]
$^2H_{11/2}, ^4S_{3/2}$	550	9
$^4F_{9/2}$	660	5
$^4I_{9/2}$	800	11

5.2.2 Ho, Yb:KLuW nanocrystals as yellow emitters

Figure 5.8 shows the UC emission spectra for 1 % Ho, 10 % Yb:KLuW nanocrystals after NIR 980 nm excitation. The green emission observed at 540 nm is ascribed to the Ho³⁺ $^5S_2, ^5F_4 \rightarrow ^5I_8$ transition, and the red emission at 650 nm to the Ho³⁺ $^5F_5 \rightarrow ^5I_8$ transition. The integrated intensity ratio I_{GREEN}/I_{RED} was 0.5-0.6 in the 50-250 W/cm² excitation power density range. For both green and red emissions the power dependence of the UC emission intensity was linear, as shown in the inset of Figure 5.8, and the n slopes were $n_G = 1.38 \pm 0.04$ and $n_R = 1.30 \pm 0.4$, respectively. These emissions can be associated to two photon UC processes in the high-power limit where the UC rate of depopulation of the intermediate states is higher producing shortening of n values [8].

The proposed UC mechanism is shown in Figure 5.9. For the green emission, the electronic population of the excited Ho³⁺ $^5S_2, ^5F_4$ energy levels under 980 nm laser excitation is accomplished through two ET steps from $^2F_{5/2}$ level of Yb³⁺. In the first step, Ho³⁺ ions are excited from the ground 5I_8 to 5I_6 level by a phonon-assisted energy transfer process, and

then second ET from Yb³⁺ lead Ho³⁺ from ⁵I₆ to ⁵S₂, ⁵F₄ multiplets. From these ⁵S₂, ⁵F₄ energy levels, radiative transitions to the ground state radiate the green emission. Another non-radiative relaxation (~3000 cm⁻¹) from ⁵S₂, ⁵F₄ energy levels populates the ⁵F₅ multiplet, from which the radiative process ⁵F₅→⁵I₈ transition generates the red emission. The presence adsorbed species on the surface of the KLuW nanocrystals can favor the depopulation of ⁵S₂, ⁵F₄ levels, enhancing the red emission [9].

An optional mechanism also populating ⁵F₅ can be described through a non-radiative relaxation from ⁵I₆ to ⁵I₇ (~3400 cm⁻¹), followed by a second ET process from Yb³⁺ leading Ho³⁺ from ⁵I₇ to the ⁵F₅ state, supporting the red 650 nm emission.

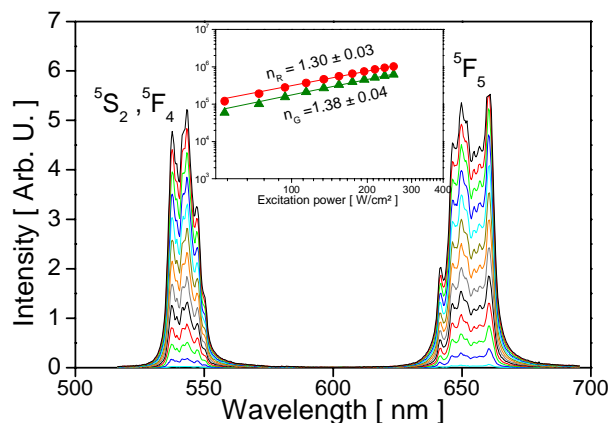


Figure 5.8. Upconversion spectra of 1 % Ho, 10 % Yb:KLuW nanocrystals. Ho³⁺ transitions to ground state ⁵F₈ are indicated by the excited state. Excitation power densities were in the 14-254 W/cm² range, with 20 W/cm² steps. The inset shows the dependence of the intensity with the excitation power and calculated slopes for green and red emissions.

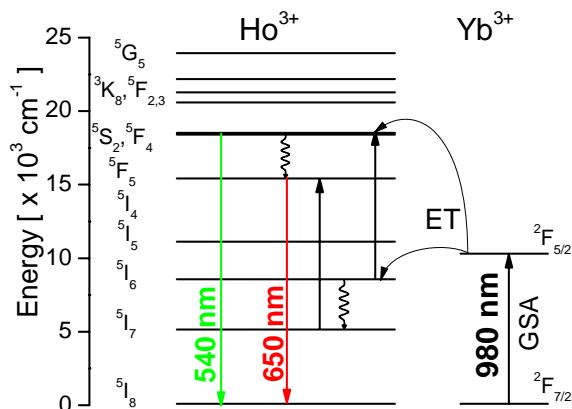


Figure 5.9. Upconversion mechanisms for 1% Ho, 10 % Yb:KLuW nanocrystals.

The observed Stokes emissions and proposed mechanisms are presented in Figure 5.10 and Figure 5.11, respectively. The emission bands at 750 nm and 1200 nm were ascribed to Ho³⁺ ⁵S₂, ⁵F₄→⁵I₇ and ⁵I₆→⁵I₈ transitions, respectively. After 460 nm excitation, the Ho³⁺ ⁵F_{2,3}

multiplet is populated. Then, in a non-radiative process, the electrons decay to ⁵S₂, ⁵F₄ multiplets, from which ⁵S₂, ⁵F₄ → ⁵I₈ and ⁵S₂, ⁵F₄ → ⁵I₇ transitions produce the emissions at 540 nm and 750 nm, respectively.

The wide emission band at 980 nm corresponds mainly to the Yb³⁺ ²F_{5/2} → ²F_{7/2} transition. It is expected that Ho³⁺ ⁵F₅ → ⁵I₇ and ⁵S₂ → ⁵I₆ transitions observed in monoclinic double tungstates at 974 and 1031 nm, respectively [10] are overlapped with the Yb³⁺ ²F_{5/2} → ²F_{7/2} emission. Since the presence of a high intensity Yb³⁺ ²F_{5/2} → ²F_{7/2} and the decrease in the red ⁵F₅ → ⁵I₈ emission intensity (*I_{GREEN}*/*I_{RED}* ~ 5), an efficient cross-relaxation mechanism (⁵F₅, ²F_{7/2}) → (⁵I₇, ²F_{5/2}) is proposed. Finally the 1200 nm emission is produced by the absorption of part of the Yb³⁺ ²F_{5/2} → ²F_{7/2} emission by Ho³⁺ radiated by the ⁵I₆ → ⁵I₈ transition.

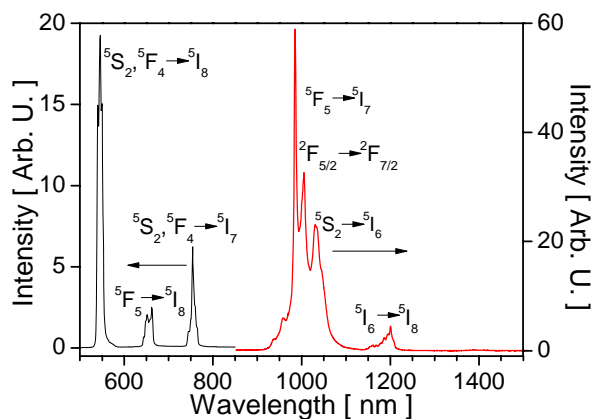


Figure 5.10. RT Stokes emission spectra of 1 % Ho, 10 % Yb:KLuW nanocrystals under 460 nm excitation.

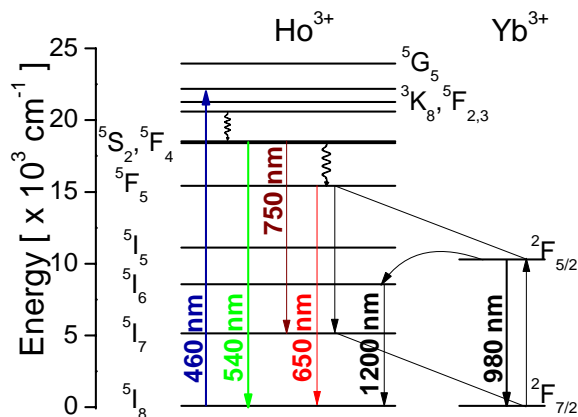


Figure 5.11. Stokes emission mechanisms for 1% Ho, 10 % Yb:KLuW nanocrystals under 460 nm excitation.

Figure 5.12 shows that photoluminescence decays of Ho³⁺ ⁵S₂ and ⁵F₅ levels are non-single exponential, with decay times of 5±1 μs and 7±1 μs, respectively. In 0.5 % Ho 2.5 % Tm:KLuW single crystal the photoluminescence decay of Ho³⁺ ⁵S₂ level is single exponential, with a decay time of ~4 μs [11]. In Ho:KGdW single crystals at low Ho³⁺ doping values decay times are 3.5 μs for ⁵S₂ and ~1 μs for ⁵F₅ [10]. Thus, measured decay times in this work are in agreement with previous data in monoclinic double tungstate single crystals. For these low decay times, the fast and slow components of decay curves in Figure 5.12 show similar time lengths. The fast component of decay, which spread up to first ~30 μs, is associated to the non-radiative relaxation of the Ho³⁺ ions lying on the surface of nanocrystals due to the presence of near high energy phonons. The slow portion associated to radiative relaxation of inner Ho³⁺ ions is expected to be single exponential for low Ho³⁺ concentration, where Ho³⁺ are nearly isolated.

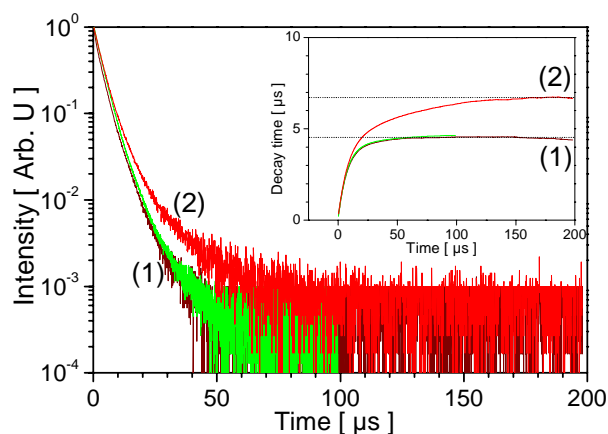


Figure 5.12. Photoluminescence decay of Ho³⁺ ⁵S₂ (1) and ⁵F₅ (2) multiplets. The inset shows the convergence of τ value in Eq. 5.3.

5.2.3 Tm,Yb:KLuW nanocrystals as blue emitters

The dependence with the power density excitation of the UC emission spectra for Yb, Tm-doped (1 % Tm, 10 % Yb:KLuW) nanocrystals after 980 nm pumping is presented in Figure 5.13. Emission bands at 475 nm (blue), 650 nm (red) and 700 nm were ascribed to Tm³⁺ ¹G₄→³H₆, ¹G₄→³F₄, and ³F_{2,3}→³H₆, transitions, respectively. The Tm³⁺ ³H₄→³H₆ emission at 800 nm showed high intensity until saturation of detector, for this reason it was not collected. For the power dependence of blue and red emission, slopes values of $n_B = 1.9 \pm 0.1$ and $n_R = 1.85 \pm 0.06$ were obtained, respectively. Figure 5.13 shows saturation of UC emissions beyond 170 W/cm². The UC is the dominant depletion mechanism of intermediate levels, which leads to the observed decrease of the slopes.

Figure 5.14 shows the proposed UC mechanisms in Yb³⁺ and Tm³⁺-doped samples. For the population of the ¹G₄ multiplet, a series of non-resonant (phonon assisted) ET processes is suggested. In the first step, Tm³⁺ ion is excited from the ground state ³H₆ to the ³F₄ level by

the ET process from the $^2F_{5/2}$ level of Yb³⁺, then a second ET process leads Tm³⁺ to the $^3F_{2,3}$ level, where part of electrons decay to the ground state producing the 700 nm emission and the rest relax non-radiatively to the 3H_4 level. A third ET process leads Tm³⁺ from 3H_4 to the 1G_4 multiplet.

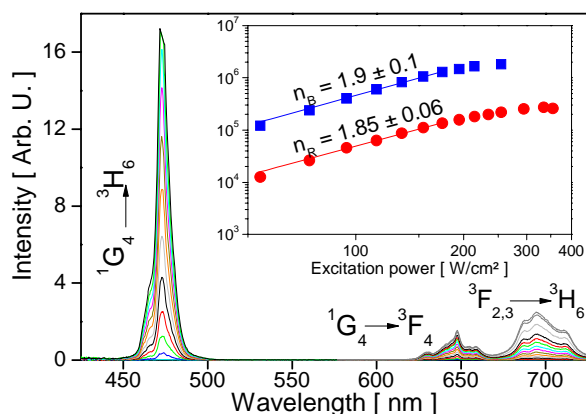


Figure 5.13. Upconversion spectra of 1 % Tm, 10 % Yb:KLuW nanocrystals. Excitation power densities were in the 14-354 W/cm² range, with 20 W/cm² steps. The inset shows the dependence of the intensity with the excitation power and calculated slopes for visible blue and red emissions.

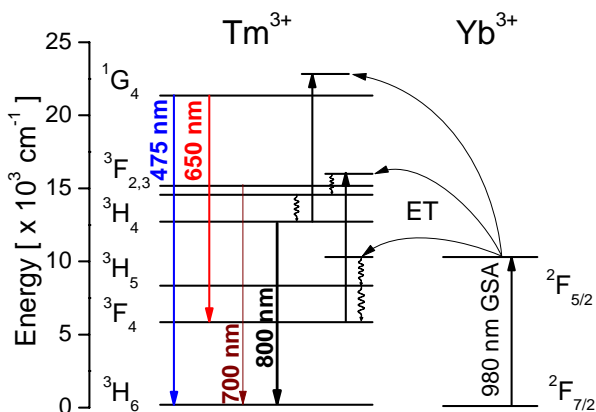


Figure 5.14. Upconversion mechanism in 1 % Tm: 10% Yb:KLuW nanocrystals.

Stokes emission spectra after excitation at 460 and 660 nm are presented in Figure 5.15. Figure 5.16 shows the proposed Stokes emission processes after 460 nm excitation. The wide emission around 800 nm corresponds to the Tm³⁺ $^3H_4 \rightarrow ^3H_6$ transition. The emission bands at 775 nm and 1200 nm are missed under 660 nm excitation. They are assigned to the $^1G_4 \rightarrow ^3H_5$ and $^1G_4 \rightarrow ^3H_4$ transitions, respectively. The 1450 nm emission band was observed in both excitation cases, and it was ascribed to the $^3H_4 \rightarrow ^3F_4$ transition. Part of the energy of Tm³⁺ 3H_4 is transferred to the Yb³⁺ $^2F_{5/2}$ multiplet, that relax radiatively to the ground state producing the broad 900-1100 nm emission [12]. This ET process is phonon-assisted since

energy gaps ${}^3\text{H}_4\text{-}{}^3\text{H}_6 \cong 12500 \text{ cm}^{-1}$ and ${}^2\text{F}_{7/2}\text{-}{}^2\text{F}_{5/2} \cong 10200 \text{ cm}^{-1}$ are slightly different, and the excess of energy (2300 cm^{-1}) is absorbed by 2-3 phonons of the KLuW host.

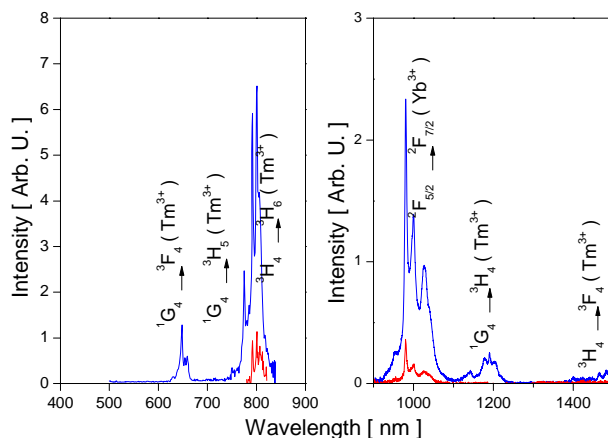


Figure 5.15. RT Stokes emission spectra of 1 % Tm, 10 % Yb:KLuW nanocrystals under 460 (blue line) and 660 nm (red line) excitation.

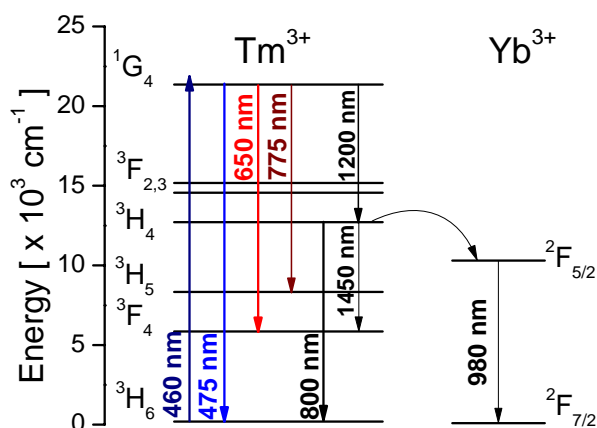


Figure 5.16. Stokes emission mechanisms for 1% Tm, 10 % Yb:KLuW nanocrystals under 460 nm excitation.

The photoluminescence decay after excitation at 460 nm is shown in Figure 5.17. The Tm³⁺ ${}^1\text{G}_4 \rightarrow {}^3\text{H}_6$ and ${}^3\text{H}_4 \rightarrow {}^3\text{H}_6$ transitions show an initial non linear fast decay and almost single exponential decay in the slow portion. Measured decay times for Tm³⁺ ${}^1\text{G}_4$ and ${}^3\text{H}_4$ multiplets were $76 \pm 1 \mu\text{s}$ and $137 \pm 1 \mu\text{s}$, respectively. Decay times of $65 \mu\text{s}$ and $90 \mu\text{s}$ have been reported for ${}^1\text{G}_4$ and ${}^3\text{H}_4$ levels in 1 % Tm: KYbW single crystal [13]. For 1 % Tm, KLuW single crystals, a decay time $160 \mu\text{s}$ for the ${}^3\text{H}_4$ multiplet with a single exponential decay profile is reported [14]. The initial fast component of the decay spreads up to the first $25 \mu\text{s}$, and it is produced by non-radiative relaxation of Tm³⁺ ions by surface phonons of OH⁻ and CO₃²⁻ bonds. The slow component is produced by nearly isolated Tm³⁺. The slight

deviation from exponential behavior decay is probably produced by the non-resonant ET processes from Tm³⁺ (donor) to Yb³⁺ (acceptor), as acceptor concentration increases [7].

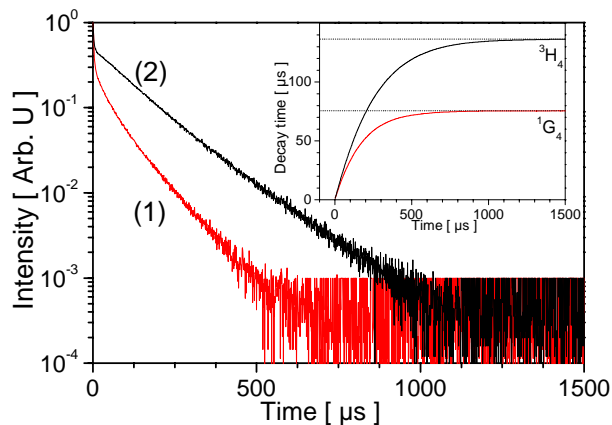


Figure 5.17. RT photoluminescence decay of ¹G₄ (1) and ³H₄ (2) multiplets to the ground state after 460 nm excitation for 1 % Tm, 10 % Yb:KLuW nanocrystals. The inset shows the convergence towards τ in Eq. 5.3.

5.2.4 Upconversion quantum yield

Photoluminescence can occur after a material absorbs light. Consider that an excitation intensity I_0 enters the material and intensity I is transmitted or reflected. The intensity of the radiation emitted by the sample, I_{UC} , must be proportional to the absorbed intensity ($I_0 - I$) [15]:

$$I_{UC} = QY(I_0 - I) \quad (5.4)$$

where QY is called the quantum efficiency. The QY is defined as the ratio between the emitted and absorbed photons, and it can vary from 0 to 1. In this work QY refers in all cases to the UC quantum yield,

$$QY \equiv \frac{\# UC \text{ emitted photons}}{\# NIR \text{ absorbed photons}} \quad (5.5)$$

As the emission intensity is proportional to the number of photons, it possible to write that [16]:

$$QY = \frac{I_{UC}}{(E_{REF} - E_S)} \left(\frac{1}{F_{ATT}} \right) \quad (5.6)$$

Where $E_{REF} - E_S$ is the absorbed intensity by the sample. F_{ATT} is the correction due to the attenuators used to measure the excitation light intensity that typically reach up two magnitude orders with regards to the emission intensity I_{UC} . The fraction of absorbed light by the sample is defined as:

$$\alpha \equiv \frac{(E_{REF} - E_S)}{E_{REF}} \quad (5.7)$$

QY and α , at room temperature, for each emission band for Ln, Yb-doped nanocrystals (Ln = Er, Ho, Tm) are tabulated in Table 5.2, following the technique proposed by Boyer *et al* [16]. The α values are in the range of reproducibility data of 10-90 %, reducing the artifacts [17]. For measuring $E_{REF} - E_S$ is required to correct the instrumental response of the equipment including detector, optical fibers and filters. Next, a reference (undoped KLuW nanocrystals) is exposed to I_0 and the intensity not absorbed by the reference, E_{REF} is measured. Then, the sample (doped with sensitizer Yb³⁺ ions) is exposed to I_0 and the intensity not absorbed by sample, E_S is measured. Finally, the net intensity absorbed by the sample corresponds to the difference $E_{REF} - E_S$.

As the excitation power density increases, QY decreases, most probably due to the operation of the KLuW nanocrystals in the high power limit, which produces the decrease of the slopes in the curves of the dependence of the intensity of the emitted light with the excitation power. One exception is the green emission in Yb, Er-doped nanocrystals with $QY_G \sim 0.2$ %, in the range of 30-150 W/cm². QY_G was around one magnitude order lower than the $QY_G \sim 4$ % reported for polycrystalline 2 % Er, 18 % Yb:NaYF₄ with similar pumping power [18]. For the Tm³⁺ blue emission, a value of $QY_B=0.017$ % was obtained for Yb, Tm-doped nanocrystals with 30 W/cm², in comparison to $QY_B=0.0866$ % reported in polycrystalline 0.25 % Tm, 6 % Yb:Y₂BaZnO₅ with 2.5 W/cm² [19] and $QY_B=0.1$ % for 0.1 % Tm, 12.9 % Yb:Y₂SO₃ with 20 W/cm² [18]. No reports on QY have been found for Ho³⁺ UC emissions using Yb³⁺ as sensitizer.

Table 5.2. Fraction of absorbed light (α) and quantum yield (QY) of UC emissions in 1% Ln, 10 % Yb:KLuW nanocrystals with the excitation power.

Ln ³⁺	I_0 [W·cm ⁻²]	α [%]	QY_B [%]	QY_G [%]	QY_R [%]	QY_{IR} [%]
Er	30	16	-	0.183	0.008	-
	50	22	-	0.241	0.010	-
	100	29	-	0.210	0.005	-
	150	25	-	0.250	0.005	-
Tm	30	32	0.017	-	0.003	0.030
	50	34	0.010	-	0.003	0.014
	100	42	0.003	-	0.003	0.005
	150	36	0.002	-	0.005	0.007
Ho	30	25	-	0.030	0.067	-
	50	22	-	0.042	0.089	-
	100	29	-	0.006	0.020	-
	150	26	-	0.004	0.013	-

5.2.5 Chromaticity properties of upconversion emission

The emitting color has been quantified in terms of the CIE (Comission Internationale d’Eclairage) 1931 color diagram [1,20]. The dependence of CIE coordinates for different power density values for 1 % Ln, 10 % Yb:KLuW nanocrystals (Ln = Er, Ho, Tm) is shown in Figure 5.18 and in Table 5.3. The UC emitted color is visible by the naked eye as shown in the inset pictures in Figure 5.18. The restricted excitation power density of Yb, Er-doped nanocrystals in Table 5.3 was a consequence of the observed saturation of the CCD detector under the fixed setup, for the Er³⁺ ²H_{11/2}, ⁴S_{3/2} → ⁴I_{15/2} green emission.

Chromaticity coordinates are near the boundary, which means high color purity. In the case of Er³⁺ and Ho³⁺ doped nanocrystals, as the excitation power density increases, the chromaticity coordinates are displaced in large steps to a shorter dominant wavelength, showing a trend towards a limit in coordinate values. In the case of Yb, Tm-doped nanocrystals the displacement of chromaticity coordinates is slight because emission saturation is reached, and the profile of the UC spectrum tends to be constant.

Table 5.3. Chromaticity properties of 1 % Ln, 10 % Yb:KLuW (Ln = Er, Ho, Tm) nanocrystals.

Active Ion Ln ³⁺	Excitation power density [W/cm ²]	Dominant wavelength [nm]	Color purity [%]
Er	15 – 100	547 - 540	96 – 97
Ho	50 – 250	574 - 563	96 – 97
Tm	50 – 250	473 - 472	84 – 87

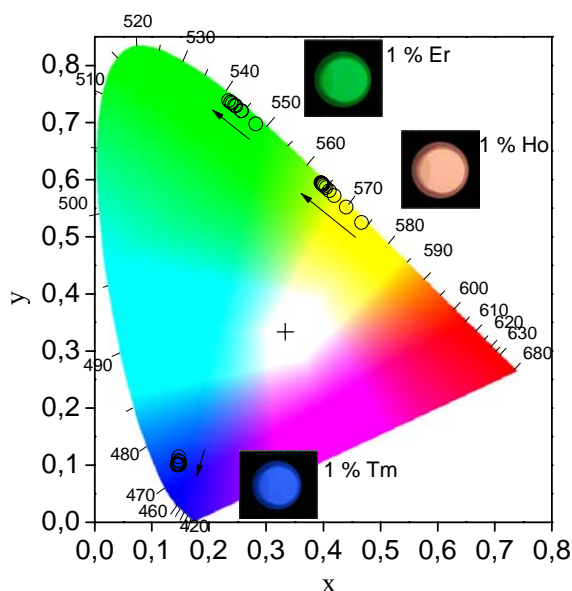


Figure 5.18. Displacement of chromaticity coordinates of UC emission in 1 % Ln, 10 % Yb:KLuW (Ln= Er, Ho, Tm) nanocrystals for excitation power densities in the range 10-250 W/cm², in the indicated arrow direction. Images of the light emissions are shown for Er-, Ho- and Tm-doped samples

5.3 Physical mixture of Ho:Yb:KLuW and Tm:Yb:KLuW nanoparticles for white light generation

In the previous section we have demonstrated the possibility of Ln,Yb-doped KLuW nanocrystals as UC green (Ln=Er) and blue (Ln=Tm) phosphor nanoparticles. For Yb, Ho-doped nanocrystals (1 % Ho, 1 % Yb:KLuW), an orange color source was obtained, and for obtaining a green or red emission, filtering of one emission is required. For the design of a white light emitter it is possible to forego the use of filters since color sources as purple, yellow or orange can be used for obtaining the white point, and it is not necessary to use monochromatic sources.

The tailoring of a white light emitter from a physical mixture with different UC powders was first reported by Milliez *et al.* [21]. To calculate the proportion of each powder to be mixed, they used a trial-error method for scaling and adding the emission spectra of each emitter collected at specific excitation conditions. It is not a straightforward way to tailor a UC white light emitter, because the intensity profile and QY are altered with the excitation irradiance depending of the active ion and the host. On the other hand, when active ions are embedded together in the same host, the combined intensity profile can strongly depart from corresponding individual spectra.

Despite above statements, it is interesting to develop a first model for the addition of the intensity distribution curves to model the different color sources and calculate the optimal

proportion to obtain the light with chromaticity near to the white point. We have followed a similar procedure as used for deduction of *RGB* from *XYZ* transformation [22].

5.3.1 Proposed model

We can suppose two kinds of luminescent powders, one activated with ion *A* and the other with *B*. The emission profile with power density *p* corresponds to $I_A(p, \lambda)$ and $I_B(p, \lambda)$, respectively. If these powders are mixed intimately in equal amounts, and we suppose that energy interactions are low and they can be neglected, the total UC emission profile can be written as proportional to the sum of the emission profiles of $I_A(p, \lambda)$ and $I_B(p, \lambda)$:

$$\Phi(p, \lambda) = C(I_A(p, \lambda) + I_B(p, \lambda)) \quad (5.9)$$

where $\Phi(p, \lambda)$ is the emission produced by the physical mixture. As no absolute intensities are measured, we introduce a normalization constant *C* relative to the intensity of $\Phi(p, \lambda)$. Now, we suppose that, if powders are mixed in different relative molar amounts, indicated by a_A and a_B coefficients, the emission intensities produced for each powder will be modified in the same proportion,:

$$\Phi(p, \lambda) = C(a_A I_A(p, \lambda) + a_B I_B(p, \lambda)) \quad (5.10)$$

We will extend our model to a mixture of several luminescent powders, each one activated by a *j* ion and with a relative molar coefficient a_j in the mixture. The *C* constant can be included as a part of the relative a_j molar proportions. Then, the resulting emission spectrum $\Phi(p, \lambda)$ can be written as a linear combination:

$$\Phi(p, \lambda) = \sum_j a_j I_j(p, \lambda), \quad (5.11)$$

The tristimulus functions for $\Phi(p, \lambda)$ can be written:

$$X_i(p) = \int \Phi(p, \lambda) \bar{x}_i(\lambda) d\lambda \quad (5.12)$$

Where index $i = 1, 2, 3$ corresponds to *X*, *Y* and *Z* in the original CIE 1931 notation respectively [23], \bar{x}_i is the color matching function corresponding to the tristimulus value X_i . Substituting Eq. 5.11 in Eq. 5.12:

$$X_i(p) = \sum_j a_j \bar{X}_{ij}(p) \quad (5.13)$$

Where $\overline{X_{ij}}(p)$ is the tristimulus function for the i coordinate corresponding to the luminescent powder with the active ion j . This expression shows that the tristimulus function $X_i(p)$ of the resulting luminescent mixture is linear combination of the tristimulus $X_{ij}(p)$ functions of each luminescent powder. The chromaticity coordinates are defined as [23]:

$$x_i(p) \equiv \frac{X_i(p)}{\sum_i X_i(p)} \quad (5.14)$$

Combining Eq 5.13 and 5.14:

$$x_i(p) = \frac{\sum_j a_j X_{ij}(p)}{\sum_{i,j} a_j X_{ij}(p)} \quad (5.15)$$

This equation express the chromaticity coordinates for a mixture of luminescent powders, considering that energy interactions between different powders are low and they can be neglected. If the power dependence of the emission spectra of each phosphor is characterized individually, it is possible to calculate the power dependence of chromaticity coordinates $x_i(p)$ for the mixture of luminescent powders. For the produced 1 % Ln, 10 % Yb:KLuW (Ln = Er, Ho, Tm) nanocrystals, we have assigned the subindex of the active ions Er³⁺, Ho³⁺ and Tm³⁺, in the following way:

$$x(p) = \frac{a_{Er} X_{Er} + a_{Tm} X_{Tm} + a_{Ho} X_{Ho}}{a_{Er} (X_{Er} + Y_{Er} + Z_{Er}) + a_{Tm} (X_{Tm} + Y_{Tm} + Z_{Tm}) + a_{Ho} (X_{Ho} + Y_{Ho} + Z_{Ho})} \quad (5.16)$$

$$y(p) = \frac{a_{Er} Y_{Er} + a_{Tm} Y_{Tm} + a_{Ho} Y_{Ho}}{a_{Er} (X_{Er} + Y_{Er} + Z_{Er}) + a_{Tm} (X_{Tm} + Y_{Tm} + Z_{Tm}) + a_{Ho} (X_{Ho} + Y_{Ho} + Z_{Ho})} \quad (5.17)$$

where a_{Ln} corresponds to the relative molar of each kind of Ln, Yb-doped nanocrystals in the mixture. The X_{ij} functions in Figure 5.19 were calculated from emission spectra of corresponding Ln, Yb-doped nanocrystals of Figure 5.3, Figure 5.8 and Figure 5.13. Next, we impose the condition of ideal illuminant E [1] (equi-energy spectrum): $(x(p), y(p)) = (1/3, 1/3)$. Then, Eq. 5.11 and 5.12 were solved to find the relative molar coefficients a_j .

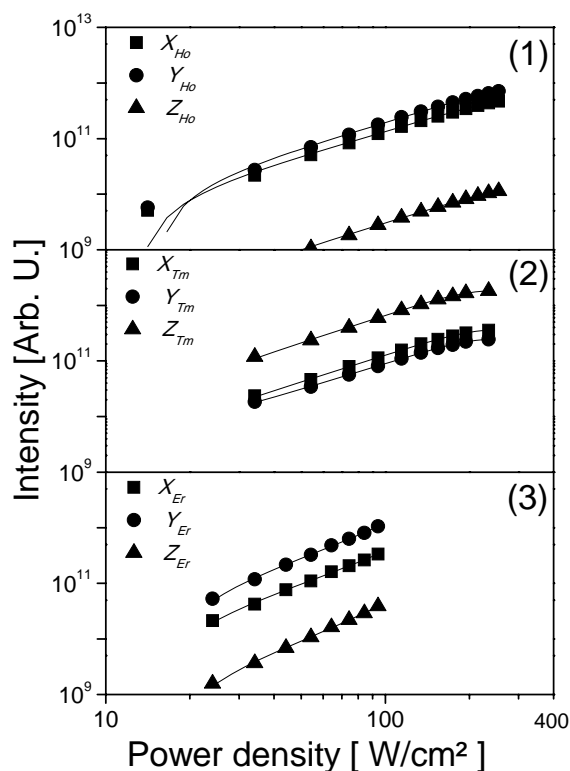


Figure 5.19. Tristimulus functions as a function of excitation power density of 1 % Ln, 10 % Yb:KLuW nanocrystals, Ln = Ho (1), Tm (2) and Er (3).

For a two-powder mixture including the indicated composition of Yb, Er-doped nanocrystals, no real solutions for a_{Er} were found, and the white light balance is not reached. This result can be explained because for mixtures with the prepared Yb, Ho-doped nanocrystals there is no a blue color source, and possible combinations lay on a line from yellow to green region. Alternatively, for mixtures with Yb, Tm-doped nanocrystals, the red-green-blue colors are present, however, the red color source is minimal and the possible color coordinates of such mixtures lay on a triangle from green to blue region, as shown in Figure 5.20.

In the case of a two-powder mixture including as the main red source the above indicated composition of Yb, Ho-doped nanocrystals, one approximated solution was found by mixing with the prepared composition of Tm- and Yb-doped nanocrystals in the ratio $a_{Tm} : a_{Ho} = 1 : 4$, as shown in Figure 5.21. In the next section, we will compare this result with a physical mixture of Yb, Tm and Ho-codoped KLuW nanocrystals under NIR radiation.

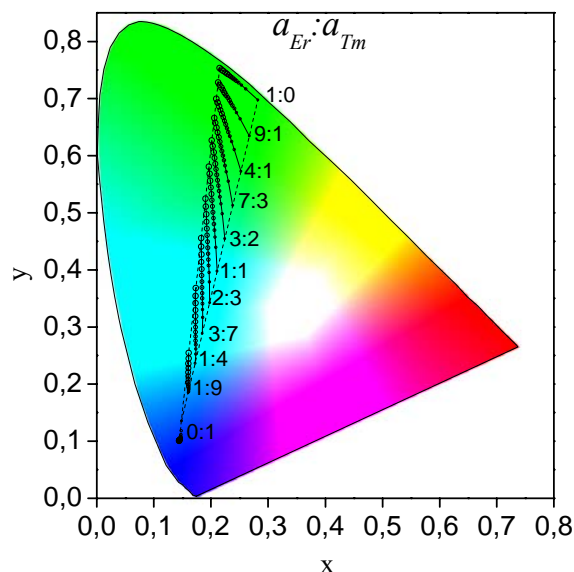


Figure 5.20. Simulated chromaticity path for relative molars of each 1 % Ln, 10 % Yb:KLuW (Ln = Er, Tm) nanocrystalline sample in the mixture. Circle diameters are proportional to the excitation power increases in the 34-94 W/cm².

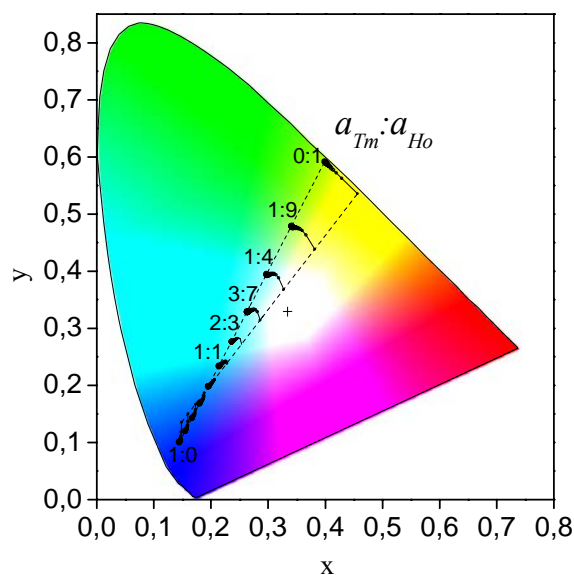


Figure 5.21. Simulated chromaticity path for different relative molars of each 1 % Ln, 10 % Yb:KLuW (Ln = Ho, Tm) nanocrystalline sample in the mixture. Circle diameters are proportional to the excitation power increases in the 34-254 W/cm².

5.3.2 Upconversion emission

The power dependence of the UC emission of the physical mixture containing both 1 % Ln, 10 % Yb:KLuW (Ln = Ho, Tm) nanocrystals in the relative molar $a_{Tm} : a_{Ho} = 1 : 4$, and the assignation of emission bands are presented in Figure 5.22. Calculated values for slopes in the double logarithmic plot of the UC emission intensity versus the excitation power density (inset of Figure 5.22) are higher than those obtained for individual Yb, Ho-doped and Yb, Tm-doped KLuW nanocrystals. The slopes of the red ($n_R = 1.7 \pm 0.2$) and green emissions ($n_G = 2.2 \pm 0.3$) can be associated to a two-photon UC process, and the blue emission ($n_B = 2.7 \pm 0.4$) to a three-photon process.

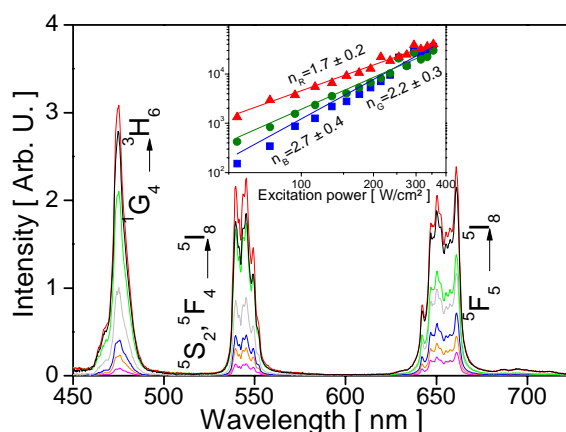


Figure 5.22. Upconversion spectra of the mixture of 1 % Ho, 10 % Yb: KLuW and 1 % Tm, 10 % Yb:KLuW nanocrystals, with relative molar of $a_{Tm} : a_{Ho} = 1 : 4$. Power density in W/cm^2 corresponds to 94 (magenta), 134 (orange), 174 (blue), 234 (gray), 255 (green), 297 (red) and 335 (black).

In the mixture of Yb, Ln-doped nanocrystals, a reduction of the total Ln to Yb ratio is realized, and therefore a proportional quenching of the UC emission could be expected. The excitation is produced through Yb³⁺ ions. Individual samples of nanocrystals have the same 1 % Yb³⁺ content, in consequence, the mixture has 1 % Yb³⁺ content. Before mixture the total Tm-to-Yb (Ho-to-Yb) ratio is 1/10 (1/10). After a mixture with the relative molar $a_{Tm} : a_{Ho} = 1 : 4$, it changes to 0.2/10 (0.8/10), so we expect a reduction in intensity of 80 % (20 %) in comparison with the corresponding emissions in the Ln, Yb:KLuW samples. Figure 5.23 shows the UC emission spectra for mixture at low excitation power. From the integrated emission intensities listed in Table 5.4, we found for 30 W/cm^2 (100 W/cm^2) a reduction of 61 % (68 %) of intensity for the blue emission, shorter than the expected 80 %. We obtain 30 % (33 %) for green emission and 35 % (34 %) for the red emission, larger than the expected 20 %, and independent of the excitation power in the 30-100 W/cm^2 range.

As we observe in the inset images in Figure 5.23, E_S increases after mixture, i.e. the mixture of nanocrystals absorb less NIR radiation. We propose that this effect is produced by an

increment of the scattering of the NIR radiation by surface defects created after grinding of nanocrystalline powders. For the larger quenching of the Tm³⁺ ¹G₄→³H₆ blue emission, we propose a self-absorption process of this radiation through the Ho³⁺ ⁵F_{2,3} multiplet. The temperature can play an important role by modifying the UC efficiency of each emission. Here we can say that interactions between Yb, Ho-doped and Yb, Tm-doped nanocrystals can not be discarded. The UC process is nonlinear in nature and tailoring of a UC white light emitter by mixture of powders does not follow a simple addition of the spectra of each powder, that is, in the mixture different UC emission properties can be expected.

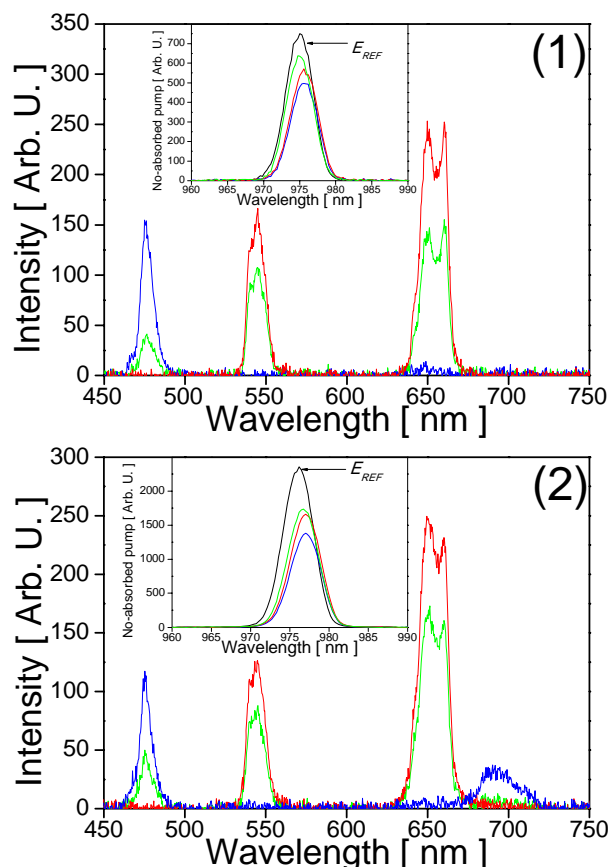


Figure 5.23. Upconversion spectra of 1 % Ln, 10 % Yb:KLuW nanocrystals (Ln = Ho, Tm): $a_{Tm}:a_{Ho}=1:0$ (blue line), $a_{Tm}:a_{Ho}=0:1$ (red line), $a_{Tm}:a_{Ho}=1:4$ (green line). Excitation source was a 975 nm InGaAs diode laser operating at 30 W/cm² (1) and 100 W/cm² (2). The inset shows the 975 nm non-absorbed pump excitation E_S for the corresponding samples, and for undoped KLuW nanocrystalline powder E_{REF} (black line).

Table 5.4. Red, green and blue integrated intensities of UC spectra in Figure 5.23.

I_0 [W/cm ²]	$a_{Tm}:a_{Ho}$	I_R	I_G	I_B
		[Arb. U.]		
30	1:0	-	-	1089
	0:1	5282	1688	-
	1:4	3436	1186	420
100	1:0	-	-	1543
	0:1	4574	2084	-
	1:4	3057	1324	404

5.3.3 Upconversion quantum yield

We compare the fraction of absorbed light (α) and QY before and after mixture in Table 5.5 and Table 5.6, respectively. We have calculated the expected value for the mixture $\alpha_{1:4}$ was computed using a weighted average of the proportions of the individual components in the mixture $a_{Tm}:a_{Ho}$

$$\alpha_{1:4} = (1/5)\alpha_{1:0} + (4/5)\alpha_{0:1} \quad (5.18)$$

The calculated $\alpha_{1:4}$ values are presented in Table 5.5. Experimental $\alpha_{1:4}$ values are reduced from 26 to 32 % respect calculated ones, as excitation power increases from 50 to 150 W/cm². As proposed before, an increment of the scattering of the NIR radiation by surface defects created after grinding of nanocrystalline powders can probably reduce the fraction of absorbed light.

QY values at 30 W/cm² in Table 5.6 correspond to $\alpha = 11$ just in the reproducibility limit for low absorption of the excitation [17], so we can discard this result from analysis. QY_B and QY_{IR} are similar at 50-150 W/cm² excitation power. QY_G was reduced around 40 % at 50 W/cm² and become similar for higher excitation power. Finally QY_R was reduced 34-38 % at 50-150 W/cm² excitation power.

Table 5.5. Power dependence of the fraction of absorbed light (α) in mixture of 1 % Tm, 10% Yb KLuW and 1 % Ho, 10 % Yb KLuW nanocrystals with $a_{Tm}:a_{Ho}$ molar ratio.

I_0 [W·cm ⁻²]	α [%]			
	1:0	0:1	1:4 calculated	1:4 experimental
30	32	25	14	11
50	34	22	24	18
100	42	29	32	24
150	36	26	28	19

Table 5.6. Quantum yield (QY) of UC emission in mixture of 1 % Tm, 10% Yb KLuW and 1 % Ho, 10 % Yb KLuW nanocrystals with $a_{Tm}:a_{Ho}$ molar ratio.

I_0 [W·cm ⁻²]	QY_B		QY_G		QY_R		QY_{IR}	
	1:0	1:4	0:1	1:4	0:1	1:4	1:0	1:4
30	0.017	0.013	0.030	0.042	0.067	0.098	0.031	0.030
50	0.010	0.009	0.042	0.024	0.089	0.058	0.014	0.014
100	0.003	0.002	0.006	0.005	0.020	0.015	0.004	0.005
150	0.002	0.001	0.004	0.004	0.013	0.008	0.002	0.007

5.3.4 Chromaticity

The chromaticity coordinates for the mixture of Yb, Ho-doped and Yb, Tm-doped nanocrystals start moving across the upper part of the white region in the chromaticity diagram in Figure 5.25, from the yellow to the blue region, as the power density increases in the 94-354 W/cm² range. Simulated data only coincide in following the direction path traced by experimental chromaticity coordinates. In the 94-354 W/cm² power density range, deviations of the simulated chromaticity coordinates correspond to a large contribution of the Tm³⁺ ¹G₄→³H₆ blue emission at low power excitation and the saturation of this emission at high power excitation. These phenomena are not observed in the UC emission spectra of the nanocrystals mixture, indicating that there is an energy interaction between Yb, Ho- and Yb, Tm-doped nanocrystals for the UC process and the proposed model can not explain these results.

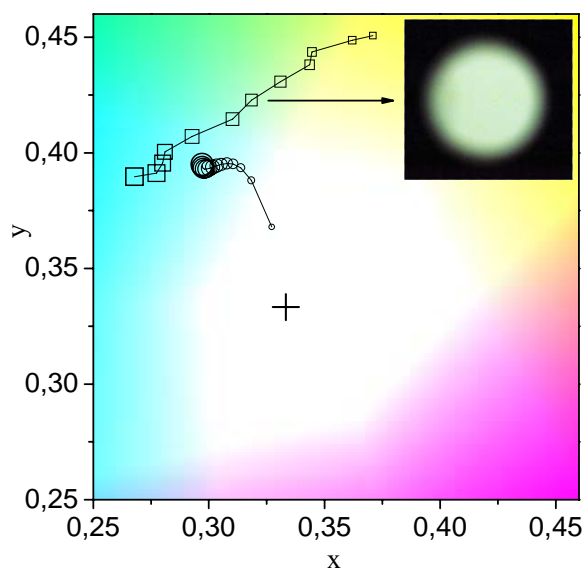


Figure 5.24. Chromaticity coordinates for the mixture of 1 % Ho, 10 % Yb: KLuW and 1 % Tm, 10 % Yb: KLuW nanocrystals, with relative molar $a_{Tm}:a_{Ho}=1:4$. The symbol size is proportional to excitation power density, from 94 to 354 W/cm². Simulated data (circles), experimental data (squares).

5.3.5 Stokes emission

It was interesting to check the proposed model for the addition of the intensity distribution of Stokes emissions. Comparison of the Stokes emission spectra of the mixed sample with Yb, Ho-doped and Yb,Tm-doped nanocrystals under 460 nm excitation, and assignments of transitions are presented in Figure 5.25. Ho³⁺ ⁵S₂,⁵F₄→⁵I₈ ⁵F₅→⁵I₈ ⁵S₂,⁵F₄→⁵I₇ are almost unchanged in the mixture with regards to individual nanocrystals. The Tm³⁺ ¹G₄→³F₄

appears overlapped to the red Ho³⁺ ⁵F₅→⁵I₈ emission. The observed intensity for the Tm³⁺ ³H₄→³H₆ transition in the mixed sample corresponds to the 20 % of the intensity shown in the spectrum of Yb, Tm-doped nanocrystals. This observed intensity reduction agrees with the proposed model, since the relative content of Tm in the mixed sample with $a_{Tm}:a_{Ho}=1:4$ corresponds to $a_{Tm}/(a_{Tm}+a_{Ho})=0.20$.

The proposed model fits well in the case of Stokes emission, probably because 460 nm excitation can reach more nanocrystals with less dispersion than NIR radiation for UC emission. Excitation radiation can be absorbed for more Tm³⁺ ¹G₄ and Ho³⁺ ⁵F_{2,3} multiplets in only one step, instead of the UC process, that requires multi-step energy transfer processes from nearby Yb³⁺ ions.

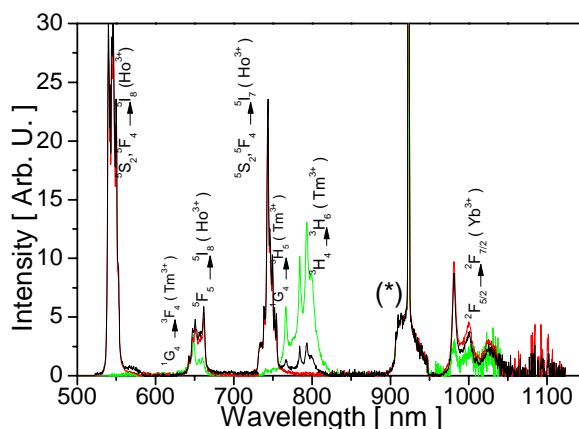


Figure 5.25. Room temperature Stokes emission of doped KLuW nanocrystals under 460 nm excitation. $a_{Tm}:a_{Ho}=1:0$ (dot line), $a_{Tm}:a_{Ho}=0:1$ (dash line), $a_{Tm}:a_{Ho}=1:4$ (solid line). The asterisk indicates the second order diffraction of the partially transmitted laser pumping.

5.4 Effect of Ho³⁺ in Tm:Yb:KLuW nanocrystals

5.4.1 Upconversion emission and quantum yield

Figure 5.26 shows UC spectra of 1 % Tm, 1 % Yb:KLuW nanocrystals doped with 0.5 and 2 % of Ho³⁺, with emissions labeled in Figure 5.26 (1). The intensity of UC bands is enhanced when Ho³⁺ content is increased in the studied range. Insets of Figure 5.26 show the power dependence of the UC intensity. As Ho³⁺ content increases from 0.5 to 2 %, n_R slope is almost constant, whereas n_G and n_B slopes show a slight increment. Table 5.7 list the QY_s , which are around two magnitude orders lower than for 1 % Ln, 10 % Yb:KLuW (Ln = Ho or Tm) nanocrystals. For 0.5 % Ho doped nanocrystals QY_s are below the limit of detection of 0.0001 %.

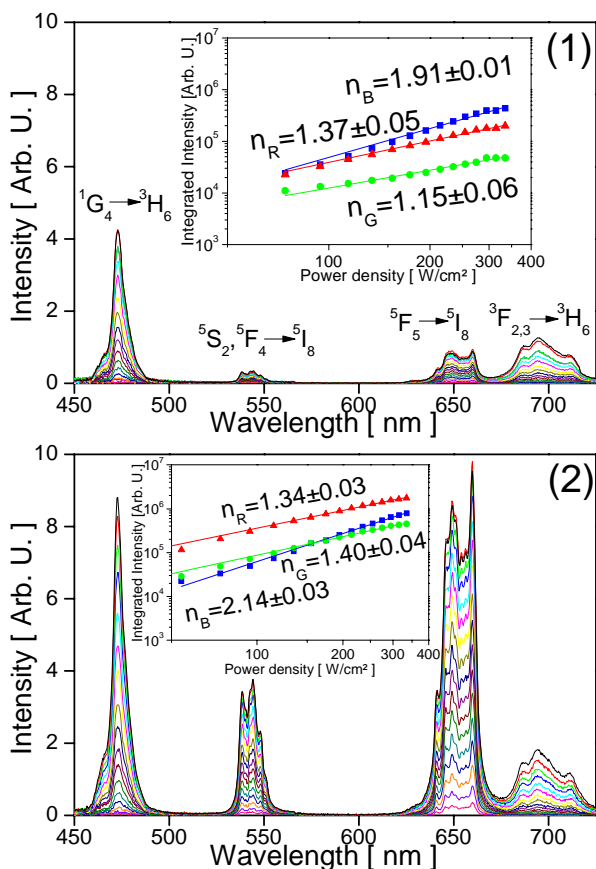


Figure 5.26. Evolution with the excitation power density (30-350 W/cm²) of the upconversion spectra for 1 % Tm, 1 % Yb:KLuW nanocrystals with 0.5 % Ho (1) and 2 % Ho (2)

Table 5.7. Fraction of absorbed light (α) and quantum yield (QY) of upconverted emissions in Ho³⁺ doped 1 % Tm, 1 % Yb:KLuW nanocrystals with the excitation power

Ho ³⁺ [%]	I ₀ [W·cm ⁻²]	α [%]	QY _B [%]	QY _G [%]	QY _R [%]	QY _{IR} [%]
0.5	30	45	-	-	-	-
	50	23	-	-	-	-
	100	38	-	-	-	-
	150	39	-	-	-	-
2.0	30	21	-	0.0001	0.0007	0.0003
	50	8	-	0.0006	0.0025	0.0014
	100	15	0.001	0.0006	0.0023	0.0011
	150	34	-	-	-	-

5.4.2 Chromaticity

The dependence of chromaticity coordinates with the excitation power density is shown in Figure 5.27. For 0.5 % Ho doped nanocrystals, cyan region is reached below 100 W/cm², however chromaticity coordinates shift to the blue region as power density increases and Tm³⁺ blue ¹G₄→³H₆ emission intensity increases. An optimal white light emission was obtained for 2 % Ho doped nanocrystals, where chromaticity coordinates lay always through the white region for 50-350 W/cm² power density, offering a suitable range for tuning the white light emission. These nanocrystals show an easy tendency to the (0.333, 0.333) point associated to the ideal illuminant E [1].

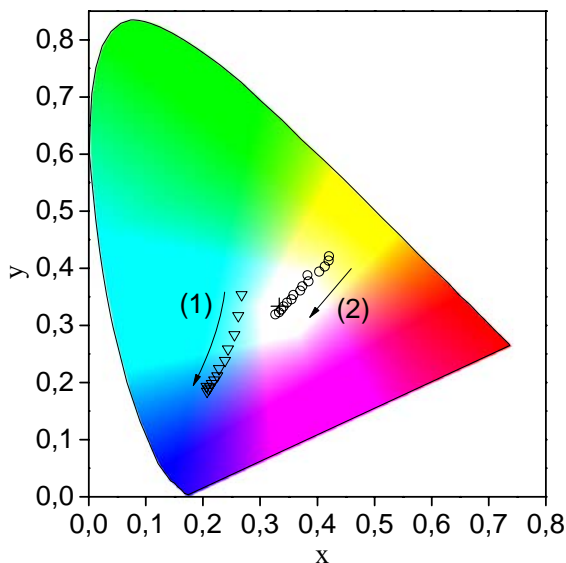


Figure 5.27. Chromaticity coordinates path for excitation power densities 50-350 W/cm² for 1 % Tm, 1 % Yb: KLuW nanocrystals doped with 0.5 % Ho (1) and 2 % Ho. Excitation power density increases in the arrow direction.

5.4.3 Photoluminescence decay after 460 nm excitation

Photoluminescence decay curves in Figure 5.28 show non-single exponential behavior for Ho³⁺ ⁵S₂,⁵F₄ → ⁵I₈ and ⁵F₅ → ⁵I₈ and Tm³⁺ ³H₄ → ³H₆ transitions. Decay times of Ho³⁺ (see Table 5.8) emissions are similar to those observed for 1 % Ho, 10 % Yb:KLuW nanocrystals (5 ± 1 μs for Ho³⁺ ⁵S₂,⁵F₄ → ⁵I₈, and 7 ± 1 μs for Ho³⁺ ⁵F₅ → ⁵I₈). Decay times of Tm³⁺ ³H₄ → ³H₆ transition were reduced as Ho³⁺ content increases.

The slight increment of the decay time in Ho³⁺ ⁵S₂,⁵F₄ → ⁵I₈ can be related with a trend to optimal Ho³⁺ content in the 1% Tm, 1 % Yb:KLuW system. This behavior has been observed in other multidoped systems as Li:Tm:Ho:Yb:GdVO₄ [24]. No modification was observed for the decay time in Ho³⁺ ⁵F₅ → ⁵I₈, however this value is shorter than the one obtained for 1 % Ho, 10 % Yb:KLuW nanocrystals (7 ± 1 μs). As Ho³⁺ content increased,

the decay times of the $\text{Tm}^{3+} \ ^3\text{H}_4 \rightarrow \ ^3\text{H}_6$ transition is reduced, and they are shorter than that obtained for 1 % Tm, 10 % Yb:KLuW nanocrystals ($137 \pm 1 \ \mu\text{s}$). To explain the shortening of the decay time from $\text{Tm}^{3+} \ ^3\text{H}_4$, we propose the presence of a phonon-assisted ET from Tm^{3+} to Ho^{3+} ion. In next section, an ET mechanism will be proposed after the analysis of the effect of Tm^{3+} doping in Ho:Yb:KLuW nanocrystals.

Table 5.8. Photoluminescence decay times of Ho^{3+} doped 1 % Tm, 1 % Yb: KLuW nanocrystals after 460 nm excitation.

Ho^{3+}	$^5\text{S}_2, ^5\text{F}_4$	$^5\text{F}_5$	$^3\text{H}_4$
[%]	[μs]		
0.5	6 ± 1	5 ± 1	108 ± 9
2.0	8 ± 1	5 ± 1	97 ± 1

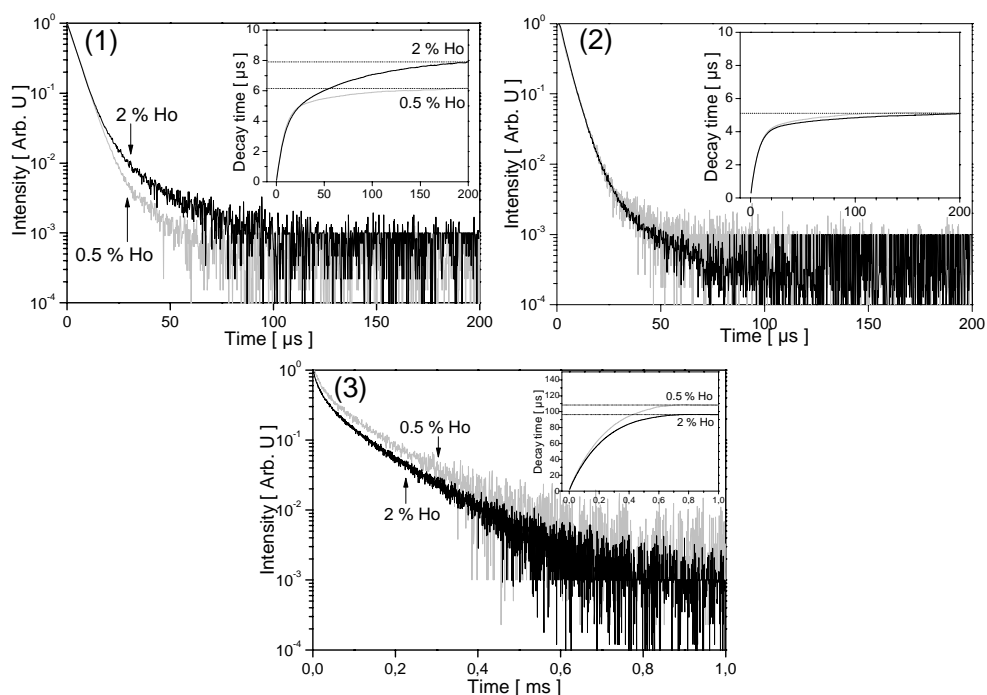


Figure 5.28. RT photoluminescence decay of $^5\text{S}_2, ^5\text{F}_4 \rightarrow ^5\text{I}_8$ (1), $^5\text{F}_5 \rightarrow ^5\text{I}_8$ (2) and $^3\text{H}_4 \rightarrow ^3\text{H}_6$ (3) transitions. The inset shows in each case the convergence of the τ value.

5.5 Effect of Tm³⁺ in Ho:Yb:KLuW nanocrystals

5.5.1 Upconversion emission and quantum yield

UC spectra of Tm³⁺ doped 2 % Ho, 1 % Yb:KLuW nanocrystals and plots of the dependence of the intensity of emissions with the excitation power are presented in Figure 5.29. The intensity of emission bands experiences an increase for Tm³⁺ contents from 0.25 % to 0.75 %, but a quenching of these intensities is observed for 1 % Tm³⁺, and in fact for 0.75 % Tm³⁺ content the highest intensity and n slopes were reached. For 0.25 and 0.75 % the slopes follow the $I_{UC} \propto I_0^n$ relationship, where n is the number of absorbed photons involved in the UC process [25].

In a similar way as reported by Lima *et al* [26], we propose a mechanism of relaxation of one Tm³⁺ ion in the ³H₄ multiplet that leads two Tm³⁺ ions in the ³F₄ state via cross relaxation (³H₄, ³H₆) → (³F₄, ³F₄), followed by a ET from these Tm³⁺ ions to the ⁵I₇ state of Ho³⁺ ions. As Tm³⁺ increases, the mechanism gets more efficient. This mechanism can explain the enhancement of UC emissions after 980 nm excitation, until an optimal ET process is reached for 0.75 % Tm doped nanocrystals. For higher content, cross-relaxation and ET compete with the Tm³⁺ concentration quenching. Figure 5.30 resumes the UC mechanisms from Yb³⁺ to Tm³⁺ and Ho³⁺ ions, and the cross relaxation in Tm³⁺ ions and ET transfer from Tm³⁺ ³F₄ to Ho³⁺ ⁵I₇. The UC processes in Ho³⁺ and Tm³⁺ follow similar descriptions to those explained previously in this chapter for 1% Ho, 10% Yb:KLuW and 1 % Tm, 10% Yb:KLuW nanocrystals, respectively.

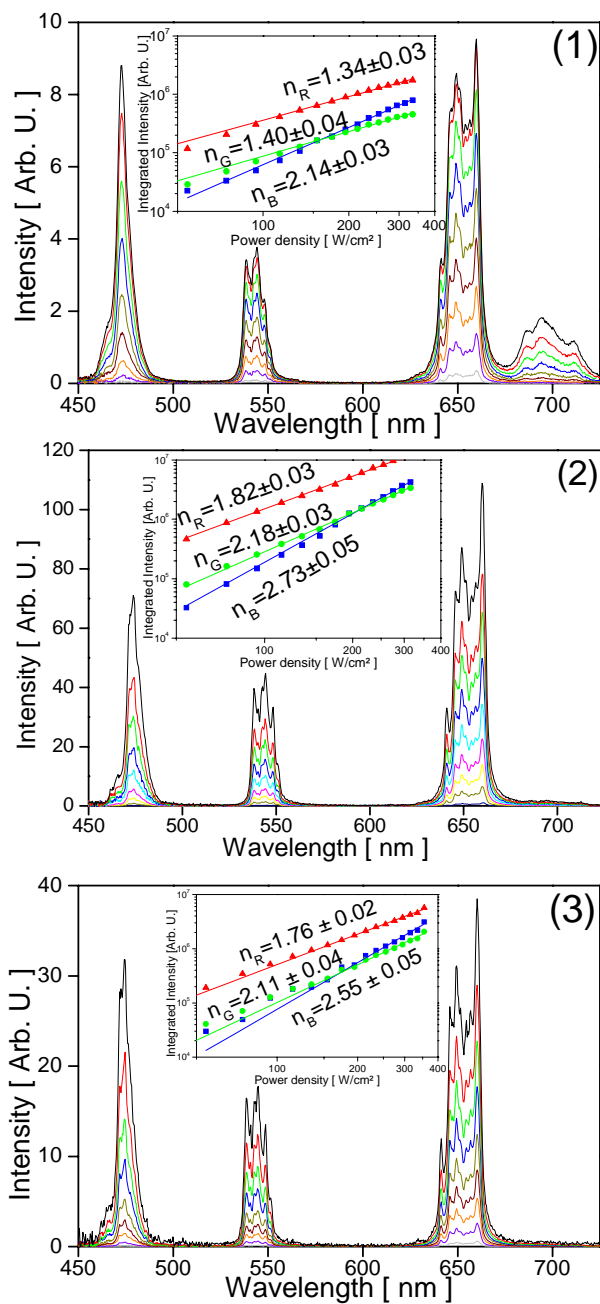


Figure 5.29. Upconversion spectra of 2 % Ho, 1 % Yb: KLuW nanocrystals doped with 1 % (1), 0.75 % (2) and 0.25 % (3) Tm^{3+} . The insets show the dependence of the intensity of upconverted emissions with the excitation power.

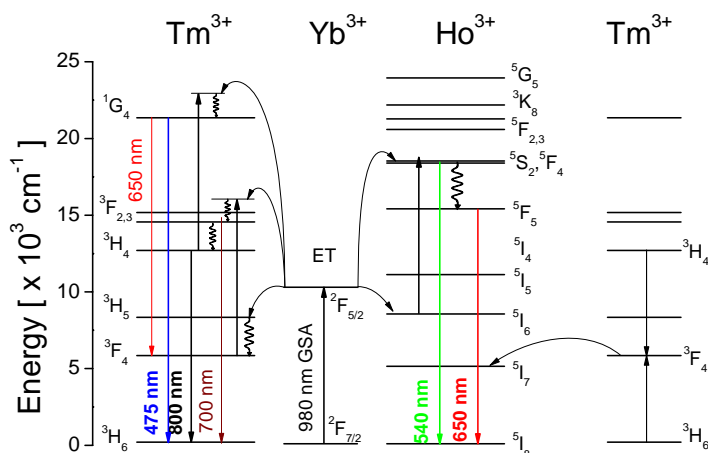


Figure 5.30. Upconversion mechanisms in Ho:Tm:Yb:KLuW nanocrystals.

Table 5.9 lists the calculated QYs , which show a trend to decrease as Tm^{3+} content increases. For 0.75 and 1 %, maximum values are reached with excitation power density of 50 W/cm², and Q_{IR} ($Tm^{3+} \ ^3H_4 \rightarrow \ ^3H_6$) increases in detriment of Q_{Y_B} ($Tm^{3+} \ ^1G_4 \rightarrow \ ^3H_6$), however with high enough excitation power the depopulation of 3H_4 to 1G_4 by UC will be larger, increasing Q_{Y_B} . Finally, for the lowest Tm^{3+} content (0.25 %), all QYs increase monotonously as the excitation power increases.

Table 5.9 Fraction of absorbed light (α) and quantum yields (QY) values of upconverted emissions of Tm^{3+} doped 2 % Ho, 1% Yb:KLuW nanocrystals with the excitation power.

Tm^{3+}	I_0	α	QY_B	QY_G	QY_R	QY_{IR}
[%]	[W·cm ⁻²]	[%]	[%]	[%]	[%]	[%]
1.00	30	21	-	0.0001	0.0007	-
	50	8	-	0.0006	0.0025	0.0014
	100	15	0.0001	0.0006	0.0023	0.0011
	150	34	-	-	0.0001	-
0.75	30	8	-	0.0007	0.0034	0.0009
	50	4	0.0003	0.0027	0.0124	0.0040
	100	12	0.0005	0.0014	0.0057	0.0027
	150	17	-	0.0001	0.0006	0.0003
0.25	30	18	-	0.0003	0.0014	0.0005
	50	18	0.0001	0.0005	0.0024	0.0009
	100	23	0.0002	0.0006	0.0030	0.0016
	150	25	0.0005	0.0012	0.0050	0.0025

5.5.2 Chromaticity

Figure 5.31 shows the chromaticity coordinates of Tm³⁺ doped 2 % Ho, 1 % Yb:KLuW nanocrystals, for different excitation power density values. For Tm doping in the range 0.25-1 % the chromaticity coordinates trace quasi-linear paths crossing the white region. As the excitation power increases, the coordinates displace from yellow to cyan color regions, crossing near to the (0.333, 0.333) illuminant E point [1]. The inset photographs in Figure 5.31 are partially blue-shifted because the pumping filter absorbs part of the emission at 600-700 nm.

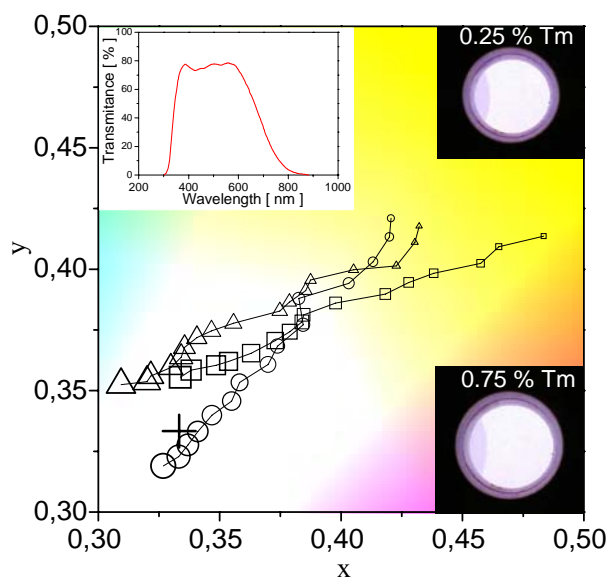


Figure 5.31. Chromaticity coordinates of 2 % Ho, 1 % Yb:KLuW nanocrystals doped with 1 % (circles), 0.75 % (squares) and 0.25 % (triangles) of Tm³⁺. The symbol size is proportional to the excitation power density. Inset photographs correspond to 350 W/cm². Transmission of the filter used for the photographs is also included.

5.5.2 Photoluminescence decay after 460 nm excitation

Non-single exponential photoluminescence decay curves were observed for Ho³⁺ ⁵S₂, ⁵F₄ → ⁵I₈ and ⁵F₅ → ⁵I₈ and for Tm³⁺ ³H₄ → ³H₆ in Tm³⁺ doped 2 % Ho, 1 % Yb:KLuW nanocrystals, as shown in Figure 5.32. Decay times have been calculated with Eq. 5.3, and they are listed in Table 5.10. Decay times of Ho³⁺ ³S₂, ⁵F₄ and ⁵F₅ multiplets after excitation with λ_{EXC}=460 nm in samples codoped with Tm were almost similar to the ones without Tm³⁺, so we can conclude that Ho³⁺ ⁵S₂, ⁵F₄ and ⁵F₅ do not interact with Tm³⁺ states.

Decay time of the Tm³⁺ ³H₄ → ³H₆ transition was reduced as Tm³⁺ content increases from 0.25 % to 0.75 %. Shortening of the decay time as Tm³⁺ increases is produced by a concentration quenching above 0.75 % Tm doped nanocrystals. Again, we propose a phonon-assisted ET process from Tm³⁺ ³F₄ to ⁵I₇ level of Ho³⁺ ions. The ³H₄ decay time

values are similar to the ones reported in 1 % Tm:KLuW (160 μs) [14] and 1 % Tm: KYbW (90 μs) [12] bulk single crystals.

Table 5.10 RT photoluminescence decay times of Tm³⁺ doped 2 % Ho, 1 % Yb:KLuW nanocrystals after 460 nm excitation.

Tm ³⁺ [%]	⁵ S ₂ , ⁵ F ₄ [μs]	⁵ F ₅ [μs]	³ H ₄ [μs]
0.25	7 ± 1	5 ± 1	107 ± 1
0.75	8 ± 1	5 ± 1	119 ± 1
1.00	8 ± 1	5 ± 1	97 ± 1

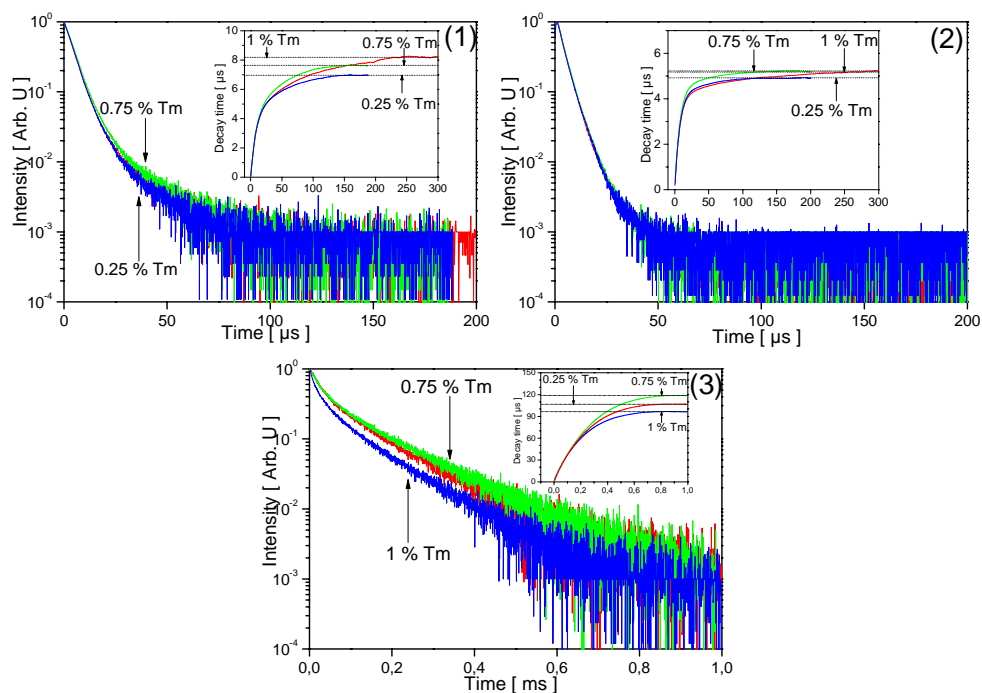


Figure 5.32. RT photoluminescence decay observed for the ⁵S₂, ⁵F₄ → ⁵I₈ (1), ⁵F₅ → ⁵I₈ (2) and ³H₄ → ³H₆ (3) transitions after 460 nm excitation. The insets show the convergence of the τ value.

5.6 Effect of Eu³⁺ in Tm:Ho:Yb:KLuW nanocrystals

One of the most studied lanthanide active ions in optical materials is Eu³⁺ because it is an efficient luminescent center, and abundance of literature reports their spectroscopic properties [27], however few works report the sensitization of the Eu³⁺ ⁵D₀ → ⁷F₂ emission by UC with Yb³⁺ ion [28,29], or the capabilities to modify the UC dynamics between Yb³⁺ and other Ln³⁺ ions [30,31]. In the case of double tungstates, Eu:Yb:KYbW single crystals have shown an efficient UC emission [32], so it is attractive to study the possibility of designing a white light emitter with a red UC emission from Eu³⁺. In this work, we studied the effect of Eu³⁺ doping concentration onto 2 % Ho, 1 % Tm, 1% Yb:KLuW nanocrystals, because they have shown the nearest chromaticity to the white point (1/3, 1/3).

5.6.1 Upconversion spectra and quantum yield

Figure 5.33 shows the evolution with the power density of the UC spectra of Eu³⁺ doped 2 % Ho, 1 % Tm, 1 % Yb:KLuW nanocrystals. Optical emissions from Ho³⁺ and Tm³⁺ ions were assigned in a similar way as described in previous sections. As the Eu³⁺ content increased, the emission intensity of the observed bands decreased, specially the Ho³⁺ ⁵F₅ → ⁵I₈ red emission. For 2 % Eu doped nanocrystals, a weak red emission at 610 nm was observed and it is attributed to Eu³⁺ ⁵D₀ → ⁷F₂ transition.

Eu³⁺ doping produces a modification of the excitation power dependence of the UC emission intensities (log-log insets in Figure 5.33). In the 54-154 W/cm² range the *n* slopes tend to increase, reaching the highest values for 1 % Eu content. For the 164-354 W/cm², slopes increase reaching values higher than 3 for green and red emissions, and even near 5 for the blue emission. Figure 5.34 shows that intensities of blue and green emission increase monotonously with the Eu³⁺ content in this high-power limit under 354 W/cm² excitation and red emission tends to decrease reaching a minimum at 0.5 % Eu³⁺.

Measured *QYs* are listed in Table 5.11. The Eu³⁺ doped nanocrystals show one magnitude order shortening respect to *QYs* obtained for the Eu³⁺-undoped 2 % Ho, 1 % Tm, 1 % Yb:KLuW nanocrystals.

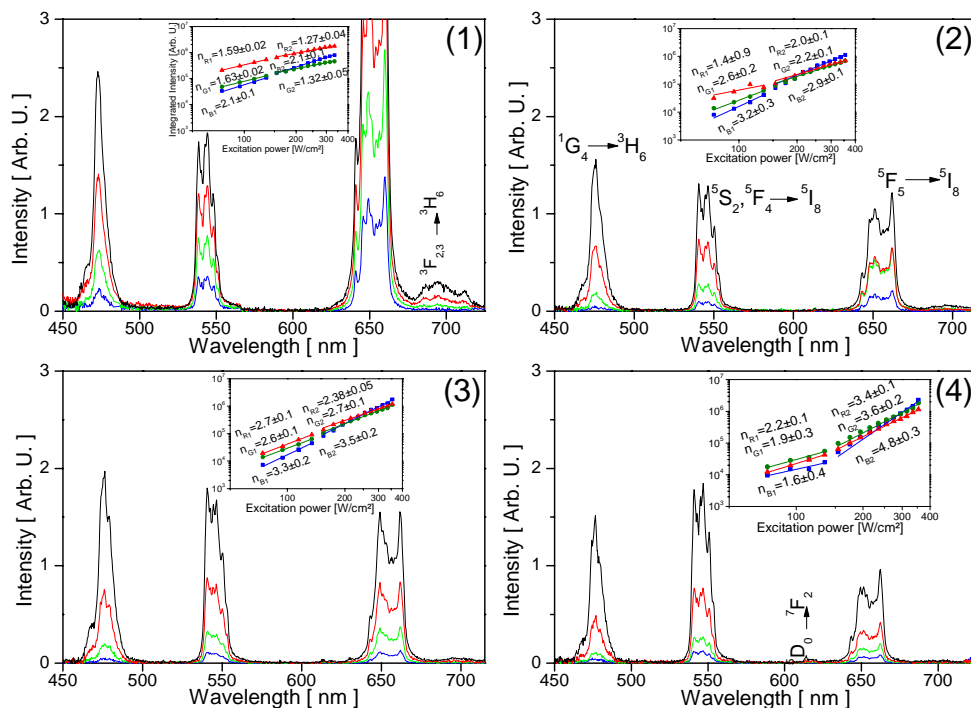


Figure 5.33. Upconversion spectra of 2 % Ho, 1 % Tm, 1 % Yb: KLuW nanocrystals (1), doped with 0.5 % (2), 1 % (3), and 2 % (4) of Eu³⁺ at 74 (blue line), 94 (green line), 114 (red) and 134 (black) W/cm² power density. Insets show the dependence of the emission intensities with the excitation power density in the whole 54 to 354 W/cm² range.

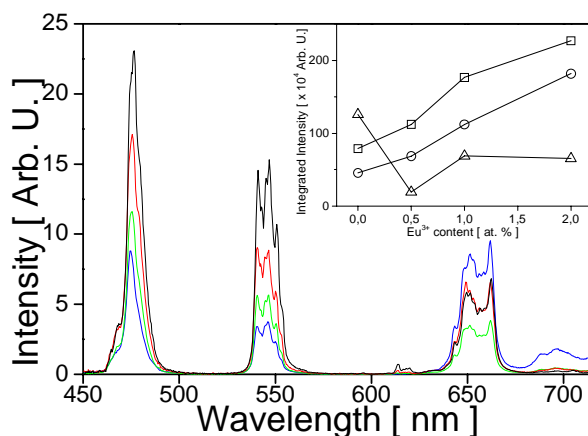


Figure 5.34 Upconversion spectra of 2 % Ho, 1 % Tm, 1 % Yb: KLuW nanocrystals (blue line), doped with 0.5 % (2), 1 % (3), and 2 % (4) of Eu³⁺. Insets show the dependence of the emission intensities with Eu³⁺ content. Excitation power corresponds to 354 W/cm².

Table 5.11. Fraction of absorbed light (α) and quantum yield (QY) of upconverted emissions in Eu³⁺-doped 2 % Ho, 1% Tm, 1% Yb:KLuW nanocrystals with the excitation power

Eu ³⁺ [%]	I_0 [W·cm ⁻²]	α [%]	QY_B [%]	QY_G [%]	QY_R [%]	QY_{IR} [%]
undoped	30	21	-	1·10 ⁻⁴	7·10 ⁻⁴	-
	50	8	-	6·10 ⁻⁴	25·10 ⁻⁴	14·10 ⁻⁴
	100	15	1·10 ⁻⁴	6·10 ⁻⁴	23·10 ⁻⁴	1·10 ⁻⁴
	150	34	-	-	1·10 ⁻⁴	-
0.5	30	13	-	1·10 ⁻⁴	1·10 ⁻⁴	-
	50	9	-	2·10 ⁻⁴	3·10 ⁻⁴	-
	100	14	-	1·10 ⁻⁴	2·10 ⁻⁴	1·10 ⁻⁴
	150	25	-	-	1·10 ⁻⁴	-
1.0	30	5	-	3·10 ⁻⁴	2·10 ⁻⁴	-
	50	10	-	1·10 ⁻⁴	1·10 ⁻⁴	1·10 ⁻⁴
	100	18	-	1·10 ⁻⁴	1·10 ⁻⁴	1·10 ⁻⁴
	150	12	-	1·10 ⁻⁴	1·10 ⁻⁴	-
2.0	30	13	-	2·10 ⁻⁴	2·10 ⁻⁴	-
	50	8	-	3·10 ⁻⁴	1·10 ⁻⁴	1·10 ⁻⁴
	100	18	-	3·10 ⁻⁴	2·10 ⁻⁴	1·10 ⁻⁴
	150	12	1·10 ⁻⁴	7·10 ⁻⁴	5·10 ⁻⁴	2·10 ⁻⁴

5.6.2 Chromaticity

Chromaticity coordinates as a function of the excitation power density are shown in Figure 5.35. We started from the white light emitting 2 % Ho, 1 % Tm, 1% Yb:KLuW nanocrystals, with the nearest chromaticity coordinates to the white point. As Eu³⁺ content was increased the red emission was quenched de-tuning the red-green-blue combination that compose the white light emission, and the chromaticity coordinates are displaced to the green-cyan color region.

5.6.3. Stokes emission

Figure 5.36 shows the room temperature Stokes emission of the 2 % Eu, 2 % Ho, 1 % Tm, 1 % Yb:KLuW nanocrystals. Ho³⁺ and Tm³⁺ emissions have been labeled previously. Under excitation at 460 nm, sharp emissions peaking at 590, 610 and 700 nm were ascribed to the Eu³⁺ ⁵D₀→⁷F₁, ⁵D₀→⁷F₂ and ⁵D₀→⁷F_{5,6} transitions. Under excitation at 660 nm, no Eu³⁺ emission was observed.

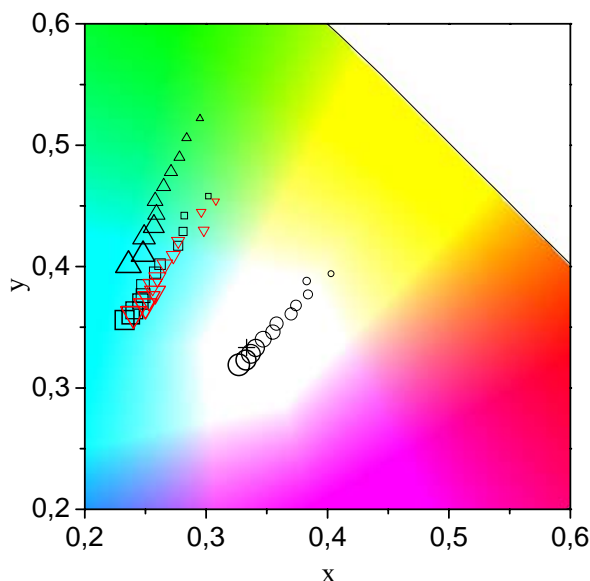


Figure 5.35. Chromaticity coordinates path for 2 % Ho, 1 % Tm, 1 % Yb: KLuW nanocrystals (circles) doped with 0.5 % (squares), 1 % (down triangles) and 2 % Eu (up triangles). Excitation power density, in the range 94-314 W/cm², is proportional to the symbol size.

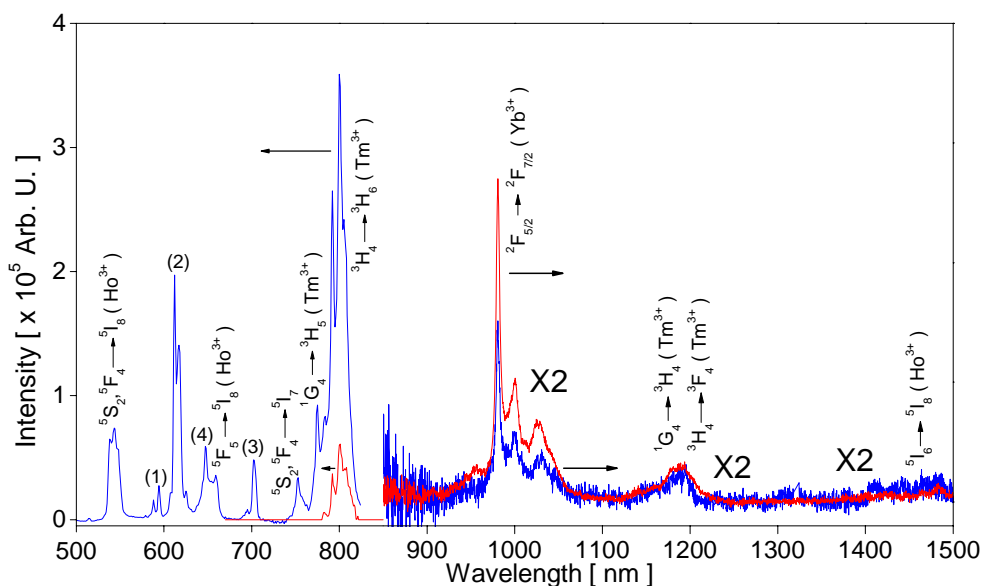


Figure 5.36. Room temperature Stokes emission spectra under 460 (blue line) and 660 nm (red line) excitation of 2 % Eu, 2 % Ho, 1 % Tm, 1 % Yb:KLuW nanocrystals. Labeled transitions corresponds to Eu³⁺ ⁵D₀→⁷F₁ (1), ⁵D₀→⁷F₂ (2), ⁵D₀→⁷F_{5,6} (3) and Tm³⁺ ¹G₄→³F₄ (4).

5.6.4. Photoluminescence decay

Room temperature photoluminescence decay curves for Eu³⁺ doped 2 % Ho, 1 % Tm, 1 % Yb:KLuW nanocrystals are shown in Figure 5.37, and obtained decay times are listed in Table 5.8. Ho³⁺ ⁵S₂, ⁵F₄ and ⁵F₅ → ⁵I₈ decay times are not affected with Eu³⁺ doping, however the decay times of Eu³⁺ ⁵D₀ → ⁷F₂ and Tm³⁺ ³H₄ → ³H₆ are reduced as Eu³⁺ content increases from 0.5 to 2 %.

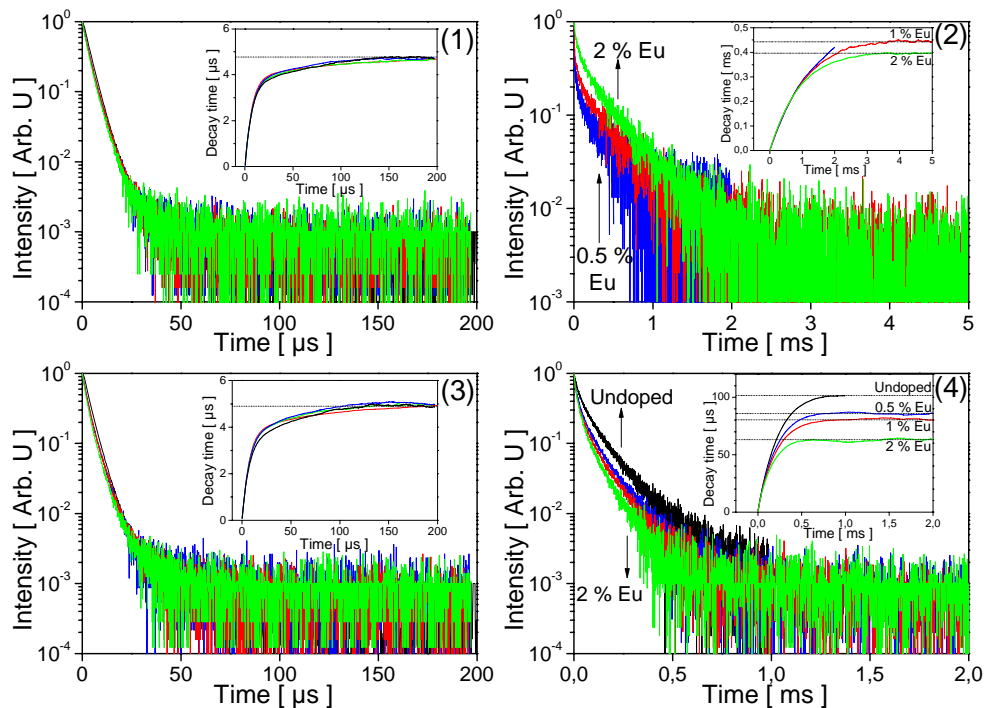


Figure 5.37. Room temperature photoluminescence decay of Ho³⁺ ⁵S₂, ⁵F₄ → ⁵I₈ (1), Eu³⁺ ⁵D₀ → ⁷F₂ (2) Ho³⁺ ⁵F₅ → ⁵I₈ (3) and Tm³⁺ ³H₄ → ³H₆ (4) transitions. The insets show the convergence of τ value.

Table 5.12. Room temperature photoluminescence decay times of Eu³⁺ doped 2% Ho, 1 % Tm, 1 % Yb: KLuW nanocrystals after 460 nm excitation.

Eu ³⁺ [%]	⁵ S ₂ , ⁵ F ₄ [μs]	⁵ D ₀ [μs]	⁵ F ₅ [μs]	³ H ₄ [μs]
undoped	5 ± 1	-	5 ± 1	101 ± 4
0.5	5 ± 1	-	5 ± 1	85 ± 4
1.0	5 ± 1	440 ± 10	5 ± 1	80 ± 4
2.0	5 ± 1	400 ± 10	4 ± 1	63 ± 4

5.6.5. Discussion

In the UC spectra, the Eu³⁺ ⁵D₀ → ⁷F₂ transition at 610 nm was observed for 2 % Eu, 2 % Ho, 1 % Tm, 1 % Yb:KLuW nanocrystals. We propose that the 610 nm emission is produced by an ET process from Tm³⁺ ¹G₄ to the Eu³⁺ ⁵D₂ level, with two non-radiative relaxations to reach the ⁵D₀ level, as illustrate in the energy diagram in Figure 5.38.

Increment of Eu³⁺ doping reduces the UC emission intensities, especially the Ho³⁺ ⁵F₅ → ⁵I₈ emission, and increases the *n* slope values for all visible emissions, indicating that the Eu³⁺ ion modifies the depopulation of the intermediate multiplets involved in UC processes. In comparison with Ln:Yb:KLuW (Ln=Tm or Ho) and Ho:Tm:Yb:KLuW nanocrystals, we have observed a reduction of the *QY* of nearly one magnitude order after extra Eu³⁺ adding. As an example, Table 5.13 lists the results for Ho³⁺ ⁵F₅ → ⁵I₈ red emission.

Table 5.13. Upconversion quantum yield of the Ho³⁺ ⁵F₅ → ⁵I₈ red emission at 50 W/cm² in the Eu:Ho:Tm:KLuW nanocrystals.

Eu	Ho	Tm	Yb	<i>QY_R</i>
[%]	[%]	[%]	[%]	[%]
-	1	-	10	0.0890
-	2	1	1	0.0025
2	2	1	1	0.0001

We propose that the presence of the Eu³⁺ ⁷F_J multiplet is enhancing the non-radiative depopulation of some intermediate states of Tm³⁺ and Ho³⁺ ions, leading to the increment of the required photons to reach higher multiplets by UC. This increment in the *n* slopes has been originally reported for Eu³⁺ doped Er:Yb:Y₂O₃ [30] and Ho:Yb:Y₂O₃ nanocrystals [31]. Previously, we have discussed the depopulation of the ³H₄ energy level via cross-relaxation between Tm³⁺ ions (³H₄, ³H₆) → (³F₄, ³F₄) and the energy transfer from Tm³⁺ ³F₄ to Ho³⁺ ⁵I₇. In a similar way, the presence of the Eu³⁺ ⁷F_J multiplet allows a more efficient depopulation of the ³F₄ energy level (see Figure 5.38), increasing the effect of the cross relaxation (³H₄, ³H₆) → (³F₄, ³F₄) process, that produces the shortening of the decay time observed for the ³H₄ → ³H₆ transition. The effect of Eu³⁺ ⁷F_J multiplet increases for excitation power densities larger than 150 W/cm² excitation, producing slopes values with *n* > 3.

UC processes in Tm³⁺ and Ho³⁺ by ET process from Yb³⁺ have been described previously. However, the quenching of the Ho³⁺ red ⁵F₅ → ⁵I₈ emission in presence of Eu³⁺ suggests that along with the previously described ⁵F₅ population by non-radiative relaxation from ⁵F₄ after two successive ET from Yb³⁺ ²F_{5/2}, there is other mechanism that also populates the Ho³⁺ ⁵F₅ energy level, and this second mechanism should be hampered by the presence of Eu³⁺. This second mechanism is presented in Figure 5.38, and it can be explained through the non radiative decay of the Ho³⁺ ⁵I₆ intermediate level to the ⁵I₇ and direct pumping to the ⁵F₅ by ET from Yb³⁺ ion. The energy mismatch between Ho³⁺ ⁵I₇ and Eu³⁺ ⁷F₆ is around 200 cm⁻¹, so in the case of Eu³⁺ doping, electrons in the Ho³⁺ ⁵I₇ may transfer their energy to a nearby

Eu³⁺ ion populating the ⁷F₆ level. Electrons in the ⁷F₁ multiplet relax fast to the ground state through phonon decays [30,31] because the energy spacing of Eu³⁺ ⁷F₁ multiplets can be bridged by phonons of the KLu(WO₄)₂ host ($\hbar\omega=908\text{ cm}^{-1}$) [4].

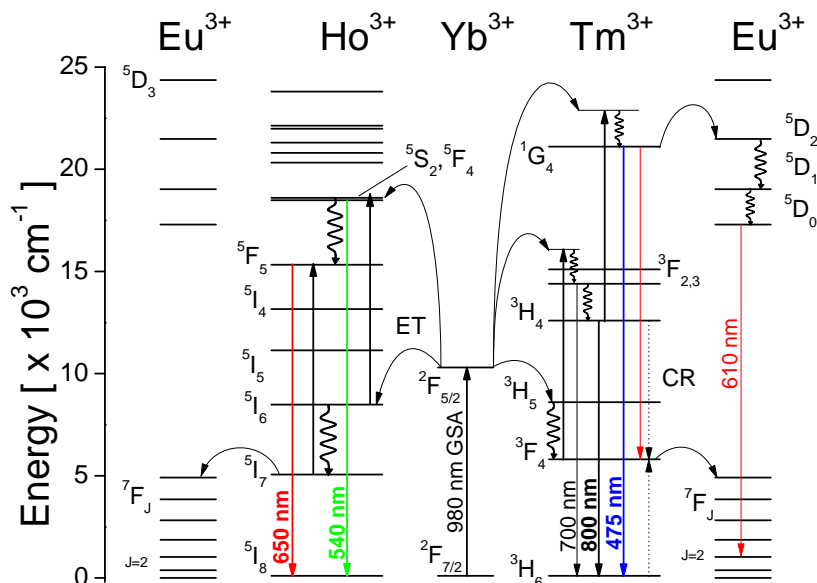


Figure 5.38. Upconversion mechanisms in Eu³⁺ doped Ho:Tm:Yb:KLuW nanocrystals.

5.7 Conclusions

For synthesized KLuW nanocrystals we have studied the possibility of white light generation by the physical mixture of nanocrystalline powders codoped with Ho, Yb and Tm, Yb, as well as in the Ho, Tm, Yb:KLuW system. In the last case, the effect of adding Eu³⁺ has been also studied. Visible and NIR emissions were identified and their dynamics were described for UC emission under 980 nm excitation. Room temperature Stokes emissions and decay times under 460 nm excitation were also analyzed.

We have synthesized 1% Ln, 10% Yb:KLuW nanocrystals as green (Ln=Er), yellow (Ln=Ho) and blue (Ln=Tm) UC emitters. Chromaticity coordinates are near the boundary of CIE 1931 diagram, showing high color purity. Shortening of slopes, in the intensity of emissions-versus-excitation power curves, was commonly observed under 100-350 W/cm² excitation. This is produced by the depopulation of the intermediate states to higher multiplets by UC, instead to linear decay to lower multiplets. This excitation range was identified as a high-power limit for UC emission in Yb³⁺ sensitized KLuW nanocrystals. As the excitation power density increases, *QY* decreases, most probably to the operation of the KLuW nanocrystals in the high-power limit. One exception is the red emission in Yb, Er-doped nanocrystals with *QY_G* ~ 0.2 %, in the range of 30-150 W/cm². The large *I_{GREEN}*/*I_{RED}* emission ratio in 1% Er, 10% Yb:KLuW nanocrystals is produced by deactivation of the

cross-relaxation mechanism (⁴F_{7/2}, ⁴I_{11/2}) → (⁴F_{9/2}, ⁴F_{9/2}) between Er-Er pairs, favored by the large phonon energy in KLuW, $\hbar\omega_{\max} = 908 \text{ cm}^{-1}$

We have studied the possibility of white light generation by the physical mixture of nanocrystalline powders, using a proposed model for the addition of the intensity distribution curves at specific excitation powers, and calculating the optimal proportion to obtain light with chromaticity near to the white point. A white light emitter was predicted for a mixture of 1 % Tm, 10 % Yb:KLuW and 1 % Ho, 10 % Yb:KLuW nanocrystals with relative molar ratio $a_{Tm}:a_{Ho}=1:4$. The comparison with experimental data shows a fast departure of the white color region towards cyan color region as the excitation power increases. In this mixture, at low excitation power, the reduction in the intensities of red-green emissions were found to be slightly larger than expected, around 33% instead of 20 %, while the reduction of intensity of the blue light was shorter than expected, around 65% instead of the expected 80% .

In the mixture some physical properties are modified. In the range of 50-150 W/cm² excitation power, the fraction of absorbed light was reduced around 26-32 % respect to the expected value for red-green-emissions, Q_{Y_B} and $Q_{Y_{IR}}$ were almost constant, Q_{Y_G} was reduced around 40 % and Q_{Y_R} was reduced 34-38 %. Increment of NIR scattering by evanescent defects, created after grinding of nanocrystalline powders, were associated to the low absorption of the mixture.

The proposed model for the addition of the intensity distribution curves, fits well in the case of Stokes emission, probably because the 460 nm excitation can reach more nanocrystals with less dispersion than 980 nm radiation for exciting the UC emission. The 460 nm radiation can be absorbed for more Tm³⁺ ¹G₄ and Ho³⁺ ⁵F_{2,3} multiplets in only one step, instead of the UC process, that requires multi-step energy transfer processes from nearby Yb³⁺ ions.

An initial fast component was observed in decay time curves spreading up to first 25-75 μs, in comparison to single exponential decays of bulk single crystals with similar Ln³⁺ doping. The initial fast component is produced by non-radiative relaxation of radiative levels involving surface phonons of OH⁻ and CO₃²⁻ bonds with vibrational energies of 3350 and 1500 cm⁻¹, respectively. The slow component comes from more nearly isolated Ln³⁺ ions inside nanocrystals. These latter decay time values for doped KLuW nanocrystals were similar to those for monoclinic double tungstates single crystals.

In the case of Ho:Tm:Yb:KLuW nanocrystals, the intensity of UC emission bands experiences an increase for Tm³⁺ contents from 0.25 % to 0.75 %, but a quenching of these intensities is observed for 1 % Tm³⁺. For 0.75 % Tm³⁺ content, highest intensity, n slopes and Q_{Y_R} (0.0124 % at 50 W/cm²) were observed. For 0.75 and 1 %, maximum values are reached with 50 W/cm², with Q_{IR} band (Tm³⁺ ³H₄ → ³H₆) increasing in detriment of Q_{Y_B} (Tm³⁺ ¹G₄ → ³H₆), however with high enough excitation power the population of ¹G₄ will be enhanced, increasing Q_{Y_B} . Finally, for the lowest Tm³⁺ content (0.25 %), all QY increases monotonously as the excitation power increases. White light emitting nanocrystals were found for the 0.25-1.00 % Tm³⁺ doped, 2% Ho, 1 % Yb:KLuW compositions, whose color

coordinates trace quasi-linear paths crossing the white color region, from yellow to cyan color regions as the excitation power increases.

No changes have been observed in the depopulation of Ho³⁺ ⁵S₂, ⁵F₄ and ⁵F₅ multiplets after doping with Tm³⁺ and Eu³⁺. The Tm³⁺ ³H₄ level was identified as an important intermediate level that it is affected not only by Tm³⁺ concentration quenching but even by Ho³⁺ and Eu³⁺ doping. In presence of Ho³⁺ ions, Tm³⁺ ³H₄ multiplet is depopulated by cross-relaxation (³H₄, ³H₆) → (³F₄, ³F₄), followed by a ET from these Tm³⁺ ions to the ⁵I₇ level of Ho³⁺ ions, explaining the slight increment in *n* slope values when Ho³⁺ or Tm³⁺ contents are increased. When Eu³⁺ is present, Tm³⁺ ³F₄ and Ho³⁺ ⁵I₇ energy levels transfer their energies more efficiently to Eu³⁺ ⁷F₆ due to the small energy mismatch. The Eu³⁺ ⁷F₇ multiplet produces a fast depletion to the ground state due to the ladder-like structure. These mechanisms can explain the quenching of UC visible emissions, the one magnitude order shortening of the *QY* and the slope values with *n* > 3 observed for excitation power densities larger than 150 W/cm². Red UC emission from Eu³⁺ was non-efficient, and Eu³⁺ ⁵D₀ → ⁷F₂ transition at 610 nm was observed only for 2 % Eu³⁺ at high excitation power.

5.8 References

- [1] *Colorimetry*, CIE Technical report No. 15.3 3rd edition (2004).
- [2] R. C. Ropp, *Luminescence and the Solid State in Studies in Inorganic Chemistry Vol 21*, Elsevier, Amsterdam (2004).
- [3] D. R. Gamelin, H. U. Güdel, *Upconversion Processes in Transition Metal and Rare Earth Metal Systems* Top. Curr. Chem. 214 1 (2001).
- [4] V. Petrov, M. C. Pujol, X. Mateos, O. Silvestre, S. Rivier, M. Aguiló, R. M. Sole, J. Liu, U. Griebner, F. Diaz, *Growth and properties of KLu(WO₄)₂ and novel ytterbium and thulium lasers based on this monoclinic crystalline host* **Laser & Photon. Rev.** 1, 179-212 (2007).
- [5] L. Laversenne, Y. Guyot, C. Goutaudier, M.Th. Cohen-Adad, G. Boulon *Optimization of spectroscopic properties of Yb³⁺-doped refractory sesquioxides: cubic Y₂O₃, Lu₂O₃ and monoclinic Gd₂O₃* **Opt. Mater.** 16 475-483 (2001).
- [6] M. Inokuti, F. J. Hirayama *Influence of Energy Transfer by the Exchange Mechanism on Donor Luminescence* **J. Chem. Phys.** 43 1978-1989 (1965).
- [7] R. K. Watts, H. J. Richter *Diffusion and Transfer of Optical Excitation in YF₃:Yb,Ho* **Phys. Rev. B** 6 1584 (1972).
- [8] M. Pollnau, D.R. Gamelin, S.R. Lüthi, H.U. Güdel *Power dependence of upconversion luminescence in lanthanide and transition-metal-ion systems* **Phys. Rev. B** 61 3337 (2000).
- [9] R. Calderón-Villajos, C. Zaldo, C. Cascales *Enhanced upconversion multicolor and white light luminescence in SiO₂-coated lanthanide-doped GdVO₄ hydrothermal nanocrystals* **Nanotechnology** 23 505205 (2012).
- [10] M. C. Pujol, J. Massons, M. Aguiló, F. Díaz, M. Rico, C. Zaldo, *Emission Cross Sections and Spectroscopy of Ho³⁺ Laser Channels in KGd(WO₄)₂ Single Crystal* **IEEE J. Quantum Elect.** 38 93-100 (2002).
- [11] V. Jambunathan *Infrared lasers based on Ho³⁺:KRE(WO₄)₂ crystals with Tm³⁺ or Yb³⁺ as sensitizers*, p72 Ph.D. Dissertation. Universitat Rovira i Virgili, Tarragona (2011).
- [12] A. N. Kuzmin A. V. Kachynski, P. N. Prasad, A. A. Demidovich, L. E. Batay, A. Bednarkiewicz, W. Strek, A. N. Titov *Blue up-conversion emission in Yb- and Tm-codoped potassium yttrium tungstate* **J. Appl. Phys.** 95, 12 (2004).
- [13] M. C. Pujol, F. Güell, X. Mateos, Jna. Gavalda, R. Solé, J. Massons, M. Aguiló, F. Díaz, G. Boulon, A. Brenier *Crystal growth and spectroscopic characterization of Tm³⁺-doped KYb(WO₄)₂ single crystals* **Phys. Rev. B** 66, 144304 (2002).
- [14] O. Silvestre, M. C. Pujol, M. Rico, F. Güell, M. Aguiló, F. Diaz *Thulium doped monoclinic KLu(WO₄)₂ single crystals: growth and spectroscopy* **Appl. Phys. B** 87 707-716 (2007).
- [15] J. García Solé, L. E. Bausá, D. Jaque. *An introduction to the optical spectroscopy of inorganic solids*, John Wiley & Sons Ltd, (2005).
- [16] J. -C. Boyer, F. C. J. M. van Veggel *Absolute quantum yield measurements of colloidal NaYF₄: Er³⁺, Yb³⁺ upconverting nanoparticles* **Nanoscale** 2, 1417 (2010).
- [17] J.-C. G.Bünzli, S. V. Eliseeva, *Basics of Lanthanide Photophysics* In *Lanthanide Luminescence: Photophysical, Analytical and Biological Aspects*; P. Hänninen, H. Härmä, Eds.; Springer-Verlag, Berlin, (2010).

- [18] R. H. Page, K. I. Schaffers, P. A. Waide, J. B. Tassano, S. A. Payne, W. F. Krupke, W. K. Bischel *Upconversion-pumped luminescence efficiency of rare-earth-doped hosts sensitized with trivalent ytterbium* **J. Opt. Soc. Am. B**, 15 996-1008 (1998).
- [19] I. Etchart, I. Hernández, A. Huignard, M. Bérard, M. Laroche, W. P. Gillin, R. J. Curry, A. K. Cheetham *Oxide phosphors for light upconversion; Yb³⁺ and Tm³⁺ co-doped Y₂BaZnO₅* **J Appl Phys** 109, 063104 (2011).
- [20] J. Schanda *Colorimetry: understanding the CIE system*, John Wiley & Sons Hoboken, New Jersey (2007).
- [21] J. Milliez, A. Rapaport, M. Bass, A. Cassanho, H.P. Jenssen, *High-Brightness White-Light Source Based on Up-Conversion Phosphors* **J. Display Technol.** 2 307-311 (2006).
- [22] H. S. Fairman, M. H. Brill, H. Hemmendinger *How the CIE 1931 Color-Matching Functions Were Derived from Wright-Guild Data* **COLOR RES. Appl.** 22 11-23 (1997).
- [23] *Colorimetry: understanding the CIE system* János Schanda, John Wiley & Sons (2007).
- [24] V. Mahalingam R.Naccache F. Vetrone J. A. Capobianco *Enhancing upconverted white light in Tm³⁺/Yb³⁺/Ho³⁺-doped GdVO₄ nanocrystals via incorporation of Li⁺ ions* **Optics Express** 20, 111-119 (2012).
- [25] M. Pollnau, D.R. Gamelin, S.R. Lüthi, H.U. Güdel, *Power dependence of upconversion luminescence in lanthanide and transition-metal-ion systems* **Phys. Rev. B** 61 3337 (2000).
- [26] K. -S. Lima, P. Babua, S. -K. Leea, V.-T. Phama, D.S. Hamilton *Infrared to visible up-conversion in thulium and holmium doped lutetium aluminum garnet* **J. Lumin.** 102 737–743 (2003).
- [27] G. Liu, X. Chen *Spectroscopic properties of lanthanides in nanomaterials* In *Handbook on the physics and chemistry of rare earths vol. 37* edited by K. A. Gschneider, Jr., J.-C. G. Bünzli and V. K. Pecharsky Elsevier B. V. Amsterdam (2007).
- [28] R. Martín-Rodríguez, R. Valiente, S. Polizzi, M. Bettinelli, A. Speghini, F. Piccinelli *Upconversion Luminescence in Nanocrystals of Gd₃Ga₅O₁₂ and Y₃Al₅O₁₂ Doped with Tb³⁺-Yb³⁺ and Eu³⁺-Yb³⁺* **J. Phys. Chem. C** 113 12195–12200 (2009).
- [29] H. Wang, C. Duan, P. A. Tanner *Visible Upconversion Luminescence from Y₂O₃:Eu³⁺, Yb³⁺* **J. Phys. Chem. C** 112 16651-16654 (2008).
- [30] Y.Q. Sheng, L.L. Xu, J. Liu, D. Zhai, Z.G. Zhang *Improving monochromaticity of upconversion luminescence by codoping Eu³⁺ ions in Y₂O₃:Ho₃₊, Yb₃₊ nanocrystals* **J. Lumin**, 130 338-341 (2010).
- [31] Y. Q. Sheng, J. Liu, L. L. Xu, D. Zhai, Z. G. Zhang, W. W. Cao *Effect of Eu³⁺ codoping on upconversion luminescence in Y₂O₃:Er³⁺, Yb³⁺ nanocrystals* **Solid State Comm.** 15, 1048-1051 (2010).
- [32] W. Strek, P. J. Deren, A. Bednarkiewicz, Y. Kalisky, P. Boulanger *Efficient up-conversion in KYb_{0.8}Eu_{0.2}(WO₄)₂ crystal.* **J. Alloys Compd.**, 180 300-301 (2000).

Chapter 6

Conclusions

UNIVERSITAT ROVIRA I VIRGILI
LANTHANIDE-BASED DIELECTRIC NANOPARTICLES FOR UPCONVERSION LUMINESCENCE
Elixir William Barrera Bello
Dipòsit Legal: T. 450-2013

6.1 Conclusions

In this thesis, the luminescence and upconversion properties of lanthanide doped inorganic nanocrystalline cubic $Ia\bar{3}$ Lu_2O_3 and monoclinic $C2/c$ KLuW materials synthesized by two different methods have been investigated. Lu_2O_3 nanorods were synthesized by a soft hydrothermal method and Lu_2O_3 and KLuW nanocrystals were prepared by a modified Pechini procedure. Furthermore, for obtaining $\text{SiO}_2@ \text{Lu}_2\text{O}_3$ core-shell particles modified-Pechini as well as hydrothermal preparative protocols were presented.

As the Tm^{3+} content was increased in the 0.5-15 %, $\text{Tm}:\text{Lu}_2\text{O}_3$ nanocrystals show no dependence of the crystallite size and low increment of the linear thermal expansion coefficient $\sim 7.5 \times 10^{-6} \text{ K}^{-1}$, supporting the use of Lu_2O_3 as a host for Tm^{3+} ions in $\text{Tm}:\text{Lu}_2\text{O}_3$ ceramic lasers made from nanocrystalline precursors. Tm^{3+} absorption maximum centered around 800 nm is in agreement with results obtained in single crystal and Tm^{3+} energy level positions were not affected by the crystal dimension.

Increasing the Tm^{3+} concentration in Lu_2O_3 nanocrystals further reduces the lifetime due to Tm-Tm interactions as energy migration (${}^3\text{H}_4, {}^3\text{H}_6 \rightarrow {}^3\text{H}_6, {}^3\text{H}_4$) and cross relaxation (${}^3\text{H}_4, {}^3\text{H}_6 \rightarrow {}^3\text{F}_4, {}^3\text{F}_4$) similarly to that observed in single crystals. The lifetimes measured for $\text{Tm}:\text{Lu}_2\text{O}_3$ nanocrystals dispersed in ethylene glycol ($n_{rf} = 1.52$) and fluorolube ($n_{rf} = 1.94$), show no influence of the refractive index of the medium on the measured lifetimes. This indicates that the crystal size of the presently used nanocrystals is above the threshold to produce modifications of the radiative lifetime.

The presence of contaminant functional groups OH^- and CO_3^{2-} , adsorbed on the surface of the nanostructures modifies the luminescence dynamics of Ln^{3+} ions. For $\text{Er}, \text{Yb}:\text{Lu}_2\text{O}_3$ nanorods, the red-to-green emission ratio observed in cathodoluminescence and upconversion spectra increases as the Yb^{3+} concentration increases favored by the presence of large phonons in current nanorods, originating upconversion mechanisms that privilege the population of the ${}^4\text{F}_{9/2}$ emitting level through phonon-assisted energy transfer and non-radiative relaxations. The slopes of the intensity-versus-power graph with values ~ 1 indicate large upconversion rates for the depletion of intermediate excited states produced by a high power excitation.

We have synthesized 1% Ln, 10% Yb:KLuW nanocrystals as green (Ln=Er), yellow (Ln=Ho) and blue (Ln=Tm) upconverting emitters with high color purity. These samples show reduced slopes in the intensity-versus-power graphs under 100-350 W/cm^2 excitation, identified as the high-power limit for upconversion emission in Yb^{3+} sensitized KLuW nanocrystals. Quantum yields are reduced as excitation power increases except in Yb, Er-doped nanocrystals where $QY_G \sim 0.2$ % was practically constant in all the measured excitation range of 30-150 W/cm^2 . In comparison with $\text{Er}, \text{Yb}:\text{Lu}_2\text{O}_3$ nanostructures, red-to-green ratio enhancement is not observed in $\text{Er}, \text{Yb}:\text{KLuW}$ nanocrystals, because the phonons in KLuW ($\hbar\omega = 908 \text{ cm}^{-1}$) de-active the cross relaxation mechanism (${}^4\text{F}_{7/2}, {}^4\text{I}_{11/2} \rightarrow {}^4\text{F}_{9/2}, {}^4\text{F}_{9/2}$) that support the red enhancement observed in Lu_2O_3 nanostructures. The photoluminescence decay curves showed two components, an initial fast decay spreading up

to the first 25-75 μs associated by non-radiative relaxation of Ln^{3+} ions by surface phonons and a slow component from more isolated Ln^{3+} ions inside nanocrystals. Measured lifetimes doped KLuW nanocrystals in air were similar to those for monoclinic double tungstates single crystals.

A model for calculating the optimal proportion to obtain light with chromaticity near to the white point was proposed from the physical mixture of Ln, Yb:KLuW (Ln = Er, Ho, Tm) prepared nanocrystals. A white light emitter was predicted for a mixture of 1 % Tm, 10 % Yb:KLuW and 1 % Ho, 10 % Yb:KLuW nanocrystals with relative molar ratio $a_{\text{Tm}}:a_{\text{Ho}}=1:4$. The comparison with experimental data shows a fast departure of the white color region towards the cyan color region as the excitation power increases. Upconversion spectra of the mixture do not correspond to a linear superposition of the original Tm:Yb:KLuW and Ho:Yb:KLuW nanocrystals. In the mixture, profile deviations of the corresponding UC emissions were observed in the 30-100 W/cm^2 excitation range. From the integrated emission intensities, we found a reduction of 61-68 % of intensity for the blue emission, shorter than the expected 80 % for the emissions from Tm, Yb:KLuW nanocrystals. Reduction of 30-33 % in green emission and ~ 35 % for the red emission, larger than the expected 20 % from Ho, Yb:KLuW nanocrystals, and independent of the excitation power. These results indicate that some physical properties of the original powders are modified in the mixture of these two kinds of nanocrystals. The fraction of absorbed light is reduced around 26-32 % respect to the weighted average value calculated from the original nanocrystals. Quantum yields were also modified after mixture in different ways: QY_B and QY_{IR} were almost constant, QY_G was reduced around 40 % and QY_R was reduced 34-38 %. The increment of the 980 nm pumping scattering by defects created after grinding of nanocrystalline powders was proposed to explain the reduction of absorbed light and quantum yields.

White light emission was produced for the 0.25-1.00 % Ho doped 1 % Tm, 1 % Yb:KLuW nanocrystals with 14-354 W/cm^2 excitation power. Especially for 0.75 % Tm with the highest emission intensity was obtained with a $QY_B = 0.0003$ %, $QY_G = 0.0027$ %, $QY_R = 0.0124$ % with 50 W/cm^2 excitation. Eu^{3+} doping reduces these QYs in one magnitude order. Also it produces a quenching on upconversion visible emissions in Ho:Tm:Yb:KLuW nanocrystals due to the interaction of the $\text{Eu}^{3+} {}^7\text{F}_J$ multiplet with $\text{Tm}^{3+} {}^3\text{H}_4$ and $\text{Ho}^{3+} {}^5\text{I}_7$ levels, for excitation power density below the observed high power limit of 150 W/cm^2 . Above this limit, upconversion emission increases and the power dependence of upconversion emission shows a fast increment with slopes larger than 3, which are not related with the number of energy transfer processes from Yb^{3+} ions.

Chapter 7

Printed Version Erratum

UNIVERSITAT ROVIRA I VIRGILI
LANTHANIDE-BASED DIELECTRIC NANOPARTICLES FOR UPCONVERSION LUMINESCENCE
Elixir William Barrera Bello
Dipòsit Legal: T. 450-2013

Page 18

In the third aim of thesis should be “SiO₂@Ln:Yb:Lu₂O₃”

Page 32

The wavelengths of Cu source are $\lambda_{K\alpha 1} = 1.540560 \text{ \AA}$ and $\lambda_{K\alpha 2} = 1.544390$

Page 42 Figure 2.10

There are no two detectors in the spectrophotometer. The beam reaches a single detector by different ways by the action of chopper beam splitter.

Page 45 second paragraph and Figure 2.14

We refer to a second harmonic Nd:GdVO₄ laser

Page 45 last paragraph

The sentence “for papers VIII, IX, X and XI” should be “KLuW nanocrystals”.

Page 47 Figure 2.16

Ordinate axis should be “Intensity [No units]”.

Page 47 last paragraph, last line

The quantum yield is given in %.

Page 49 fourth paragraph

The expression “paper VIII” should be removed.

Page 52 Figure 2.22

The Raman scattering corresponds to the Stokes Raman scattering emission. Anti-Stokes Raman scattering is missed.

Page 65 Figure 3.5

The labels (a),(b),(c) and (d) should be removed.

Page 71 Table 3.5

The 10 % Yb³⁺ samples should be the third group of samples in ascending Yb³⁺ order.

Page 72 Section 3.5.3

The motivation to produce gold decorated nanorods is missed.

Page 74 Table 3.10

Paper XI corresponds to a draft paper to be submitted and it was not attached to the electronic and printed versions.

Page 77 Figure 3.15

The labels (a), (b), (c) and (d) are missed in the figure.

Page 81 Table 3.8

The sample M8 with formula $\text{Lu}_{1.889}\text{Yb}_{0.110}\text{Tm}_{0.001}\text{O}_3$ is missed. The sample was synthesized with the same conditions as M7.

Page 83 Figure 3.21

The pH value corresponds to 11.

Page 92, 93 Table 3.10

Paper VIII, IX, X corresponds to draft papers to be submitted and they were attached to the electronic and printed versions.

Page 95

The sentence “Further TEM images are shown in papers VIII, IX and X” should be removed.

Page 106

The text of the figure description ends on “... (I/I_0) vs t dependence”. The page text starts on “Table 4.2 list the decay results...”

Page 115 Figure 4.14

In the color bar the label “intensity” is missed.

Page 116 Tables 4.4 and 4.5

The number 4 is missed in the $\text{Er}^{3+} {}^4\text{F}_{9/2}$ level

Page 120 Figure 4.19 and 4.21

The concentration of sample is missed. It corresponds to 0.05 % Tm, 5.50 % Yb: Lu_2O_3 with experimental formula $\text{Lu}_{1.889}\text{Yb}_{0.110}\text{Tm}_{0.001}\text{O}_3$.

Page 121 Figure 4.21

The transition at 540-550 nm is “ ${}^1\text{D}_2 \rightarrow {}^3\text{H}_5$ ” as in the text.

Page 130 Figure 5.1

The ordinate axis label should be “Intensity [Arb. U]”.

Page 131 Figures 5.3, 5.5, 5.10, 5.15, 5.22, 5.26, 5.33

In the ordinate axis, the “ $\times 10^{-4}$ ” should be removed.

Page 132 Figures 5.2, 5.18, 5.20, 5.21, 5.4, 5.7, 5.31 and 5.35

The chromaticity coordinates labels of abscissa and ordinate axes should be in lower-case letter to avoid confusion with tristimulus values in capital letter.

Page 131

The intensity of the radiation emitted by the sample corresponds to I_{UC} , and I is the transmitted intensity. We consider that the absorption and emission wavelengths are different.

Pages 131, 140, 141 and 157

The notation should be I_{UC} instead of I_{VIS} .

Page 144, 145, 147, 148, 151, 152, 169 and 176

The relative concentration of the products a_j is defined in molar, not weight.

Page 154 Figure 5.26 and Figure 5.29

The calculated slope deviation should be " ± 0.0 " instead of " \pm ".

Paper IV Figure 8

"Er_x" instead of "Er_{0.0x}".

Paper IV Figure 17

"nA" instead of "nm".

Paper I

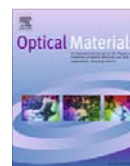
E. W. Barrera, M. C. Pujol, C. Cascales, J. J. Carvajal, X. Mateos, M. Aguiló, and F. Díaz, *Synthesis and structural characterization of Tm:Lu₂O₃ nanocrystals. An approach towards new laser ceramics* **Optical Materials** 33 722–727 (2011).



Contents lists available at ScienceDirect

Optical Materials

journal homepage: www.elsevier.com/locate/optmat



Synthesis and structural characterization of Tm:Lu₂O₃ nanocrystals. An approach towards new laser ceramics

E. William Barrera^a, M. Cinta Pujol^{a,*}, Concepción Cascales^b, Joan J. Carvajal^a, X. Mateos^a,
Magdalena Aguiló^a, Francesc Díaz^a

^a Física i Cristal·lografia de Materials i Nanomaterials (FICMA-FICNA), Universitat Rovira i Virgili (URV), Campus Sescelades, c/ Marcel·lí Domingo, s/n, E-43007 Tarragona, Spain

^b Instituto de Ciencia de Materiales de Madrid, CSIC, Calle Sor Juana Inés de la Cruz, Cantoblanco, E-28049 Madrid, Spain

ARTICLE INFO

Article history:

Received 3 March 2010

Received in revised form 16 June 2010

Accepted 17 September 2010

Available online 12 October 2010

Keywords:

Nanocrystals

Sesquioxides

Laser ceramics

Linear thermal expansion

Grain crystal growth

ABSTRACT

Nanocrystals of Tm³⁺ Thulium doped cubic sesquioxides, Tm:Lu₂O₃, with a maximum size around 30 nm have been synthesized by a modified Pechini sol–gel method. The calcination temperature for the synthesis is 1073 K. Electron microscopy was used to analyze the presence of aggregates, and the type of boundary between the nanocrystals. The linear coefficient of thermal expansion for these nanocrystals has been determined to be around $7.5 \times 10^{-6} \text{ K}^{-1}$. The growth of the nanocrystals has been studied in terms of temperature and time. Nanocrystals start to grow at temperatures around 1267 K. Finally, the grain growth activation energy of this material has been evaluated to be 76 kJ/mol, indicating a diffusion growth mechanism. Linear thermal expansion of prepared nanocrystals is $\approx 7.5 \times 10^{-6} \text{ K}^{-1}$.

© 2010 Elsevier B.V. All rights reserved.

1. Introduction

In recent years, nanotechnology has been a very important area of investigation in materials science because these novel nanomaterials can show different or improved properties due to their nanoscale dimensions. Some differences are expected due to the confinement effects in the nanocrystals, the increased importance of the impurity ions at the surface, whose optical properties are modified by the disorder at the surface, and the alteration of the electronic bands of the host. This makes nanocrystals interesting both in terms of their fundamental properties and their potential in a variety of applications.

On the other hand, the synthesis and preparation of nanocrystals of some laser materials is the first step in order to obtain their transparent laser ceramic. The use of ceramics as an alternative to single crystals is justified in some compounds, in which the crystal growth is difficult and has a high cost. Furthermore, the ceramics show better thermo-mechanical properties, such as the thermal shock parameter and resistance to the laser damage [1]. The thermal shock parameter is directly related to the thermal properties of the material; specifically, it is inversely proportional to the linear coefficient of thermal expansion. Furthermore, special attention must be paid to the size of the crystal grains in the ceramic material. It is well-known that ceramics with nano grain size may dis-

play enhanced magnetic and electronic properties with great potential for new applications [2]. Besides, ceramic materials with nano grain size can achieve the theoretical density of the material and their mechanical properties can be improved respect micro-grain size ceramics. Nevertheless, the sintering process to fabricate the ceramic usually causes the grains to grow to a size on the order of a micrometer, range due to the high temperature applied. It has already been reported that the lanthanide doping can affect this grain growth: in Nd:YAG, at higher concentrations than 4 at.% affect the grain size [3].

Two important steps are needed to obtain transparent laser ceramic materials from nanocrystalline powders: high crystalline quality and a narrow size distribution. These two factors allow to prepare a ceramic with a low porosity and a reduced density of scattering defects.

The aim of this paper is to report a low cost method for the synthesis of Lu_{2-x}Tm_xO₃ nanocrystals ($x = 0.01-0.3$), which have been prepared by a modified Pechini method. The rare earth sesquioxides Re₂O₃ can crystallize with the space group *Ia* $\bar{3}$. These compounds are interesting as laser materials for high power applications due to their high thermal conductivity, the possibility of high dopant content and strong crystal field for the active ion. However, obtaining large sesquioxide crystals is a difficult task due to their high melting point (higher than 2773 K) [4].

The Tm³⁺ ion has a large absorption around 785–810 nm which is suitable for GaAlAs laser diode pumping [5]. There is increasing interest in finding new solid state laser systems emitting at around

* Corresponding author.

E-mail address: mariacinta.pujol@urv.cat (M.C. Pujol).

2 μm . At this wavelength range, there is a line of water absorption in the eye safe region, generating many applications of this emission, such as surgery and other medical laser applications, as well as remote sensing of the atmosphere (LIDAR devices) [6]. Furthermore, Tm^{3+} also shows an interesting visible emission located in the blue range, required for applications in colour displays, printing and data recording. Laser Tm^{3+} emission in bulk crystal sesquioxides has been recently reported in [7] exhibiting a broad tunability in the two micron range.

In the present study, we present results on the evolution of the growth of nanoparticles of $\text{Lu}_{2-x}\text{Tm}_x\text{O}_3$ with different Tm^{3+} concentration in function of temperature and the linear thermal expansion coefficient obtained from the analysis of X-ray powder diffraction patterns.

2. Experimental procedure

2.1. Synthesis of the nanocrystals

Tm^{3+} doped Lu_2O_3 nanocrystals $\text{Lu}_{2-x}\text{Tm}_x\text{O}_3$ with $x = 0.01\text{--}0.3$ (i.e., 0.5–15 at.% Tm^{3+}) were synthesized by a modified Pechini method [8] using analytic grade purity reagents (99.9999%). Lu_2O_3 and Tm_2O_3 were dissolved in hot nitric acid to form the nitrate salts. We used ethylenediaminetetraacetic acid (EDTA) as the complexation agent and ethyleneglycol (EG) as the polymerization agent. The nitrates salts were dissolved in an aqueous solution with a molar ratio of EDTA to metal cations $C_M = [\text{EDTA}]/[\text{METAL}] = 1$. In this way, the EDTA forms complexes with the metal cations. Further, EG was added to the mixture in a molar ratio $C_E = [\text{EDTA}]/[\text{EG}] = 2$, and then heated on a hot plate under constant stirring. The solution was dehydrated on the hot plate at 363 K. When the water was removed, an esterification reaction began forming a polymeric viscous white gel, where the cations are randomly dispersed in an organic network. The gel was calcinated at 573 K to eliminate the organic compounds. A brown foam was formed when the organic compounds were calcinated and released in gas form, resulting in a fragile black mass, the precursor powders. Finally, the precursor powders were calcinated at 1073 K for 2 h to obtain the nanocrystalline powder.

2.2. Characterization techniques

Differential thermal analysis (SDT 2960 from TA instruments) of the precursor powders (approximately 10 mg) was conducted using a DTA-TG equipment in an air flow of $90\text{ cm}^3/\text{min}$ at a heating rate of 10 K/min in order to characterize the thermal decomposition. Alumina was used as a reference.

The identification of as synthesized crystallographic phase and the refinement of the unit-cell parameters of the $\text{Tm}:\text{Lu}_2\text{O}_3$ nanocrystals were performed by X-ray powder diffraction (XRPD) analysis by using a Bruker-AXS D8-Discover diffractometer with a parallel incident beam (Göbel mirror) and vertical goniometer, a 0.02 receiving slit and a scintillation counter as the detector. $\text{CuK}\alpha$ radiation was obtained from a copper X-ray tube operated at 40 kV and 40 mA. The measurements were made in step-scanning mode, recorded at $2\theta = 10\text{--}70^\circ$, step size = 0.02° , and step time = 16 s.

The evolution of the unit-cell parameters of $\text{Tm}:\text{Lu}_2\text{O}_3$ nanocrystals as a function of temperature were measured by XRPD analysis using a Siemens D-5000 diffractometer (Bragg–Brentano parafocusing geometry and vertical $\theta\text{--}\theta$ goniometer) equipped with a high-temperature chamber (Anton-Paar HTK10). XRPD patterns were recorded at $2\theta = 10\text{--}70^\circ$, step size = 0.03° , step time = 5 s, at temperatures of 298 K and intervals of 100 K up to 1273 K. The samples were placed on a platinum support. The chosen range of temperatures was large enough to study the behavior

of the nanocrystals during the high temperature sintering process that we plan to apply in the future.

The chemical composition of the nanocrystals was examined by electron probe microanalysis (EPMA) in a Cameca SX50 microprobe analyzer operating in wavelength-dispersive mode. Thulium was measured using the $\text{L}\alpha$ line and Lithium fluoride (LiF) as the analyzing crystal.

An environmental scanning electronic microscope FEI QUANTA 600 was used to observe the prepared $\text{Tm}:\text{Lu}_2\text{O}_3$ nanocrystals. ESEM equipment was used to observe the degree of homogeneity. A transmission electron microscope JEOL JEM-1011 with a MegaView III Soft Imaging System was also used to observe the shape and size of nanoparticles, using a current accelerating voltage of 100 kV. The grain size distributions were measured by the software iTEM Olympus Soft Imaging software, and high-resolution transmission electron microscopy images were obtained by a HRTEM 300 kV Philips CM30 with spectrophotometer Link LZ5.

The crystal habit and morphology of grown nanocrystals were simulated with a Donnay-Harker-based SHAPE software [9].

3. Results and discussion

3.1. Differential thermal analysis and thermogravimetry

Fig. 1 shows the DTA-TG measurements of the precursor powder of $\text{Tm}^{3+}:\text{Lu}_2\text{O}_3$ nanocrystals for Tm^{3+} concentrations between 0.5–15 at.% in the temperature, T , range from 300 to 1200 K. Between 300–550 K, the dehydration of the powder causes a weight loss of about 3%. The strong exothermic peak at 700 K is attributed to the decomposition of the polyester formed by the esterification of ethylene glycol and EDTA, and it is associated on the releasing of CO_2 , H_2O and NO_2 . The interval from 750 to 900 K corresponds to the transformation of the amorphous phase into the crystalline cubic structure. The temperature of the decomposition peak and the final weight loss are not affected in Tm^{3+} content.

3.2. Structural characterization

In all cases, XRPD patterns of the obtained nanocrystals correspond to the pure cubic phase, with space group $Ia\bar{3}$. To facilitate the identification of Bragg reflections corresponding to this phase, Fig. 2 shows the XRPD scheme for Lu_2O_3 (JCPD File 43-1021). The

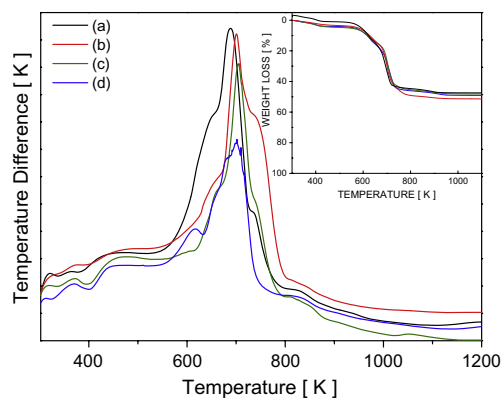


Fig. 1. DTA curves of the precursor powders of $\text{Tm}:\text{Lu}_2\text{O}_3$. (a) 0.5 at.%. (b) 5 at.%. (c) 8 at.%. (d) 15 at.%. TG curves are shown in the inset.

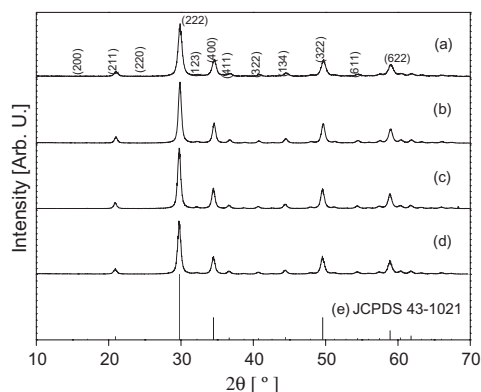


Fig. 2. X-ray diffraction patterns of the Tm:Lu₂O₃ obtained at a calcination temperature of 973 K and 2 h. (a) 15 at.%. (b) 8 at.%. (c) 5 at.%. (d) 0.5 at.%. (e) JCPDS 43-1021 corresponding to Lu₂O₃.

XRPD patterns obtained for the different compositions showed no extra peaks of residual or by-products.

For each composition the lattice parameter *a* was refined using the FULLPROF program [10] based on the Rietveld method [11]. The crystallite size *D*, was estimated using Scherrer's equation $D = K\lambda/(\beta\cos\theta_B)$ for peak broadening due to size effects. β is the FWHM measured in radians on the 2θ scale, λ is the wavelength used, θ_B is the Bragg angle for the measured *hkl* peak and *K* is a constant equal to 0.9 for *D* taken as the volume-averaged crystallite dimension perpendicular to the *hkl* diffraction plane [12].

Table 1 summarizes the refined *a* parameters and estimated *D* values for all prepared Tm³⁺ concentrations. EPMA measured Tm³⁺ concentration values are also included in Table 1. An increase of *a* when the Tm³⁺ concentration increases (Tm³⁺ ionic radii, *r* = 0.880 Å for coordination number, *cn* = 6; Lu³⁺ ionic radii, *r* = 0.861 Å in a coordination number, *cn* = 6) is expected and is present in the results. The distribution of the nanocrystals size was found from 10 to 30 nm with a mean particle size of 17 nm, showing that Tm³⁺ substitution does not change significantly the size of the nanocrystals.

3.3. Morphological characterization

ESEM images displayed in Fig. 3, indicate that the agglomerate size decreases when increases the Tm³⁺ content and their constituting nanocrystals become more easily distinguished. Thus, the Tm³⁺ content play a role on the general aspect of the aggregates, which is similar to changes observed in the morphology of the final product derived of the organic acid used as chelating agent [13].

TEM images of the prepared Tm:Lu₂O₃ nanoparticles are shown in Fig. 4, left. These nanoparticles have a polygonal shape and their size distribution is narrow, ranging from 10 to 30 nm, with mean particle size of 17–23 nm, similar to that estimated from XRPD.

Table 1
Unit cell parameters of the Tm:Lu₂O₃ nanocrystals.

at.% Tm	Stoichiometry	<i>a</i> [Å]	<i>V</i> [Å ³]	<i>D</i> [nm]
0	Lu ₂ O ₃	10.3900(1)[1]	1121.6(1)[1]	–
0.5	Lu _{1.991} Tm _{0.009} O ₃	10.3915(8)	1124.3(2)	15.7
5	Lu _{1.899} Tm _{0.101} O ₃	10.3984(7)	1124.6(3)	17.2
8	Lu _{1.851} Tm _{0.149} O ₃	10.4028(7)	1125.8(2)	16.9
15	–	10.4111(7)	1128.5(2)	16.8

Using SHAPE that applies the Wulff theory to explain the crystal habit and applying that the morphological importance is proportional to $1/d_{hkl}$ (Donnay-Harker theory [14]), we have modeled the crystal habit for Tm:Lu₂O₃ see the regular polyhedron in Fig. 4, right, which is dominated by the crystallographic planes {2 0 0} and {1 1 2}. The crystalline morphology of the grains shown in the TEM micrographs corresponds to this habit.

Fig. 5 shows the size distribution of the nanocrystals, which can be fitted by a lognormal function [15], indicating that they were formed by nucleation, condensation, and particle growth [16,17]. The size distribution histogram has been fitted by the lognormal $N(D) = A \exp[-(\log D - \log D_0)^2/2\sigma^2]$ where *N*(*D*) is the number of particles with a determined size (*D*), *A* is the amplitude of the mode, *D*₀ is the mean value of the studied parameter, and σ is the standard deviation of the mode (2σ is the dispersion of the mode). Fits were done directly on the histogram data, describing a unimodal size distribution. The crystallite size determined by XRPD line broadening, for the samples annealed at 1073 K, correlates rather well with TEM observations, indicating that the particles are individual nanocrystals. The results are summarized in Table 1 and indicate that for all the Tm³⁺ concentrations analyzed, the crystallite size remained almost the same for a given calcination temperature.

In order to get more structural information on the Tm:Lu₂O₃ nanoparticles, high-resolution transmission electron microscopy (HRTEM) analysis was performed. Two HRTEM images obtained at different magnifications are shown in Fig. 6. Lattice fringes with no detectable defects indicate that synthesized materials are composed by single-crystal nanoparticles with high crystallinity degree. Distances between fringes are equal to 5.2 and 3.7 Å, which correspond to the (2 0 0) and (2 2 0) crystallographic planes of the cubic sesquioxide structure, respectively.

3.4. Linear thermal expansion

Usually, the sintering temperature is expected to be around 50–80% of the melting temperature of the compound [4]. As mentioned in the Section 1, the melting temperature of sesquioxides is 2773 K, so the sintering temperature would be in the range 1386–2218 K, following the process reported by Serivalsati et al. [18]. Furthermore, to achieve nanoceramics of YAG materials, by the high pressure low temperature (HPLT) method, a low temperature, such as 723 K, is enough for the preparation of the ceramic material [19]. So, the linear thermal expansion coefficient of each Tm:Lu₂O₃ samples has been measured from room temperature up to 1273 K in an attempt to describe the sintering process.

The linear thermal expansion coefficients in a given crystallographic direction can be expressed as $\alpha = (\Delta L(T)/\Delta T)/L$, where *L* is the initial unit cell parameter at 298 K, $\Delta L(T)$ is the change in this parameter with the temperature *T*, and ΔT is the temperature increase above *T*. The slope of the linear relationship between $(\Delta L(T)/L)$ and *T* coincides with the value of the linear thermal expansion coefficient α . Since Lu₂O₃ has a cubic cell, it exists a unique unit cell parameter *a*, so in this case $L = a$ and Fig. 7 shows the linear relationship between $(\Delta a/a)$ and *T* using a refined values.

Table 2 summarizes α values obtained for Tm:Lu₂O₃ nanocrystals with different Tm³⁺ concentrations. In line with previous values for Tm₂O₃ and Lu₂O₃ bulk single crystals measured by the dilatometric technique [20], $\alpha = 6.8 \times 10^{-6}$ and $\alpha = 5.9 \times 10^{-6} \text{ K}^{-1}$, respectively, we observed an increase of this parameter for the nanocrystals with increasing Tm³⁺ content. There's a dependence of the values of the linear thermal expansion in relation with lanthanide ion concentration and the nature of the lanthanide doping ion [20]. It is expected that mostly in all the cases, the lanthanide doping in Lu₂O₃ will show a linear dependence, as observed in the inset of Fig. 7, an increase of the linear thermal expansion value in

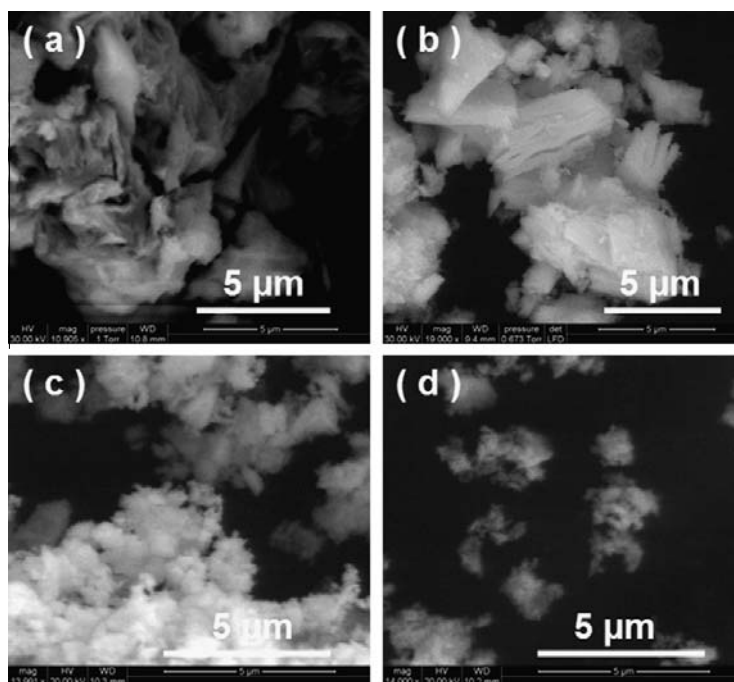


Fig. 3. ESEM images of the Tm:Lu₂O₃ obtained at a calcination temperature of 973 K and 2 h. (a) 0.5 at.%. (b) 5 at.%. (c) 8 at.%. (d) 15 at.%.

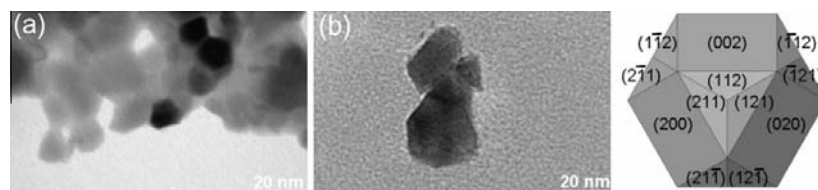


Fig. 4. (left) TEM images of the Tm:Lu₂O₃ obtained at calcination temperature of 973 K and 2 h. (a) 8 at.%. (b) 15 at.%. (right). Scheme of the Lu₂O₃ habit model drawn by Shape software based on the Wulff plot. Projection normal to the [1 1 1] direction.

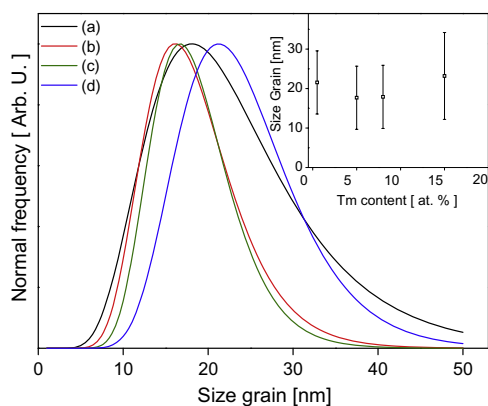


Fig. 5. Size distribution of the Tm:Lu₂O₃ obtained by the Pechini Sol–Gel method. The distributions were measured from TEM micrographs. The mean values are plotted in the inset graph.

relation with the increase of Ln³⁺ doping concentration. The effect of the change of α due to the nano size has not been studied extensively in literature, and it is generally expected an increase of this property with the decrease of the grain size [21]. To elucidate if in the current case this increase can be related to the nano size, an evaluation of α for commercial Lu₂O₃ was performed, which yielded a value of $\alpha = 7.0 \times 10^{-6} \text{ K}^{-1}$. From results summarized in Table 2, it seems that the nano size of prepared materials has no effect on α values. On the other hand, the introduction of Tm³⁺ in the Lu₂O₃ structure of nanocrystals produces the expected slight increase of this coefficient.

3.5. Crystal grain growth as a function of temperature and time

The peak broadening analysis on the diffraction peak (2 2 2) was used to evaluate changes in the size of the crystallite, in relation with temperature and time during isothermal sintering processes. Fig. 8 shows the grain growth during the heat-treatment; this grain growth is very slow or almost nonexistent below 900 K, but above 900 K grain growth develops quickly, increasing

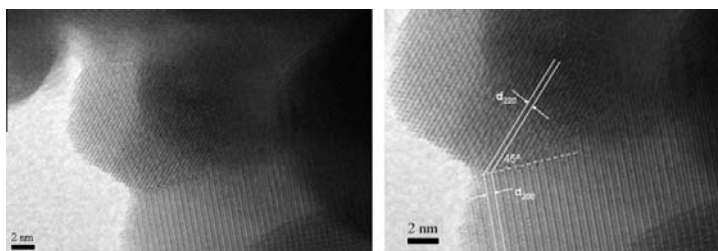


Fig. 6. HRTEM images showing two adjacent grains presenting different crystallographic orientation.

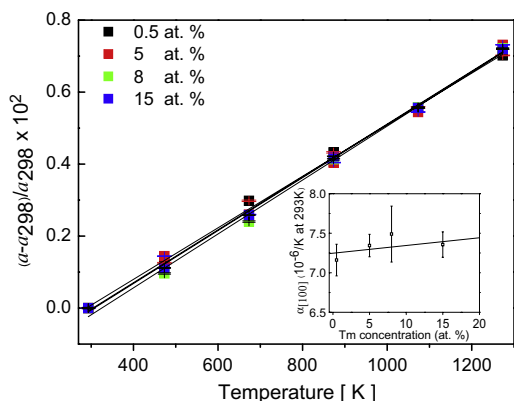


Fig. 7. Relative thermal evolution of the cell parameter a for Tm:Lu₂O₃ nanocrystals. In the inset, the thermal expansion coefficient versus thulium content.

Table 2
 Linear thermal expansion coefficients at 298 K for Tm:Lu₂O₃ nanocrystals.

at.% Tm	Stoichiometry	$\alpha_{[100]}$ [10^{-6} K^{-1}]
0	Lu ₂ O ₃	7.0
0.5	Lu _{1.991} Tm _{0.009} O ₃	7.2(2)
5	Lu _{1.899} Tm _{0.101} O ₃	7.4(1)
8	Lu _{1.851} Tm _{0.149} O ₃	7.5(4)
15	–	7.4(2)

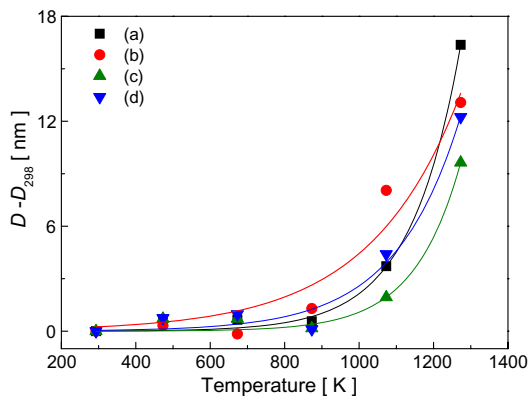


Fig. 8. Thermal dependence of the crystallite size of Tm:Lu₂O₃ obtained from XRD patterns at different temperatures.

the crystallite size. It can also be deduced from Fig. 8, that the grain growth rate does not depend on the Tm³⁺ concentration.

With heating, it is expected that the as-crystallized Tm:Lu₂O₃ nanocrystals can grow by activated atomic diffusion processes at certain temperatures. The Ostwald ripening mechanism describes this process that is due to the merging of the smaller particles into larger ones, and results on potential energy differences between small and large particles. This process can occur through solid state diffusion, so the larger particles grow at the expense of the smaller ones.

The nanocrystal growth was studied as a function of time, (t), versus the isothermal exposure. In this case, crystal growth is found to follow the kinetics $D_t^n - D_{298}^n = Kt$, where D_{298} is the initial nanocrystal size, D_t the crystal size at time t , and K is a time-independent constant that follows the Arrhenius equation $K = K_{298} \exp(-Q/RT)$, in which K_{298} is a constant, Q is the activation energy for grain growth, R is the gas constant, and T is temperature. Normally, the grain growth exponent is equal to $n = 2$, but this exponent depends on different factors, related to the movement of the grain boundary [22]. For the studied sample with 8 at.% Tm³⁺ we estimated values of 1.44 and 1.21 for grain growth at 723 and 873 K, respectively. At 1267 K an exponent value of 2.28 was calculated for the same sample, revealing the activation of the grain growth process.

This kinetics is related with the reduction of the total amount of surface energy, and the growth rate is grain boundary diffusion-controlled [23]. The activation energy, Q , for this surface diffusion and nanocrystals growth process can be extracted from the slope of the plot of $\ln(D_t^2 - D_{298}^2)/t$ versus $1/T$. Fig. 9 shows the plot of crystallite size with time at different isothermal exposures. At temper-

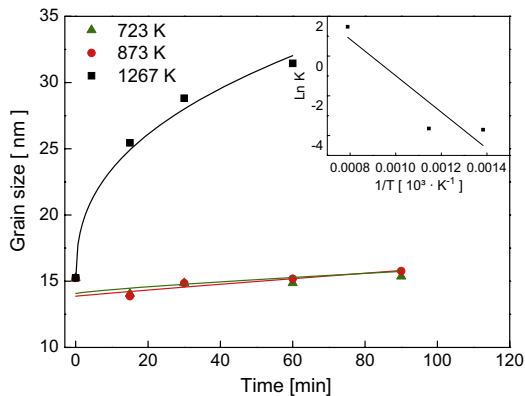


Fig. 9. Curves of the crystallite size of Tm:Lu₂O₃ vs time at different temperatures. Arrhenius plot of Tm:Lu₂O₃ nanocrystals (inset).

atures below 1173 K, the activation energy of the nanocrystalline grain growth process can be estimated as 76 kJ/mol. No previous values were found on the literature for the grain growth activation energy of Lu_2O_3 , however from the order of magnitude of this result, we suggest a diffusion growth mechanism [14,15].

4. Conclusions

Nanocrystals $\text{Tm}:\text{Lu}_2\text{O}_3$ with 0.5%, 5%, 8% and 15% at. Tm^{3+} concentrations were synthesized by a Pechini Sol–Gel method, with a maximum calcination temperature of 1073 K during 2 h. These nanocrystals show a high crystalline degree, with the symmetry of the space group $1a\bar{3}$. No dependence of the size was observed as a function of Tm^{3+} content in $\text{Tm}:\text{Lu}_2\text{O}_3$ nanocrystals, however the increase of the doping level reduces the presence of the agglomerates. The distribution of the nanoparticles was found from 10 to 30 nm with a mean particle size of 17 nm.

Linear thermal expansion has been determined for these nanocrystals, $\alpha \approx 7.5 \times 10^{-6} \text{ K}^{-1}$ and the low increment in this value related to Tm^{3+} content, supports the use of Lu_2O_3 as a host for thulium ions in laser applications.

The crystal growth activation energy between 723–1267 K is $Q \approx 76 \text{ kJ/mol}$, with a grain growth exponent of $n = 2.28$ in the case of $\text{Lu}_{1.851}\text{Tm}_{0.149}\text{O}_3$ nanocrystals.

Acknowledgments

This work was supported by the Spanish government by the Project MAT2008-06729-C02 and from the Catalan government by Project 2009SGR235. E. W. Barrera is supported by Catalan Government for the fund provided through the fellowship 2009FI00148J. J. Carvajal is supported by the Science Ministry of Spain and European Social Fund under the Ramón y Cajal program RYC2006-858. The authors thank the staff of Serveis Científic-Tèc-

nic of the University of Barcelona for the EPMA and electron diffraction measurements.

References

- [1] A. Ikesue, Y.L. Aung, Nat. Photonics 2 (2008) 721.
- [2] H. Gleiter, Nanostruct. Mater. 6 (1995) 3.
- [3] A. Ikesue, I. Furusato, K.J. Kamata, J. Am. Ceram. Soc. 78 (1995) 225.
- [4] L. Fornasiero, E. Mix, Petermann K. Peters, G. Huber, Cryst. Res. Technol. 34 (1999) 255.
- [5] Y. Kalisky, "Two-Micron Lasers: Holmium- and Thulium-Doped Crystals" in The Physics and Engineering of Solid State Lasers, SPIE Press, Bellingham, WA (2006), DOI: 10.1117/3.660249.ch9.
- [6] V. Petrov, F. Güell, J. Massons, J. Gavalda, R.M. Solé, M. Aguiló, F. Díaz, U. Griebner, IEEE J. Quantum Electron. 40 (2004) 1244.
- [7] P. Koopmann, R. Peters, K. Petermann, G. Huber, CLEO/Europe and EQEC 2009 Conference Digest, (Optical Society of America, 2009), paper CA10_3.
- [8] M.P. Pechini, US Patent Specification 3330697 (1967).
- [9] E. Dowty, SHAPE for Windows, Software for Drawing Crystal Shapes, v.7.2.1, 2006.
- [10] J. Rodríguez-Carvajal, Reference Guide for the Computer Program Fullprof. Laboratoire León Brillouin, CEA-CNRS, Saclay, France, 2000.
- [11] H.M. Rietveld, J. Appl. Cryst. 2 (1969) 65.
- [12] B.D. Cullity, Element of X-Ray Diffraction, Addison-Wesley, 1978.
- [13] A. Dupont, C. Parent, B. Le Garrec, J.M. Heintza, Size and morphology control of Y_2O_3 nanopowders via a sol–gel route, J. Solid State Chem. 171 (2003) 152–160.
- [14] J.D.H. Donnay, D. Harker, Am. Mineralogist 22 (1937) 446.
- [15] M. Galceran, M.C. Pujol, J.J. Carvajal, S. Tkaczyk, I.V. Kityk, F. Díaz, M. Aguiló, Nanotechnology 20 (2009), 035705_1–035705_10.
- [16] C.G. Granqvist, R.A. Buhrman, J. Appl. Phys. 47 (1976) 2200–2219.
- [17] J. Söderlund, L.B. Kiss, G.A. Niklasson, C.G. Granqvist, Phys. Rev. Lett. 80 (1998) 2386–2388.
- [18] K. Serivalsatit, B. Yazgan Kokuoz, B. Kokuoz, J. Ballato, Optics Lett. 34 (2009) 1033.
- [19] R. Fedyk, D. Hreniak, W. Lojkowski, W. Strek, H. Matysiak, E. Grzanka, S. Gierlotka, P. Mazur, Opt. Mater. 29 (2007) 1252.
- [20] S. Stecura, W.J. Campbell, Thermal expansion and phase inversion of rare-earth oxides, US Dept. of the Interior, Bureau of Mines, Washington, 1961.
- [21] K. Lu, M.L. Suif, Acta Metall. Mater. 43 (1995) 3325.
- [22] J.E. Burke, D. Turnbull, Prog. Met. Phys. 2 (1952) 220.
- [23] P. Feltham, Acta Metall. 5 (1957) 97.

Paper II

E. W. Barrera, C. Cascales, M. C. Pujol, K. H. Park, S. B. Choi, F. Rotermond, J. J. Carvajal, X. Mateos, M. Aguiló, F. Díaz. *Synthesis of Tm:Lu₂O₃ nanocrystals for phosphor blue applications* **Physics Procedia** 8 142-150 (2010).



VI Encuentro Franco-Español de Química y Física del Estado Sólido
VI^{ème} Rencontre Franco-Espagnole sur la Chimie et la Physique de l'État Solide

Synthesis of Tm:Lu₂O₃ nanocrystals for phosphor blue applications

E. William Barrera^{1,*}, Concepción Cascales², M. Cinta Pujol¹, Kyung Ho Park³, Su Bong Choi⁴, Fabian Rotermund⁴, Joan J. Carvajal¹, X. Mateos¹, Magdalena Aguiló¹, and Francesc Díaz¹

1. Física i Cristal·lografia de Materials i Nanomaterials (FiCMA-FiCNA), Universitat Rovira i Virgili (URV), Campus Sescelades, c/ Marcel·li Domingo, s/n, E-43007 Tarragona, Spain

2 Instituto de Ciencia de Materiales de Madrid, CSIC, Calle Sor Juana Inés de la Cruz, Cantoblanco, E-28049 Madrid, Spain

3. Korea Advanced Nano Fab Center (KANC), 443-270 Suwon, Republic of Korea

4. Division of Energy Systems Research, Ajou University, San 5 Wonchun, 443-749 Suwon, Republic of Korea.

Abstract

Nanocrystalline powder of Tm³⁺ doped lutetium oxide, Tm:Lu₂O₃, has been synthesized by the sol-gel Pechini method. Differential thermal analysis, X-ray powder diffraction and transmission electron microscopy were used to investigate the effect of Tm³⁺ ion on the structure and morphology of samples. In all cases, the obtained nanoparticles crystallize in the cubic system, with space group of symmetry *Ia* $\bar{3}$. The mean particle size was 100–200 nm with crystallite size of 20–30 nm. Optical absorption and cathodoluminescence spectra were recorded. The cathodoluminescence spectra showed an intense blue emission associated to the ¹G₄→³H₆ transition. CIE chromatic coordinates, dominant wavelength and color purity were determined for the evaluation of this material as a potential blue phosphor.

© 2010 Published by Elsevier Ltd.

Keywords : blue phosphor, rare-earth sesquioxide, lutetium oxide, Pechini sol-gel method, thulium spectroscopy.

1. Introduction

Highly transparent cubic ceramic materials Y₃Al₅O₁₂ (YAG) and rare-earth sesquioxides RE₂O₃ have received great attention due to the improvement reached in nanocrystalline technology [1,2,3]. Particularly, the rare earth sesquioxides, the crystal hosts subject of the study of this work, have a very large thermal conductivity and low phonon energy values and they can be highly doped with lanthanide ions. Specially the Lu₂O₃ matrix is highly

* Corresponding author. Tel.: +34- 977-558-790; Fax: +34-977-559-563
Email address: elixirwilliam.barrera@urv.cat

chemically and thermally stable and has a broad optical transparency from the visible to the NIR regions [4]. Due to the similarity of ionic radii between Tm^{3+} and Lu^{3+} ions, Lu_2O_3 shows a high suitability to be doped with thulium ion.

The Tm^{3+} ion has a large absorption around 785-810 nm which is suitable for AlGaAs laser diode pumping [5]. Two micron laser Tm^{3+} emission in bulk crystal sesquioxides has been recently reported in [6] exhibiting a broad tunability. This wavelength emission possesses interesting applications for remote sensing and medicine, for instance, based on the atmospheric transparency window and the absorption of water at this wavelength range. Furthermore, Tm^{3+} also shows an interesting visible emission located in the blue range, required for applications in colour displays, printing and data recording. In this field of applications, the Eu-doped Y_2O_3 sesquioxide, discovered decades ago, is still considered to be one of the best red oxide phosphors, mainly because of its excellent luminescence efficiency, color purity, and stability.

In order to study the possibility of a Tm^{3+} based sesquioxide phosphor, we prepared $\text{Lu}_{2-x}\text{Tm}_x\text{O}_3$ nanocrystals ($x=0.01-0.3$), using a sol-gel Pechini method and optical absorption and cathodoluminescence properties were investigated.

2. Experimental Procedure

2.1-Synthesis of the nanocrystals

Tm^{3+} doped Lu_2O_3 nanocrystals $\text{Lu}_{2-x}\text{Tm}_x\text{O}_3$ with $x = 0.01 - 0.3$ (i.e., 0.5 - 15 at. % Tm^{3+}) were synthesized by a sol-gel Pechini method [7] using analytic grade purity reagents (99.9999%). The precursor oxides, Lu_2O_3 and Tm_2O_3 , were dissolved in hot nitric acid and heated until evaporation to precipitate the nitrate salts. We used ethylenediaminetetraacetic acid (EDTA) as complexation agent and ethylenglycol (EG) as polymerization agent. The nitrates salts were dissolved in an aqueous solution with a molar ratio of EDTA to metal cations $C_M=[\text{EDTA}]/[\text{METAL}] = 1$. In this way, the EDTA forms complexes with the metal cations. Further, EG was added to the mixture in a molar ratio $C_E=[\text{EDTA}]/[\text{EG}]=2$, and then heated on a hot plate under constant stirring. The obtained solution was dehydrated on the hot plate at 363 K. When the water was removed, an esterification reaction began forming a polymeric viscous white gel, where the cations are randomly dispersed in an organic network. The gel was calcinated at 573 K, generating a brown foam that finally became into a fragile black mass, the precursor powder. Finally, the precursor powder were calcinated at 1073 K for 2 h to obtain the nanocrystalline product.

2.2-Characterization techniques

The precursor powders were analyzed by differential thermal analysis (using DTA-TG equipment SDT 2960 from TA instruments) in air flow of $90 \text{ cm}^3/\text{min}$ at a heating rate of 10 K/min in order to characterize the thermal decomposition. The weight of the sample and the weight of alumina used as a reference was approximately 10 mg. The structural identification of the synthesized crystallographic phase and the refinement of the unit cell parameters of the $\text{Tm}:\text{Lu}_2\text{O}_3$ nanocrystals was carried out with X-ray powder diffraction (XRPD) data collected by using a Bruker-AXS D8-Discover diffractometer with a parallel incident beam (Göbel mirror) and vertical goniometer, a 0.02 receiving slit and a scintillation counter as detector. $\text{Cu } K\alpha$ radiation was obtained from a copper X-ray tube operated at 40 kV and 40 mA. Step-scanning mode was used, recorded at $2\theta=10-70^\circ$ with a step size $=0.02^\circ$, and step time = 16 s.

The evolution of the unit-cell parameters of $\text{Tm}:\text{Lu}_2\text{O}_3$ nanocrystals as a function of temperature were measured by XRPD analysis using a Siemens D-5000 diffractometer (Bragg-Brentano parafocusing geometry and vertical $\theta-\theta$ goniometer) equipped with a high-temperature chamber (Anton-Paar HTK10). XRPD patterns were recorded also at $2\theta = 10-70^\circ$, step size = 0.03° and step time = 5 s, at temperatures of 298 K and intervals of 100 K up to 1273 K.

The chemical composition of the nanocrystals was examined by electron probe microanalysis (EPMA) in a Cameca SX50 microprobe analyzer operating in wavelength-dispersive mode. Thulium and lutetium concentrations were measured using the $L\alpha$ line and Lithium fluoride (LiF) as analyzing crystal.

A transmission electron microscope JEOL JEM-1011 equipped with MegaView III Soft Imaging System was also used to observe the shape and size of the nanoparticles, using a current accelerating voltage of 100 kV. The grain size histograms were measured by the iTEM Olympus Soft Imaging software and adjusted to a log-normal distribution to calculate the mean size and standard deviation. High-resolution transmission electron microscopy images were obtained by a HRTEM 300 kV Philips CM30 with spectrophotometer Link LZ5.

The crystal habit and morphology of the grown nanocrystals were simulated using a Donnay-Harker-based SHAPE software [8].

Optical absorption of Tm:Lu₂O₃ nanocrystals was recorded at room temperature (RT) and low temperature (6 K) using a Cary Varian 500 spectrophotometer. In each case, the sample was cooled with a Leybold RDK-6-320 closed-cycle Helium cryostat. Cathodoluminescent properties of the thulium doped nanocrystals have been investigated by an excitation voltage of 15 kV and the probe current 20 nA.

3. Results and Discussion

3.1- Differential thermal analysis and thermogravimetry

Figure 1 shows the DTA-TG measurements of the precursor powder of Tm³⁺:Lu₂O₃ nanocrystals for Tm³⁺ concentrations between 0.5-15 at. % in the temperature range from 300 to 1200 K. Between 300-550 K, the dehydration of the powder causes a weight loss of about 3%. The strong exothermic peak at 700 K is attributed to the decomposition of the polyester formed by the esterification of ethylene glycol and EDTA, and it is associated on the releasing of CO₂, H₂O and NO₂. The interval from 750 K to 900 K corresponds to the transformation of the amorphous phase into the crystalline cubic structure. The temperature of decomposition and the final weight loss of the sample seem not be affected by the Tm³⁺ content. EPMA measured Tm³⁺ concentration of the final product matches in each case the expected one from the stoichiometry of the corresponding precursors. No evaporation of the metal ions has been observed.

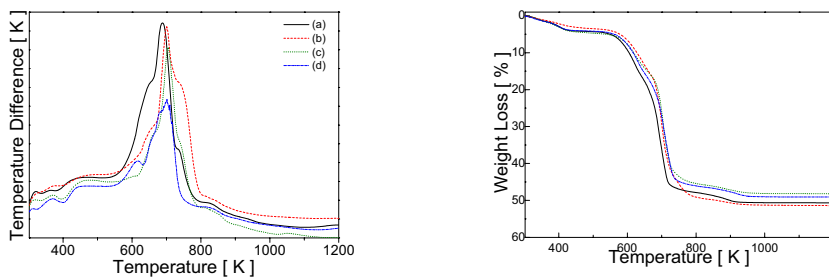


Figure 1. DTA curve of the precursor powders of Tm:Lu₂O₃ (left). TG curves showing the weight loss during the calcination process (right) 0.5 at. % Tm³⁺ (b) 5 at. % Tm³⁺ (c) 8 at. % Tm³⁺ (d) 15 at. % Tm³⁺.

3.2- Structural characterization

In all cases, the XRPD patterns of the obtained nanocrystals correspond to the pure cubic phase, with space group *Ia* $\bar{3}$. To facilitate the identification of Bragg reflections corresponding to this phase, Figure 2 shows the XRPD pattern for Lu₂O₃ (JCPD File 43-1021).

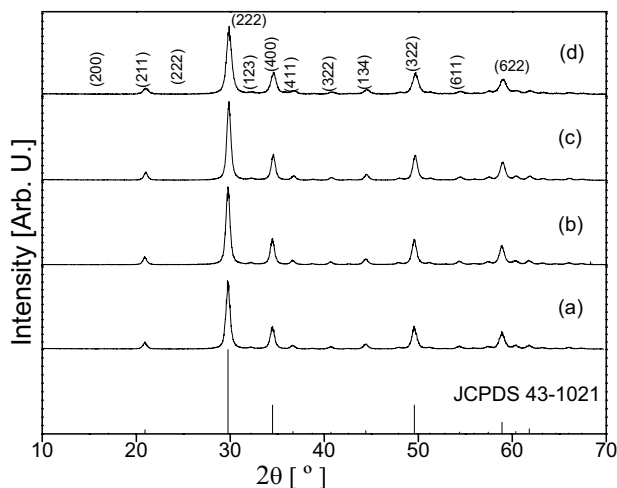


Figure 2. X-ray diffraction patterns of the Tm:Lu₂O₃ nanocrystals obtained at a calcination temperature of 1073 K during 2 h. 0.5 at. % Tm³⁺ (b) 5 at. % Tm³⁺ (c) 8 at. % Tm³⁺ (d) 15 at. % Tm³⁺.

The XRPD patterns obtained for the different compositions showed no extra peaks of residual products. For each composition the lattice parameter a was refined using the Fullprof program [9] based on the Rietveld method [10]. An increase of a when the Tm³⁺ concentration increases (Tm³⁺ ionic radii, $r_{\text{ir}} = 0.880 \text{ \AA}$ for coordination number, $\text{cn} = 6$; Lu³⁺ $r_{\text{ir}} = 0.861 \text{ \AA}$, $\text{cn} = 6$) is expected and it was observed in the results presented in Figure 3.

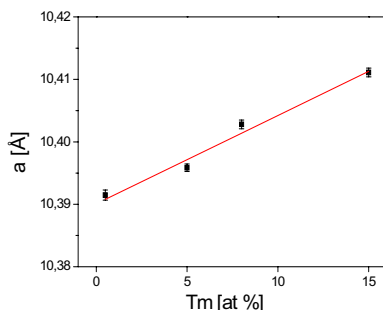


Figure 3. Cell parameters versus Tm doping concentration in the Lu₂O₃

The crystallite size D , was estimated using the Scherrer's equation $D = K\lambda / (\beta \cos \theta_B)$ for peak broadening due to size effects. β is the full-width at half maximum measured in radians on the 2θ scale, λ is the wavelength used, θ_B is the Bragg angle for the measured hkl peak and K is a constant equal to 0.9 for D taken as the volume-averaged

crystallite dimension perpendicular to the hkl diffraction plane [11]. The crystallite sizes determined by XRPD line broadening are presented in Table 1.

Table 1. Tm:Lu₂O₃ nanocrystals composition and size distribution

at. % Tm	Stoichiometry	Crystallite Size [nm]	Particle Size [nm]
0.5	Lu _{1.991} Tm _{0.009} O ₃	15.7	87±30
5	Lu _{1.899} Tm _{0.101} O ₃	17.2	233±119
8	Lu _{1.851} Tm _{0.149} O ₃	16.9	236±138
15	Lu _{1.713} Tm _{0.287} O ₃	16.8	200±133

3.3- Morphology and size distribution characterization

Using the Shape utility that applies the Wulff theorem $R(hkl)$, we have modeled the crystal habit for Tm:Lu₂O₃ shown as a regular polyhedron in Figure 4, which is dominated by the crystallographic planes $\{2\ 0\ 0\}$ and $\{1\ 1\ 2\}$. The morphology of the crystallites in the TEM micrographs shown as insets in Figure 5 seems to correspond to this habit. The detailed observation of these images indicates that the crystallite size is approximately 20 - 30 nm, near to those values estimated from XRPD data. There is no effect of the Tm³⁺ content on the size of individual nanocrystallites. Particle size distributions of Tm:Lu₂O₃ powders calcined at 1073 K for 2 h are shown in Figure 5. These distributions were fitted to a lognormal distribution [12], indicating that the particles were formed by nucleation, condensation, and particle growth [13,14]. The mean values and standard deviations obtained from fittings of the histograms are summarized in Table 1. Aggregation of the nanocrystals into larger polycrystalline particles was observed in all samples, forming particles with 100-300 nm in size. It was not possible to resolve these aggregates as groups of nanoparticles in all cases, so the size distributions became wider because they were taken in account as single particle by the software.

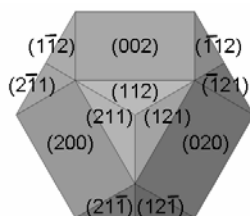


Figure 4. Scheme of the Lu₂O₃ habit model. Projection normal to the [111] direction

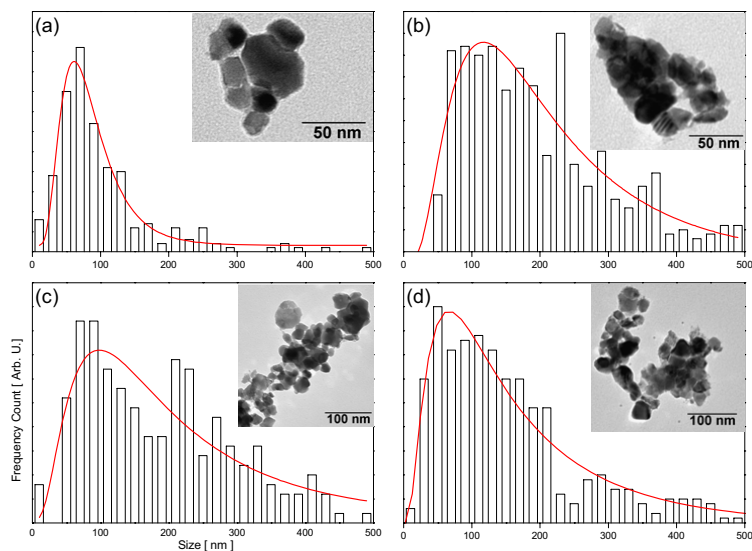


Figure 5. Size distributions and TEM micrographs for (a) 0.5 at. % Tm³⁺ (b) 5 at. % Tm³⁺ (c) 8 at. % Tm³⁺ (d) 15 at. % Tm³⁺.

In order to get more structural information of the Tm:Lu₂O₃ nanoparticles, HRTEM analysis was performed. The image shown in Figure 6 presents the grain boundary between two adjacent grains, distinguished by the lines corresponding to different crystallographic planes. Lattice fringes with no detectable defects indicate that the synthesized materials are composed by single-crystal nanoparticles with high crystallinity degree. Distances between fringes are equal to 5.2 Å and 3.7 Å, which correspond to the (200) and (220) crystallographic planes of the cubic sesquioxide Lu₂O₃ structure, respectively.

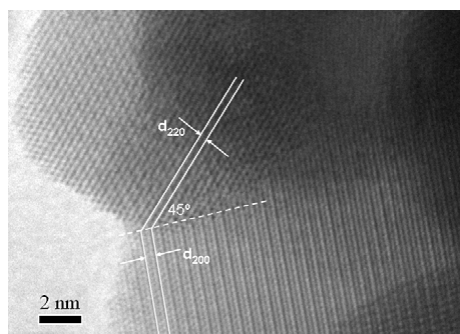


Figure 6. HRTEM images showing two adjacent nanocrystals of Tm-Lu₂O₃

3.4. Optical Absorption

Figure 7 shows the main optical absorption bands observed for Tm:Lu₂O₃ nanocrystals in the 430-1720 nm (23255-5814 cm⁻¹) spectral range. Tm³⁺ is expected to substitute the Lu³⁺ ion in the two C₂ and C_{3v}, C_{3i} symmetry sites present in the unit cell of Lu₂O₃, in 3:1 ratio, without preferential occupation. C_{3i} is a centro symmetric site, so only magnetic dipole transitions will be allowed from it. Thus, the optical absorption peaks in Figure 7 correspond to the allowed induced dipole electronic transitions from 4f¹² Stark levels of Tm³⁺ located in C₂ sites and magnetic dipole transitions (i.e., the ³H₆→³H₅ transition) from both kinds of sites. [15]. The highest absorption intensity observed for Tm³⁺ in these nanocrystals is, as expected, for the electronic transition ³H₆ → ³H₄ located at 800 nm. The maximum intensity peak of absorption in this manifold is located at 796 nm.

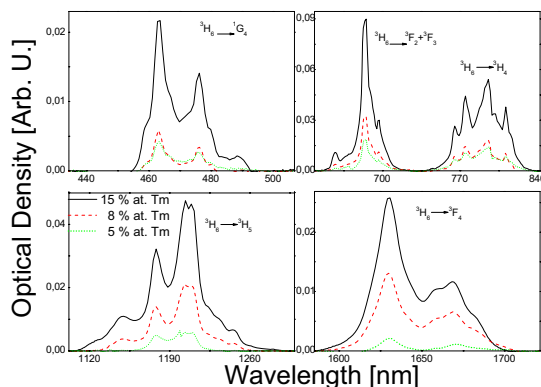


Figure 7. Room temperature optical absorption in the range 430 -1720 nm for Tm:Lu₂O₃ nanocrystals.

3.5. Cathodoluminescence and Chromaticity

Figure 8 shows the cathodoluminescence spectrum for the 15 at. % Tm³⁺ sample at room temperature. The major peak centered at 457 nm corresponds to the transition from ¹G₄→³H₆, while the transitions from ¹D₂→³H₆, and ¹G₄→³H₅ of the Tm³⁺ ion are related to the emission peaks at 364 and 813 nm, respectively. Furthermore, a broad band emission, acting as background is observed in the 300-550 spectral region. It could be attributed to radiative recombination at defects involving oxygen vacancies [16], and it is characteristic of nanocrystalline particles [17].

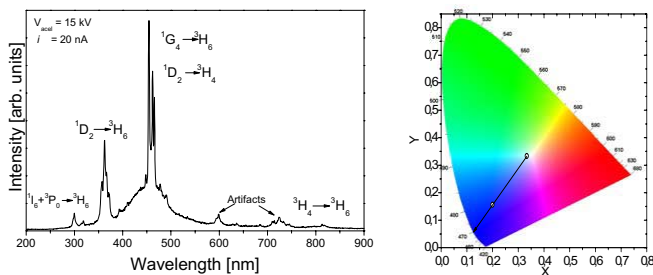


Figure 8. Cathodoluminescence spectra of 15 at. % Tm:Lu₂O₃ at room temperature (left). CIE Diagram corresponding to the cathodoluminescent emission (right).

A careful determination of the characteristics of the color is important for further applications of this material as a phosphor. The CIE chromatic coordinates (x, y, z) can be calculated from the tristimulus ratios as follow

$$x = \frac{X}{X + Y + Z}$$
$$y = \frac{Y}{X + Y + Z}$$
$$z = \frac{Z}{X + Y + Z}$$

Where the tristimulus values (X, Y, Z) can be calculated by following integrations over the entire visible spectrum:

$$X = \int \bar{x}(\lambda) s(\lambda) d\lambda$$

$$Y = \int \bar{y}(\lambda) s(\lambda) d\lambda$$

$$Z = \int \bar{z}(\lambda) s(\lambda) d\lambda$$

$\bar{x}(\lambda)$, $\bar{y}(\lambda)$ and $\bar{z}(\lambda)$ are the color matching functions that model the response of the photoreceptors in the human eye, and $s(\lambda)$ is the emission spectrum of interest. The blue emission of the thulium doped nanocrystals has a CIE chromaticity coordinates of $x=0.200$, $y=0.156$. The dominant wavelength was calculated by extrapolation of the line from the white point (1/3, 1/3) to the boundary of the diagram that includes a given point (x, y) . The dominant wavelength value was 468 nm.

The color purity is defined as the ratio of the distance from the white point (1/3, 1/3) to a given coordinate (x, y) and distance from the white point to the boundary intersection [18]. A color purity of 54% has been obtained in comparison with CIE Standard Illuminant C. This values are similar to the ones reported in the literature for Tm:Y₂O₃ films with CIE (x, y) (0.158, 1.50), dominant wavelength at 476 nm and 78% purity [19].

4. Conclusions

Nanocrystals Tm:Lu₂O₃ with 0.5, 5, 8 and 15 at. % Tm³⁺ concentrations were synthesized by the Sol-Gel Pechini method, with a calcination temperature of 1073 K during 2 h. These nanocrystals show a high crystalline degree in the cubic system, with the space group symmetry $Ia\bar{3}$. For all Tm³⁺ concentrations analyzed, there is not effect of Tm³⁺ content on the crystallite size. The maximum absorption is centered at 796nm, corresponding to the electronic transition ³H₆→³H₄, in agreement with the bulk single crystal. Cathodoluminescence spectra showed that the Tm doped Lu₂O₃ have a light emission in the blue region at the wavelength of 457 nm corresponding to the ¹G₄→³H₆ transition, with a rather low purity of 54%.

Acknowledgments

This work is supported by the Spanish Government under projects MAT2008-06729-C02-01-02/NAN, MAT2008-04046-E/MAT, TEC2010-21574-C02-02 and the project PI09/90527; and the Catalan Authority under project 2009SGR235 and FP7-SPA-2010-263044. E. W. Barrera is supported by Catalan Government for the fund provided through the fellowship 2009FI00148. J. J. Carvajal is supported by the education and Science ministry of Spain and European Social Fund under Ramon y Cajal program RYC2006-258.

References

-
- [1] T. Yanagitani, H. Yagi, Y. Yamasaki. (1998) *Japanese Patent No. 10-101411*
- [2] A. Ikesue, Y. Lin Aung, (2008) *Nature Photonic*, 2, 721-727.
- [3] T. Yanagitani, M. H. Yagi, M. Ichikawa. (1998) *Japanese Patent No. 10-101333*
- [4] Q. Chen, Y. Shi, L. An, J. Chen and J. Shi (2006) *J. Am. Ceram. Soc* 89, 2038 - 2042
- [5] Y. Kalisky, (2006) *The Physics and Engineering of Solid State Lasers*, SPIE Press, Bellingham, WA.
- [6] P. Koopmann, R. Peters, K. Petermann, G. Huber, (2009) *Highly Efficient, Broadly Tunable Tm:Lu₂O₃ Laser at 2 μm*. In: CLEO/Europe and EQEC 2009 Conference Digest, (2009), paper CA10_3.
- [7] M. Galceran, M. C. Pujol, M. Aguiló, F. Díaz, (2008) *Mat. Sci. Eng. B* 146 7.
- [8] E. Dowty, (2006) *SHAPE for Windows, Software for Drawing Crystal Shapes*, v.7.2.1.,
- [9] J. Rodriguez-Carvajal, (2000) *Reference Guide for the Computer Program Fullprof*. Laboratoire Léon Brillouin. CEA-CNRS.Saclay, France..
- [10] H. M. Rietveld, (1969) *J. Appl. Cryst.* 2 65.
- [11] B. D. Cullity, (1978) *Element of X-Ray Diffraction*, Addison-Wesley.
- [12] M. Galceran, M.C. Pujol, J. J. Carvajal, S. Tkaczyk, I.V. Kityk, F. Díaz, M. Aguiló, (2009) *Nanotechnology* 20 035705_1-035705_10.
- [13] C. G. Granqvist, R. A. Buhrman (1976) *J. Appl. Phys.* 47 2200-2219.
- [14] J. Söderlund, L. B. Kiss, G. A. Niklasson, C. G. Granqvist, (1998) *Phys. Rev. Lett.* 80 2386-2388
- [15] G. Concas, G. Spano, M. Bettinelli, and A. Speghini (2003) "Investigation of Eu³⁺ Site Occupancy in Cubic Y₂O₃ and Lu₂O₃ Nanocrystals" *Z. Naturforsch.* 58a, 551 – 557
- [16] E. Nogales ; B. Méndez; J. Piqueras, (2008), *Nanotech*, 19, 035713
- [17] C. M. Donega, E. Zych, A. Meijerink, (2001) *Mat. Res. Soc. Symp. Proc.* 667.
- [18] R.C. Ropp, *Luminescence and the Solid State*, (1991), Elsevier.
- [19] J. Hao, S.A. Studenikin, M. Cocivera, (2001) *J. Luminescence* 93 313–319

UNIVERSITAT ROVIRA I VIRGILI
LANTHANIDE-BASED DIELECTRIC NANOPARTICLES FOR UPCONVERSION LUMINESCENCE
Elixir William Barrera Bello
Dipòsit Legal: T. 450-2013

Paper III

E. W. Barrera, M. C. Pujol, C. Cascales, C. Zaldo, K. H. Park, S. B. Choi, F. Rotermond, J. J. Carvajal, X. Mateos, M. Aguiló, and F. Díaz, *Spectroscopic characterization of sol-gel synthesized Tm:Lu₂O₃ nanocrystals* **Applied Physics B: Lasers and Optics**, 106 409-417 (2012).

Spectroscopic characterization of sol–gel synthesized Tm:Lu₂O₃ nanocrystals

E.W. Barrera · M.C. Pujol · C. Cascales · C. Zaldo ·
K.H. Park · S.B. Choi · F. Rotermund · J.J. Carvajal ·
X. Mateos · M. Aguiló · F. Díaz

Received: 29 March 2011 / Revised version: 30 June 2011 / Published online: 28 August 2011
© Springer-Verlag 2011

Abstract Thulium-doped Lu₂O₃ nanocrystals with $Ia\bar{3}$ cubic phase and mean grain size of 17 nm were synthesized by using a modified Pechini method. Their spectroscopic properties have been characterized by Raman, optical absorption, photoluminescence and cathodoluminescence spectroscopies at low and room temperatures, with emphasis on blue and infrared emissions. The reduction of the crystal size induces an increase of the optical line widths and new non-radiative de-excitation paths ascribed to a surface effect.

1 Introduction

Improvements in nanotechnology have motivated the recent development of nanocrystalline rare earth (RE) cubic sesquioxides RE₂O₃ as precursors for fabricating highly transparent nanoceramics aimed at laser applications [1].

Laser applications are promoted by the high thermal conductivity and moderate phonon energies of RE₂O₃ materials, which also can be doped with fluorescent trivalent lanthanide (Ln) ions up to the stoichiometric composition. In this field, the interest for Tm³⁺–RE₂O₃ laser nanoceramics is driven by the broadly tunable, $\lambda = 1.8$ – $2.1 \mu\text{m}$, ³F₄ → ³H₆ laser emission. Such spectral region includes atmospheric transparency windows as well as absorption bands of common pollutant gases, such as CO₂ and NO, and therefore Tm lasers are used for remote sensing. Alternatively, Tm-based lasers are being developed as depth-selective surgical scalpels due to the favorable coincidence with the 1.94- μm absorption peak of water [2, 3].

On the other hand, in lighting applications Eu-doped Y₂O₃ is still considered to be one of the best red down-converting oxide phosphors, mainly because of its excellent luminescence efficiency, color purity and stability [4]. Furthermore, other Ln–RE₂O₃ nanostructures are searched for as lighting phosphors by up-conversion. In this context, several effects related with the nanodimension have been reported, including the redistribution of the emission intensity of the possible de-excitation paths and the modification of the radiative and non-radiative processes [5–7]. Tm³⁺–RE₂O₃ nanocrystals whose blue (¹G₄ → ³H₆) emission can be excited in the near infrared (NIR) ($\lambda_{\text{EXC}} \sim 800 \text{ nm}$, ³H₆ → ³H₄) by up-conversion are an option for blue phosphors. The long lifetime of the intermediate state (³H₄) favors the up-conversion process.

Among the different RE₂O₃ host options, Lu₂O₃ has high chemical and thermal stability and broad optical transparency from the visible to the mid-infrared (MIR) optical regions [8]. Due to the similar ionic radii between Tm³⁺ and Lu³⁺, Lu₂O₃ is the most appropriate host for Tm³⁺. Furthermore, Tm³⁺ in Lu₂O₃ shows optical absorption and emission cross sections as well as crystal field split-

E.W. Barrera · M.C. Pujol (✉) · J.J. Carvajal · X. Mateos ·
M. Aguiló · F. Díaz
Física i Cristallografia de Materials i Nanomaterials
(FiCMA-FiCNA), Universitat Rovira i Virgili (URV),
Campus Sescelades, c/ Marcell·l Domingo, s/n, 43007 Tarragona,
Spain
e-mail: mariacinta.pujol@urv.cat

C. Cascales · C. Zaldo
Instituto de Ciencia de Materiales de Madrid,
CSIC, c/ Sor Juana Inés de la Cruz 3, Cantoblanco,
28049 Madrid, Spain

K.H. Park
Korea Advanced Nano Fab Center (KANC), 443-270 Suwon,
Republic of Korea

S.B. Choi · F. Rotermund
Division of Energy Systems Research, Ajou University, San 5
Wonchun, 443-749 Suwon, Republic of Korea

tings superior to those observed for corresponding Y- or Gd-based sesquioxides. The growth of high-quality Tm^{3+} - Lu_2O_3 bulk single crystals is difficult due to the high melting temperature (over 2673 K). Therefore, the synthesis at low temperature of Tm^{3+} - Lu_2O_3 nanocrystals with high crystalline quality and narrow distribution of size is of prime interest for obtaining the optimum precursor for sintering transparent Lu_2O_3 ceramics. Here we report the synthesis at 1073 K (i.e. 1600 K below the Lu_2O_3 melting point) of Lu_2O_3 nanocrystals doped with different concentrations of Tm^{3+} (0.5, 5, 8 and 15 at.%). For this purpose, a modified Pechini sol-gel method was used. The optical spectroscopic properties (absorption, photoluminescence and cathodoluminescence) of these nanocrystals are presented.

2 Experimental procedure

A modified Pechini method with previously optimized experimental parameters [9] was used to prepare the Tm-doped Lu_2O_3 nanocrystals. This method uses the ability of a carboxylic acid, in this case ethylenediaminetetraacetic acid (EDTA), to form in solution chelated complexes with metallic cations (METAL). The used sources of metallic cations were commercial 99.9999% Lu_2O_3 and Tm_2O_3 (Metall. China) oxides. These oxides were dissolved in nitric acid (68%) to form nitrate salts after water evaporation. The nitrates were dissolved in an aqueous EDTA solution with a molar ratio of complexing agent (CA) to metal ions of $C_M = 1$ (molar ratio $C_M = [\text{CA}]/[\text{METAL}]$ [10]). Subsequently, ethylene glycol (EG), acting as an esterification agent, was added with a molar ratio to organic acid of $C_E = 2$ (molar ratio $C_E = [\text{CA}]/[\text{EG}]$ [10]). This solution was dried in a muffle preheated at 573 K to obtain the precursor powder. A calcination program was applied to the precursor powder as described previously [10]. The optimal temperature at which these crystals were synthesized was 1073 K.

The shape and size of nanocrystals were observed by transmission electron microscopy (TEM) in a JEOL JEM-1011 microscope with a MegaView III Soft Imaging System. The microscope was operated at a current accelerating voltage of 100 kV. The composition of the nanocrystals was measured by electron probe microanalysis (EPMA) using a Cameca Camebax SX 50. $L\alpha$ and $K\alpha$ X-ray emissions were used for the evaluation of the Lu and O compositions, respectively, taking as reference the signal of $\text{KLu}(\text{WO}_4)_2$ single crystal. The Tm $L\alpha$ emission and a REE2 standard (P&H Developments) were used to determine the Tm concentration.

X-ray powder diffraction (XRD) patterns were recorded using a Bruker-AXS D8-Discover diffractometer with a parallel incident beam (Göbel mirror) and vertical goniometer.

The signal on the scintillation counter detector was limited by a 0.02 mm receiving slit. $\text{Cu K}\alpha$ radiation ($\lambda = 0.154247$ nm) was obtained from an X-ray tube operated at 40 kV and 40 mA. Measurements were taken in step-scanning mode, the diffraction angle (2θ) ranged from 10° to 70° with a step size of 0.02° and the integration time at each step was 16 s. Crystal lattice parameters were calculated using the FULLPROF program based on the Rietveld method [11].

Raman measurements were performed using a Renishaw inVia micro-Raman system equipped with a microscope and a CCD camera as the detector. An Ar laser (514 nm) at a power level of 25 mW was used as the excitation source.

Optical absorption (OA) measurements were collected at room temperature (RT) and low temperature (6 K) by using a Varian Cary 500 spectrophotometer and a Leybold RDK-6-320 closed-cycle helium cryostat. Lu_2O_3 powder was mixed with KBr in a weight ratio of 1:10 to form pellets.

Tm^{3+} photoluminescence (PL) was excited at 300 K with a Quanta-Ray MOPO-HF optical parametric oscillator. This tunable laser system provides optical pulses shorter than 5 ns from 730 to 1750 nm. Pulse energy at $\lambda = 800$ nm was ≈ 32 mJ. Fluorescence was dispersed by a single-grating SPEX spectrometer ($f = 34$ cm) and measured by a Hamamatsu H9170-75 InP/InGaAs cooled photomultiplier tube (PMT) working at 213 K sensitive in the 950–1700 nm range with a rise time of 0.9 ns, or by an InAs Hamamatsu photovoltaic detector cooled with liquid nitrogen and sensitive in the 1500–3100 nm range with a rise time of 0.1 ms. The electrical signals were recorded with either a lock-in amplifier for emission and excitation spectra or with a Tektronix TDS-520 500-MHz oscilloscope for lifetime measurements. A long-wavelength pass filter with a cutting edge at 1000 nm was used to remove background excitation light.

Cathodoluminescence (CL) of the thulium-doped nanocrystals was measured at room temperature using a Gatan MonoCL3+ system attached on a Schottky-type field-emission scanning electron microscope (SEM: Hitachi S4300SE). The CL signal was dispersed by a 1200 lines/mm grating blazed at 500 nm and CL spectra and images were recorded using a Peltier-cooled Hamamatsu R943-02 PMT.

3 Results and discussion

3.1 Morphological characterization

Figure 1a–d show a collection of TEM images of nanocrystals with increasing Tm concentration synthesized by 1-h annealing at 1073 K. The reproducibility of the synthesis process is observed, with the grain size in the range of 10–60 nm, and similar polygonal shape for the different Tm^{3+} contents. All TEM images show agglomerates, which indicate strong Van der Waals surface interactions between the nanocrystals.

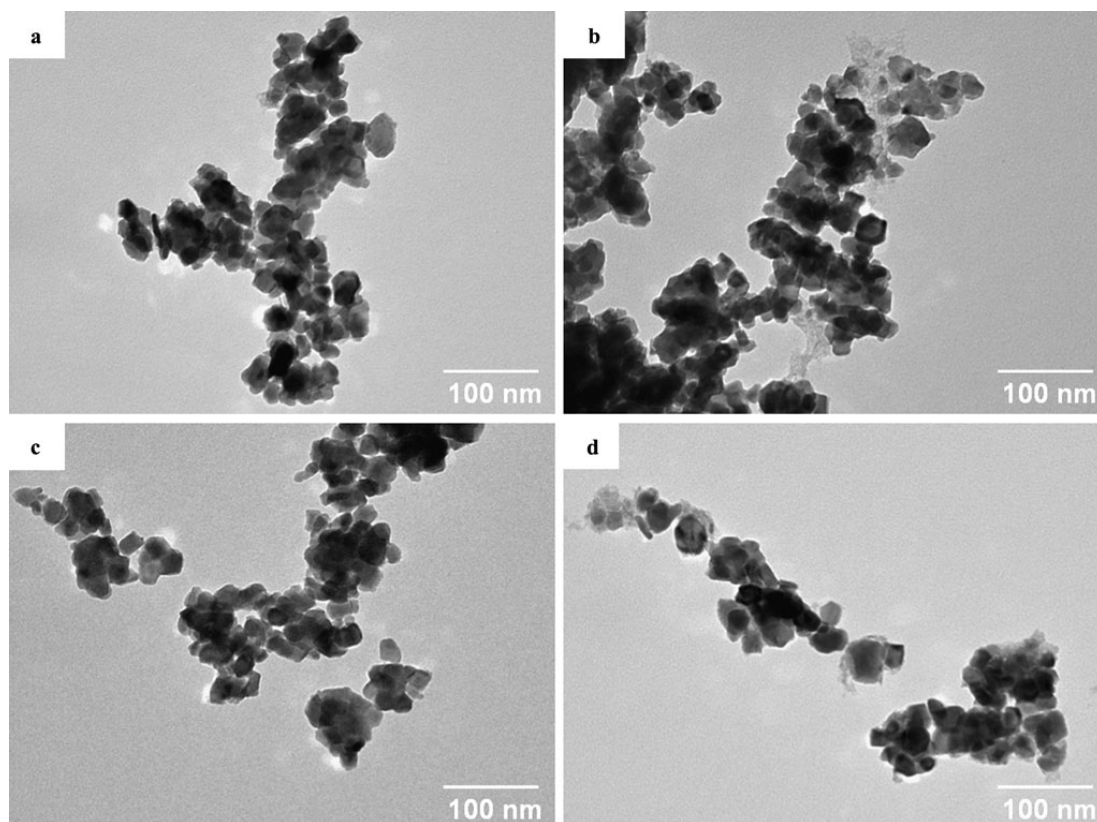


Fig. 1 TEM images of nanocrystals with different Tm concentrations. 0.5 at.% (a), 5 at.% (b), 8 at.% (c) and 15 at.% (d)

3.2 Structural characterization

XRD patterns were indexed by the cubic $Ia\bar{3}$ space group structure (JCPDS 43-1021 card). The refinement of the crystalline structure provided the unit-cell parameters and cell volumes summarized in Table 1. The incorporation of Tm³⁺ to the Lu₂O₃ host increases the cell volume according to previous discussions [12]. Tm atomic densities, [Tm], also summarized in Table 1 were determined using the compositions obtained by EPMA and the cell parameters obtained by XRD. The crystallite sizes, D , included in Table 1 were determined by using Scherrer's equation $D = K\lambda/(\beta \cos \theta_B)$ for peak broadening due to size effects, in the range of validity for small particles <500 nm [13]. In the formula above, K is a peak shape related constant ($K = 0.9$ for a Gaussian peak), β represents the X-ray peak line width and θ_B is the diffraction angle for the selected X-ray reflection.

A Raman study was also performed to assess the crystalline structure of the nanopowders. Possible shifting and broadening in the Raman peaks of nanocrystals have been

attributed to the presence of dislocations and oxygen vacancies in nanocrystals as compared to bulk single crystals due to the preparation method and to the high surface area of nanocrystals [14]. Figure 2 shows the Raman spectra observed for Lu_{2-x}Tm_xO₃ nanocrystals. The optically active phonons can be separated into two groups: above 300 cm⁻¹ the observed modes correspond to internal vibrations of Lu(Tm)O₆ octahedra, whereas below 200 cm⁻¹ the modes are ascribed to translational motions of these octahedra. Also, in the Raman spectra in air, OH⁻ bands related with the hydroscopic nature of Lu₂O₃ were observed above 3000 cm⁻¹, but not presented here.

Taking into account the irreducible representation of the factor group analysis for $Ia\bar{3}$, the selection rules predict 22 Raman-active modes ($4A_g + 4E_g + 14F_g$). The main peak is located around 390 cm⁻¹, as is characteristic for the Lu₂O₃ cubic phase [15, 16], corresponding to a mixture of Tg + Ag modes. The peak assignment is summarized in Table 2. The vibration frequencies of Lu_{2-x}Tm_xO₃ nanocrystals show, in relation to the bulk Lu₂O₃ single crystals, a very slight shift

Table 1 Composition, unit-cell parameters and average crystallite size of the $\text{Lu}_{2-x}\text{Tm}_x\text{O}_3$ nanocrystals

Tm concentration			a (Å)	V (Å ³)	Average crystallite size (nm)
(at.%)	x	(10^{20} at/cm ³)			
0	–	–	10.3900(1) [1]	1121.6(1) [1]	–
0.5	0.009	1.2808(2)	10.3915(8)	1124.3(2)	15.7
5	0.101	14.369(4)	10.3984(7)	1124.6(3)	17.2
8	0.149	21.176(4)	10.4028(7)	1125.8(2)	16.9
15	0.287	42.534(8)	10.4111(7)	1128.5(2)	16.8

Table 2 Raman peak frequencies (in cm^{-1}) observed in $\text{Lu}_{1.713}\text{Tm}_{0.287}\text{O}_3$ nanocrystals and their assignment and comparison with single-crystal Raman peaks [15, 16]

Assignment T_h factor group	Nanocrystals	Bulk single crystal
Tg (or Fg) + Ag	118–119	120
	135	137
	145	146
Tg (or Fg)	–	191
Tg (or Fg) + Eg	–	289
	328	330
Eg	346	348
Tg (or Fg) + Ag	389–391	393
Tg (or Fg)	451	454
Tg (or Fg)	497	499
	589	589
Tg (or Fg)	612	614

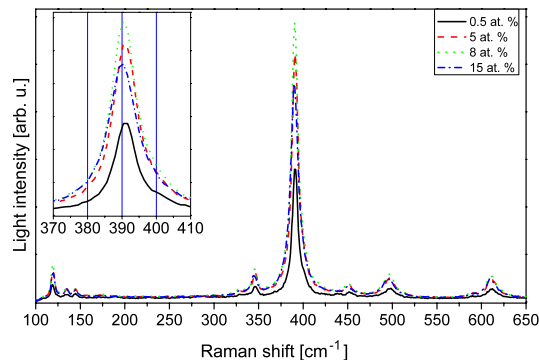


Fig. 2 Raman spectra of $\text{Lu}_{2-x}\text{Tm}_x\text{O}_3$ nanocrystals

to shorter values, see the inset of Fig. 2. This effect is most likely related to the decrease of the force constant of Tm–O bonds with regard to Lu–O ones due to the longer distance among the oxygens and the cations by the increase of the unit-cell parameters [17].

Kaminskii [18] reported that the spontaneous Raman spectra of bulk single crystals are almost indistinguishable from those of the RE_2O_3 (RE = Y, Sc and Lu) ceramics. The maximum Raman gain in similar conditions for

stimulated Raman scattering (SRS) operation has been obtained for Sc_2O_3 ceramic. The Stokes and anti-Stokes generation under steady-state excitation conditions is governed by $\tau_p \gg T_2 = 1/\pi \Delta\nu_R$, in which τ_p is the pumping pulse duration and T_2 and $\Delta\nu_R$ are the dephasing time and the line width of the strongest spontaneous Raman scattering line, respectively. This width has been reported to be around 4 cm^{-1} for RE_2O_3 ceramics; in our case, the line width of the phonon mode at 391 cm^{-1} is about 8 cm^{-1} .

3.3 Optical absorption and photoluminescence

The electronic configuration of Tm^{3+} is $4f^{12}$, with an even number of electrons. In the Lu_2O_3 host, Tm^{3+} is expected to replace Lu^{3+} with the same preferential occupancy among the C_2 and C_{3i} symmetry sites, namely 3:1 ratio [19]. Most of the spectroscopic features observed for Tm^{3+} in the Lu_2O_3 host are related to the electric dipole transitions of ions in the C_2 symmetry site, since the inversion centre of the C_{3i} site only allows magnetic dipole transitions.

Tm^{3+} energy levels in Lu_2O_3 nanocrystals have been determined by the 6-K OA measurements shown in Fig. 3. Table 3 lists the energies of the Stark levels of Tm^{3+} , which are quite consistent with those already reported for Lu_2O_3 single crystals [8]. Despite the low measurement temperature,

Fig. 3 Low-temperature (6 K) optical absorption of 15 at.% Tm³⁺ nanocrystals

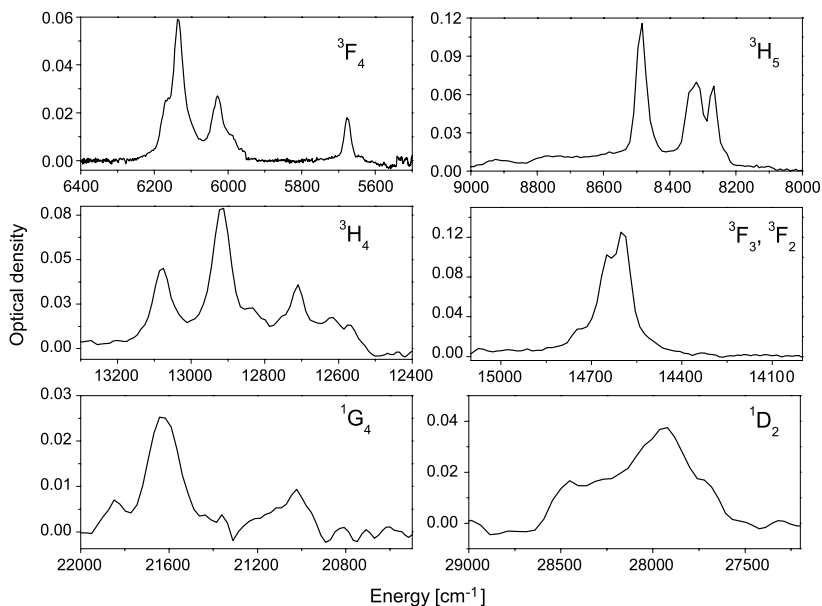


Table 3 Comparison of the experimental Stark energy levels, E_{exp} in cm^{-1} , of Tm³⁺ ions observed in Lu₂O₃ nanocrystals and single crystal [8]

$2S+1L_J$	Nanocrystals	Bulk single crystal
3F_4	–, 5678, 5990, 6029, 6135, 6168, –, –	5613, 5680, 6033, 6045, 6127, 6141, 6174, 6223
3H_5	8227, 8266, –, –, 8318, 8340, –, 8483, –, –, –	8232, 8267, 8282, 8303, 8318, 8340, 8475, 8487, 8578, 8785, 8938
3H_4	12568, 12617, 12710, 12800, 12833, 12915, –, 13078, –, –, –	12562, 12710, 12831, 12915, 12936, 13080, 13140, 13254, 13484
$^3F_3, ^3F_2$	–, 14600, 14650, –, 14745, –, –, –, 15070, 15210, 15276, –	14558, 14592, 14688, 14695, 14760, 14841, 14922 15029, 15080, 15213, 15272, 15390
1G_4	21017, 21619, 21842	–
1D_2	27711, 27935, 28267, 28455	–

the spectra of nanocrystals show a significant band broadening. The present results show that the size reduction from bulk crystals to the nanocrystals does not modify the average energy of the ion levels but it enlarges the optical line widths.

Tm³⁺ lasers are suitably excited with the AlGaAs diode laser emission close to 800 nm. Figure 4 shows some relevant RT absorption bands of Lu_{2–x}Tm_xO₃ nanocrystals in the 430–1300 nm spectral range. As in single crystals, in the current nanocrystals one of the strongest absorptions of Tm³⁺ also corresponds to the $^3H_6 \rightarrow ^3H_4$ electronic transition at 796 nm. This transition can be used for pumping Tm:Lu₂O₃ ceramic lasers made from nanocrystal precursors. After 3H_4 optical excitation, Tm³⁺ interacts with near enough neighboring Tm³⁺ ions in the 3H_6 ground state to reach two ions at the intermediate 3F_4 excited multiplet by cross relaxation, increasing in this way

the electronic population in the emitting level for the two-micron (≈ 1950 nm) $^3F_4 \rightarrow ^3H_6$ laser channel and at the same time reducing the photon energy transferred as heat to the host.

The operation efficiency of such lasers relies on a large lifetime of the 3F_4 excited level; however, the accumulation of surface defects in nanocrystals may lead to a significant reduction of the lifetime and correspondingly of the PL yield. The analysis of this effect by using the 3F_4 lifetime is difficult because the emission reabsorption induces an apparent lifetime enhancement which masks possible lifetime reductions. Therefore, we will examine first the PL of the 3H_4 level which is free of reabsorption; it allows us to study the lifetime modifications associated to the size reduction from single-crystal to nanocrystal dimensions.

Fig. 4 Optical absorption spectra collected at room temperature, for 5 at.%, 8 at.% and 15 at.% of Tm^{3+} in $\text{Lu}_{2-x}\text{Tm}_x\text{O}_3$ nanocrystals

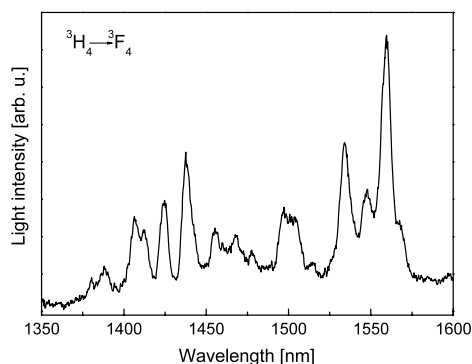
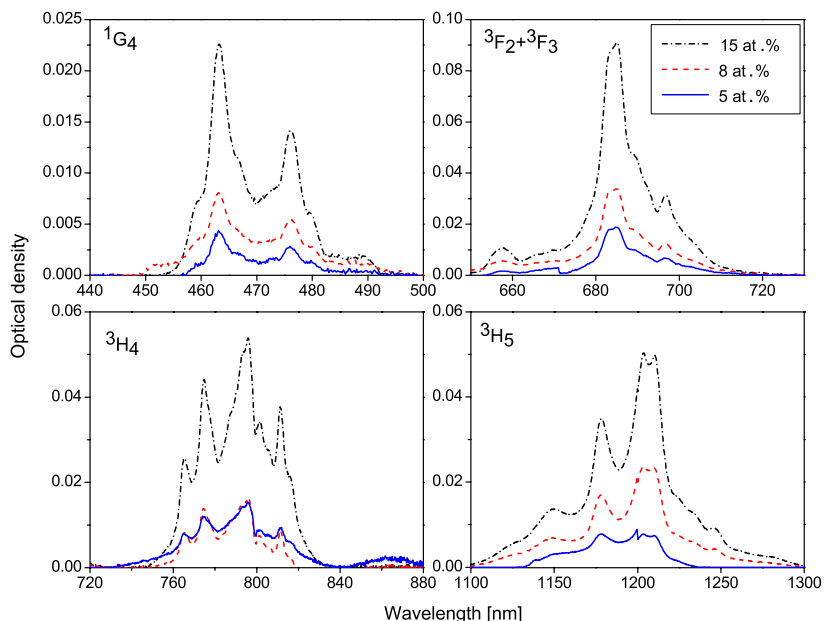


Fig. 5 Room-temperature ${}^3\text{H}_4 \rightarrow {}^3\text{F}_4$ photoluminescence of $\text{Lu}_{1.899}\text{Tm}_{0.101}\text{O}_3$ nanocrystals excited at $\lambda_{\text{EXC}} = 800$ nm

3.3.1 ${}^3\text{H}_4$ photoluminescence

Figure 5 shows the 300-K PL associated with the ${}^3\text{H}_4 \rightarrow {}^3\text{F}_4$ ($\lambda \approx 1350\text{--}1600$ nm) transition. The spectrum shows the large crystal field splitting characteristic of sesquioxides. The emission spectrum shows the three most intense peaks at 1559, 1534 and 1437 nm. This spectrum for $\text{Lu}_{2-x}\text{Tm}_x\text{O}_3$ nanocrystals is similar to that reported for 4 at.% Tm^{3+} -doped Lu_2O_3 single crystals [8].

It has been reported that the radiative lifetime of Ln-doped nanoparticles may be affected by the refractive index of the surrounding medium [20]. As a preliminary methodological procedure, we assess the validity of the results

obtained by measuring the ${}^3\text{H}_4$ lifetime of $\text{Tm}^{3+}:\text{Lu}_2\text{O}_3$ nanocrystals in air ($n = 1$) and dispersed in liquids with different refractive indices, namely ethylene glycol (EG) with $n = 1.52$ and fluorolube (FL) with $n = 1.94$. The refractive index of undoped Lu_2O_3 sesquioxides at 800 nm and 300 K is about 1.92 [8]; therefore, it is expected that we can discriminate if such effect is present or not in our measurements.

After short-pulse excitation at 800 nm, the PL intensity decays at the wavelengths of the three most intense peaks of the ${}^3\text{H}_4 \rightarrow {}^3\text{F}_4$ emission were similar. None of the decays observed was exponential. This is illustrated in Fig. 6 for the lowest thulium composition, i.e. $\text{Lu}_{1.991}\text{Tm}_{0.009}\text{O}_3$, for which non-radiative Tm–Tm losses are negligible. The complex time dependency of the fluorescence intensity of Tm^{3+} in these nanocrystals is different to the exponential behavior documented in Lu_2O_3 single crystals with low enough Tm^{3+} concentration.

The decays measured in nanocrystals have been described by two exponential terms, the shorter is ascribed to the emission of Tm^{3+} ions on the surface of the nanocrystals and the longer to Tm^{3+} ions in the body of the nanocrystals, which should approach the value obtained in Tm-doped Lu_2O_3 single crystals. The quenching of fluorescence by OH[−] attached groups could be related with this fast component of the decay time related to the active surface ions in the nanocrystals. This effect is observable in the nanocrystalline samples due to their high ratio of surface ions in relation with ions in the body of the nanocrystals. In order to ob-

tain significant results, the long-lived lifetime was first calculated from the tail of the $\ln(I/I_0)$ vs time representations as shown in Fig. 6a. Later, we fitted the intensity decay, $I(t)$, to the curve $I(t) = I_1 e^{-t/\tau_1} + I_2 e^{-t/\tau_2}$, where $I_1 + I_2 = 1$. In this fit, the previously calculated lifetime was used as an initial value to achieve convergence, but in the final refinement step this was also left to vary freely. This procedure systematically produced good fits of the experimental intensity decays, as shown in Fig. 6b for Lu_{1.991}Tm_{0.009}O₃ nanocrystals.

Table 4 presents the results of the lifetime analysis of the Lu_{2-x}Tm_xO₃ nanocrystals. The most significant features of

these results are the following: (a) the results obtained are highly independent of the surrounding medium; this indicates that the crystal size of the presently used nanocrystals is above the threshold to produce modifications of the radiative lifetime. (b) The analysis of the PL decay kinetics with two exponential regimes yields good results for Tm concentrations of up to 8 at.% ($x = 0.149$) Tm. At higher Tm concentrations, the decay occurs too fast and the signal intensity becomes so weak that reliable analysis of the decays was not possible. The short-lived component is about five times shorter than the long-lived one. The long-lived value obtained for 0.5 at.% ($x = 0.009$) in nanocrystals is similar to the experimental value of 300 μ s obtained at 300 K in 0.2 at.% Tm-doped Lu₂O₃ single crystal [21]. Both values are clearly shorter than the ³H₄ radiative value expected for Tm³⁺ in Lu₂O₃, i.e. 690 μ s [8]. (c) Both the fast and slow decay components decrease as Tm concentration increases as a consequence of non-radiative Tm-Tm interaction losses.

3.3.2 ³F₄ photoluminescence

In comparison to the multiplet above, the lifetime of the ³F₄ multiplet was more difficult to observe because of the relatively weak photoluminescence intensity at 1950 nm and the lower response of the InAs photovoltaic detector used. However, decay signals could be observed using a $\times 10$ amplifier.

Because ³F₄ photoluminescence is excited through the ³H₄ multiplet, fluorescence intensity initially grows corresponding to the electron population growth of the ³F₄ multiplet. Therefore, decay signals for times shorter than twice the lifetime of ³H₄ were ignored. The remaining decay was analyzed in a similar manner to that described for the analysis of ³H₄ decays.

The decay of the Lu_{1.991}Tm_{0.009}O₃ nanocrystals fits well with two exponentials: $I(t) = 0.61 \exp(-t/0.87 \text{ ms}) + 0.39 \exp(-t/2.21 \text{ ms})$. The long-lived value, $\tau = 2.21 \text{ ms}$, that we associate with the Tm³⁺ ions in the crystal body, is only slightly shorter than the corresponding value found in bulk single crystals, $\tau = 3.38 \text{ ms}$. The measured ³F₄ lifetime systematically decreased as the thulium concentration

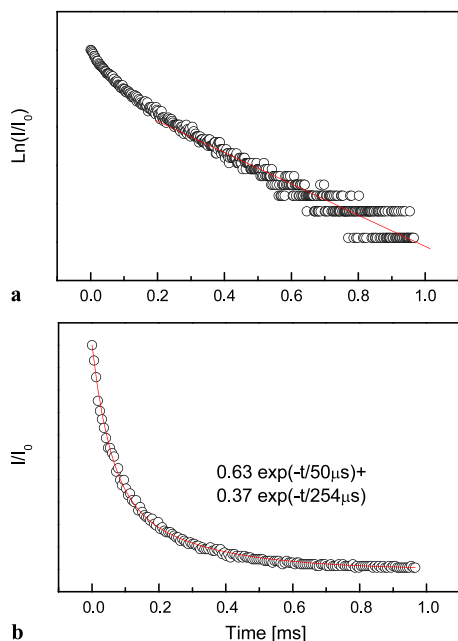


Fig. 6 Room-temperature photoluminescence intensity decay at 300 K of the ³H₄ multiplet of Tm³⁺ in Lu_{1.991}Tm_{0.009}O₃ nanocrystals. $\lambda_{\text{EXC}} = 800 \text{ nm}$, $\lambda_{\text{EMI}} = 1558 \text{ nm}$. The open circles are the experimental results, and the lines are (a) a linear fit of the tail of the $\ln(I/I_0)$ vs t dependency and (b) a fit with two exponential decays of the (I/I_0) vs t dependency

Table 4 Experimental lifetimes (τ) and intensities (I) of the ³H₄ de-excitation (at 300 K) of Lu_{2-x}Tm_xO₃ nanocrystals prepared by the sol-gel method. $\lambda_{\text{EXC}} = 800 \text{ nm}$, $\lambda_{\text{EMI}} = 1558 \text{ nm}$

Tm ³⁺ (at. %)	Air ($n = 1$) x	EG ($n = 1.52$)				FL ($n = 1.94$)							
		I_1	τ_1 (μ s)	I_2	τ_2 (μ s)	I_1	τ_1 (μ s)	I_2	τ_2 (μ s)				
0.5	0.009	0.63	50	0.37	254	0.79	110	0.21	340	0.77	13	0.23	340
5	0.101	0.75	0.9	0.25	5.1	0.78	0.7	0.22	4.1	0.74	0.8	0.26	4.5
8	0.149	0.85	0.4	0.15	3.1	0.72	0.6	0.18	2.1	0.76	0.4	0.24	2.2
15	0.287			1	0.3					0.65	0.04	0.35	0.2

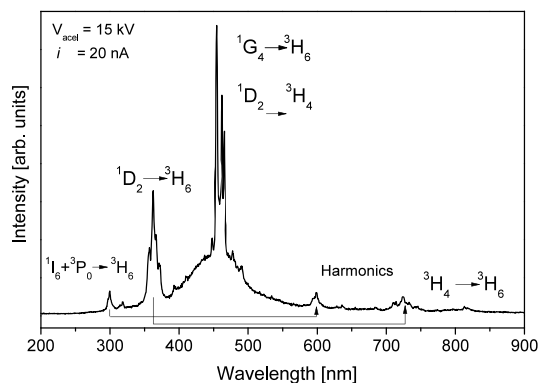


Fig. 7 Room-temperature cathodoluminescence of $\text{Lu}_{1.713}\text{Tm}_{0.287}\text{O}_3$ nanocrystals

increased. For $x = 0.101$ and 0.149 compositions single-exponential decays were found with lifetimes $\tau = 29 \mu\text{s}$ and $\tau = 10 \mu\text{s}$, respectively. The analysis of the $x = 0.287$ samples was not reliable due to the low signal intensity.

These results reflect the strong contribution of Tm–Tm interactions to non-radiative processes, including energy migration by fast diffusion, and show the apparently weak influence of fluorescence reabsorption in our results.

3.4 Cathodoluminescence

Figure 7 shows the cathodoluminescence spectrum for the $\text{Lu}_{1.713}\text{Tm}_{0.287}\text{O}_3$ nanocrystals at room temperature. The major blue emission peaking at 454.7 nm corresponds to the transition $^1\text{G}_4 \rightarrow ^3\text{H}_6$ and is strongly overlapped to the $^1\text{D}_2 \rightarrow ^3\text{F}_4$ emission at 462 nm . Other minor bands are the ultraviolet emissions observed at 299 nm and 364 nm , assigned to $^1\text{I}_6 + ^3\text{P}_0 \rightarrow ^3\text{H}_6$ and $^1\text{D}_2 \rightarrow ^3\text{H}_6$ Tm^{3+} transitions, respectively, and the NIR one at 815 nm , corresponding to the $^1\text{G}_4 \rightarrow ^3\text{H}_5$ transition. Residual peaks at 598 nm and 728 nm are second-order diffraction harmonics of ultraviolet 299-nm and 364-nm emissions inside the spectrometer.

Furthermore, a broad band emission can be seen acting as a background, centered around 450 nm . A similar broad band has been detected by cathodoluminescence and also PL in previous works [20, 21] and it was attributed to radiative recombination at defect centers.

A careful determination of the characteristics of color is important for further applications as a phosphor. The blue emission of Tm– Lu_2O_3 nanocrystals has CIE chromaticity coordinates of $x = 0.200$, $y = 0.156$ with a dominant wavelength of 468 nm . A color purity of 54% has been obtained in comparison with CIE Standard Illuminant C. These values are quite comparable to the ones reported in the literature for Tm: Y_2O_3 films with CIE(x, y) (0.158, 1.50), dominant wavelength at 476 nm and 78% purity [22].

4 Conclusions

$\text{Lu}_{2-x}\text{Tm}_x\text{O}_3$ phosphor nanocrystals with a grain size in the $15\text{--}60 \text{ nm}$ range and with high crystallinity were prepared using a modified Pechini method. The nanocrystals belong to the cubic system in the $Ia\bar{3}$ space group.

The maximum of the $^3\text{H}_6 \rightarrow ^3\text{H}_4$ Tm^{3+} absorption in these nanocrystals is centered at 796 nm , in agreement with the results obtained in single crystals. The Tm^{3+} energy level positions are not affected by the crystal dimension but the optical line widths increase due to the small grain size of the crystals.

We found that the $^3\text{H}_4$ and $^3\text{F}_4$ luminescence intensity decays of Tm^{3+} in sol–gel synthesized nanocrystals exhibit non-exponential dynamics even at very low Tm concentration. The shortest one is about five times faster than the long-lived one. These two regimes are associated with the different rates of non-radiative relaxations in defects and adsorbed OH^- groups at the surface and in the body of the nanocrystals, respectively. Increasing the Tm concentration further reduces the lifetime due to Tm–Tm interactions similarly to that observed in single crystals. No influence of the refractive index of the medium on the measured lifetimes was found for these Tm-doped Lu_2O_3 nanocrystals.

Cathodoluminescence spectra showed that $\text{Lu}_{2-x}\text{Tm}_x\text{O}_3$ nanocrystals emit light in the blue region at the wavelength of 457 nm corresponding to the $^1\text{G}_4 \rightarrow ^3\text{H}_6$ transition, with a purity of 54% .

Acknowledgements This work is supported by the Spanish Government under projects MAT2008-06729-C02/NAN, the Catalan Authority under project 2009SGR235 and EU project CLEAN SPACE (FP7-SPACE-2010-1-GA-263044). E.W. Barrera is supported by the Catalan Government through the fellowship 2009FI00148. J.J. Carvajal is supported by the Spanish Ministry of Education and Science and the European Social Fund under the Ramon y Cajal program RYC2006-258. F. Rotermund is supported by a NRF grant (2010-0029617) funded by the Korea government.

References

1. A. Ikesue, Y. Lin Aung, *Nat. Photonics* **2**, 721 (2008)
2. P. Cérny, H. Jelínková, *Developing Thulium Lasers for Depth-selective Scalpels* (SPIE Newsroom, 2006). doi:10.1117/2.1200607.0281
3. S. Popov, in *Tunable Laser Applications*, 2nd edn. (CRC Press, Rochester, New York, 2009), pp. 197–226, Chap. 7
4. J.H. Gwak, S.H. Park, J.E. Jang, S.J. Lee, J.E. Jung, J.M. Kim, Y.W. Jin, N.S. Lee, W.K. Yi, V.A. Vorobyov, *J. Vac. Sci. Technol. B* **18**, 1101 (2000)
5. F. Vetrone, J.C. Boyer, J.A. Capobianco, A. Spgehini, M. Bettinelli, *J. Appl. Phys.* **96**, 661 (2004)
6. E.W. Barrera, M.C. Pujol, F. Díaz, S. Bong Choi, F. Rotermund, K. Yung Ho Park, M. Seok Jeong, C. Cascales, *Nanotechnology* **22**, 075205 (2010)
7. F. Esteban-Betegón, C. Zaldo, C. Cascales, *Inorg. Chem.* **50**, 2836 (2011)

8. L. Fornasiero, Nd³⁺- und Tm³⁺-dotierte Sesquioxides, Ph.D. dissertation, Universität Hamburg, 1999
9. M. Galceran, M.C. Pujol, M. Aguiló, F. Díaz, Mater. Sci. Eng. B **146**, 7 (2008)
10. M. Galceran, M.C. Pujol, M. Aguiló, F. Díaz, J. Sol-Gel Sci. Technol. **42**, 79 (2007)
11. J. Rodríguez-Carvajal, *Reference Guide for the Computer Program Fullprof* (Laboratoire León Brillouin, CEA-CNRS, Saclay, 2000)
12. E.W. Barrera, M.C. Pujol, C. Cascales, J.J. Carvajal, X. Mateos, M. Aguiló, F. Díaz, Opt. Mater. **33**, 722 (2011)
13. B.D. Cullity, *Elements of X-ray Diffraction* (Addison-Wesley, Reading, 1978)
14. E. de la Rosa, L.A. Díaz-Torres, P. Salas, A. Arredondo, J.A. Montoya, C. Angeles, R.A. Rodríguez, Opt. Mater. **27**, 1793 (2005)
15. A. García-Murillo, C. Le Luyer, C. Pedrini, J. Mugnier, J. Alloys Compd. **323–324**, 74 (2001)
16. L. Laversenne, Y. Guyot, C. Goutadier, M.Th. Cohen-Adad, G. Boulon, Opt. Mater. **16**, 475 (2001)
17. A. Ubaldini, M.M. Carnasciali, J. Alloys Compd. **454**, 374 (2008)
18. A.A. Kaminskii, Laser Photonics Rev. **1**, 93 (2007)
19. L. Pauling, M.D. Shapell, Z. Kristallogr. **75**, 128 (1930)
20. C.M. Donegá, E. Zych, A. Meijerink, Mater. Res. Soc. Symp. Proc. **667**, 1 (2001)
21. H.D. Müller, J. Schneider, H. Lüth, R. Strümpfer, Appl. Phys. Lett. **57**, 2422 (1990)
22. J. Hao, S.A. Studenikin, M. Cocivera, J. Lumin. **93**, 313 (2001)

ERRATUM

Erratum to: Spectroscopic characterization of sol–gel synthesized Tm:Lu₂O₃ nanocrystals

E. W. Barrera · M. C. Pujol · C. Cascales · C. Zaldo ·
K. H. Park · S. B. Choi · F. Rotermund · J. J. Carvajal ·
X. Mateos · M. Aguiló · F. Díaz

Received: 29 March 2011 / Revised: 30 June 2011
© Springer-Verlag 2012

Erratum to: Appl Phys B (2012) 106:409–417
DOI 10.1007/s00340-011-4691-0

Unfortunately there has been an error in the references.

Ref. 21 has to be as follows:

21. P. Koopmann, R. Peters, K. Petermann, G. Huber, Crystal growth, spectroscopy, and highly efficient laser operation of thulium-doped Lu₂O₃ around 2 μm, Appl. Phys. B **102**, 19–24 (2011)

The citation of ref. 21 in paragraph “3.4 Cathodoluminescence” has to be deleted.

The online version of the original article can be found under
doi:[10.1007/s00340-011-4691-0](https://doi.org/10.1007/s00340-011-4691-0).

E. W. Barrera · M. C. Pujol (✉) · J. J. Carvajal · X. Mateos ·
M. Aguiló · F. Díaz
Física i Cristallografia de Materials i Nanomaterials
(FiCMA-FiCNA), Universitat Rovira i Virgili (URV),
Campus Sescelades, c/ Marcell·l Domingo, s/n,
43007 Tarragona, Spain
e-mail: mariacinta.pujol@urv.cat

C. Cascales · C. Zaldo
Instituto de Ciencia de Materiales de Madrid,
CSIC, c/ Sor Juana Inés de la Cruz 3, Cantoblanco,
28049 Madrid, Spain

K. H. Park
Korea Advanced Nano Fab Center (KANC), 443-270 Suwon,
Republic of Korea

S. B. Choi · F. Rotermund
Division of Energy Systems Research, Ajou University, San 5
Wonchun, 443-749 Suwon, Republic of Korea

Paper IV

E. W. Barrera, M. C. Pujol, F. Díaz, S. B. Choi, F. Rotermond, K. H. Park, M. S. Jeong, C. Cascales *Emission properties of hydrothermal Yb^{3+} , Er^{3+} and Yb^{3+} , Tm^{3+} -codoped Lu_2O_3 nanorods: upconversion, cathodoluminescence and assessment of waveguide behavior* **Nanotechnology** 22 075205 (2011).

UNIVERSITAT ROVIRA I VIRGILI
LANTHANIDE-BASED DIELECTRIC NANOPARTICLES FOR UPCONVERSION LUMINESCENCE
Elixir William Barrera Bello
Dipòsit Legal: T. 450-2013

Emission properties of hydrothermal Yb^{3+} , Er^{3+} and Yb^{3+} , Tm^{3+} -codoped Lu_2O_3 nanorods: upconversion, cathodoluminescence and assessment of waveguide behavior

Elixir William Barrera¹, María Cinta Pujol¹, Francesc Díaz¹,
Soo Bong Choi², Fabian Rotermund², Kyung Ho Park³,
Mun Seok Jeong⁴ and Concepción Cascales^{5,6}

¹ Física i Cristal·lografia de Materials, Universitat Rovira i Virgili, Campus Sescelades
c/ Marcel·lí Domingo s/n, E-43007 Tarragona, Spain

² Division of Energy Systems Research, Ajou University, 443-749 Suwon, Republic of Korea

³ Korea Advanced Nano Fab Center, 443-270 Suwon, Republic of Korea

⁴ Advanced Photonics Research Institute, Gwangju Institute of Science and Technology,
500-712 Gwangju, Republic of Korea

⁵ Instituto de Ciencia de Materiales de Madrid, Consejo Superior de Investigaciones
Científicas, c/Sor Juana Inés de la Cruz, 3 Cantoblanco, E-28049 Madrid, Spain

E-mail: ccascales@icmm.csic.es

Received 14 September 2010, in final form 30 November 2010

Published 14 January 2011

Online at stacks.iop.org/Nano/22/075205

Abstract

Yb^{3+} and Ln^{3+} ($\text{Ln}^{3+} = \text{Er}^{3+}$ or Tm^{3+}) codoped Lu_2O_3 nanorods with cubic $Ia\bar{3}$ symmetry have been prepared by low temperature hydrothermal procedures, and their luminescence properties and waveguide behavior analyzed by means of scanning near-field optical microscopy (SNOM). Room temperature upconversion (UC) under excitation at 980 nm and cathodoluminescence (CL) spectra were studied as a function of the Yb^{3+} concentration in the prepared nanorods. UC spectra revealed the strong development of $\text{Er}^{3+} {}^4\text{F}_{9/2} \rightarrow {}^4\text{I}_{15/2}$ (red) and $\text{Tm}^{3+} {}^1\text{G}_4 \rightarrow {}^3\text{H}_6$ (blue) bands, which became the pre-eminent and even unique emissions for corresponding nanorods with the higher Yb^{3+} concentration. Favored by the presence of large phonons in current nanorods, UC mechanisms that privilege the population of ${}^4\text{F}_{9/2}$ and ${}^1\text{G}_4$ emitting levels through phonon-assisted energy transfer and non-radiative relaxations account for these observed UC luminescence features. CL spectra show much more moderate development of the intensity ratio between the $\text{Er}^{3+} {}^4\text{F}_{9/2} \rightarrow {}^4\text{I}_{15/2}$ (red) and ${}^2\text{H}_{11/2}$, ${}^4\text{S}_{3/2} \rightarrow {}^4\text{I}_{15/2}$ (green) emissions with the increase in the Yb^{3+} content, while for Yb^{3+} , Tm^{3+} -codoped Lu_2O_3 nanorods the dominant CL emission is $\text{Tm}^{3+} {}^1\text{D}_2 \rightarrow {}^3\text{F}_4$ (deep-blue). Uniform light emission along Yb^{3+} , Er^{3+} -codoped Lu_2O_3 rods has been observed by using SNOM photoluminescence images; however, the rods seem to be too thin for propagation of light.

(Some figures in this article are in colour only in the electronic version)

⁶ Author to whom any correspondence should be addressed.

1. Introduction

Insulating nanocrystals (NCs) doped with optically active trivalent lanthanides (hereafter Ln) are systems in which the spectroscopic properties derived from the specific features of the 4f electronic transitions can be highly modified via dimensionality and shape effects. Given the localized nature of 4f orbitals, changes in the local environment around Ln centers induced by size reduction and surface defects rather than modification of the energy levels of $4f^N$ states can influence (mainly through electron–phonon coupling) the dynamics of f–f luminescence transitions. The result is that emission lifetimes, luminescence efficiency and concentration quenching can be substantially affected [1]. Besides, enhanced or even novel upconversion fluorescence properties compared with bulk counterparts have been found in NCs of single-doped Er^{3+} and codoped Yb^{3+} , Ln^{3+} ($\text{Ln} = \text{Er}^{3+}$ or Tm^{3+}) compounds [2–8]. These findings support the use of nanostructures of optically active Ln-containing compounds as highly functionalized materials in nanoscale electronics, photonics and bioanalysis [4, 8]. Special attention has been devoted to 1D crystalline nanostructures [9–11], which additionally can play an important role as functional building units for the fabrication of nanodevices based on 2D or 3D ordered structures.

Evaluation of the optical response of Ln embedded in nanocrystalline hosts and the comparison with their bulk counterparts seems to be a rational approach to the development of such novel devices. From this point of view, nanosized cubic Ln-doped RE_2O_3 ($\text{RE} = \text{Sc}$, Y , Gd , Lu) sesquioxides are currently receiving considerable attention, either as an alternative to circumvent difficulties associated with the production of corresponding bulk single crystals, for which Ln lasing has been demonstrated [12, 13], or with the aim of exploring new optical properties deriving from the size reduction. In this way, the new possibilities offered by NCs of optically active Ln-doped RE_2O_3 range from the fabrication of transparent laser ceramics through dense sintering of nanoparticles [14] to their incorporation in hybrid photonic composites by infiltration, merging or coating with other transparent materials—in the latter case mostly focused on the design of ultrasensitive biolabels [15].

It has been reported that after near-infrared (NIR) excitation with $\lambda_{\text{EXC}} = 980$ nm NCs of Er^{3+} -doped and Yb^{3+} , Er^{3+} -codoped cubic RE_2O_3 emit upconverted green and red light whose relative intensities considerably differ from those observed in the corresponding bulk crystals [2, 3, 8, 16–23]. The most extended research on these altered or even new upconverting emission processes is for doped Y_2O_3 nanoparticles [2, 3, 16–19]; studies of well-defined 1D structures are scarce [18–20, 24]. Giving the similar mass, size and electronic configuration, Lu_2O_3 is a better choice for the favorable incorporation of the highest concentrations of Ln, with absorption and emission cross sections larger than in the more usual Y_2O_3 host [13]. Furthermore, Lu_2O_3 has a broad transparency range (240 nm– ~ 8 μm), relatively low phonon energies (phonon cutoff 618 cm^{-1}), and a high refractive index (1.91 at 1050 nm), all advantageous features

for waveguide behavior in nanocrystalline 1D Lu_2O_3 . But for 1D Yb^{3+} , Er^{3+} -codoped Lu_2O_3 only one specific composition has been considered in the analysis of the upconversion emission [20]. All these optical studies so far have been based on ensemble measurements, and thus the information that they provide should be assigned to surface effects more than to the nanocrystalline architecture of the studied material.

By using a large variety of methods and experimental conditions, nanosized pure or Ln-doped (mainly Eu) Lu_2O_3 crystals with diverse morphologies have been achieved, which in most cases consist of more or less agglomerated nanoparticles [25–30]; preparations yielding well-defined 1D [31–34], 2D [32, 34] or 3D [34–36] architectures are considerably limited. Among all the methods of synthesis, soft hydrothermal routes, i.e. through autogenic pressure and low temperatures, allow one to obtain precisely defined compositions with adequate control over the morphology of the desired material, aspects that have been demonstrated to be crucial for high luminescence performance [37]. However, previous hydrothermal preparations of nanotubes of Lu_2O_3 have required the use of a template agent [33], and to obtain 1D Eu– Lu_2O_3 alkaline [31] or even strongly alkaline [32] solutions were needed.

In this work we combine a highly efficient approach for preparing nanocrystalline Ln-doped Lu_2O_3 with 1D morphology, namely hydrothermal synthesis, with one of the most powerful optical characterization techniques of nanostructures, namely scanning near-field optical microscopy (SNOM), to measure the NIR to visible upconversion (UC) and the cathodoluminescence (CL) emission properties of Ln^{3+} in the prepared materials. In this way, we present the results for the preparation of nanocrystalline 1D Yb^{3+} , Er^{3+} and Yb^{3+} , Tm^{3+} -codoped Lu_2O_3 using the softest hydrothermal reaction conditions, namely the lowest required temperature and minimum reaction time while keeping the reaction medium so close as possible to neutral pH. Furthermore, these reactions have been carried out without using surfactants and external template agents. In the prepared materials the role of Yb^{3+} is to act as the sensitizer of the NIR excitation ($\lambda_{\text{EXC}} = 980$ nm). The determination of the UC and CL emission properties, which are of importance for the interpretation of excitation mechanisms of luminescent and laser materials, has been performed by modifying the Yb^{3+} concentration in the prepared 1D sesquioxides, and the differences from isostructural bulk single crystals [2, 21–23, 38] or ceramic powder [39], which are related to the features associated with nanocrystals (shape, size, specific surface, porosity), have been established through comparisons of the corresponding data for both kinds of size regime. Finally, the evaluation of possible waveguiding behavior in 1D Yb^{3+} , Er^{3+} – Lu_2O_3 has been carried out via SNOM photoluminescence images as well as numerical simulations [40] of their basic waveguiding characteristics.

2. Experimental section

Sets of Yb^{3+} , Ln^{3+} ($\text{Ln}^{3+} = \text{Er}^{3+}$ or Tm^{3+}) codoped Lu_2O_3 samples with $\text{Lu}_{1.96-x}\text{Yb}_x\text{Er}_{0.04}\text{O}_3$ ($x = 0.04, 0.12$,

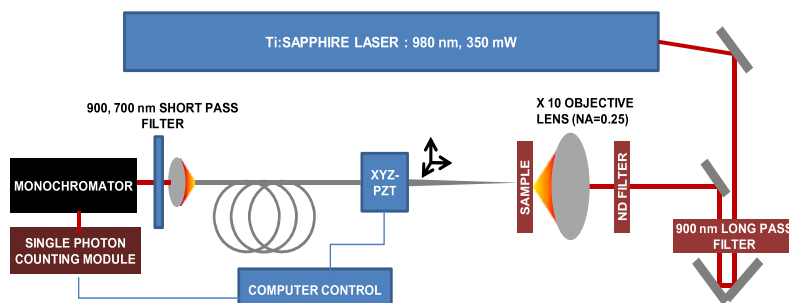


Figure 1. Experimental setup for scanning near-field optical microscopy on Yb^{3+} , Ln^{3+} ($\text{Ln}^{3+} = \text{Er}^{3+}$, Tm^{3+}) codoped Lu_2O_3 nanorods prepared by hydrothermal synthesis.

0.20, 0.25, 0.30), $\text{Lu}_{1.80-x}\text{Yb}_{0.20}\text{Er}_x\text{O}_3$ ($x = 0.04, 0.10, 0.15$) and $\text{Lu}_{1.96-x}\text{Yb}_x\text{Tm}_{0.04}\text{O}_3$ ($x = 0.04, 0.12, 0.20$) compositions were prepared by a hydrothermal procedure. The corresponding stoichiometric molar amount of the starting sesquioxides Yb_2O_3 (99.998% Alfa Aesar), Lu_2O_3 and Er_2O_3 (99.99% WuXi YiFeng Rare Earth Co. Ltd) were dissolved under heating with agitation in a dilute HCl solution (10 ml distilled water and 5 ml 38 wt% HCl). After complete evaporation, 20 ml of distilled water was added to form a clear solution, and the pH was adjusted to 7 and 10 with dilute NH_4OH . In each case the white suspension was subsequently heated during 24 h to 185 °C in Teflon-lined autoclaves of 75 ml capacity. The product obtained in the hydrothermal reaction was separated by centrifugation and washed with distilled water several times, dried and then annealed at 800 °C for 30 min.

The purity of the cubic sesquioxide phase was verified in each case by 300 K powder x-ray diffraction (XRD) performed in a Bruker AXS D-8 Advance diffractometer, using $\text{Cu K}\alpha$ radiation.

Fourier transform infrared absorption (FT-IR) spectra of pellets with nanocrystalline sesquioxides mixed with KBr (Strem Chemicals, 99.999% in K) were collected using a Nicolet 20SXC spectrophotometer in the range 4000–250 cm^{-1} .

Micromeritics ASAP 2010 equipment was used for N_2 adsorption/desorption isotherm measurement performed at 77 K, and the distribution of pore sizes and cumulative volume of pores were established from Barret–Joyner–Halenda (BJH) calculations using data from the isotherm.

Field-emission scanning electron microscopy (FE-SEM) images and energy dispersive x-ray (EDX) spectroscopy line-scanning analysis were performed with FEI NOVA SEM230 equipment. Transmission electron microscopy (TEM) images were recorded with a JEOL 2000FXII microscope with an accelerating voltage of 200 kV.

SNOM measurements of Yb^{3+} , Ln^{3+} -codoped Lu_2O_3 nanorods were carried out at room temperature. These nanorods were dispersed in a xylene(99) + PMMA(1) (diffractive indices $n_{\text{xy}} = 1.5$, $n_{\text{PMMA}} = 1.48$ at 1 μm) mixture, and deposited onto a quartz substrate by spin-coating (five times at 5000 rpm, and curing at 80 °C for 20 min). The

very thin (<5 nm) PMMA layer, which does not have any significant nonlinear effects in our experimental conditions, was enough to fix the nanorod on the quartz, being the location of the nanorod easily displaced by shear force between the SNOM tip and the nanorod. The sample was then mounted on the computer controlled piezo-stage for SNOM measurements. The experimental configuration is illustrated in figure 1. The photoluminescence (PL) was excited by using a Ti:sapphire laser in continuous wave operation ($\lambda_{\text{exc}} = 980 \text{ nm}$). To block the undesired PL from the Ti:sapphire laser, two 900 nm long-pass filters were inserted in the beam path, and a neutral density filter was used to avoid damage to the SNOM tip. The sample was illuminated from the backside by an objective lens (10 \times magnification, $\text{NA} = 0.25$), which focused the laser beam of 30 mW to a 3 μm spot size. The upconverted PL was collected by a SNOM tip with a 100 nm aperture. To eliminate the strong pump laser line in the measurement, we used two short-pass filters ($\lambda_{\text{cut-off}} = 900$ and 700 nm) and a monochromator after the SNOM tip. For CL measurements the excitation voltage was 15 kV, and the probe current was 20 nA. In addition to UC and CL emission spectra, SEM images were also collected for prepared samples.

3. Results and discussion

3.1. Structural, compositional and morphological characterization of Yb^{3+} , $\text{Er}^{3+}/\text{Tm}^{3+}$ -codoped Lu_2O_3

The described preparations of $\text{Lu}_{1.96-x}\text{Yb}_x\text{Er}_{0.04}\text{O}_3$ ($x = 0.04, 0.12, 0.20, 0.25, 0.30$), $\text{Lu}_{1.80-x}\text{Yb}_{0.20}\text{Er}_x\text{O}_3$ ($x = 0.04, 0.10, 0.15$) and $\text{Lu}_{1.96-x}\text{Yb}_x\text{Tm}_{0.04}\text{O}_3$ ($x = 0.04, 0.12, 0.20$) compositions at pH = 7 and 10 have yielded in all cases the pure cubic $Ia\bar{3}$ phase [41]. A mean particle size of $\sim 25 \text{ nm}$ is calculated from the full width at half maximum (FWHM) of broadened Bragg peaks by using the Debye–Scherrer formula assuming spherical particles, with no important differences arising either from the pH of the hydrothermal reaction medium or the Er^{3+} or Tm^{3+} content. Figure 2 show the XRD patterns of Yb^{3+} , Ln^{3+} (Er^{3+} , Tm^{3+}) codoped Lu_2O_3 samples prepared at pH = 7.

For further evaluation of possible differences between sesquioxides prepared with pH = 7 or 10, we have compared

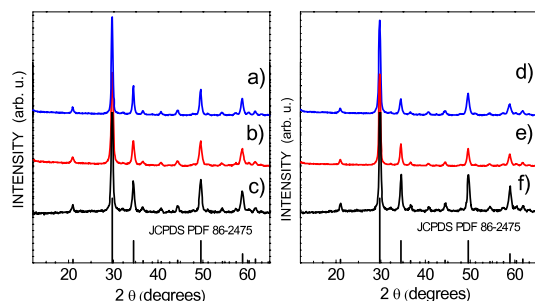


Figure 2. Room temperature x-ray diffraction patterns of $\text{Lu}_{1.96-x}\text{Yb}_x\text{Ln}_{0.04}\text{O}_3$ nanorods prepared by hydrothermal synthesis after 24 h at 185°C with $\text{pH} = 7$ using Yb- and Ln-chlorides: left, $\text{Ln} = \text{Er}^{3+}$, (a) $x = 0.20$, (b) $x = 0.12$, (c) $x = 0.04$; right, $\text{Ln} = \text{Tm}^{3+}$, (d) $x = 0.20$, (e) $x = 0.12$, (f) $x = 0.04$. All Bragg peaks correspond to the cubic $Ia\bar{3}$ phase of Lu_2O_3 , JCPDS 86-2475 [41].

the corresponding room temperature FT-IR spectra for the same composition (see figure 3). Both spectra are nearly identical. Bands observed from ~ 305 to 605 cm^{-1} are basically the same and are assigned to modes of skeletal vibrations of Lu_2O_3 [42]. Bands centered at 1630 cm^{-1} and at $\sim 3440\text{ cm}^{-1}$ correspond to HOH bending modes and to OH^- stretching vibrations of lattice water, respectively [43], but since they are also observed in the blank KBr pellet, whose spectrum is also included in figure 3, we can suppose that they might be related to some extent to the KBr used. Very weak bands observed at ~ 1400 and at $\sim 1530\text{ cm}^{-1}$ can be assigned to the symmetric and antisymmetric stretching vibrations of surface-adsorbed carboxylate ions [43].

Figures 4(a)–(g) show a panel of representative SEM, panchromatic CL and TEM images of cubic sesquioxides $\text{Lu}_{1.96-x}\text{Yb}_x\text{Ln}_{0.04}\text{O}_3$ prepared at $\text{pH} = 7$. The morphology can be described as consisting of rods of $\sim 45\text{ }\mu\text{m}$ in length and $\sim 90\text{ nm}$ of diameter, which are gathered to form micro-sized bunches tied in the middle. These rods are not homogeneous but porous (see figures 4(e) and (f)) and they are made up of pseudo-hexagon-shaped highly crystalline nanoparticles with size (circular section) of $\sim 20\text{ nm}$ (see figure 4(g)), consistent with results from the XRD analysis.

SEM, panchromatic CL and TEM images of $\text{Lu}_{1.96-x}\text{Yb}_x\text{Ln}_{0.04}\text{O}_3$ prepared from hydrothermal syntheses in an alkaline $\text{pH} = 10$ medium are displayed in figures 5(a)–(c). 1D morphology is also observed, with primary nanorods having diameters of $\sim 20\text{ nm}$ (figure 5(c)) considerably thinner than previous nanorods in figure 4(f). Nanorods from this preparative route appear, in general, to be assembled side by side.

Panchromatic CL images of 1D sesquioxides prepared in $\text{pH} = 7$ and $\text{pH} = 10$ media (figures 4(c) and 5(b), respectively) reveal that the incorporation of optically active cations is homogeneous in both kinds of morphologies.

EDX analysis of prepared porous nanorods reveals the homogeneous distribution of Ln cations. Figure 6 shows color maps of Lu, Yb and Er together with plots of the

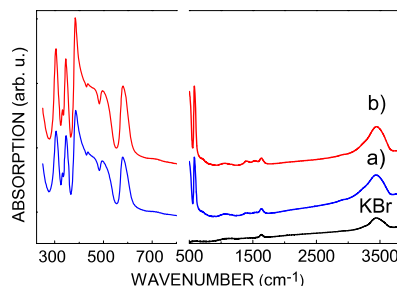


Figure 3. Room temperature FT-IR spectra of $\text{Lu}_{1.76}\text{Yb}_{0.20}\text{Tm}_{0.04}\text{O}_3$ nanorods prepared by hydrothermal synthesis after 24 h at 185°C with (a) $\text{pH} = 7$, (b) $\text{pH} = 10$. The spectrum of KBr used for preparing pellets (black line) is shown for reference.

relative amount of each element, obtained by EDX line-scanning analysis, as function of the relative position along the marked line for $\text{Lu}_{1.65}\text{Yb}_{0.20}\text{Er}_{0.15}\text{O}_3$ nanorods. The plateau in figure 6(e) between ~ 5 and $20\text{ }\mu\text{m}$ corresponds to constant Lu, Yb and Er contents along the line, while the observed band at $\sim 2\text{--}3\text{ }\mu\text{m}$ on the left side is related to horizontal nanorods in the top of figure 6(a), also crossed by the indicated line. Quantitative results (figure 6(f)) agree with the nominal composition (82.5% Lu, 10% Yb and 7.5% Er) of $\text{Lu}_{1.65}\text{Yb}_{0.20}\text{Er}_{0.15}\text{O}_3$ nanorods.

The described morphologies for cubic Yb^{3+} , $\text{Ln}^{3+}\text{--Lu}_2\text{O}_3$ sesquioxides prepared at different pHs, are in each case basically the same as for the corresponding hydrothermal precursor, i.e. the product of the hydrothermal synthesis *before* the 30 min thermal annealing at 800°C , and the observed porosity is due to the removal of anionic groups from previous precursor frameworks. Thus, the mechanisms of formation of currently prepared nanorods should be understood mainly as being related to some specific crystallographic features of these hydrothermal precursors, and consequently the morphologies of the final nanorods will depend on the main crystal phase constituting the corresponding precursor. The identification of these crystal phases is complex, given the small number of crystallographic studies on solution-derived Lu-containing compounds compared with those for other Lns. Despite this, in the hydrothermal process at $\text{pH} = 7$ it has been possible to distinguish the presence of a mixture of two hexagonal $P6_3/m$ phases, the first one isostructural to $\text{Ln}(\text{OH})_3$ [44] and the other isostructural to $\text{Er}(\text{ClO}_4)_3$ [45], whereas for $\text{pH} = 10$ the crystal phase has been identified as monoclinic $\text{LuO}(\text{OH})$ [46]. The formation of nanorods for cubic sesquioxides at $\text{pH} = 7$ can be explained as deriving from a rolling mechanism acting under specific hydrothermal conditions over the quasi-layered 2D structures adopted by hexagonal $\text{Ln}(\text{OH})_3$ [47, 48] or $\text{Er}(\text{ClO}_4)_3$ [47]. In the case of thinner primary nanorods at $\text{pH} = 10$ the growth mechanism consists of the aggregation or coalescence of nanoparticles having a suitable crystallographic orientation—‘oriented attachment’—[49], to give a larger crystalline structure [50].

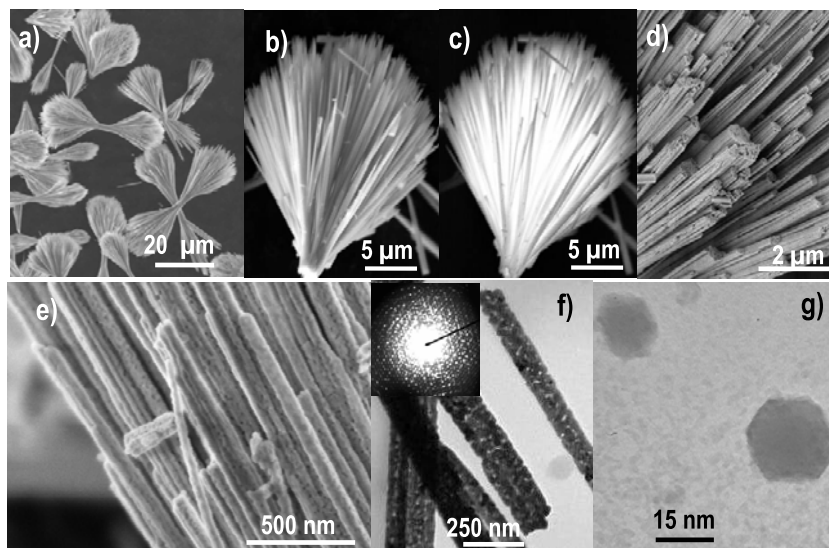


Figure 4. (a), (b) SEM images of bunches made up of nanorods of $\text{Lu}_{1.76}\text{Yb}_{0.20}\text{Er}_{0.04}\text{O}_3$ prepared by 24 h hydrothermal synthesis at 185°C and $\text{pH} = 7$. (c) Panchromatic cathodoluminescence image of the bunch in (b). (d), (e) SEM micrographs of nanorods of $\text{Lu}_{1.76}\text{Yb}_{0.20}\text{Er}_{0.04}\text{O}_3$ showing their characteristic porosity. (f) TEM image revealing the porosity of nanorods, with a SAED image in the top left inset. (g) TEM image of free-standing pseudo-hexagon-shaped nanocrystals like those forming the nanorods.

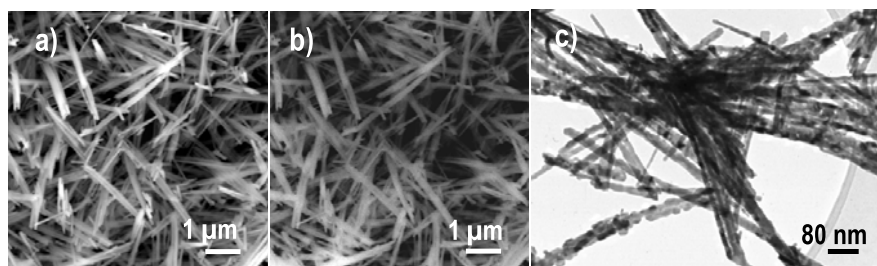


Figure 5. Micrographs of $\text{Lu}_{1.92}\text{Yb}_{0.04}\text{Tm}_{0.04}\text{O}_3$ nanorods prepared by 24 h hydrothermal synthesis at 185°C and $\text{pH} = 10$: (a) SEM image of nanorods; (b) panchromatic cathodoluminescence view of nanorods in (a); (c) TEM image of thin nanorods with a diameter of ~ 20 nm and their assemblies.

3.2. NIR to VIS upconversion and cathodoluminescence emission spectra

Yb^{3+} , Ln^{3+} -codoped Lu_2O_3 prepared either with $\text{pH} = 7$ or 10 have very similar FT-IR spectra, despite their different morphological aspects. A previous analysis in single-doped $\text{Tm}^{3+}\text{-Lu}_2\text{O}_3$ nanorods prepared with both pH values through the same hydrothermal syntheses indicated nearly identical room temperature lifetimes and decay intensities for Tm^{3+} $^3\text{H}_4$ de-excitation ($\lambda_{\text{EXC}} = 802$ nm, $\lambda_{\text{EMI}} = 1446$ nm) [51]. In view of these similarities and given that nanorods prepared at $\text{pH} = 7$ allow better handling for SNOM measurements, the following spectroscopic measurements have been carried out for this type of prepared nanorod.

The bixbyite-type structure [52] of the Lu_2O_3 sesquioxide belongs to the cubic space group $Ia\bar{3}$ with two different crystal sites of point symmetries C_2 and C_{3i} (in 3:1 ratio in

the unit cell), which are randomly occupied by the Ln [53]. Selection rules derived from the inversion center associated with the latter site forbid electric dipole transitions from it; thus emission spectra in the following figures mainly show induced electric dipole transitions for Er^{3+} or Tm^{3+} located in C_2 sites, and magnetic dipole transitions, only rarely seen, from both kind of site.

3.2.1. Upconversion spectra under excitation at $\lambda_{\text{EXC}} = 980$ nm on Yb^{3+} , $\text{Er}^{3+}\text{-Lu}_2\text{O}_3$ nanorods. The room temperature UC spectra in the range 350–700 nm for $\text{Lu}_{1.96-x}\text{Yb}_x\text{Er}_{0.04}\text{O}_3$ ($x = 0.30, 0.25, 0.20, 0.12$ and 0.04) and $\text{Lu}_{1.80-x}\text{Yb}_{0.20}\text{Er}_x\text{O}_3$ ($x = 0.15, 0.10, 0.04$) nanorods under excitation into the $^2\text{F}_{5/2}$ state of Yb^{3+} ($\lambda_{\text{EXC}} = 980$ nm) are shown in figures 7(a)–(e) and 8(a)–(c). Two main groups of bands are observed in these spectra. The green

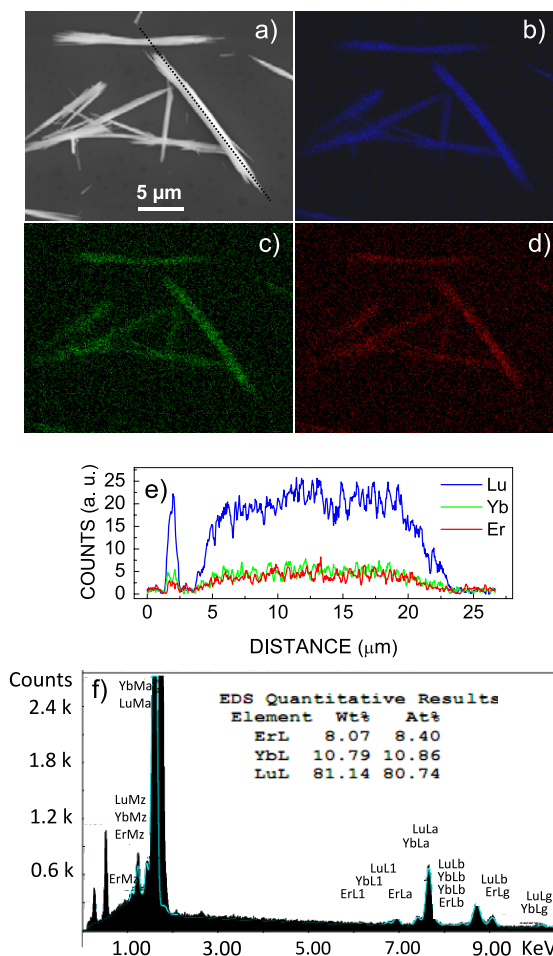


Figure 6. (a) Field-emission SEM image of $\text{Lu}_{1.65}\text{Yb}_{0.20}\text{Er}_{0.15}\text{O}_3$ nanorods. EDX color maps of (b) Lu, (c) Yb, (d) Er. (e) plots of the relative amounts of each element (Lu, Yb, Er) as a function of the position along the marked line in (a). (f) EDX quantitative analysis.

emission (figures 7(d) and (e)) is attributed to ${}^2\text{H}_{11/2} \rightarrow {}^4\text{I}_{15/2}$ and ${}^4\text{S}_{3/2} \rightarrow {}^4\text{I}_{15/2}$ transitions, centered at 525 and 550 nm, respectively. The red emission is observed at 650–690 nm, which corresponds to the ${}^4\text{F}_{9/2} \rightarrow {}^4\text{I}_{15/2}$ transition. Additionally, the very weak blue emission that can be seen at 405–420 nm is attributed to ${}^2\text{H}_{9/2} \rightarrow {}^4\text{I}_{15/2}$. Splittings of these optical transitions are comparable to those reported for Er^{3+} -doped bulk single crystal [54], indicating that in all cases the crystal site(s) for Er^{3+} is kept in the prepared nanorods. However, possible changes in the local structure around Er^{3+} in NCs cannot be dismissed, since some broadening is observed in the corresponding spectra.

The important change observed in the relative intensities of green and red UC emissions in the series of figures 7(a)–(e), i.e. the strong development of ${}^4\text{F}_{9/2} \rightarrow {}^4\text{I}_{15/2}$ red emission with regard to the green bands ${}^4\text{S}_{3/2} \rightarrow {}^4\text{I}_{15/2}$ and ${}^2\text{H}_{11/2} \rightarrow {}^4\text{I}_{15/2}$, which even vanish for $\text{Yb}^{3+} x \geq 0.20$, is directly related to the increase in the Yb^{3+} concentration, since this

first group of samples were prepared with the same Er^{3+} concentration. On the other hand, the magnitude of this enhancement is drastically superior to that observed in bulk counterparts—see for instance the corresponding UC spectra for $\text{Er}^{3+}\text{-Yb}^{3+}$ -codoped Y_2O_3 [17], or Lu_2O_3 [20] single crystals. Alternatively, for nanorods with the same high Yb^{3+} concentration ($\text{Yb}^{3+} x = 20$) only the red emission is observed, without appreciable differences in the Er^{3+} content (see figures 8(a)–(c)).

Following NIR excitation $\lambda_{\text{EXC}} = 980$ nm, the established UC mechanisms responsible for the population of ${}^4\text{F}_{7/2}$ in Er^{3+} , Yb^{3+} -codoped bulk systems proceed through two successive near-resonant transfers of energy from Yb^{3+} to Er^{3+} , the first exciting Er^{3+} to the intermediate ${}^4\text{I}_{11/2}$ state and then to ${}^4\text{F}_{7/2}$, although UC processes through Er^{3+} ions can also play a role. The lower emitting levels ${}^2\text{H}_{11/2}$ and ${}^4\text{S}_{3/2}$ (green), and then ${}^4\text{F}_{9/2}$ (red) and ${}^4\text{I}_{9/2}$ and ${}^4\text{I}_{11/2}$ (IR) will be populated by multiphonon relaxation from ${}^4\text{F}_{7/2}$. On this basis,

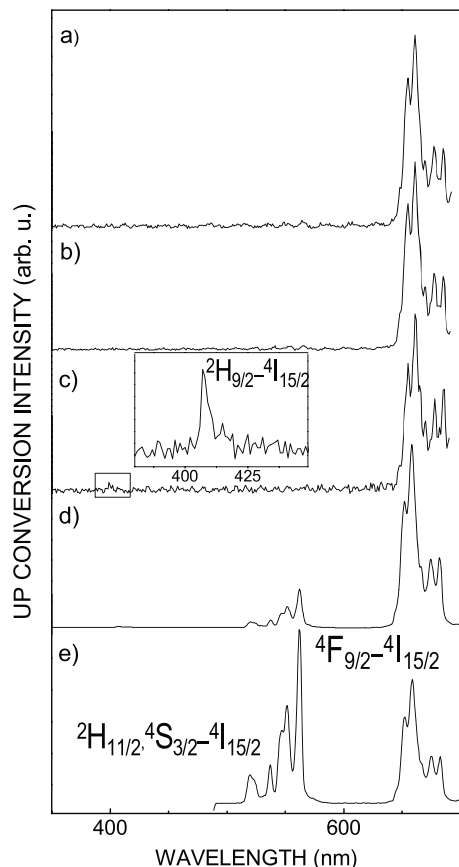


Figure 7. Room temperature Yb^{3+} concentration-dependent upconversion ($\lambda_{\text{EXC}} = 980 \text{ nm}$) luminescence spectra of $\text{Lu}_{1.96-x}\text{Yb}_x\text{Er}_{0.04}\text{O}_3$ nanorods: (a) $x = 0.30$, (b) $x = 0.25$, (c) $x = 0.20$, (d) $x = 0.12$, (e) $x = 0.04$.

the expected Er^{3+} emission would be predominantly green, as the red-emitting ${}^4\text{F}_{9/2}$ is populated by non-radiative decay from ${}^4\text{S}_{3/2}$. However, the low intensity of the green emission and its gradual decrease with regards to the red emission for higher Yb^{3+} contents points to an increase in the efficiency of the ion-pair cross-relaxation (CR) process (${}^4\text{F}_{7/2}, {}^4\text{I}_{11/2}$) \rightarrow (${}^4\text{F}_{9/2}, {}^4\text{F}_{9/2}$) that directly populates ${}^4\text{F}_{9/2}$ bypassing ${}^2\text{H}_{11/2}$ and ${}^4\text{S}_{3/2}$ [39]. This process, which fully explains the observed emphasized red emission following NIR excitation in both bulk crystals [17] and polycrystalline ceramic powders [39], does not account for the larger intensity differences in the red emission between bulk and nanocrystalline size regimes. Thus, another mechanism also populating ${}^4\text{F}_{9/2}$ and favored by the specific characteristics of prepared Yb, Er- Lu_2O_3 nanorods must be additionally operative under NIR excitation. A proposed process [17] indicates that after initial energy transfer from Yb^{3+} in ${}^2\text{F}_{5/2}$, Er^{3+} in ${}^4\text{I}_{11/2}$ non-radiatively decays to ${}^4\text{I}_{13/2}$, the energy gap between both states being $\sim 3600 \text{ cm}^{-1}$. This relaxation process can be very effective

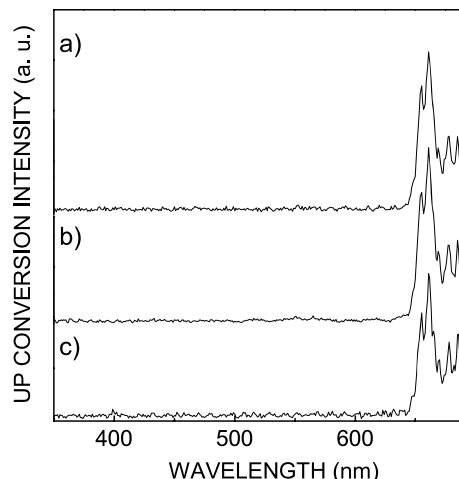


Figure 8. Room temperature upconversion ($\lambda_{\text{EXC}} = 980 \text{ nm}$) luminescence spectra of $\text{Lu}_{1.80-x}\text{Yb}_{0.20}\text{Er}_{0.0x}\text{O}_3$ nanorods: (a) $x = 0.15$, (b) $x = 0.10$, (c) $x = 0.04$.

given the previously indicated availability of large phonons at ~ 1400 , ~ 1530 , ~ 1630 and 3440 cm^{-1} from adsorbed CO_2 and/or H_2O species [3, 20], which can easily cover the gap. Next, another energy transfer from Yb^{3+} in ${}^2\text{F}_{5/2}$ will populate $\text{Er}^{3+} {}^4\text{F}_{9/2}$ through the non-resonant ${}^4\text{I}_{13/2} \rightarrow {}^4\text{F}_{9/2}$ transition, and the excess energy ($\sim 1600 \text{ cm}^{-1}$) was also dissipated through phonons of the lattice. The full phonon-assisted process is clearly dependent on the Yb^{3+} concentration, since an increase in the latter results in a corresponding increase in red enhancement. Figure 9 shows a scheme of these proposed mechanisms for populating ${}^4\text{F}_{9/2}$ under excitation at $\lambda_{\text{EXC}} = 980 \text{ nm}$, which would account for the red emission enhancement. Furthermore, in heavily Yb^{3+} -doped sesquioxide nanocrystalline materials the vanishing green Er^{3+} emission has been explained by the change from a two-photon to a three-photon process for populating ${}^4\text{S}_{3/2}$ [17].

Even though the population mechanisms of multiphoton excited UC emitting levels in nanocrystalline materials can be different and often more complex than for bulk counterparts, important information about the order of the processes involved and their physical origin and strength can be extracted from the interpretation of the dependence of the measured intensity of the UC luminescence on the excitation pump power. In fact, the above previously described UC mechanisms have been supported by results on the power dependence of the intensity of the UC emissions, from its usually assumed proportionality to an n th power of the IR excitation intensity, $I_{\text{VIS}} \propto I_{\text{IR}}^n$, where the integer n represents the number of photons required to populate the visible states per upconverted photon emitted from them. In this way, slopes of ~ 2 have been obtained in double-logarithmic plots of the UC luminescence intensity of ${}^4\text{F}_{9/2} \rightarrow {}^4\text{I}_{15/2}$, ${}^2\text{H}_{11/2} \rightarrow {}^4\text{I}_{15/2}$ and ${}^4\text{S}_{3/2} \rightarrow {}^4\text{I}_{15/2}$ versus the excitation power [3, 17, 20], and slopes of nearly 3 for ${}^4\text{S}_{3/2} \rightarrow {}^4\text{I}_{15/2}$ in highly Yb^{3+} -doped samples [17].

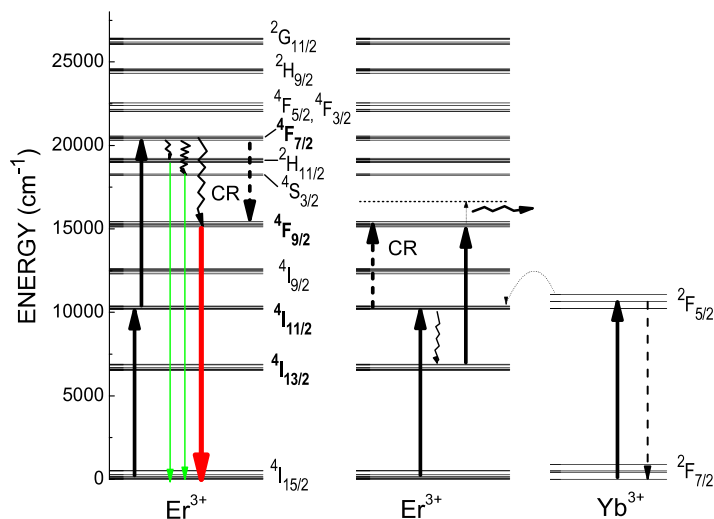


Figure 9. Scheme of energy levels of Er^{3+} and Yb^{3+} in Lu_2O_3 and the proposed mechanisms responsible for populating $^4\text{F}_{9/2}$ in Yb^{3+} , Er^{3+} - Lu_2O_3 nanorods after pumping at $\lambda_{\text{EXC}} = 980$ nm.

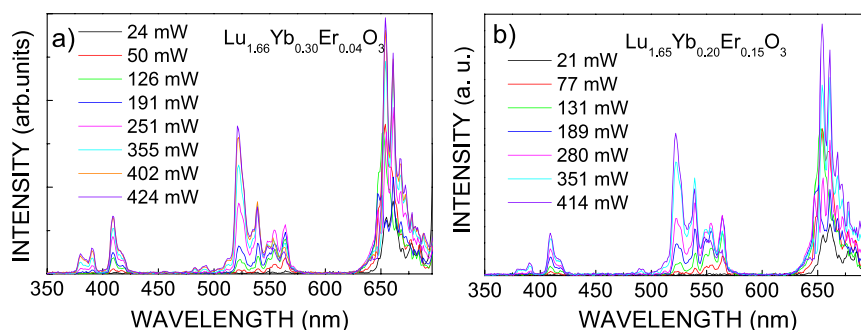


Figure 10. Power dependence of the upconverted luminescence in Yb, Er-doped Lu_2O_3 nanorods following NIR excitation: (a) $\text{Lu}_{1.66}\text{Yb}_{0.30}\text{Er}_{0.04}\text{O}_3$, (b) $\text{Lu}_{1.65}\text{Yb}_{0.20}\text{Er}_{0.15}\text{O}_3$.

For the current prepared Yb^{3+} , Er^{3+} - Lu_2O_3 nanorods the validity of the above described processes have been tested by analyzing the power dependence of the UC visible emissions on selected compositions, i.e. with variable Yb^{3+} concentrations, $\text{Lu}_{1.96-x}\text{Yb}_x\text{Er}_{0.04}\text{O}_3$ ($x = 0.30, 0.25, 0.20$), and variable Er^{3+} concentrations, $\text{Lu}_{1.80-x}\text{Yb}_{0.20}\text{Er}_x\text{O}_3$ ($x = 0.15, 0.10, 0.04$). Figures 10(a) and (b) show the UC spectra collected under different power excitations (up to ~ 425 mW) for the first composition in each series, and figures 11(a)–(c), 12(a) and (b) are the double-logarithmic plots of the integrated UC intensities for red, green and blue emissions versus the laser power for all analyzed samples.

For the $^4\text{F}_{9/2}$ - $^4\text{I}_{15/2}$ red emission, for any given composition, two different slopes evolve along the range of measured excitation power: the first slope ($n = 0.4$ – 1.0) starts at the lower measured power and extends up to ~ 150 mW, and then it increase ($n = 0.8$ – 1.2) between ~ 180 mW and the higher measured power. For both kinds of red slope the

general trend is a decrease with increasing Yb^{3+} concentration (see figures 11(a)–(c)), while for constant Yb^{3+} content these slopes decrease with increasing concentration of Er^{3+} (see figures 11(c), 12(a) and (b) in the indicated order).

For the $^4\text{S}_{3/2}$ - $^4\text{I}_{15/2}$ green emission the slope ($n = 0.9$ – 1.3) clearly increases with the decrease of the Yb^{3+} concentration (see figures 11(a)–(c)), and it seems to also experience an enhancement ($n = 1.1$ – 1.2) with increase in the Er^{3+} concentration (see figures 11(c), 12(a) and (b)). Furthermore, in the series $\text{Lu}_{1.80-x}\text{Yb}_{0.20}\text{Er}_x\text{O}_3$ the minimum n value corresponds to $\text{Er}^{3+} x = 0.10$ (figure 12(a)). However, except for $\text{Lu}_{1.76}\text{Yb}_{0.20}\text{Er}_{0.04}\text{O}_3$, the material with the lowest Er^{3+} concentration, the plots gradually bend downward with excitation pump powers higher than ~ 250 mW.

Although with unequivocally higher n values, the evolution of the slope of the $^2\text{H}_{11/2}$ - $^4\text{I}_{15/2}$ green emission intensity follows a similar trend to that for $^4\text{S}_{3/2}$ - $^4\text{I}_{15/2}$, i.e. a decrease (1.9–1.6) with increase in Yb^{3+} concentration, and an

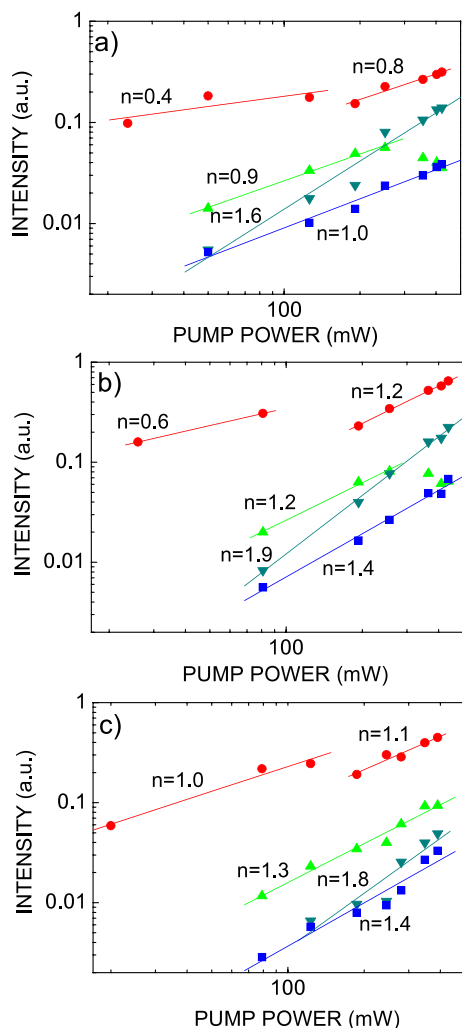


Figure 11. Measured intensities for ${}^4F_{9/2}\text{-}{}^4I_{15/2}$ (circles), ${}^4S_{3/2}\text{-}{}^4I_{15/2}$ (up triangles), ${}^2H_{11/2}\text{-}{}^4I_{15/2}$ (down triangles) and ${}^2H_{9/2}\text{-}{}^4I_{15/2}$ (squares) versus excitation pump power for $\text{Lu}_{1.96-x}\text{Yb}_x\text{Er}_{0.04}\text{O}_3$ nanorods: (a) $x = 0.30$, (b) $x = 0.25$, (c) $x = 0.20$. The numbers denote the slope in double-logarithmic representation.

enhancement (1.8–1.9) towards the higher Er^{3+} concentration. In this latter Er^{3+} variable series the minimum n value, $n = 1.7$, corresponds to the Er^{3+} content $x = 0.10$.

The evolution of the slope of the ${}^2H_{9/2}\text{-}{}^4I_{15/2}$ blue emission with pump power exhibits a marked increase (1.0–1.4) as the Yb^{3+} concentration decreases, and conversely a decrease (1.4–1.2) when the Er^{3+} concentration increases.

With regard to reported results on sesquioxides [3, 17, 20], the severely reduced slopes for the ${}^4F_{9/2}\text{-}{}^4I_{15/2}$, ${}^4S_{3/2}\text{-}{}^4I_{15/2}$, ${}^2H_{11/2}\text{-}{}^4I_{15/2}$ and ${}^2H_{9/2}\text{-}{}^4I_{15/2}$ visible UC emissions observed in Yb , $\text{Er}\text{-Lu}_2\text{O}_3$ nanorods point to larger UC rates in schemes of competition between linear decay and UC processes for depletion for intermediate excited states [55]. Large UC rates

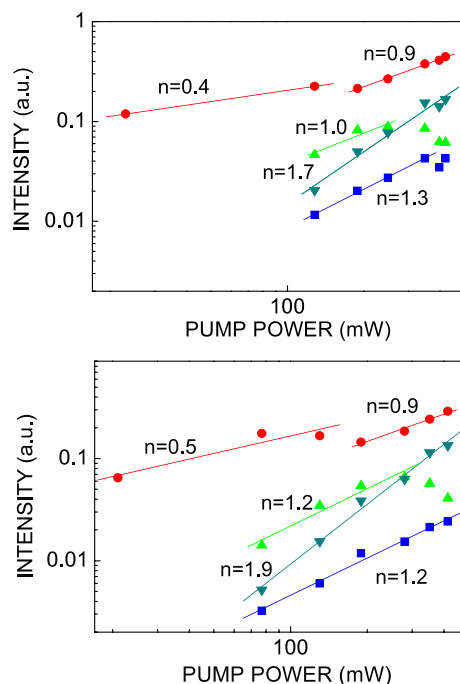


Figure 12. Measured intensities for ${}^4F_{9/2}\text{-}{}^4I_{15/2}$ (circles), ${}^4S_{3/2}\text{-}{}^4I_{15/2}$ (up triangles), ${}^2H_{11/2}\text{-}{}^4I_{15/2}$ (down triangles) and ${}^2H_{9/2}\text{-}{}^4I_{15/2}$ (squares) versus excitation pump power for $\text{Lu}_{1.80-x}\text{Yb}_{0.20}\text{Er}_x\text{O}_3$ nanorods: (a) $x = 0.10$, (b) $x = 0.15$. The numbers denote the slope in double-logarithmic representation.

in bulk systems producing detectable UC luminescence are associated with power dependences of the UC luminescence of less than I^n [55]. In these bulk systems high absorbed pump intensities are required for UC acting as the main depletion process of intermediate excited states (see the examples in [55]). For nanocrystalline materials the situation can be somewhat different [56].

In the case of prepared Yb , $\text{Er}\text{-Lu}_2\text{O}_3$ nanorods the mechanisms responsible for the reduced slopes are present at NIR excitation powers lower than in bulk systems. For the ${}^4F_{9/2}\text{-}{}^4I_{15/2}$ red emission, low n slopes and their observed discontinuity along the measured NIR pump power range in our nanorods suggest the existence of different underlying processes. When the NIR excitation power is low (under ~ 150 mW), the explained mechanisms that populate ${}^4F_{9/2}$ and account for the large enhancement of its emission with regards to ${}^2H_{11/2}$ and ${}^4S_{3/2}$ support large UC rates and thus reduced slopes. One is the two-photon phonon-assisted energy transfer upconversion from ${}^2F_{5/2}$ Yb^{3+} that effectively populates ${}^4F_{9/2}$ with ${}^4I_{13/2}$ as the intermediate excited state. As the Yb^{3+} concentration increases, the energy transfer from Yb^{3+} to Er^{3+} will make UC from the intermediate ${}^4I_{13/2}$ more efficient, resulting in the increasing importance of UC. The slope of the red UC luminescence from ${}^4F_{9/2}$ will lessen from quadratic to almost linear [55], thus explaining the observed low ~ 1 slopes in the power dependence for higher Yb^{3+} -doped nanorods.

Furthermore, under comparable sizes and surface to volume ratios, for higher Er^{3+} concentrations the proportion of Er^{3+} active centers located at the surface of nanorods close to high energy phonons from adsorbed species will be larger, which favor lower UC luminescence slopes. Another operative UC process involves ${}^4\text{F}_{9/2}$ population by phonon-assisted CR (${}^4\text{F}_{7/2}$, ${}^4\text{I}_{11/2}$) \rightarrow (${}^4\text{F}_{9/2}$, ${}^4\text{F}_{9/2}$). The lower slopes for heavily Yb^{3+} -doped nanorods can be due, in addition, to the increasing efficiency of the CR process. Alternatively, within the series of nanorods with the same Yb^{3+} concentration, the maximum efficiency will be reached for a given Er^{3+} concentration, which will show the minimum slope, as can be seen in the figure 12(a) corresponding to Er^{3+} $x = 0.10$. On the other hand, for NIR excitation at high enough powers (over ~ 180 mW), the thermal effect caused in nanorods [56] would largely remove the high energy phonons from their surface. Thus, since phonon-assisted UC mechanisms are no longer supported, the UC rate will be smaller and the slopes of the power dependence will increase. The competition between the first two UC mechanisms and the opposite latter effect along the range of NIR excitation powers determines the discontinuity in the slopes for the red ${}^4\text{F}_{9/2}$ - ${}^4\text{I}_{15/2}$ emission.

As indicated above, the slopes of the ${}^2\text{H}_{11/2}$ - ${}^4\text{I}_{15/2}$ green emission are in all cases closer to 2 than to 1. In this case the intermediate excited level is ${}^4\text{I}_{11/2}$. Because of the non-radiative relaxation of ${}^4\text{I}_{11/2}$ to ${}^4\text{I}_{13/2}$, the importance of the UC decreases, leading the slope of this green emission to be ~ 2 . The UC luminescence power dependence for the other two-photon ${}^4\text{S}_{3/2}$ - ${}^4\text{I}_{15/2}$ green and three-photon ${}^2\text{H}_{9/2}$ - ${}^4\text{I}_{15/2}$ blue emissions presents slopes closer to 1, which indicates once again the dominating influence of UC over linear decay for the depletion of corresponding intermediate excited states. Furthermore, the downward curvature starting at ~ 250 mW observed in the slopes of ${}^4\text{S}_{3/2}$ - ${}^4\text{I}_{15/2}$ is an indication of a typical saturation phenomenon caused by the population exhaustion to the ground state along with thermal quenching effects at these high pump powers [56].

It is noteworthy that other nanocrystalline Yb, Er-Lu₂O₃ materials with various shapes, nanoparticles, nanosheets and even nanorods [20], present a very different behavior from that of the currently analyzed nanorods, with a relative ratio of the red UC emission intensity to the green one increasing for the smaller nanocrystals, and a synchronously enhanced three-photon process accounting for the green emission. The large ${}^4\text{I}_{11/2}$ - ${}^4\text{I}_{13/2}$ non-radiative relaxation rate interpreted as derived from the presence of phonons from surface hydroxyl groups is invoked to induce these two correlative phenomena. However, in this case the determination of the slope of the green UC luminescence power dependence ($n = 2.38$ for Lu_{1.88}Yb_{0.1}Er_{0.02}O₃ nanorods) has been calculated without discriminating the contribution of each ${}^2\text{H}_{11/2}$ - ${}^4\text{I}_{15/2}$ and ${}^4\text{S}_{3/2}$ - ${}^4\text{I}_{15/2}$ green transition, masking their individual features, that anyway do not seem to be the same.

3.2.2. Cathodoluminescence spectra on Yb³⁺, Er³⁺-Lu₂O₃ nanorods. Room temperature CL spectra of Lu_{1.96-x}Yb_xEr_{0.04}O₃ ($x = 0.30, 0.25, 0.20, 0.12$ and 0.04) and Lu_{1.80-x}Yb_{0.20}Er_xO₃ ($x = 0.15, 0.10, 0.04$) nanorods in the

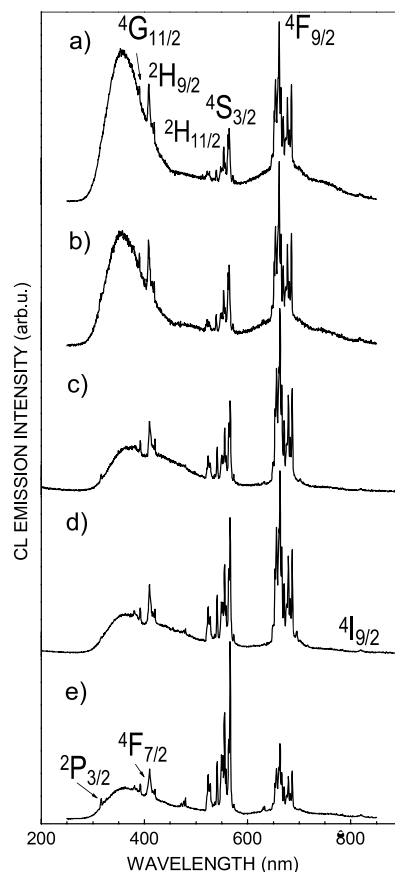


Figure 13. Cathodoluminescence spectra of Lu_{1.96-x}Yb_xEr_{0.04}O₃ nanorods under an electron beam excitation voltage of $V_{\text{accel}} = 15$ kV and probe current 20 nA: (a) $x = 0.30$, (b) $x = 0.25$, (c) $x = 0.20$, (d) $x = 0.12$, (e) $x = 0.04$, all transitions are from the indicated states to the ground ${}^4\text{I}_{15/2}$ multiplet.

200–900 nm range are shown in figures 13(a)–(e) and 14(a)–(c), respectively. The sharp observed lines arise from the intra-shell $4f^{11}$ transitions of the Er^{3+} configuration, and have been assigned on the basis of previously determined energy levels of Er^{3+} in Lu₂O₃ single crystals [54], whereas the broad background emission in the 300–500 nm spectral region results from non-rare-earth defect centers in the host, mainly transitions involving oxygen vacancies [57, 58]. The first difference from the above UC spectra is the observation of well-developed UV bands, among which the more important contribution corresponds to the ${}^2\text{H}_{9/2}$ - ${}^4\text{I}_{15/2}$ transition centered at ~ 410 nm. Furthermore, the intensity ratio between red and green emissions, and also between red and UV emissions, again evolve, getting higher with increasing Yb^{3+} content, and although the differences are not so extreme as with 980 nm excitation, it is clear that the red ${}^2\text{F}_{9/2}$ - ${}^4\text{I}_{15/2}$ transition dominates the CL spectrum for Lu_{1.96-x}Yb_xEr_{0.04}O₃ nanorods with $x \geq 0.12$, that is, for $[\text{Yb}^{3+}] \geq 6$ mol%.

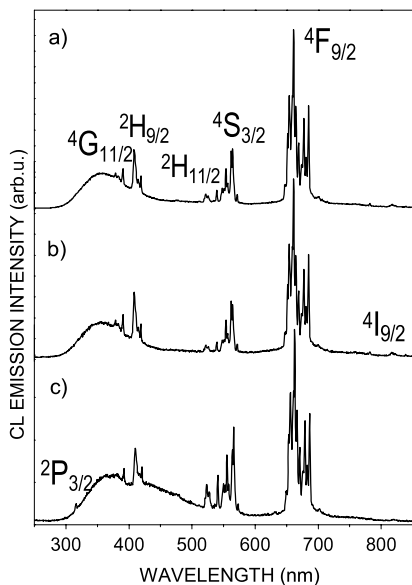


Figure 14. Cathodoluminescence spectra of $\text{Lu}_{1.80-x}\text{Yb}_{0.20}\text{Er}_x\text{O}_3$ nanorods under an electron beam excitation voltage of $V_{\text{accel}} = 15$ kV and probe current 20 nA: (a) $x = 0.15$, (b) $x = 0.10$, (c) $x = 0.04$, all transitions are from the indicated states to the ground $^4\text{I}_{15/2}$ multiplet.

On the other hand, in CL spectra for nanorods with the same high concentration of Yb^{3+} ($\text{Yb}^{3+} x = 20$), the intensity of observed bands in the green region is somewhat lower for the higher Er^{3+} content, but the main difference along this group concerns evolution of the two bands, whereas the $^4\text{S}_{3/2}\text{--}^4\text{I}_{15/2}$ band remains well developed for nanorods with the higher Er^{3+} concentration, the intensity of $^2\text{H}_{11/2}\text{--}^4\text{I}_{15/2}$ decreased (see figures 14(a)–(c)).

The analysis of UC and CL spectra in Yb , $\text{Er}\text{--}\text{Lu}_2\text{O}_3$ nanorods has shown that the ($^4\text{F}_{9/2}\text{--}^4\text{I}_{15/2}$) red/($^2\text{H}_{11/2}$, $^4\text{S}_{3/2}\text{--}^4\text{I}_{15/2}$) green emissions ratio changes differently in each case. If the origin of the excitation is a NIR laser ($\lambda_{\text{EXC}} \sim 980$ nm), UC mechanisms populating the red-emitting level are enhanced by the presence of high energy phonons from adsorbed species at the surface of nanorods, which moreover constitute a closer environment to a fraction of Yb^{3+} and optically active Er^{3+} centers involved in UC energy transfer processes. Reduced slopes for the dependence of UC luminescence intensities on pump powers (~ 1 for $^4\text{F}_{9/2}\text{--}^4\text{I}_{15/2}$, and < 2 for $^2\text{H}_{11/2}\text{--}^4\text{I}_{15/2}$), even at low powers, indicate the predominance of UC in competition with linear decay for the depletion of Er^{3+} excited states in our nanorods. Alternatively, by using electron beams, Er^{3+} emissions in CL spectra are linear decays from higher lying excited multiplets, and the optically active centers involved are those in the body of nanorods, while the surface phonons quench the luminescence efficiency.

3.2.3. *Upconversion spectra under excitation at $\lambda_{\text{EXC}} = 980$ nm on Yb^{3+} , $\text{Tm}^{3+}\text{--}\text{Lu}_2\text{O}_3$ nanorods.* The room

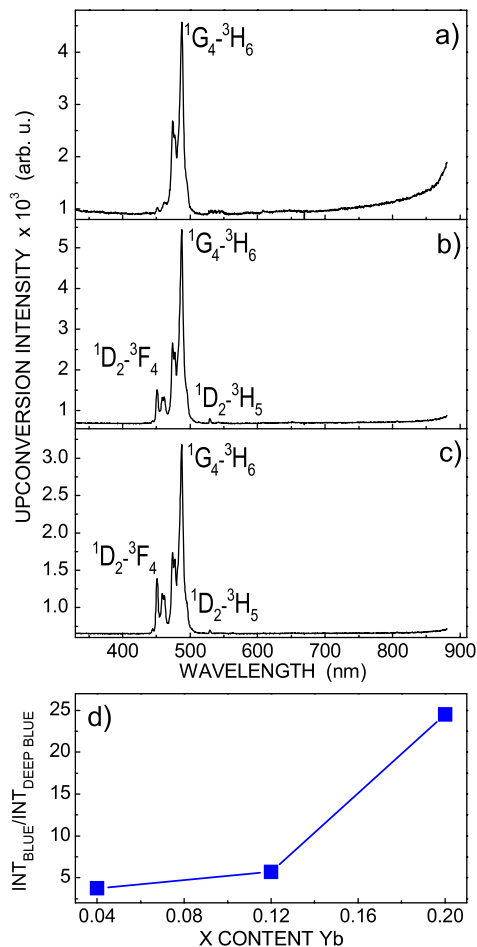


Figure 15. Room temperature concentration-dependent upconversion ($\lambda_{\text{EXC}} = 980$ nm) luminescence spectra of hydrothermal $\text{Lu}_{1.96-x}\text{Yb}_x\text{Tm}_{0.04}\text{O}_3$ nanorods: (a) $x = 0.20$, (b) $x = 0.12$, (c) $x = 0.04$; (d) intensity ratio of blue to deep-blue upconversion bands.

temperature UC spectra in the range $\sim 330\text{--}900$ nm for $\text{Lu}_{1.96-x}\text{Yb}_x\text{Tm}_{0.04}\text{O}_3$ ($x = 0.20, 0.12, 0.04$) nanorods under excitation at $\lambda_{\text{EXC}} = 980$ nm are shown in figures 15(a)–(c). The observed deep-blue emission at $\sim 450\text{--}465$ nm is attributed to $^1\text{D}_2\text{--}^3\text{F}_4$, and the very intense blue emission observed at $\sim 470\text{--}490$ nm is ascribed to the $^1\text{G}_4 \rightarrow ^3\text{H}_6$ transition. Additionally, the very weak green emission centered at ~ 529 nm can be assigned to the $^1\text{D}_2\text{--}^3\text{H}_5$ transition. A clear development of the dominant $^1\text{G}_4\text{--}^3\text{H}_6$ transition with regard to $^1\text{D}_2\text{--}^3\text{F}_4$ results when the Yb^{3+} content increases (see figure 15(d)). No traces appear of the characteristic NIR peaks at ~ 800 nm accounting for the $^3\text{H}_4 \rightarrow ^3\text{H}_6$ transition, which typically is the dominant one in UC spectra of Yb^{3+} , Tm^{3+} -codoped nanoparticles, for example in the case of the highly efficient upconverting Yb^{3+} , $\text{Tm}^{3+}\text{--}\text{NaYF}_4$ nanoparticles at low excitation densities [5, 59, 60], Yb^{3+} , $\text{Tm}^{3+}\text{--}\text{GdF}_3$ [61],

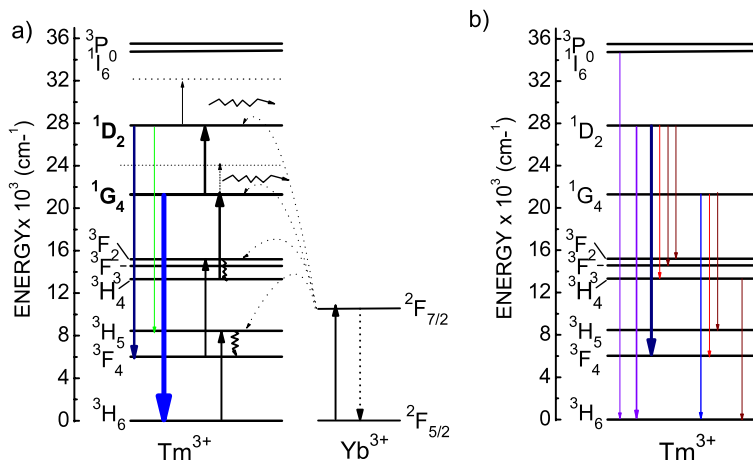


Figure 16. (a) Scheme of energy levels for of Tm^{3+} and Yb^{3+} configurations in Lu_2O_3 , and energy transfers proposed for observed upconversion emission (excitation $\lambda_{\text{EXC}} = 980 \text{ nm}$) in hydrothermal $\text{Lu}_{1.96-x}\text{Yb}_x\text{Tm}_{0.04}\text{O}_3$ nanorods. (b) Cathodoluminescence transitions observed in $\text{Lu}_{1.96-x}\text{Yb}_x\text{Tm}_{0.04}\text{O}_3$ nanorods.

and also for Yb^{3+} , Tm^{3+} - Lu_2O_3 agglomerated particles [62]. The $^1\text{G}_4$ - $^3\text{F}_4$ red emission at $\sim 650 \text{ nm}$, which although weak is usually seen in Yb^{3+} , Tm^{3+} - Lu_2O_3 nanoparticles [8, 61], is also absent in the current Yb^{3+} , Tm^{3+} - Lu_2O_3 nanorods. The population of $\text{Tm}^{3+}^3\text{H}_4$, $^1\text{G}_4$ and $^1\text{D}_2$ excited states is accomplished by sequential two-, three- and four-photon energy transfer processes from excited $\text{Yb}^{3+}^2\text{F}_{5/2}$ to Tm^{3+} , respectively (see figure 16(a)), thus the probabilities of these mechanisms get lower in the same order. Given the non-existent emission from $^3\text{H}_4$, and the emphasized emission from $^1\text{G}_4$, some alteration of the usual UC mechanisms to privilege the population of $^1\text{G}_4$ through phonon-assisted energy transfer and non-radiative relaxations, favored by the presence of large phonons in current nanorods or/and through the decrease in the number of required absorbed photons [60], are currently acting on the prepared Yb^{3+} , Tm^{3+} - Lu_2O_3 nanorods.

3.2.4. Cathodoluminescence spectra on Yb^{3+} , Tm^{3+} - Lu_2O_3 nanorods. Room temperature CL spectra of $\text{Lu}_{1.96-x}\text{Yb}_x\text{Tm}_{0.04}\text{O}_3$ nanorods in the 200–900 nm range are shown in figures 17(a)–(c). The sharp observed lines arise from the intra-shell $4f^{12}$ transitions of the Tm^{3+} configuration, and have been assigned taking into account the crystal field energy levels scheme of Tm^{3+} in the Lu_2O_3 sesquioxide host [54]. Also in these spectra we see the broad background emission in the 300–500 nm spectral range, with the same origin as indicated for $\text{Lu}_{1.96-x}\text{Yb}_x\text{Er}_{0.04}\text{O}_3$. Superimposed on this emission we can observe UV bands at ~ 380 – 390 nm attributed to the $^1\text{D}_2$ - $^3\text{H}_6$, the very intense deep-blue emission at 450–470 nm corresponding to the $^1\text{D}_2$ - $^3\text{F}_4$, which is the dominant band in these spectra, while the blue emission $^1\text{G}_4$ - $^3\text{H}_6$ and other red ($^1\text{D}_2$ - $^3\text{H}_4$, $^1\text{G}_4$ - $^3\text{F}_4$) and NIR ($^1\text{D}_2$ - $^3\text{F}_{2,3}$, $^1\text{G}_4$ - $^3\text{H}_5$, $^3\text{H}_4$ - $^3\text{H}_6$) transitions are very weak. Figure 16(b) shows a scheme of these observed transitions. Furthermore, the intensity ratio

between deep-blue and blue emissions, and also between deep-blue and UV emissions, increases with the Yb^{3+} content (see the figure 17(d)), with the opposite trend to the observed behavior in the evolution of the UC spectra with 980 nm excitation.

3.3. Assessment of single-mode waveguiding behavior of Yb^{3+} , Er^{3+} -doped Lu_2O_3 nanorods

To investigate light propagation into the prepared nanorods, SNOM photoluminescence images have been collected for assemblies like those shown in figures 4(d) and (e), which are somewhat thicker than the individual nanorods depicted in figure 4(f). Figures 18(a) and (b) show the refined topographical image and the corresponding photoluminescence image of a 1D structure with a cross section of $\sim 300 \text{ nm}$. The photoluminescence view indicates uniform light emission through the whole rod. However, the light propagation has currently not been seen.

To determine the requirements that govern the waveguiding behavior in the current Lu_2O_3 nanorods, and thus to find reasons for the unsuccessful observation, we have performed numerical simulations of the mode distribution following a previously established model [40]. Since the refractive index of Lu_2O_3 is sufficiently higher than that of the xylene-PMMA polymeric film ($n = 1.48$ at $1 \mu\text{m}$) in which the prepared nanorods have been dispersed, and the wrap layer thickness is negligible ($< 5 \text{ nm}$), prepared subwavelength Yb^{3+} , Er^{3+} Lu_2O_3 nanorods can be considered as air-clad rods in our calculations. The diameter d for achieving the condition of a single-mode waveguide in such rods can be obtained from the equation

$$V = \frac{\pi d}{\lambda_0} (n_1^2 - n_{\text{air}}^2)^{1/2} < 2.405 \quad (1)$$

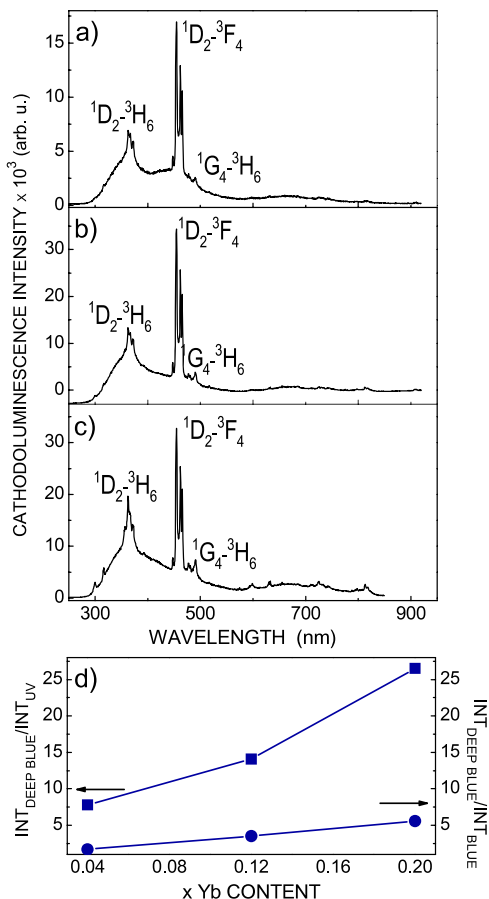


Figure 17. Cathodoluminescence spectra of hydrothermal $\text{Lu}_{1.96-x}\text{Yb}_x\text{Tm}_{0.04}\text{O}_3$ nanorods under excitation by an electron beam $V_{\text{accel}} = 15$ kV, $i = 20$ nA, (a) $x = 0.20$, (b) $x = 0.12$, (c) $x = 0.04$. (d) Intensity ratio of deep-blue to UV (squares) and deep-blue to blue (circles) cathodoluminescence emission bands.

where d is the rod diameter, λ_0 is the vacuum wavelength of the excitation light and n_1 and n_{air} are the refractive indices of the waveguide core, Lu_2O_3 , and the cladding layer, air, respectively. As previously seen in figures 4(d) and (e), prepared nanorods have some porosity. To properly account for the influence of pores in the effective refractive index n_{eff} of the nanorod (to be used instead of n_1 in equation (1)) a *filling factor* f will be considered. The filling factor f and the void porosity p have been defined in terms of the void volume V_v , solid volume V_s and total volume V_t as $f = V_s/V_t$ and $p = V_v/V_t$, satisfying the condition $f + p = 1$ [63]. When f is expressed as a function of the experimental parameters, i.e. the crystal density of solid Lu_2O_3 (neglecting the influence of doping), $\rho_{\text{Lu}_2\text{O}_3}$, and the total volume of pores per gram of prepared Lu_2O_3 nanorods obtained from N_2 adsorption–

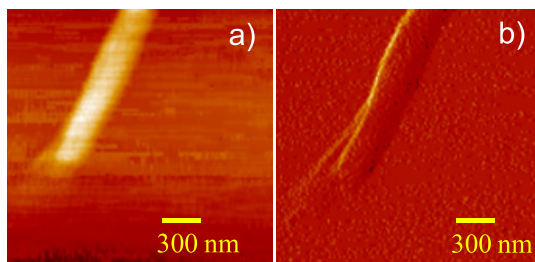


Figure 18. (a) Optical and (b) topographic SNOM images of $\text{Lu}_{1.76}\text{Yb}_{0.20}\text{Er}_{0.04}\text{O}_3$ nanorods.

desorption measurements, V_{BHH} , it can be calculated as

$$f = \frac{1}{1 + \rho_{\text{Lu}_2\text{O}_3} V_{\text{BHH}}} \quad (2)$$

with $\rho_{\text{Lu}_2\text{O}_3} = 9.42$ g cm^{-3} and $V_{\text{BHH}} = 0.0716$ cm^3 g^{-1} yielding a value of $f = 0.6$. Then, using the Maxwell–Garnett approximation [64], n_{eff} is expressed as a weighted sum of the square refractive indices

$$n_{\text{eff}}^2(f) = f n_{\text{Lu}_2\text{O}_3}^2 + p n_{\text{air}}^2. \quad (3)$$

The dispersion of the refractive index of Lu_2O_3 can be calculated with a Sellmeier-type expression as

$$n_{\text{Lu}_2\text{O}_3}^2(\lambda) = D_1 + \frac{D_2}{(\lambda^2 - D_3)} - D_4 \lambda^2 \quad (4)$$

with coefficients $D_1 = 3.62004$, $D_2 = 0.0412526$, $D_3 = 0.0239454$ and $D_4 = 0.0086344$ in the wavelength range of 0.3 to 3.0 μm . In this way, using n_{eff} of equation (3) in the expression of equation (1) single-mode conditions for air-clad Lu_2O_3 waveguides with respect to the wavelengths and rod diameters are obtained (see figure 19). These results indicate that single-mode guiding in a subwavelength-diameter Lu_2O_3 rod would occur for diameters lying below the solid line. For example, at a wavelength of 633 nm (He–Ne laser), a Lu_2O_3 rod of diameter less than 380 nm will always be a single-mode waveguide; and at the wavelength of 1.5 μm , to be a single-mode waveguide, diameters should be less than about 910 nm. Further, taking into account that the UV absorption edge for Lu_2O_3 is ~ 240 nm, its minimum critical diameter is about 120 nm. Considering that individual nanorods prepared at pH = 7 have typical diameters of ~ 90 nm, they would always act as single-mode waveguides.

Thus, although measured Yb^{3+} , Er^{3+} -doped Lu_2O_3 nanorods seem to be too thin for propagation of light, bigger assemblies with cross sections up to 700 nm can offer more adequate diameter sizes. So, the possibility of waveguiding could not be rejected and further studies are in progress. In addition, if these nanorods cannot achieve the strict requirements on diameter uniformity and sidewall smoothness that are required for low-loss optical waveguiding, especially when their small diameters are taken into account [65, 66], they could show interesting properties such as enhanced evanescent

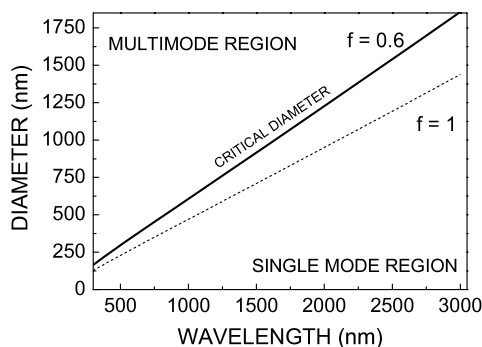


Figure 19. Single-mode condition of an air-clad Lu_2O_3 nanorod waveguide; the solid line indicates the critical diameter for single-mode operation for the current prepared nanorods, and the dotted line is a comparison with an ideal pore-free nanorod waveguide.

fields or large waveguide dispersions, which may provide opportunities for developing a number of high-performance and novel types of nanophotonic device.

4. Conclusions

A soft (185 °C and autogenic pressure) hydrothermal process was found to be an efficient way to prepare pure cubic $Ia\bar{3}$ codoped Yb, Ln- Lu_2O_3 , Ln = Er^{3+} , Tm^{3+} . Specifically, chloride reagents and pH = 7 produce rods of up to 45 μm length and 90 nm diameter. SNOM measurements have shown that the NIR to visible UC luminescence experiences strong developments of the red and blue emissions of Er^{3+} and Tm^{3+} , respectively, with increase in Yb^{3+} concentration, through mechanisms with large UC rates involving the presence of large phonons at the surface of the current nanorods. Evidence of the presence of Er^{3+} active centers at the surface and in the body of the nanorods can be extracted from the different evolution of the red/green emissions in UC and CL spectra of materials with variable Er^{3+} and Yb^{3+} concentrations. SNOM photoluminescence images reveal uniform light emission along Yb^{3+} , Er^{3+} -codoped Lu_2O_3 nanorods, but the reduced diameter of the latter currently prevents waveguiding behavior. The prospects for the present low-cost and environmentally benignly synthesized nanorods for incorporation in 2D or 3D patterned photonic structures or for waveguiding purposes seem to be favorable. The development of their potential requires specific adjustments of the relative $\text{Yb}^{3+}/\text{Ln}^{3+}$ content in Lu_2O_3 or the adaptation of the synthesis conditions to yield thicker rods.

Acknowledgments

This work was supported by the Spanish Ministry of Science and Innovation under projects MAT 2008-06729-C02-01-02 and PI09/90527, and by the National Research Foundation of Korea (NRF) under grants 2009-0094048 and 2010-0018855.

EWB acknowledges the support of the Catalan Government through the fellowship 2009FI00148.

References

- [1] Liu G and Chen X 2007 Spectroscopic properties of lanthanides in nanomaterials *Handbook on the Physics and Chemistry of Rare Earths* vol 37, ed K A Gschneidner Jr, J-C G Bünzli and V K Pecharsky (Amsterdam: Elsevier) chapter 233
- [2] Capobianco J A, Vetrone F, Boyer J, Speghini A and Bettinelli M 2002 *J. Phys. Chem. B* **106** 1181
- [3] Vetrone F, Boyer J C, Capobianco J A, Speghini A and Bettinelli M 2003 *J. Phys. Chem. B* **107** 1107
- [4] Heer S, Kömpen K, Güdel H U and Haase M 2004 *Adv. Mater.* **16** 2102
- [5] Boyer J C, Vetrone F, Cuccia L A and Capobianco J A 2006 *J. Am. Chem. Soc.* **128** 7444
- [6] Sivakumar S, van Veggel F C J M and May P S 2007 *J. Am. Chem. Soc.* **129** 620
- [7] Schietinger S, de Menezes L S, Lauritzen B and Benson O 2009 *Nano Lett.* **9** 2477
- [8] Wang F and Liu X 2009 *Chem. Soc. Rev.* **38** 976
- [9] Song H, Yu H Q, Pan G, Bai X, Dong B, Zhang X T and Hark S K 2008 *Chem. Mater.* **20** 4762
- [10] Dong G, Chi Y, Xiao X, Liu X, Qian B, Ma Z, Wu E, Zeng H, Chen D and Qiu J 2009 *Opt. Express* **17** 22514
- [11] Wang L and Li Y 2006 *Nano Lett.* **6** 1645
- [12] Koopmann P, Lamrini S, Scholle K, Fuhrberg P, Petermann K and Huber G 2010 High power diode pumped 2 μm laser operation of $\text{Tm}:\text{Lu}_2\text{O}_3$ CLEO: *Conf. on Lasers and Electro-Optics. Technical Digest (CD)* (Optical Society of America, 2010) paper CMDD1 <http://www.opticsinfobase.org/abstract.cfm?URI=CLEO-2010-CMDD1>
- [13] Fornasiero L 1999 Nd^{3+} -und Tm^{3+} -dotierte sesquioxides *PhD Dissertation* University of Hamburg
- [14] Tokurakawa M, Takaichi K, Shirakawa A, Ueda K, Yagi H, Hosokawa S, Yanagitani T and Kaminskii A A 2006 *Opt. Express* **14** 12832
- [15] Bridot J L et al 2007 *J. Am. Chem. Soc.* **129** 5076
- [16] Vetrone F, Boyer J C, Capobianco J A, Speghini A and Bettinelli M 2003 *Chem. Mater.* **15** 2737
- [17] Vetrone F, Boyer J C, Capobianco J A, Speghini A and Bettinelli M 2004 *J. Appl. Phys.* **96** 661
- [18] De G, Qin W, Zhang J, Zhang J, Wang Y, Cao C and Cui Y 2006 *J. Lumin.* **119/120** 258
- [19] Li X, Li Q, Wang J and Li J 2007 *J. Lumin.* **124** 351
- [20] Li Y, Zhang J, Zhang X, Luo Y, Ren X, Zhao H, Wang X, Sun L and Yan C 2009 *J. Phys. Chem. C* **113** 4413
- [21] Guyot Y, Moncorgé R, Merkle L D, Pinto A, McIntosh B and Verdun H 1996 *Opt. Mater.* **5** 127
- [22] Capobianco J A, Vetrone F, Boyer J C, Speghini A and Bettinelli M 2002 *Opt. Mater.* **19** 259
- [23] Vetrone F, Boyer J C, Capobianco J A, Speghini A and Bettinelli M 2002 *J. Phys. Chem. B* **106** 5622
- [24] Mao Y, Huang J Y, Ostroumov R, Wangand K L and Chang J 2008 *J. Phys. Chem. C* **112** 2285
- [25] Polizzi S, Bucella S, Speghini A, Vetrone F, Naccache R, Boyer J C and Capobianco J A 2004 *Chem. Mater.* **16** 1330
- [26] Trojan-Piegeza J and Zych E 2004 *J. Alloys Compounds* **380** 118
- [27] An L, Zhang J, Liu M and Wang S 2005 *J. Am. Ceram. Soc.* **88** 1010
- [28] Zych E, Hreniak D and Strek W 2002 *J. Phys. Chem. B* **106** 3085
- [29] Zych E, Wójtowicz M, Kepinski L and Malecka M A 2008 *Opt. Mater.* **31** 341
- [30] Galcerán M, Pujol M C, Aguiló M and Díaz F 2008 *Mater. Sci. Eng. B* **146** 7

- [31] Guang J, Zheng Y, Liu K, Song Y, You H and Zhang H 2009 *J. Phys. Chem. C* **113** 153
- [32] Wang J, Liu Q and Liu Q 2005 *J. Mater. Chem.* **15** 4141
- [33] Yada M, Mihara M, Mouri S, Kuroki M and Kijima T 2002 *Adv. Mater.* **14** 309
- [34] Cascales C, Esteban-Betegón F and Zaldo C 2010 *Phys. Status Solidi C* **7** 2675
- [35] Yang J, Li C, Quan Z, Zhang C, Yang P, Li Y, Yu C and Lin J 2008 *J. Phys. Chem. C* **112** 12777
- [36] Yada M, Taniguchi C, Watari T, Furuta S and Katsuki H 2004 *Adv. Mater.* **16** 1448
- [37] Esteban-Betegón F, Zaldo C and Cascales C 2010 *Chem. Mater.* **22** 2315
- [38] Weber M J 1968 *Phys. Rev.* **171** 283
- [39] Wittke J P, Ladani I and Yocom P N 1972 *J. Appl. Phys.* **43** 595
- [40] Tong L, Lou J and Mazur E 2004 *Opt. Express* **12** 1025
- [41] Joint Committee Powder Diffraction Standards Powder Diffraction File Number 86-2475
- [42] Schnaak G and Konigstein J A 1970 *J. Opt. Soc. Am.* **60** 1110
- [43] Nakamoto K 1986 *Infrared and Raman Spectra of Inorganic and Coordination Compounds* (New York: Wiley-Interscience)
- [44] Milligan W O, Mullica D F and Hall M A 1980 *Acta Crystallogr. B* **36** 3086 (JCPDF No. 72-0928)
- [45] Beall G W, Milligan W O and Wolcott H A 1977 *J. Inorg. Nucl. Chem.* **39** 65
- [46] Wickleder M S and Schaefer W 1999 *Z. Anorg. Allg. Chem.* **625** 309
- [47] Wang X and Li Y 2006 *Pure Appl. Chem.* **78** 45
- [48] Wang X, Sun X, Yu D, Zhou B and Li Y 2003 *Adv. Mater.* **15** 1442
- [49] Penn R L and Banfield J F 1998 *Science* **281** 969
- [50] Karakoti A S, Kuchibhatla S V N T, Baer D R, Thevuthasan S, Sayle D C and Seal S 2008 *Small* **4** 1210
- [51] Cascales C and Zaldo C 2010 at press
- [52] Pauling L and Shappell M D 1930 *Z. Kristallogr.* **75** 128
- [53] Kisliuk P, Frupke W F and Gruber J B 1964 *J. Chem. Phys.* **40** 3606
- [54] Peters V 1998 *Spektroskopie und lasereigenschaften erbium-und praseodym-dotierter hochschmelzender oxide Master's Thesis* Institute of Laser-Physics, University of Hamburg, Germany
- [55] Pollnau M, Gamelin D R, Lüthi S R and Güdel H U 2000 *Phys. Rev. B* **61** 3337
- [56] Lei Y, Song H, Yang L, Yu L, Liu Z, Pan G, Bai X and Fan L 2005 *J. Chem. Phys.* **123** 174710
- [57] Müller H D, Schneider J, Lüth H and Strümpfer R 1990 *Appl. Phys. Lett.* **57** 2422
- [58] Nogales E, Méndez B and Piqueras J 2008 *Nanotechnology* **19** 035713
- [59] Yi G S and Chow G M 2007 *Chem. Mater.* **19** 341
- [60] Wong H T, Wa H L and Hao J 2010 *Opt. Express* **18** 6123
- [61] An L, Zhang J, Liu M and Wang S 2008 *J. Alloys Compounds* **451** 538
- [62] Wang G, Qin W, Wang L, Wei G, Zhu P and Kim R 2008 *Opt. Express* **16** 11907
- [63] Latham J P, Munjiza A and Lu Y 2002 *Powder Technol.* **125** 10
- [64] Abrarova S M, Kimb T W and Kanga T W 2006 *Opt. Commun.* **264** 240
- [65] Ladouceur F 1997 *J. Lightwave Technol.* **15** 1020
- [66] Lee K K, Lim D R, Luan H C, Agarwal A, Foresi J and Kimerling L C 2000 *Appl. Phys. Lett.* **77** 1617

Paper V

E. W. Barrera, C. Cascales, M. C. Pujol, J. Carvajal, X. Mateos, M. Aguiló, F. Díaz. *White Upconversion Luminescence in nanocrystalline (Ho,Tm,Yb):KLuW phosphor*, **Physica Status Solidi** 8 2676–2679 (2011).

UNIVERSITAT ROVIRA I VIRGILI
LANTHANIDE-BASED DIELECTRIC NANOPARTICLES FOR UPCONVERSION LUMINESCENCE
Elixir William Barrera Bello
Dipòsit Legal: T. 450-2013

White upconversion luminescence in nanocrystalline (Ho,Tm,Yb):KLu(WO₄)₂ phosphor

E. William Barrera^{*1}, M. Cinta Pujol¹, Concepción Cascales², Joan J. Carvajal¹,
X. Mateos¹, Magdalena Aguiló¹, and Francesc Díaz¹

¹ Física i Cristallografia de Materials i Nanomaterials (FiCMA-FiCNA), Universitat Rovira i Virgili (URV), Campus Sescelades
c/Marcel·lí Domingo, s/n, 43007 Tarragona, Spain

² Instituto de Ciencia de Materiales de Madrid, CSIC, Calle Sor Juana Inés de la Cruz, Cantoblanco, 28049 Madrid, Spain

Received 3 October 2010, accepted 4 February 2011

Published online 24 May 2011

Keywords white phosphor, monoclinic double tungstates, nanocrystals, upconversion

* Corresponding author: e-mail elixirwilliam.barrera@urv.cat

Highly crystalline codoped Ho³⁺, Tm³⁺, Yb³⁺ KLu(WO₄)₂ monoclinic nanocrystals with the *C2/c* space group symmetry were synthesized by the modified Pechini method. Powder X-ray diffraction, transmission electron microscopy, upconversion photoluminescence spectra, and kinetic decay were used to characterize the samples. The nanocrystals belonged to the monoclinic phase, with a crystallite size of 30–

70 nm. Under 930 nm laser excitation, red, green and blue upconversion emissions were simultaneously observed, due to the energy transfer from the Yb³⁺ ²F_{5/2} excited level. The decay times of the emitting states were studied at room temperature to describe the photoluminescence dynamics. The influence of excitation power and calcination conditions on CIE chromaticity coordinates were evaluated.

© 2011 WILEY-VCH Verlag GmbH & Co. KGaA, Weinheim

1 Introduction In recent years, there has been a great interest in generation of white light sources for a variety of applications, such as solid-state multicolour three-dimensional displays, back light in LCDs, etc. [1]. One of the possible ways for generating white light is the energy transfer upconversion (UC) process in which low energy near infrared radiation is converted to higher energies such as visible or UV radiation. UC in optical active trivalent lanthanide (Ln³⁺) doped crystals is multi step process where an infrared photon excites the ion from the ground-state to an intermediate state, which necessarily must possess a long lifetime. In this way, with an appropriate choice of the Ln³⁺ ions, it can be achieved simultaneously the emission in blue, green and red, RGB emission, to obtain the desired white light.

Ln³⁺ ions, such as Ho³⁺ and Tm³⁺ are suitable candidates for the UC processes due to their abundant energy levels and narrow emission spectral lines. Furthermore, the sharp lines of the photoluminescence of the Ln³⁺ emission assure a high color purity of the emitted light [2]. Yb³⁺ acts as sensitizer allowing the possibility to be excited in the infrared IR and followed by efficient energy transfer (ET) to the visible where Ho³⁺ and Tm³⁺ ions emit. Furthermore, Yb³⁺ acts as an excellent absorbing of the IR pump wavelength

due to its broad absorption band. Thus, the requirements to the linewidth of the pump sources are not crucial. Besides, Yb³⁺ only contains an excited energy level in its electronic structure, avoiding processes such as excited state absorption and minimizing the losses.

Several examples of the use of Ho³⁺, Tm³⁺ and Yb³⁺ ions in different hosts can be found in the literature [3,4,5]. On the other hand, nanocrystals have received special attention due to the enhanced intensity of emission detected for smaller size particles [6] and their different morphologies expand the possibility to construct new architecture photonic devices.

Monoclinic ordered KLu(WO₄)₂ (hereafter KLuW) host is a well-known material for laser applications [7], and more recently optical waveguide applications [8]. Its main advantages are the high Ln³⁺ doping admittance with low concentration quenching due to the relatively large Lu-Lu distances in the structure [9], and the high optical absorption and emission cross sections for these Ln³⁺. Among the series of KREW (RE=Y, Gd and Lu) hosts, the Lu-based crystal shows a higher crystal field, due to their short inter-atomic distances and high distortion at the Lu³⁺ point site [9, 10]. In addition, the Lu³⁺ in this structure accepts to be easily substituted for Yb³⁺, Tm³⁺ and Ho³⁺ with

very low crystalline lattice distortion, due to the similarity of ionic radii and the fact that stoichiometric KREW are isostructural compounds [11, 12, 13].

In this paper, we report the synthesis of lanthanide doped KLuW nanocrystals by the sol-gel modified Pechini method and its spectroscopic characterization. Under 930 nm CW excitation, visible UC emissions were recorded at room temperature. Finally, the CIE coordinates have been evaluated for this new white light phosphor.

2 Experimental procedure $\text{Ho}^{+3}, \text{Tm}^{+3}, \text{Yb}^{+3}:\text{KLuW}$ nanocrystals were synthesized by the modified Pechini Method, which has been applied already successfully to prepare monoclinic KREW nanocrystals [14]. Previous results of our group shows the generation of white light generation from a triply doped KLuW single crystal with the optimized molar concentrations as 1:2:2 [15], and specifically in this work: 0.5% at Ho, 1% at. Tm and 1% at. Yb substitution of Lu in KLuW. Different calcination temperatures (T_{cal}) in the range of 923-1023 K and calcination times ($t_{\text{cal}} = 1, 2, 5$ h) have been applied to obtain a narrow nanoparticle size distribution. Previous studies in non doped KYbW and KGdW showed an optimal calcination step of 973 K during 2 h [14].

Structural characterization was carried out with a Bruker-AXS D8-Discover diffractometer using $\text{Cu K}\alpha$ radiation. The X-ray powder diffraction patterns were recorded with a step size = 0.02° and a step time = 16 s. To determine the chemical composition of the nanocrystals, we carried out electron probe microanalysis (EPMA) in a Cameca SX50 microprobe analyzer operating in wavelength dispersive mode.

Transmission electron microscopy (TEM) was performed with a JEOL JEM-1011 microscope operating with an accelerating voltage of 100 kV. Decay times were measured by exciting with 930 nm from an optical parametric oscillator (OPO) with pulse duration of around 6 ns and a repetition frequency of 10 Hz. Fluorescence spectra were collected on CW excitation at 930 nm with a Ti-sapphire tuneable laser. The spectra were recorded using a Jobin-Yvon-Spex HR 460 monochromator. The signal was collected using a Hamamatsu R928 photomultiplier connected to the lock-in amplifier (Perkin-Elmer DSP-7265) for photoluminescence measurements and a Tektronix TDS 714L oscilloscope for decay time measurements. All the measurements were performed at room temperature.

3 Results and discussion

3.1 Structural characterisation The formula of our synthesized nanoparticles was $\text{KH}_{0.007}\text{Tm}_{0.009}\text{Yb}_{0.011}\text{Lu}_{0.973}(\text{WO}_4)_2$, slightly different than the mentioned above theoretical 1:2:2 ratio.

Figure 1 shows the X-Ray powder diffraction patterns obtained at 973 K for 2 h. The highly crystallized powder obtained belongs to the monoclinic system, with the space group $C2/c$ of the KLuW single crystal [9]. From TEM im-

ages the grain size was estimated between 30-70 nm (inset in Fig. 1).

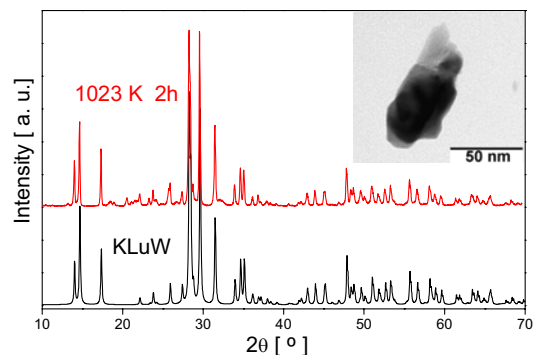


Figure 1 X-ray powder diffraction pattern of the obtained nanocrystals. TEM micrograph showing $(\text{Ho}, \text{Tm}, \text{Yb}):\text{KLuW}$ nanocrystals.

3.2 Photoluminescence The UC emission spectra between 400-700 nm recorded at different excitation powers are shown in Fig. 2. They show a white emission composed by the red Tm^{3+} emission $^3\text{F}_{2,3} \rightarrow ^3\text{H}_6$ and $^1\text{G}_4 \rightarrow ^3\text{F}_4$, and red Ho^{3+} emission $^5\text{F}_5 \rightarrow ^5\text{I}_8$, the green Ho^{3+} emission $^5\text{F}_4, ^5\text{S}_2 \rightarrow ^5\text{I}_8$ and the blue Tm^{3+} emission, $^1\text{G}_4 \rightarrow ^3\text{H}_6$. With the increase of excitation power, the spectrum shows different profiles and an increment in intensities as well; the most significant change is in the blue emission peak at 475 nm. The others fluorescence intensities became stronger monotonously with the increase of excitation power. The color coordinates change with the laser power, so this means a possible tunability of the white color of the same sample in relation with the power intensity.

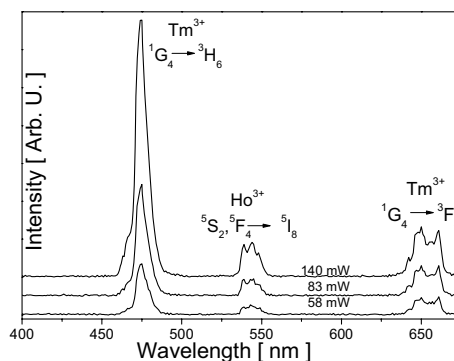


Figure 2 Upconversion emission spectra under 930 nm excitation, $T_{\text{cal}} = 1023$ K $t_{\text{cal}} = 5$ h, at different excitation powers.

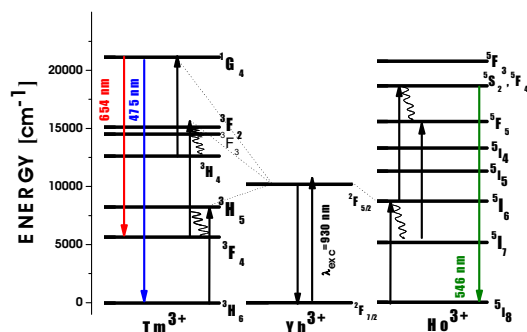


Figure 3 Energy diagram of Ho³⁺, Tm³⁺ and Yb³⁺ in KLuW with arrows indicating radiative and non-radiative processes.

Table 1 Measured decay times of the visible emissions in (Ho,Tm,Yb):KLuW nanocrystals in relation with the temperature and time of calculation.

<i>T</i> _{cal} [K]	<i>t</i> _{cal} [h]	Rise blue [μs]	Blue [μs]	Green [μs]	Red [μs]
973	2	33	214	94	221
1023	1	28	183	79	270
1023	2	27	233	92	269
1023	5	39	195	95	215

3.3 Upconversion mechanisms and dynamics

To identify the mechanisms involved in multicolor emission in the codoped KLuW, a composite energy level diagram for all the three ions is shown in Fig. 3. Table 1 summarizes the measured decay times. It is not expected a large reabsorption effect at this short wavelength emissions. The decay times observed were described mainly by a single exponential. The radiative lifetimes of excited levels of Ln³⁺ ions are usually calculated within the framework of the Judd–Ofelt theory using three phenomenological parameters Ω_{*i*} that are derived from an analysis of absorption spectra.

Decay kinetics from Tm³⁺ ¹G₄ A complete description of the Tm³⁺ spectroscopy in KLuW host is reported in [10,16]. The red emission has been assigned to the electronic transitions ³F_{2,3} → ³H₆ (Tm³⁺) and ¹G₄ → ³F₄ (Tm³⁺) [15]. The wavelength of the red emission is more related to the ¹G₄ → ³F₄ transition than ³F_{2,3} → ³H₆ transition (not showed), which would be located at longer wavelength transitions, furthermore the probability of the transition for ¹G₄ → ³F₄ is larger than ³F_{2,3} → ³H₆.

Although ESA (excited state absorption) of Tm³⁺ ions has been frequently reported in the literature [17, 18, 19], this has not been the case for Tm³⁺-Yb³⁺ co-doped systems. The expected mechanism is ETU (energy transfer upconversion) non resonant (phonon assisted) process.

The time dependent rate equation describing the electronic population, *N*_{T₃}, of the ¹G₄ manifold (level 3) is given by:

$$\frac{dN_{T_3}(t)}{dt} = W_3 N_{Yb1}(t) N_{T_2}(t) - \frac{N_{T_3}}{\tau_{T_3}} \quad (1)$$

*W*₃ is coefficient of ETU between Yb³⁺ ²F_{5/2} level (level 1), populated by *N*_{Yb1}, and population in the intermediate level ³H₄ (level 2), *N*_{T₂} of Tm³⁺. The solution will contain two exponential components each with their amplitude and characteristic time constant, resulting in a non-exponential decay waveform. The rise time observed corresponds to the time required for the donor-acceptor energy transfer to take place and the decay is the luminescence decay of the acceptor ions. The rise time is related with the first term, and the simple exponential decay with the second term, where τ_{T₃} is the experimental decay time of the ¹G₄ state.

So, in the described experimental measurements, for the blue ¹G₄ → ³H₆ emission and red ¹G₄ → ³F₄ emission; the rise time observed for the blue emission, around 30 μs can be attributed to the energy transfer rate between Yb-Tm, and the decay time around 210 μs, can be attributed to the experimental decay time of Tm³⁺ ¹G₄ level. A similar behavior was observed in Tm:KYbW single crystals, in which the rise time was also around 30 μs, but the decay time was shorter than in our nanocrystals, around 70 μs [20]. Nevertheless, the radiative time of ¹G₄ in Tm:KREW has been calculated to be around 406 μs [20] and 225 μs [21]. The reduction of the experimental time observed in the nanocrystals should be attributed to the presence of nonradiative depopulation mechanisms.

The slight increase of the decay time measured in the red emission, should be attributed to the participation of the red emission of Ho³⁺ ⁵F₅ → ⁵I₈, with a non-radiative population mechanism for the emitting level. The radiative lifetime of this ⁵F₅ emitting level is tabulated to be around 150 μs in KGdW; but the experimental lifetime is very short (below 1 μs) [22]. There is a possible way for the population of ⁵F₅ (Ho³⁺) emitting level by (²F_{5/2}, ⁵I₇) → (²F_{7/2}, ³F₅) where the ⁵I₇ level is populated through the non-radiative decay of the ⁵I₆ level.

Decay kinetics from Ho³⁺ ⁵S₂ The green emission has been attributed to the Ho³⁺ transition ⁵F₄, ⁵S₂ → ⁵I₈. The measured decay time is around 90 μs. The electronic population in the excited ⁵F₄, ⁵S₂ levels under IR laser excitation is accomplished through two successive steps. In the first step, Ho³⁺ ions are excited from the ground state the ⁵I₈ to ⁵I₆ level and the second step is carried out from the ⁵I₆ level to the ⁵S₂+⁵F₄ level. From the latter level, non-radiative relaxations take place populating the ⁵S₂ level of Ho³⁺ allowing the generation of the green emission.

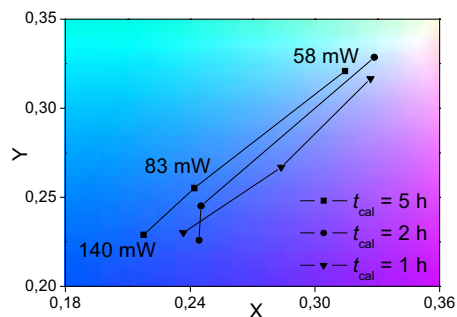


Figure 4 CIE diagram indicating the color coordinates from emission spectrum for different calcination times.

No rise time has been detected, so, this can be related with a faster process of energy transfer between Yb-Ho in relation with the Yb-Tm, already observed in other hosts [23]. This would mean that in this case, the ESA process is predominant over the ETU in relation with the time decay kinetics. So, the single exponential decay should be assigned to the lifetime of the emitting state $\text{Ho}^{3+} \ ^5\text{S}_2$. The radiative lifetime of this state in $\text{Ho}^{3+}:\text{KREW}$ was calculated to be 181 μs . The evaluation of the quantum efficiency η of a luminescent level is commonly approximated by a ratio of experimental luminescence lifetime to the radiative lifetime of the level. Thus, the intrinsic quantum efficiency for this emission is around 50 %.

3.4 Phosphor evaluation The emission spectra for each sample have converted to the CIE 1931 color coordinate system, calculating the tristimulus X, Y, and Z values. The CIE coordinates are plotted in Fig. 4. The color coordinates in KLuW for the white emission in our experiments have been calculated for 58-140 mW of excitation laser power. CIE coordinates were displaced to the blue – green region for longer calcination times, i.e. for bigger nanoparticles. The increment of pumping power produce a more intensive blue emission of Tm^{3+} displacing the CIE coordinates to the blue region.

4 Conclusions

$\text{KH}_{0.007}\text{Tm}_{0.009}\text{Yb}_{0.011}\text{Lu}_{0.973}(\text{WO}_4)_2$ nanocrystals with a grain size of 30-70 nm have been prepared by the modified Pechini method after calcination up to 1023 K for 2 h. The UC spectra have been studied using IR excitation and red-green-blue emission has been obtained. The produced nanocrystals are highly crystalline, belonging to the monoclinic system, with space group $C2/c$. Luminescence dynamics has been also presented in detail. This may be useful to tune the emission of this phosphor by two phenomena: the increment of grain size by longer calcination time (to the blue-green region) and the increment of the pumping power (blue region).

Acknowledgments This work is supported by the Spanish Government under projects MAT2008-06729-C02-01-02/NAN,

MAT2008-04046-E/MAT, TEC2010-21574-C02-02 and the project PI09/90527; and the Catalan Authority under project 2009SGR235 and FP7-SPA-2010-263044. E. W. Barrera is supported by Catalan Government for the fund provided through the fellowship 2009FI00148. J. J. Carvajal is supported by the education and Science ministry of Spain and European Social Fund under Ramon y Cajal program RYC2006-258.

References

- [1] D. Q. Chen, Y. S. Wang, K. L. Zheng, T. L. Guo, Y. L. Yu, and P. Huang, *Appl. Phys. Lett.* **91**, 251903 (2007).
- [2] K. Binneemans, *Chem. Rev.* **109**, 4283 (2009).
- [3] N. K. Giri, D. K. Rai, and S. B. Rai, *J. Appl. Phys.* **104**, 113107 (2008).
- [4] N. Q. Wang, X. Zhao, C. M. Li, E. Y. B. Pun, and H. Lin, *J. Lumin.* **130**, 1044 (2010).
- [5] D. Chen, Y. Wang, Y. Yu, P. Huang, and F. Weng, *J. Solid State Chem.* **181**, 2763 (2008).
- [6] T. Schmidt, G. Muller, L. Spanhel, K. Kerker, and A. Forchel, *Chem. Mater.* **10**, 65 (1998).
- [7] V. Petrov, M. C. Pujol, X. Mateos, O. Silvestre, S. Rivier, M. Aguiló, R. M. Sole, J. Liu, U. Griebner, and F. Diaz, *Laser Photon. Rev.* **1**, 179 (2007).
- [8] W. Bolaños, J. J. Carvajal, X. Mateos, M. Aguiló, and F. Díaz, *IEEE Photon. J.* **2**, 482 (2010).
- [9] M. C. Pujol, X. Mateos, A. Aznar, X. Solans, S. Surinach, J. Massons, F. Diaz, and M. Aguiló. *J. Appl. Cryst.* **39**, 230 (2006).
- [10] M. C. Pujol, C. Cascales, M. Aguiló, and F. Díaz, *J. Phys.: Condens. Matter* **20**, 345219 (2008).
- [11] M. C. Pujol, R. Solé, J. Massons, J. Gavalda, X. Solans, F. Diaz, and M. Aguiló, *J. Appl. Crystallogr.* **35**, 108 (2002).
- [12] P. V. Klevtsov, L. P. Kozeeva, and L. Y. Kharchenko, *Sov. Phys. Crystallogr.* **20**, 732 (1976).
- [13] A. Majchrowski, M. T. Borowiec, E. Michalski, J. Zmija, V. Dyakonov, H. Szymczak, T. Zayarnyuk, and M. Baranski, *Cryst. Res. Technol.* **6**, 283 (2001).
- [14] M. Galceran, M. C. Pujol, M. Aguiló, and F. Díaz, *J. Sol-Gel Sci. Technol.* **42**, 79 (2007).
- [15] V. Jambunathan, X. Mateos, M. C. Pujol, J. J. Carvajal, M. Aguiló, and F. Díaz, submitted to *Appl. Phys. Lett.* (2010).
- [16] O. Silvestre, M. C. Pujol, M. Rico, F. Güell, M. Aguiló, and F. Díaz, *Appl. Phys. B* **87**, 707 (2007).
- [17] R. Caspary, M. M. Kozak, D. Goebel, and W. Kowalsky, *Opt. Commun.* **259**, 154 (2006).
- [18] T. Tamaoka, S. Tanabe, S. Ohara, H. Hayashi, and N. Sugimoto, *J. Alloys Compd.* **408**, 848 (2006).
- [19] Y. H. Tsang, D. J. Coleman, and T. A. King, *Opt. Commun.* **231**, 357 (2004).
- [20] M. C. Pujol, F. Güell, X. Mateos, Jna. Gavalda, R. Solé, J. Massons, M. Aguiló, F. Díaz, G. Boulon, and A. Brenier, *Phys. Rev. B* **66**, 144304 (2002).
- [21] A. N. Kuzmin, A. V. Kachynski, P. N. Prasad, A. A. Demidovich, L. E. Batay, A. Bednarkiewicz, W. Strek, and A. N. Titov, *J. Appl. Phys.* **95**, 7862 (2004).
- [22] M. C. Pujol, J. Massons, M. Aguiló, F. Díaz, M. Rico, and C. Zaldo, *IEEE J. Quantum Electron.* **38**, 93 (2002).
- [23] R. Lisiecki, W. Ryba-Romanowski, T. Ukasiewicz, M. Mond, and K. Petermann, *Laser Phys.* **15**, 306 (2005).

Paper VI

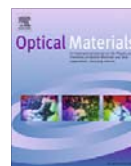
E. W. Barrera, M. C. Pujol, F. Diaz, S. B. Choi, F. Rotermund, C. Cascales.
Hydrothermal trivalent lanthanide doped Lu_2O_3 nanorods: Evaluation of the influence of the surface in optical emission properties **Optical Materials** 34 399–403 (2011).



Contents lists available at ScienceDirect

Optical Materials

journal homepage: www.elsevier.com/locate/optmat



Hydrothermal trivalent lanthanide doped Lu_2O_3 nanorods: Evaluation of the influence of the surface in optical emission properties

Elixir W. Barrera^a, Maria Cinta Pujol^a, Francesc Díaz^a, Soo Bong Choi^b, Fabian Rotermund^b, Concepción Cascales^{c,*}

^a Física i Cristal·lografia de Materials i Nanomaterials, Universitat Rovira i Virgili, Campus Sescelades c/ Marcel·li Domingo s/n, E-43007 Tarragona, Spain

^b Division of Energy Systems Research, Ajou University, 443-749 Suwon, Republic of Korea

^c Instituto de Ciencia de Materiales de Madrid, Consejo Superior de Investigaciones Científicas, c/Sor Juana Inés de la Cruz, 3. Cantoblanco, E-28049 Madrid, Spain

ARTICLE INFO

Article history:

Available online 25 June 2011

Keywords:

Nanorods
Cubic
Sesquioxide nanorods
Hydrothermal synthesis
Fluorescence lifetimes of Tm^{3+}
Visible upconversion emissions

ABSTRACT

Tm^{3+} -doped and Yb^{3+} , $\text{Er}^{3+}/\text{Tm}^{3+}$ -codoped Lu_2O_3 rods of ~ 90 nm of diameter have been prepared through a soft hydrothermal procedure. A body/surface model has been proposed to describe the dynamics exhibited by fluorescence decays of $^3\text{H}_4$ and $^3\text{F}_4$ Tm^{3+} multiplets in $\text{Tm}-\text{Lu}_2\text{O}_3$ nanorods as well as the new features of the near infrared to visible upconverted emissions of Er^{3+} and Tm^{3+} in Yb^{3+} -codoped Lu_2O_3 nanorods.

© 2011 Elsevier B.V. All rights reserved.

1. Introduction

Cubic La_2O_3 is a very attractive material for laser and photonic applications due to the advantageous conjunction of excellent thermo-mechanical properties, high refractive index, relatively low phonon energies, and high doping admittance for optically active trivalent lanthanide (Ln) cations. Furthermore, Ln^{3+} cations in this host show high optical absorption and emission cross-sections as well as large crystal-field splittings [1], superior to these for corresponding Y- or Gd-based sesquioxides. However, the high required temperature for growing Ln-doped Lu_2O_3 single crystals is an important drawback in the development of such crystals. Lower temperature routes to prepare Lu_2O_3 -based photonic materials, especially in nanocrystalline forms, are presently searched either as an alternative to bulk crystals or aiming for exploring new optical properties derived of the size reduction. Original possibilities offered by nanocrystalline Ln- Lu_2O_3 are these related to the use in the fabrication of transparent laser ceramics through dense sintering [2], the processing with other transparent materials to produce thin films for infrared excited color displays and generation of bright white light [3], and the design of luminescent nanoprobes able to convert IR radiation into visible light for high resolution bioimaging applications [4].

Among all described methods for preparing nanocrystals, soft hydrothermal processes carried out during very reduced time periods (typically between a few hours and 1 day), have shown high efficiency for preparing pure phase nanocrystalline materials, with well-controlled shape and size [5]. However, it has been observed that the emission properties of hydrothermally prepared Ln-doped nanocrystals may result substantially changed when compared to the high temperature prepared bulk crystal counterparts [6]. For Ln-doped nanocrystals changes in Ln^{3+} energy levels positions are not expected given the strongly localized nature of 4f orbitals, but on the contrary, modifications in the local environment around Ln^{3+} centers induced by the size reduction and surface defects strongly influence the dynamics of f-f electronic transitions, and consequently luminescence efficiency, emission lifetimes and concentration quenching can result substantially affected. Furthermore, enhanced or even novel up-conversion fluorescence properties with regards to bulk counterparts can be also expected in Ln-doped nanocrystals. Given the special interest of 1D crystalline nanostructures, which additionally could play an important role as functional building units for the fabrication of nanodevices based in 2D or 3D ordered structures, in this communication we explore possible size and surface effects on emission properties in hydrothermally prepared Tm^{3+} -doped and Yb^{3+} , $\text{Er}^{3+}/\text{Tm}^{3+}$ -codoped Lu_2O_3 nanorods. After the characterization of nanorods (crystal phase, morphology and Fourier-transform infrared absorption), this evaluation will be carried out by a combined overview of results of room temperature fluorescence lifetime measurements of

* Corresponding author.

E-mail address: ccascales@icmm.csic.es (C. Cascales).

3H_4 and 3F_4 Tm^{3+} multiplets involved in the relevant $2\ \mu m$ laser emission as well as these corresponding to the analysis of the Yb^{3+} -sensitized Er^{3+} and Tm^{3+} observed upconverted emissions under near infrared excitation.

2. Experimental

Sets of samples of composition $Lu_{2-x}Tm_xO_3$ ($0.004 \leq x \leq 0.20$), $Lu_{1.96-x}Yb_xTm_{0.04}O_3$ ($0.04 \leq x \leq 0.20$) and $Lu_{2-x-y}Yb_xEr_yO_3$ ($0.04 \leq x \leq 0.30$; $0.04 \leq y \leq 0.15$) were prepared by a hydrothermal procedure using the corresponding molar amounts of sesquioxides (Yb_2O_3 Alfa Aesar 99.998%, Lu_2O_3 , Tm_2O_3 , Er_2O_3 WuXi YiFeng Rare Earths Co. Ltd. 99.99%) dissolved in dilute HCl. The white suspension formed by adding 20 ml of distilled water to each dried mixture, with pH adjusted to 7 with dilute NH_4OH , was heated during 24 h to $185\ ^\circ C$ in a sealed Teflon-lined autoclave of 75 ml capacity. The white precipitate obtained in each case was separated by centrifugation and washed with distilled water, dried at $110\ ^\circ C$ and annealed to $800\ ^\circ C$ during 20 min.

Prepared sesquioxides were characterized by 300 K powder X-ray diffraction (XRD) using a Bruker AXS D-8 Advance diffractometer and $Cu\ K_\alpha$ radiation, field-emission scanning electron microscopy (FE-SEM) and energy dispersive X-ray spectroscopy (EDX) scanning analysis with a FEI NOVA SEM230 equipment, transmission electron microscopy (TEM) using a JEOL 2000FXII microscope, Fourier transform infrared absorption (FT-IR) with a Nicolet 20SXC spectrophotometer in the range $4000\text{--}250\ cm^{-1}$, and by N_2 adsorption and N_2 adsorption/desorption isotherm measurements to determine specific surface (BET) and size pore distribution with a Micromeritics ASAP 2010 equipment.

For lifetime measurements the Tm^{3+} fluorescence was excited at room temperature with a Quanta-Ray MOPO system, being the pulse energy at $\lambda = 802\ nm$ of $\approx 32\ mJ$, and measured with a Hamamatsu InP/InGaAs cooled photomultiplier, sensitive in the $950\text{--}1700\ nm$ range, or with a InAs Hamamatsu photovoltaic detector cooled to liquid nitrogen and sensitive in the $1500\text{--}3100\ nm$ range. The electrical signals were recorded with a 500 MHz Tektronix oscilloscope, model TDS-520. A long-wavelength pass filter with cutting edge at $1000\ nm$ was used to remove background excitation light. The upconverted photoluminescence was excited with a cw Ti-sapphire tunable laser at $930\ nm$ and recorded using a Jobin-Yvon-Spex HR 460 monochromator. The exciting power was controlled by regulating the power of a 532 nm Verdi laser, which excites the Ti-sapphire laser. The signal was detected using a Hamamatsu R928 photomultiplier connected to a Perkin-Elmer DSP-7265 lock-in amplifier. Liquid poly(chlorotrifluoroethylene), commercially known as fluorolube, transparent to the infrared fluorescence of Tm^{3+} and with refractive index very close to that of Lu_2O_3 was chosen as the dispersive medium for lifetime measurements, whereas for near infrared (NIR) to visible upconversion photoluminescence spectra nanocrystalline samples conformed as dense pellets were used.

3. Results and discussion

3.1. Phase and morphology of Yb^{3+} , Er^{3+}/Tm^{3+} codoped Lu_2O_3

XRD patterns of obtained products show in all cases only the cubic $Ia\bar{3}$ sesquioxide phase. The full width at half maximum (FWHM) of Bragg peaks indicates a $\sim 25\ nm$ size assuming spherical particles, with no significant differences arising from the composition of nanorods, see Fig. 1 for some selected compositions. Along with observed bands (from ~ 300 to $600\ cm^{-1}$) assigned to modes of Lu_2O_3 vibrations [7], phonon modes of lattice water (at $\sim 1630\ cm^{-1}$ and $\sim 3440\ cm^{-1}$), and of surface-adsorbed

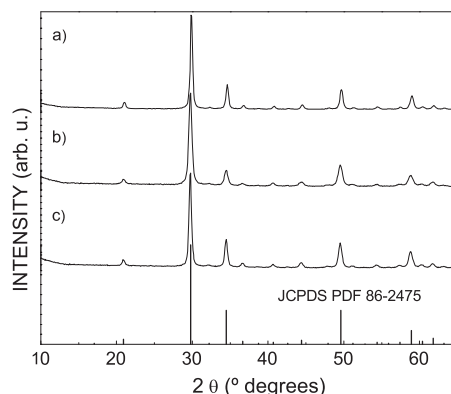


Fig. 1. Room temperature diffraction patterns of Ln-doped Lu_2O_3 nanorods prepared by hydrothermal synthesis at $185\ ^\circ C$ with $pH = 7$ during 1 day: (a) $Lu_{1.996}Tm_{0.004}O_3$, (b) $Lu_{1.76}Yb_{0.20}Er_{0.04}O_3$; (c) $Lu_{1.76}Yb_{0.20}Tm_{0.04}O_3$. All Bragg peaks can be indexed as corresponding to the cubic $Ia\bar{3}$ phase of Lu_2O_3 . Powder Diffraction File number 86-2475, included for comparison at the bottom.

carboxylate ions (at $\sim 1400\ cm^{-1}$ and $\sim 1530\ cm^{-1}$) were observed in FT-IR spectra of all samples with weak and very weak intensity, respectively.

Fig. 2a, b shows SEM images of the characteristic morphology of Ln- Lu_2O_3 , rods of up to $45\ \mu m$ of length and $\sim 90\ nm$ of diameter, which are gathered forming bunches. These nanorods are porous, see the TEM image in Fig. 2c. Measured specific surface areas S_{BET} are $\sim 22\ m^2\ g^{-1}$, with a relatively narrow pore size distribution, $7\text{--}18\ nm$. EXD color maps and scanning analyses indicate homogeneous distributions of Ln cations in prepared nanorods.

3.2. Lifetimes of 3H_4 and 3F_4 Tm^{3+} multiplets in $Tm\text{-}Lu_2O_3$ nanorods

Electronic f-f transitions of current Ln- Lu_2O_3 nanorods have splittings and intensities very similar to the reported for corresponding bulk crystals [1], which indicates that Ln in hydrothermal sesquioxides are incorporated at the same crystal sites than in bulk crystals, however their bandwidths are broadened. On the other hand, the overall intensity of photoluminescence (PL) emissions in Ln- Lu_2O_3 nanorods seems to be reduced when compared to bulk crystals. This latter behavior could be due to the lower apparent density of active ions of the nanocrystalline material with regards

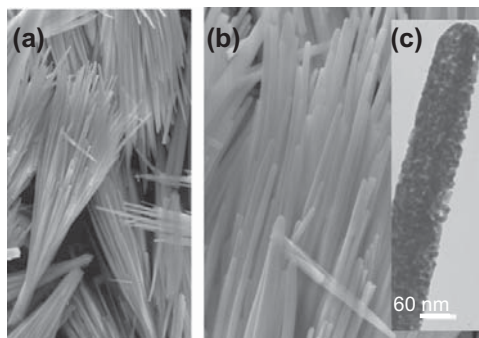


Fig. 2. (a and b) SEM micrographs of bunches of $Lu_{1.84}Yb_{0.12}Tm_{0.04}O_3$ nanorods with up to $\sim 45\ \mu m$ of length and $90\ nm$ of diameter prepared by 24 h hydrothermal synthesis at $185\ ^\circ C$ and $pH = 7$. (c) TEM image showing the characteristic porosity of nanorods.

to bulk samples, but effects induced by the reduction of the size, or related to the specific nature of the nanocrystalline material, that is, a larger density of surface defects along with the already established presence of high energy phonon modes, can be also expected.

The first approximation to evaluate and discern the origin of changes in the dynamics of electronic transitions in Tm-doped Lu_2O_3 prepared nanorods has been through monitoring room temperature lifetimes (τ) of the $^3\text{H}_4$ and $^3\text{F}_4$ Tm^{3+} multiplets.

3.2.1. $^3\text{H}_4$ lifetime in $\text{Lu}_{2-x}\text{Tm}_x\text{O}_3$ nanorods

The 300 K $^3\text{H}_4 \rightarrow ^3\text{F}_4$ PL decays excited at 802 nm ($\lambda_{\text{EMI}} = 1446$ nm) are not single exponential, even for the most diluted prepared sample, $x = 0.004$ (0.2 mol.% Tm), see Fig. 3a. For the latter Tm^{3+} doping level the cross-relaxation process involving $^3\text{H}_4$ and $^3\text{H}_6$ multiplets is not envisaged, and a single exponential regime is usually observed for the decay of $^3\text{H}_4$. In fact, in the measured

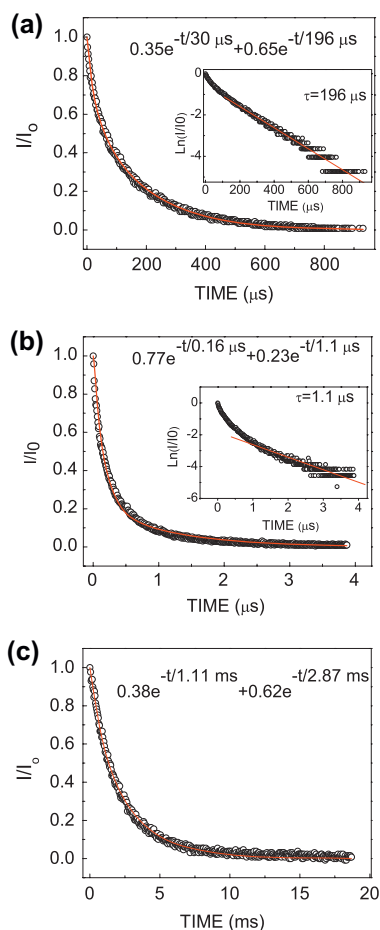


Fig. 3. 300 K Photoluminescence intensity decay of Tm^{3+} multiplets related to the 2 μm laser emission in $\text{Lu}_{2-x}\text{Tm}_x\text{O}_3$ nanorods ($\lambda_{\text{EXC}} = 802$ nm): (a) $^3\text{H}_4$ for $\text{Lu}_{1.996}\text{Tm}_{0.004}\text{O}_3$ (0.2 mol.% Tm), $\lambda_{\text{EMI}} = 1446$ nm, (b) $^3\text{H}_4$ for $\text{Lu}_{1.8}\text{Tm}_{0.2}\text{O}_3$ (10 mol.% Tm), $\lambda_{\text{EMI}} = 1446$ nm, with the linear fit of the tail of the $\text{Ln}(I/I_0)$ vs time plot shown in the corresponding inset, (c) $^3\text{F}_4$ for $\text{Lu}_{1.988}\text{Tm}_{0.012}\text{O}_3$ (0.6 mol.% Tm), $\lambda_{\text{EMI}} = 1636$ nm. The points are the experimental results and the continuous line is the fit with two exponential decays. Measurements were carried out with nanorods dispersed in fluorolube.

Tm^{3+} doping range (0.2 mol.% to 10 mol.%) the time dependence of PL intensity of $\text{Tm}^{3+}\text{-Lu}_2\text{O}_3$ nanorods is quite different with regards to behavior known in bulk single crystals [1, 8], for which at low enough Tm^{3+} concentration $^3\text{H}_4$ decays are exponential, while at an intermediate concentration regime the behavior become more complex due to Tm–Tm interactions, including resonant transfer between $^3\text{H}_4$ multiplets and the indicated ($^3\text{H}_4, ^3\text{H}_6$) $\rightarrow ^3\text{F}_4$ cross-relaxation, recovering again the single exponential decay when the increase of Tm^{3+} concentration allows fast diffusion between excited $^3\text{H}_4$ multiplets. We have analyzed the $^3\text{H}_4$ PL decays of $\text{Tm}^{3+}\text{-Lu}_2\text{O}_3$ nanorods considering a double exponential model, $I(t) = I_1 e^{-t/\tau_1} + I_2 e^{-t/\tau_2}$, with $I_1 + I_2 = 1$. In this model the fast component at short times (I_1, τ_1) would correspond to the emission of Tm^{3+} ions at the surface of nanocrystals, and the long one (I_2, τ_2), with τ_2 evaluated firstly from the tail of the $\text{Ln}(I/I_0)$ vs time decay plot, to Tm^{3+} ions within the body of nanocrystals, and this latter in principle should approach the τ value measured in Tm– Lu_2O_3 single crystals. Such procedure has systematically produced good fits of our experimental PL decays. Obtained $^3\text{H}_4$ long-lived τ progressively increase for lower Tm^{3+} concentrations, varying from 1.1 μs ($x = 0.20$, 10 mol.% Tm^{3+}), Fig. 3b, up to $\tau \sim 200$ μs ($x = 0.004$, 0.2 mol.% Tm^{3+}), Fig. 3a. Although the latter τ is reduced with regards to measured $^3\text{H}_4$ τ in single crystals of RE_2O_3 [1,8], the convergence with τ values of these single crystals is reached for our 1 mol.% $\text{Tm}^{3+}\text{-Lu}_2\text{O}_3$ nanorods, with $\tau = 172$ μs . Furthermore, the short time component of the double exponential decay is important even for lower concentrated $\text{Lu}_{2-x}\text{Tm}_x\text{O}_3$ nanorods, see the Fig. 3a for $\text{Lu}_{1.996}\text{Tm}_{0.004}\text{O}_3$ (0.2 mol.% Tm, $I_1 = 0.35$), and it experiences an enhancement with the Tm^{3+} concentration (10 mol.% Tm, $I_1 = 0.77$), Fig. 3a,b.

3.2.2. $^3\text{F}_4$ lifetime in $\text{Lu}_{2-x}\text{Tm}_x\text{O}_3$ nanorods

Although lower concentrated samples ($x \leq 0.010$, 0.5 mol.% Tm) display mostly a single exponential decay regime, $^3\text{F}_4$ PL decay of $\text{Lu}_{2-x}\text{Tm}_x\text{O}_3$ nanorods is, in general, nonsingle exponential, see Fig. 3c, and the short time component becomes also enhanced with the Tm^{3+} concentration. The maximum value of measured long-lived τ was $\tau \sim 2.9$ ms, which is close to the $\tau \sim 3.38$ ms experimental lifetime reported at 300 K for a 0.15 mol.% Tm– Lu_2O_3 single crystal [1]. Compared to the calculated radiative lifetime, 5.22 ms [1], the likely origin of the reduction in both nanosized and bulk crystals is a nonradiative probability related to intraionic up-conversion (energy transfer upconversion, ETU) giving rise to strong temperature dependence, which decreases τ measured at room temperature with regards to its value at 10 K [9]. The progressive decrease of measured long-lived $^3\text{F}_4$ τ with increasing the Tm^{3+} concentration reflects that Tm–Tm interactions are strongly contributing to nonradiative processes, including energy migration by fast diffusion, and indicates the apparently small influence of fluorescence re-absorption in our results.

3.3. NIR to visible upconversion luminescence under excitation at $\lambda_{\text{EXC}} = 930$ nm

3.3.1. $\text{Yb}^{3+}, \text{Er}^{3+}\text{-Lu}_2\text{O}_3$ hydrothermal nanorods

The most noteworthy characteristic of the room temperature upconversion (UC) spectra under low power (~ 25 mW) pumping NIR excitation is the strong development of the $\text{Er}^{3+} ^4\text{F}_{9/2} \rightarrow ^4\text{I}_{15/2}$ red transition with regards to the $^2\text{H}_{11/2}, ^4\text{S}_{3/2} \rightarrow ^4\text{I}_{15/2}$ green bands, which became pre-eminent with the increase of the Yb^{3+} content and even the unique transition for $\text{Yb}^{3+} \geq 0.20$ for any Er^{3+} content in the range $0.04 \leq \text{Er} \leq 0.15$, see the corresponding spectra in Fig. 4a, b for two selected compositions (the first one zoomed in the inset of Fig. 4a). The mechanism that favors the population of $^4\text{F}_{9/2}$ involves an initial energy transfer from Yb^{3+} in $^2\text{F}_{5/2}$ to Er^{3+} in $^4\text{I}_{11/2}$, which non-radiatively decays to $^4\text{I}_{13/2}$, a highly effective

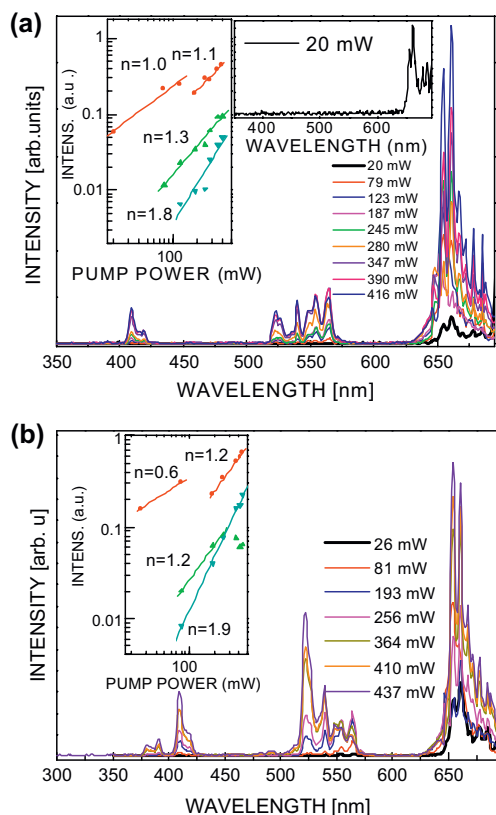


Fig. 4. Power dependence of the upconverted luminescence in Yb, Er-doped Lu_2O_3 nanorods following NIR excitation at 930 nm: (a) $\text{Lu}_{1.76}\text{Yb}_{0.20}\text{Er}_{0.04}\text{O}_3$, (b) $\text{Lu}_{1.71}\text{Yb}_{0.25}\text{Er}_{0.04}\text{O}_3$. The insets show measured intensities for ${}^4\text{F}_{9/2} \rightarrow {}^4\text{I}_{15/2}$ (circles), ${}^4\text{S}_{3/2} \rightarrow {}^4\text{I}_{15/2}$ (up triangles) and ${}^2\text{H}_{11/2} \rightarrow {}^4\text{I}_{15/2}$ (down triangles) vs excitation pump power. The numbers denote the slope in double logarithmic representation.

relaxation process since the gap between involved energy levels ($\sim 3600 \text{ cm}^{-1}$) can be easily covered by available large phonons from CO_2 and/or H_2O species adsorbed at the surface of nanorods. Then, another energy transfer from Yb^{3+} in ${}^2\text{F}_{5/2}$ will populate ${}^4\text{F}_{9/2}$ through non-resonant ${}^4\text{I}_{13/2} \rightarrow {}^4\text{F}_{9/2}$, and the energy in excess ($\sim 1600 \text{ cm}^{-1}$) was also dissipated through phonons of the lattice. This process is clearly dependent of the Yb^{3+} concentration and an increase in the latter results in the corresponding increase in the red band enhancement.

Along the prepared series of Yb^{3+} , Er^{3+} - Lu_2O_3 nanorods the analysis of the double log plots of the dependence of the measured UC intensity on the excitation pump power, $I_{\text{vis}} \propto I_{\text{IR}}^n$, with n the number of photons required to populate the visible states per upconverted emitted photon, yields slopes of 0.4–1.2, 0.9–1.3 and 1.6–1.9, for the red ${}^4\text{F}_{9/2} \rightarrow {}^4\text{I}_{15/2}$ and the two green ${}^2\text{H}_{11/2}$, ${}^4\text{S}_{3/2} \rightarrow {}^4\text{I}_{15/2}$ transitions, respectively, see the insets of Fig. 4a,b for the two selected compositions. These severely reduced slopes with regards to the usually reported for bulk crystals, ~ 2 for the red and green transitions [10,11], and even ~ 3 for ${}^4\text{S}_{3/2} \rightarrow {}^4\text{I}_{15/2}$ in heavily doped Yb^{3+} crystals [11], are associated with larger UC rates in schemes of competition between linear photoluminescence decay and UC processes for depletion of intermediate excited states [12], in other words, larger UC rates must be supported by efficient mechanisms for population of UC emitting levels.

For the ${}^4\text{F}_{9/2} \rightarrow {}^4\text{I}_{15/2}$ red emission the low slopes and their observed discontinuity in the measured NIR pump power range suggest the existence of different underlying processes. Firstly, for NIR excitation power lower than $\sim 150 \text{ mW}$ it is clear that for constant Er^{3+} concentration the reduction in the red slope with the increase of Yb^{3+} (from 1 for $\text{Lu}_{1.76}\text{Yb}_{0.20}\text{Er}_{0.04}\text{O}_3$ to $n = 0.4$ for $\text{Lu}_{1.66}\text{Yb}_{0.30}\text{Er}_{0.04}\text{O}_3$) reflects an increasing importance of the UC emission due to the improvement of the efficiency for populating the Er^{3+} intermediate excited state ${}^4\text{I}_{13/2}$. Furthermore, for comparable sizes and surface to volume ratios, for higher Er^{3+} concentration the proportion of Er^{3+} active centers at the surface of nanorods, and thus close to adsorbed species with high energy phonons, will be larger, favoring lower red slopes (from $n = 1$ for $\text{Lu}_{1.76}\text{Yb}_{0.20}\text{Er}_{0.04}\text{O}_3$ to $n = 0.4$ for $\text{Lu}_{1.70}\text{Yb}_{0.20}\text{Er}_{0.10}\text{O}_3$). Another working UC process involves ${}^4\text{F}_{9/2}$ population by phonon assisted cross-relaxation (CR) (${}^4\text{F}_{7/2}$, ${}^4\text{I}_{11/2}$) \rightarrow (${}^4\text{F}_{9/2}$, ${}^4\text{F}_{9/2}$). For highly Yb-doped nanorods the improved efficiency of the CR process can additionally account for low red slopes. On the other hand, for NIR excitation at high enough powers (over $\sim 180 \text{ mW}$), the thermal effect caused in nanorods would largely remove high energy phonons from their surface. With no longer running phonon-assisted UC mechanisms, the UC rate will be smaller and red slopes will increase, see the insets in Fig. 4a, b. The competition between the two first UC mechanisms and the opposite effect along the measured range of NIR pump powers determines the observed discontinuity for the red ${}^4\text{F}_{9/2} \rightarrow {}^4\text{I}_{15/2}$ emission.

The slopes of the ${}^2\text{H}_{11/2} \rightarrow {}^4\text{I}_{15/2}$ green emission are closer to 2 than to 1, see insets in Fig. 4a, b. In this case the intermediate excited level is ${}^4\text{I}_{11/2}$. Because of the non-radiative relaxation of ${}^4\text{I}_{11/2}$ to ${}^4\text{I}_{13/2}$, the importance of the UC decreases, leading the slope of this green emission to be ~ 2 . The UC luminescence power dependence for the other two-photon ${}^4\text{S}_{3/2} \rightarrow {}^4\text{I}_{15/2}$ green emission has slopes closer to 1, which indicates once again the dominating influence of UC over linear photoluminescence decay for the depletion of corresponding intermediate excited states. Furthermore, the downward curvature starting at $\sim 250 \text{ mW}$, see the inset in Fig. 4b, indicates a typical saturation phenomenon caused by the population exhaustion to the ground state along with thermal quenching effects at these high pump powers [13].

3.3.2. Yb^{3+} , Tm^{3+} - Lu_2O_3 hydrothermal nanorods

For $\text{Lu}_{1.96-x}\text{Yb}_x\text{Tm}_{0.04}\text{O}_3$ nanorods room temperature UC spectra under low power ($\sim 30 \text{ mW}$) pumping NIR excitation in the range ~ 330 – 900 nm shows the blue ${}^1\text{G}_4 \rightarrow {}^3\text{H}_6$ emission at ~ 470 – 490 nm and the deep-blue ${}^1\text{D}_2 \rightarrow {}^3\text{F}_4$ emission at ~ 450 – 465 nm , whose intensities appear in a 3:1 ratio for nanorods with the lower Yb^{3+} content, $x = 0.04$. Furthermore, the green ${}^1\text{D}_2 \rightarrow {}^3\text{H}_5$ emission

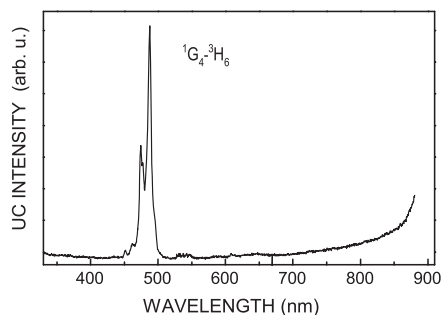


Fig. 5. Room temperature upconversion luminescence spectrum of hydrothermal $\text{Lu}_{1.76}\text{Yb}_{0.26}\text{Tm}_{0.04}\text{O}_3$ nanorods.

at ~ 529 nm has been also observed with very low intensity. The blue $^1G_4 \rightarrow ^3H_6$ band experiences a clear development when Yb^{3+} increases, in such a way that for $Lu_{1.76}Yb_{0.20}Tm_{0.04}O_3$ nanorods is the only existent emission, see the Fig. 5. The $^3H_4 \rightarrow ^3H_6$ transition at ~ 800 nm that typically dominates the UC spectra of Yb^{3+} , Tm^{3+} codoped nanoparticles, for example the high-efficient UC Yb^{3+}, Tm^{3+} - $NaYF_4$ at low excitation densities [14] or Yb^{3+}, Tm^{3+} - Lu_2O_3 agglomerated particles [15], is not currently observed. The population of $Tm^{3+} ^3H_4$, 1G_4 and 1D_2 excited states is accomplished by sequential two-, three- and four-photon energy transfer processes from excited $Yb^{3+} ^2F_{5/2}$ to Tm^{3+} , respectively, thus the probabilities of these mechanisms would be getting lower in the same order. Given the non-existent emission from 3H_4 , and the emphasized emission from 1G_4 , some alteration of the usual UC mechanisms to privilege the population of 1G_4 through phonon assisted energy-transfer and non-radiative relaxations, favored by the presence of large phonons in current nanorods, should be currently acting on prepared Yb^{3+} , Tm^{3+} - Lu_2O_3 nanorods.

4. Conclusions

Analyses of the dynamics exhibited by room temperature fluorescence decays of 3H_4 and 3F_4 Tm^{3+} multiplets in Tm - Lu_2O_3 nanorods [16] as well as proposed mechanisms accounting for the new features of NIR to visible upconverted emissions of Er^{3+} and Tm^{3+} in Yb^{3+} -codoped Lu_2O_3 nanorods [17], which have been found to be well differentiated from corresponding behavior in counterpart bulk crystals, point to a body/surface model to describe the spectroscopic response of current hydrothermal sesquioxides.

Obtained results indicate that optical active centers into the body or core of the nanocrystal retain the characteristics of the bulk crystal, for example, long-lived room temperature fluorescence lifetimes of $Tm^{3+} ^3H_4$ and 3F_4 have values very close to those of bulk crystals. On the contrary, cations at the surface, with an environment of large energy phonons from adsorbed species and defects as shown by FT-IR spectra, will be responsible of the short component of the double exponential decay curve, which is ascribed to favorable conditions for faster nonradiative relaxation rate. The important development of this short time component occurring with the increase in Tm^{3+} concentration corroborates this assumption.

Furthermore, mechanisms explaining the experienced strong development of the upconverted red $^4F_{9/2} \rightarrow ^4I_{15/2}$ and blue $^1G_4 \rightarrow ^3H_6$ luminescence emissions of Er^{3+} and Tm^{3+} , along with the very reduced slopes in the double log plots of the UC intensity dependence with the excitation power, which are associated to large UC rates for depleting the intermediate excited states, also involve the presence of high energy phonons from adsorbed species at the surface of nanorods.

Acknowledgments

Financial funding of Spanish projects MAT 2008-06729-C02-01-02 and PI09/90527 are acknowledged. E W B acknowledges the support of the Catalan Government through the fellowship 2009FI00148.

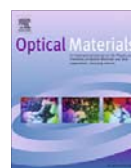
References

- [1] (a) L. Fornasiero, Nd^{3+} und Tm^{3+} -dotierte Sesquioxides, Ph.D. Dissertation, University of Hamburg, 1999.;
(b) V. Peters, Growth and Spectroscopy of Ytterbium-Doped Sesquioxides, Ph.D. Dissertation, University of Hamburg, 2001.
- [2] M. Tokurakawa, K. Takaichi, A. Shirakawa, K. Ueda, H. Yagi, S. Hosokawa, T. Yanagitani, A.A. Kaminskii, Opt. Express 14 (2006) 2832.
- [3] V. Bedekar, D.P. Dutta, M. Mahapatra, S.V. Godbole, R. Ghildiyal, A.K. Tyagi, Nanotechnology 20 (2009) 125707.
- [4] J.L. Bridot, A.C. Faure, S. Laurent, C. Rivière, C. Billotey, B. Hiba, M. Janier, V. Jossierand, J.L. Coll, L.V. Elst, R. Muller, S. Roux, P. Perriat, O. Tillement, J. Am. Chem. Soc. 129 (2007) 5076.
- [5] F. Esteban-Betegón, C. Zaldo, C. Cascales, Chem. Mater. 22 (2010) 2315.
- [6] G. Liu, X. Chen, Spectroscopic properties of lanthanides in nanomaterials, in: K.A. Gschneidner Jr., J.-C.G. Bünzli, V.K. Pecharsky (Eds.), Handbook on the Physics and Chemistry of Rare Earths, vol. 37, Elsevier B.V., 2007 (Chapter 233).
- [7] G. Schnaak, J.A. Königstein, J. Opt. Soc. Am. 60 (1970) 1110.
- [8] Y. Guyot, R. Moncorgé, L.D. Merkle, A. Pinto, B. McIntosh, H. Verdun, Opt. Mater. 5 (1996) 127.
- [9] F. Cornacchia, D. Parisi, M. Tonelli, IEEE J. Quantum Electron. 44 (2008) 1076.
- [10] F. Vetroni, J.C. Boyer, J.A. Capobianco, A. Speghini, M. Bettinelli, J. Phys. Chem. B 107 (2003) 1107.
- [11] F. Vetroni, J.C. Boyer, J.A. Capobianco, A. Speghini, M. Bettinelli, J. Appl. Phys. 96 (2004) 661.
- [12] M. Pollnau, D.R. Gamelin, S.R. Lüthi, H.U. Güdel, Phys. Rev. B 61 (2000) 3337.
- [13] Y. Lei, H. Song, L. Yang, L. Yu, Z. Liu, G. Pan, X. Bai, F. Fan, J. Chem. Phys. 123 (2005) 174710.
- [14] H.T. Wong, H.L. Wa, J. Hao, Opt. Express 18 (2010) 6123.
- [15] G. Wang, W. Qin, L. Wang, G. Wei, P. Zhu, R. Kim, Opt. Express 16 (2008) 11907.
- [16] F. Esteban-Betegón, C. Zaldo, C. Cascales, Inorg. Chem. 50 (2011) 2836.
- [17] E.W. Barrera, M.C. Pujol, F. Díaz, S.B. Choi, F. Rotermund, K.H. Park, M.S. Jeong, C. Cascales, Nanotechnology 22 (2011) 075205.

Paper VII

E. W. Barrera, M. C. Pujol, C. Cascales, J. J. Carvajal, X. Mateos, M. Aguiló, and F. Díaz, *Synthesis and characterization of core-shell $\text{SiO}_2@(\text{Er}^{3+}, \text{Yb}^{3+})\text{:Lu}_2\text{O}_3$* **Optical Materials** 34 355–359 (2011).

UNIVERSITAT ROVIRA I VIRGILI
LANTHANIDE-BASED DIELECTRIC NANOPARTICLES FOR UPCONVERSION LUMINESCENCE
Elixir William Barrera Bello
Dipòsit Legal: T. 450-2013



Synthesis and characterization of core–shell $\text{SiO}_2@(\text{Er}^{3+}, \text{Yb}^{3+})\text{:Lu}_2\text{O}_3$

E. William Barrera^a, M. Cinta Pujol^{a,*}, Concepción Cascales^b, Joan J. Carvajal^a, X. Mateos^a, R. Solé^a, J. Massons^a, Magdalena Aguiló^a, Francesc Díaz^a

^a Física i Cristal·lografia de Materials i Nanomaterials (FICMA-FICNA-EMAS), Universitat Rovira i Virgili (URV), Campus Sescelades, c/ Marcel·lí Domingo, s/n, E-43007 Tarragona, Spain

^b Instituto de Ciencia de Materiales de Madrid, CSIC, Calle Sor Juana Inés de la Cruz, Cantoblanco, E-28049 Madrid, Spain

ARTICLE INFO

Article history:

Available online 8 June 2011

Keywords:

Core–shell structure
Nanocrystals
Silica microspheres
Sesquioxides
Pechini method

ABSTRACT

We synthesized crystalline Erbium Er^{3+} and Ytterbium Yb^{3+} codoped $\text{-Lu}_2\text{O}_3$ nanolayers on SiO_2 microspheres using the modified Pechini method. Two different kinds of precursors, nitrates and chlorides, have been used leading to a layer-to-layer morphology and necklaces structures, respectively. In both cases, the size of nanocrystallites constituting the optical active layer is around 5 nm. We performed X-ray powder diffraction to confirm the cubic crystalline structure of the sesquioxides layer. High resolution transmission electron microscopy analyses corroborate the crystalline nature of the layer. The optical emission of Er^{3+} in the visible range has been recorded.

© 2011 Elsevier B.V. All rights reserved.

1. Introduction

The importance in the last years of materials that combine different physical properties for optical applications has pushed the development of a new class of structured materials in form of core–shell particles [1]. These new composite structures can present different advantages, such as mono-dispersion (given by the unique size of the starting silica core particles), spherical shape (also assured by the used core silica) and nonagglomeration; these three properties are advantageous for luminescent phosphor applications, enhancing the brightness and reducing the scattering of the light. Many methods have been developed to fabricate core–shell structured materials such as sol–gel processes, layer-by-layer techniques [2], template-directed self assembly methods [3]. These processes of synthesis lead to a fine tailoring of the material properties through the control of the thickness and composition of the active layer. Furthermore, the cost of the composite luminescent material is lowered due to the use of inexpensive cores. One of the compounds more used as core is the amorphous silica, SiO_2 , because the size and morphology can be controlled with reliability by the Stöber method [4]. The compounds deposited as layer are used as activators or host materials due to their modified optical properties by surface confinement, i.e. modifications in the spectroscopy of a luminescence ion or nonlinear optical behavior by the presence of non-centrosymmetry regions on the surface. Also, Lu_2O_3 , has been receiving growing interest recently due its potential applications in lasers, phosphors, scintillators, etc. It has favorable properties, such as phase stability, low thermal expansion,

high thermal conductivity and chemical stability. Furthermore, it possesses moderate phonon energy (about 600 cm^{-1}) [5], which is helpful for photoluminescence efficiency.

Er^{3+} is widely used since its electronic energy levels allow visible blue–green–red optical emissions by absorption of near-infrared (NIR) photons in an intermediate level that possesses a long lifetime. In this way, Er^{3+} is a convenient choice for upconversion phosphors [6] and is efficiently sensitized by Ytterbium.

For layer deposition, the Pechini method offers several advantages when compared to other deposition methods, such as homogeneous mixing of the starting materials, good control of stoichiometry, fine particle size and uniform morphology [7]. The modified Pechini method has allowed to obtain lanthanide-doped oxide nanocrystals [8] and recently lanthanide-doped core–shell nanostructured materials [1]. The modified Pechini process uses common metal salts (nitrates, chlorides, etc.) as precursors, citric acid (CA) as chelating agent of metal ions and a poly-hydroxyl alcohol (such as ethylene glycol or poly-ethylene glycol) as a cross linking agent to form a polymeric resin at a molecular level which reduce segregation of particular metal ions, ensuring compositional homogeneity. Further details of the high potential of this simple sol–gel method can be consulted elsewhere [9]. Here we describe a method to grow nanoparticles of $(\text{Er}^{3+}, \text{Yb}^{3+})\text{:Lu}_2\text{O}_3$ directly on the surface of silica nanospheres by Pechini method.

2. Experimental procedure

2.1. Synthesis of core–shell particles

$\text{Er}^{3+}, \text{Yb}^{3+}$ codoped Lu_2O_3 nanocrystals with 2 at.% Er^{3+} and 6 at.% Yb^{3+} and $\text{SiO}_2@(\text{Er}^{3+}, \text{Yb}^{3+})\text{:Lu}_2\text{O}_3$, core–shell particles with equal

* Corresponding author.

E-mail address: mariacinta.pujol@urv.cat (M. Cinta Pujol).

Table 1
 Summary of experimental details for synthesis of core-shell structures.

Precursor salt	pH	CM/CA	CA/EG	CA	EG	Lu ₂ O ₃ Yb ₂ O ₃ Er ₂ O ₃ SiO ₂			
						[×10 ⁻³ mol]			
Chloride	7	0.5	2	5.03	2.52	2.31	0.15	0.05	0.62
Chloride	11	0.5	2	5.03	2.52	2.31	0.15	0.05	0.62
Nitrates	7	0.5	2	5.03	2.52	2.31	0.15	0.05	0.62
Nitrates	11	0.5	2	5.03	2.52	2.31	0.15	0.05	0.62

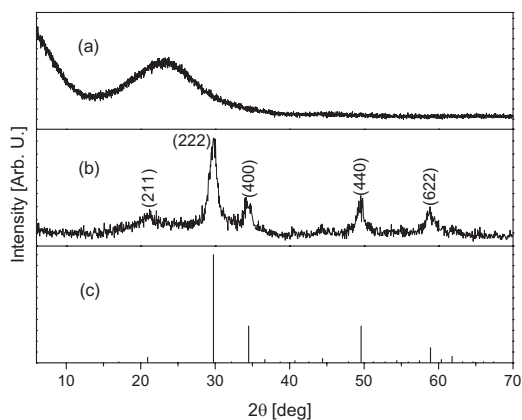


Fig. 1. X-ray powder diffraction pattern for amorphous SiO₂ (a); SiO₂@(Er³⁺, Yb³⁺):Lu₂O₃ core-shell structure (b); and the JCPDS card 43-1021 for Lu₂O₃ (c).

layer composition, were synthesized by a modified Pechini method. The ratio of active lanthanide doping ions has been chosen, taking into account that a higher concentration of the sensitizing ion (Yb³⁺) in relation with Er³⁺ favors the optical absorption of NIR excitation light. High purity 99.9999% Er₂O₃, Yb₂O₃ and Lu₂O₃ oxides were dissolved in hot nitric acid and hot hydrochloric acid to form the nitrate and chloride precursors, respectively. We used citric acid (CA) as the chelation agent and ethylene glycol (EG) as the esterification agent. The precursors were dissolved in a water/ethanol solution with a molar ratio of CA to metal cations C_M = [CA]/[METAL] = 1. Then, EG was added to the mixture in a molar ratio C_E = [CA]/[EG] = 2. These two molar ratios were optimized in previous works [10,11]. In the first stage, citric acid molecules chelate the lanthanide cations to form chelates. In the second stage the esterification process of these chelates is produced by the addition of ethylene glycol.

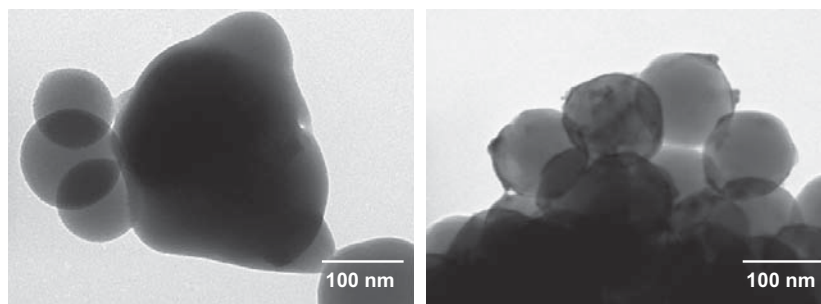


Fig. 2. TEM images of 100 nm silica blank samples calcinated at 1073 K for 2 h; for normal solution (left); with the addition of NH₄OH (right).

Amorphous silica spheres (Alpha Aesar, $d = 327 \pm 44$ nm in diameter) were added to the sol. From previous experiments, it was determined an optimal value of mass ratio Lu₂O₃/SiO₂, MR, of 27. Aqueous ammonia was used to control the pH value. The selected pH range enhance the production of silanol groups on the surface of the silica [12], where the esterified chelates of the lanthanide ions will be bonded. The solution was maintained under magnetic stirring during 24 h. After that, the microspheres were extracted by centrifugation (1 h, 6000 rpm) and washed with ethanol. This centrifugation step is crucial to warrant the obtaining of a solution of covered silica spheres without excess of Lu₂O₃. The spheres were heated at 373 K for 1 h in order to remove water, and after that calcinated at 573 K for 1 h to eliminate the organic compounds and finally at 1073 K for 2 h to provide a high crystallinity to the shell layer. Table 1 summarizes the experimental details of the synthesis performed.

2.2. Characterization techniques

The identification of the synthesized crystallographic phase of the SiO₂@(Er³⁺, Yb³⁺):Lu₂O₃ nanostructures was performed by X-ray diffraction (XRD) analysis by using a Bruker-AXS D8-Discover diffractometer. Cu K α radiation was obtained from a copper X-ray tube operated at 40 kV and 40 mA. A transmission electron microscope JEOL JEM-1011 was also used to observe the shape and size of the nanoparticles, using a current accelerating voltage of 100 kV. High-resolution transmission electron microscopy images were obtained by a HRTEM 300 kV Philips CM30 equipped with spectrophotometer a Link LZ5 spectrophotometer. A Renishaw in via Reflex Raman spectrometer provided with a 514 nm Argon laser and a 633 nm He-Ne laser, was used to analyze the structure and luminescence of core-shell particles.

3. Results and discussion

3.1. Structural characterization

Fig. 1 shows the X-ray diffraction patterns (XRD) of silica. Silica pattern shows a broad band centered at $2\theta = 22^\circ$ corresponding to the amorphous phase. The XRD pattern of the SiO₂@(Er³⁺, Yb³⁺):Lu₂O₃ spheres is presented in Fig. 1. Using nitrates or chlorides as precursors, the final crystalline phase was the same and it has been observed just after one coating process. In a previous work, the same methodology was used for YAG as active layer, but a multi-step process of coating was necessary to obtain the crystalline phase [13]. All the diffraction lines are indexed as corresponding to the cubic phase of Lu₂O₃ with space group $Ia\bar{3}$ by comparison with JCPDS card 43-1021 in Fig. 1. The size of crystallites

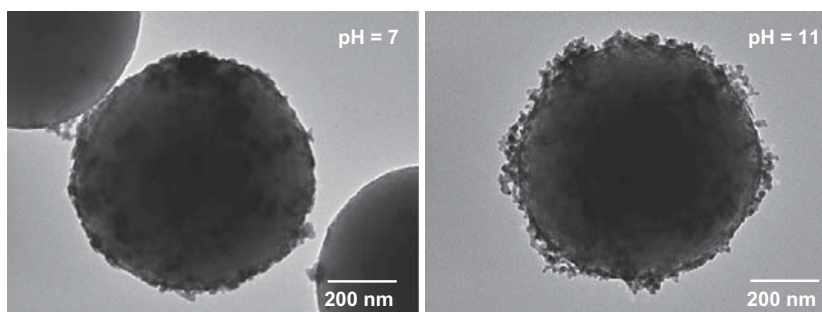


Fig. 3. TEM image showing a core-shell structure obtained from chloride precursor with pH = 7 (left) and pH = 11 (right).

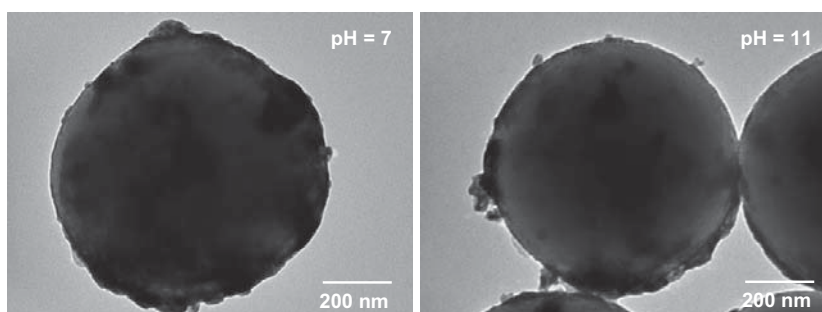


Fig. 4. TEM image showing a core-shell structure obtained from nitrate precursor with pH = 7 (left) and pH = 11 (right).

that constitute the phosphor shell was determined to be ~ 5 nm from the analysis of the full-width at half maximum (FWHM) of the (2 2 2) XRD peak, using the Scherrer equation (FWHM = 1.41° and 1.67° for chlorides and nitrates precursors, respectively).

3.2. Morphological characterization

Previous experiments were performed in blank samples with silica spheres of 100 nm in diameter, i.e. without addition of Lu_2O_3 sesquioxides and calcinated at 1073 K for 2 h, see Fig. 2. It can be observed a formation of a layer when NH_4OH was used. High-resolution TEM analyses (not showed here) revealed that this layers is amorphous and it is formed by silica deposition from other adjacent eroded silica spheres. Also some silica spheres suf-

fered partial deformation and sintering, during calcination above 1073 K. We suggest that silica particles below 100 nm in diameter reach the necessary activation energy for sintering process at 1073 K. To overcome this problem bigger silica spheres were used ($d = 327 \pm 44$ nm).

Figs. 3 and 4 show the TEM photographs of the obtained core-shell particles. The difference between the resulting particles is due to the different precursors used. The pH of the solution seems to play an important role on the formation of the layers, those being formed only when pH was above 6. However for pH values below 6, previous experiments did not show the formation of layers for

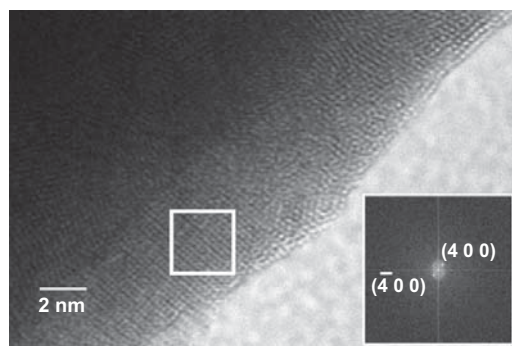


Fig. 5. HRTEM image of the $(\text{Er}^{3+}, \text{Yb}^{3+})\text{:Lu}_2\text{O}_3$ layer on SiO_2 sphere and the (hkl) reflections indicated by the interplanar distance.

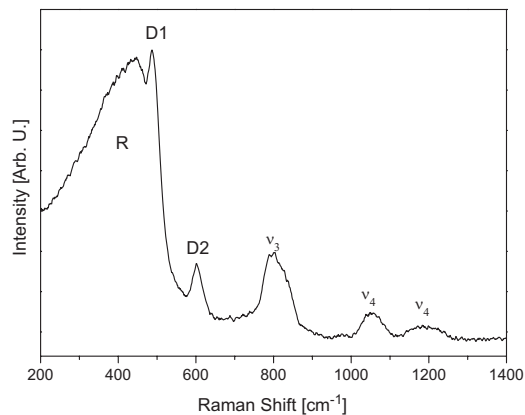


Fig. 6. Raman spectrum of the amorphous SiO_2 microspheres.

both kinds of precursors. Fig. 3 corresponds to the Lu_2O_3 layers obtained using chloride precursors, and it can be seen that shells composed of nanocrystals were obtained. Lu_2O_3 particles grow forming short necklace structures bonded on the surface of the spheres were obtained. It can be observed that the size of the nanocrystals agrees with the Scherrer estimation, around 5 nm in diameter.

In the case of nitrate precursor and $\text{pH} = 7$, polycrystalline shells composed of nanocrystalline domains were formed. When the pH value was increased to 11; only partial layers were observed to grow on the surface of the spheres and some of the nanoparticles got bonded. Again, the crystallite size is around 5 nm in agreement with the Scherrer estimation. In the previous work reported by Hreniak et al. [13]; with YAG layers after three coating processes the layer thickness was around 140 nm, assuming a particle size of 30 nm. Fig. 4 shows one silica sphere partially coated with a thin layer of 20 nm.

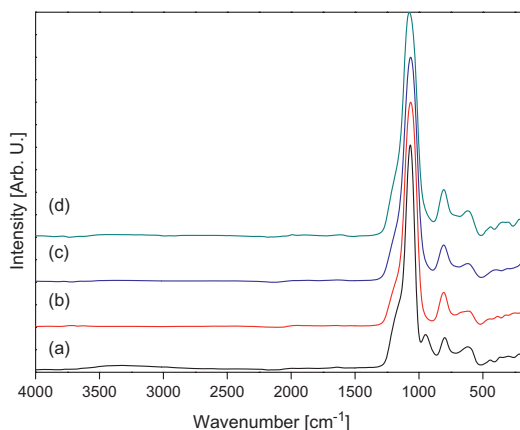


Fig. 7. FTIR spectra of the SiO_2 precursor (a), 973 K annealed SiO_2 (b), core-shell samples obtained from chloride precursors at $\text{pH} = 7$ (c) and $\text{pH} = 11$ (d).

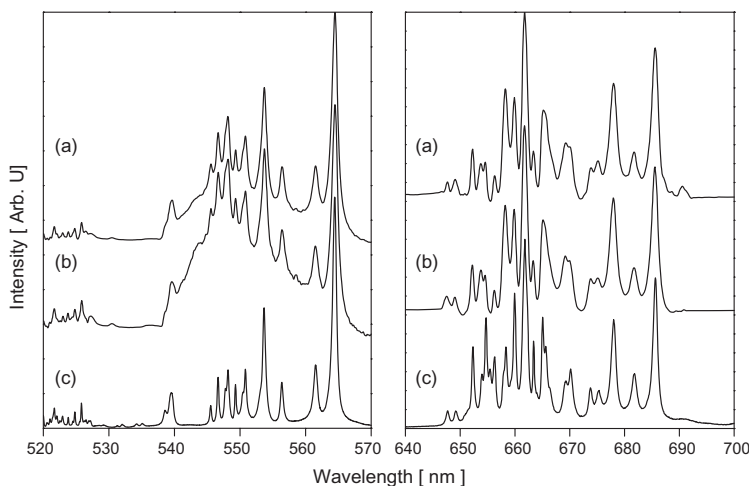


Fig. 8. Room emission spectra showing the Er^{3+} $^2\text{H}_{11/2}$, $^4\text{S}_{3/2}$ (arrow) $^4\text{I}_{15/2}$ (left) and $^4\text{F}_{9/2}$ (arrow) $^4\text{I}_{15/2}$ transitions (right) for core-shell particles processed at $\text{pH} = 7$ (a); $\text{pH} = 11$ (b) and nanocrystals (c).

Fig. 5 shows a HRTEM image of a nanocrystalline layer on the SiO_2 sphere. The lattice fringes of the crystalline phase can be easily visualized in some regions of the layer; and its Fast Fourier transform (FFT) pattern shows the diffraction spots, corresponding to the $\{400\}$ crystallographic planes with the interplanar distances of 2.6 Å.

3.3. Raman and FTIR spectroscopy

Fig. 6 shows the Raman spectrum of silica microspheres recorded in the wavelength range of $200\text{--}1400\text{ cm}^{-1}$. The typical profile of vitreous $\nu\text{-SiO}_2$ was obtained. D1 (486 cm^{-1}) and D2 (601 cm^{-1}) bands are attributed to symmetric stretching modes of vibrationally isolated rings of SiO_2 tetrahedra [14]. The broad R band at 440 cm^{-1} is associated to ν_1 bending mode of oxygen atoms in siloxane bond Si-O-Si . Other modes of Si-O-Si bond are the ν_3 stretching mode (800 cm^{-1}); ν_4 transversal optic mode (1053 cm^{-1}) and ν_4 longitudinal optic mode (1193 cm^{-1}) [14].

The FTIR spectra of the core-shell particles heated at 973 K are shown in Fig. 7. For the silica precursor the bands due to OH ($3400\text{--}3500\text{ cm}^{-1}$), Si-O-Si ν_4 transversal optic mode (1067 cm^{-1}), ν_3 stretching mode (800 cm^{-1}), and Si-OH (946 cm^{-1}) were observed. The presence of silanol group Si-OH , is important for bonding the lanthanide ions (Lu^{3+} , Er^{3+} , Yb^{3+}) from the sol to form (Er^{3+} , Yb^{3+}): Lu_2O_3 layers [1]. This band is absent in heated samples.

3.4. Room temperature emission spectroscopy

Emission spectra in the range of $520\text{--}570\text{ nm}$ and $640\text{--}700\text{ nm}$ under excitation with $\lambda_{\text{exc}} = 514\text{ nm}$ and $\lambda_{\text{exc}} = 633\text{ nm}$, are shown in Fig. 8. The green emission is attributed to the $^2\text{H}_{11/2} \rightarrow ^4\text{I}_{15/2}$ and $^4\text{S}_{3/2} \rightarrow ^4\text{I}_{15/2}$ transitions and the red emission to the $^4\text{F}_{9/2} \rightarrow ^4\text{I}_{15/2}$ transition of Er^{3+} . Emission from pure silica at $\sim 653\text{ nm}$ due to the presence of defects in the form of non-bridging oxygen hole centers [15], was not currently detected in our prepared samples. Emission spectra exhibit high intensity and broad lines, with splitting similar to these observed in measured emission spectra obtained for $\text{Er}_{0.041}\text{Yb}_{0.136}\text{Lu}_{1.824}\text{O}_3$ nanocrystals under the same conditions. However, the ratios between green and red emissions are not comparable in the current range of wavelengths and pump power conditions.

3.5. Upconversion luminescence

No upconversion luminescence was observed for the core-shell powder in the range of 350–700 nm, maybe due to the low content of luminescent optically active centers at the surface of microspheres. However, upconversion photoluminescence spectra at different pump power values were collected in nanocrystalline powder $\text{Er}_{0.041}\text{Yb}_{0.136}\text{Lu}_{1.824}\text{O}_3$, obtained from precursor solution used for coating of silica cores. The UC spectra are showed in Fig. 9.

The main emission is the visible red observed at 630–690 nm, which corresponds to $\text{Er}^{3+} {}^4\text{F}_{9/2} \rightarrow {}^4\text{I}_{15/2}$ transition. Green emission associated to $\text{Er}^{3+} {}^4\text{S}_{3/2} \rightarrow {}^4\text{I}_{15/2}$ was also observed but intensity one order of magnitude less than red emission, only for higher pump power intensities higher than 287 mW.

In the upconversion process the luminescence intensity dependence upon the pump power is related by a potential behavior $I \propto (I_{\text{UC}})^n$, where the n is the number of photons involved in the upconversion process in the regime of low pump power. Fig. 10 shows a Ln–Ln plot of integrated intensities of $\text{Er}^{3+} {}^4\text{F}_{9/2} \rightarrow {}^4\text{I}_{15/2}$ red emission (the low intensity of the green emission was not enough to extract a reliable data of log–log diagram). A slope of $n = 0.68$ was obtained from fitting. By ground state absorption Yb^{3+} is excited from its ground level ${}^2\text{F}_{7/2}$ to the ${}^2\text{F}_{5/2}$ excited energy level. After that Yb^{3+} transfer this energy to the Er^{3+} intermediate excited level

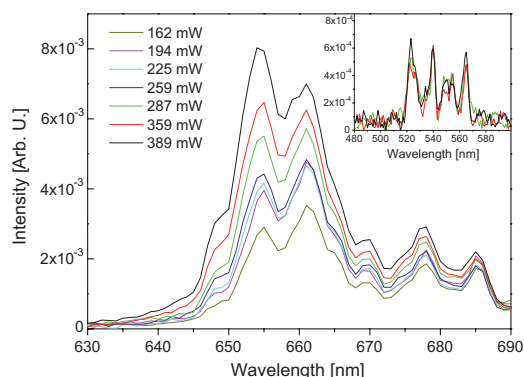


Fig. 9. Upconversion spectra of nanocrystalline $\text{Er}_{0.041}\text{Yb}_{0.136}\text{Lu}_{1.824}\text{O}_3$ powder nanocrystals ($\lambda_{\text{exc}} = 930$ nm). Showing the ${}^4\text{F}_{9/2} \rightarrow {}^4\text{I}_{15/2}$ transition and ${}^4\text{S}_{3/2} \rightarrow {}^4\text{I}_{15/2}$ transition (inset).

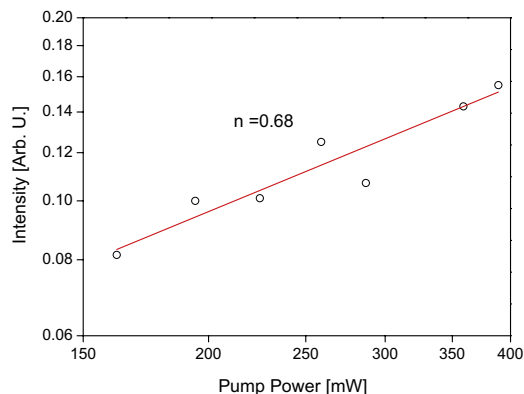


Fig. 10. Power dependence of the UC luminescence intensity for the $\text{Er}^{3+} {}^4\text{F}_{9/2} \rightarrow {}^4\text{I}_{15/2}$ transition.

${}^4\text{I}_{11/2}$. Another energy transfer from a neighboring Yb^{3+} ion leads the Er^{3+} ion to the ${}^4\text{F}_{7/2}$ excited level. From that level, nonradiative relaxation leads to the population of the emitting levels, ${}^4\text{S}_{3/2}$ and ${}^4\text{F}_{9/2}$.

A cross-relaxation process was responsible for populating the ${}^4\text{F}_{9/2}$ level and that this occurs via two resonant transitions between two Er^{3+} ion: (${}^4\text{F}_{7/2}, {}^4\text{I}_{11/2} \rightarrow {}^4\text{F}_{9/2}, {}^4\text{F}_{9/2}$). In fact, the cross-relaxation process becomes more efficient as the average distance between the doping ions decreases, therefore, the Er^{3+} concentration increases, thus enhancing the red emission. So the slope value obtained from fitting in Fig. 10 indicates that depletion of the Er^{3+} intermediate level ${}^4\text{I}_{11/2}$ in the upconversion process is dominated in a major way by the upconversion to the excited energy level ${}^4\text{F}_{7/2}$ more than the linear decay to the ground state ${}^4\text{I}_{15/2}$ [16]. This depletion is originated by the high pump power operation during photoluminescence characterization (100–400 mW). This peculiar behavior of the dominant character of the red upconversion emission versus the green and these mechanisms have been also discussed for similar nanocrystalline materials [17,6,18].

4. Conclusions

$\text{SiO}_2@(\text{Er}^{3+}, \text{Yb}^{3+})\text{:Lu}_2\text{O}_3$ core-shell particles were prepared by Pechini method in a water/ethanol solution in the pH range of 7–11. For chloride precursors, nanocrystalline shells with granular morphologies similar to a necklace structure were obtained and in the case of nitrate precursors shells present a continuous structure with nanocrystalline domains. In both cases the crystallite size was 5 nm, determined by Scherrer equation and TEM images. Green and red luminescence of core-shell particles were observed under excitation of 514 nm and 633 nm, respectively. Obtained core-shell particles offer a controlled morphology and become a first approach to develop core-shell particles to avoid degradation.

Acknowledgments

This work is supported by the Spanish Government under projects MAT2008-06729-C02-01-02/NAN; MAT2008-04046-E/MAT; TEC2010-21574-C02-02 and the project PI09/90527; and the Catalan Authority under projects 2009SGR235 and FP7-SPA-2010-263044. E.W. Barrera is supported by Catalan Government through the fellowship 2010FL_B00834. J.J. Carvajal is supported by the Education and Science Ministry of Spain and European Social Fund under Ramon y Cajal program RYC2006-258.

References

- [1] M. Yu, J. Lin, J. Fang, Chem. Mater. 17 (2005) 1783.
- [2] P. Schuetzand, F. Caruso, Chem. Mater. 14 (2000) 4509.
- [3] S.R. Hall, S.A. Davis, S. Mann, Langmuir 16 (2000) 1454.
- [4] W. Stöber, A. Fink, E. Bohn, J. Colloid Interface Sci. 26 (1968) 62.
- [5] J.A. Capobianco, F. Vetrone, J.C. Boyer, M. Bettinelli, Opt. Mater. 19 (2002) 259.
- [6] F. Vetrone, J.C. Boyer, J.A. Capobianco, A. Speghini, M. Bettinelli, Chem. Mater. 15 (2003) 2737.
- [7] M.P. Pechini, US Patent Specification 3330697.
- [8] M. Galceran, M.C. Pujol, M. Aguiló, F. Díaz, Mater. Sci. Eng. B 146 (2008) 7.
- [9] J. Lin, M. Yu, C. Lin, X. Liu, J. Phys. Chem. C 111 (2007) 5835.
- [10] M. Galceran, M.C. Pujol, M. Aguiló, F. Díaz, J. Sol-Gel Sci. Techn. 42 (2007) 79.
- [11] M. Galceran, M.C. Pujol, M. Aguiló, F. Díaz, Mater. Sci. Eng. B 146 (2008) 7.
- [12] V.G. Pol, D.N. Srivastava, O. Palchik, V. Palchik, M.A. Sliifkin, A.M. Weiss, A. Gedanken, Langmuir 18 (2002) 3357.
- [13] D. Hreniak, P. Psuja, W. Strek, J. Hölsa, J. Non-Cryst. Solids 354 (2008) 445.
- [14] F.L. Galeener, Phys. Rev. B 19 (1979) 4292.
- [15] S. Munekuni, T. Yamanaka, Y. Shimogai, R. Tohmon, Y. Ohki, J. Appl. Phys. 68 (1990) 1212.
- [16] M. Pollnau, D.R. Gamelin, S.R. Lüthi, H.U. Güdel, Phys. Rev. B 61 (2000) 3337.
- [17] Y. Li, J. Zhang, X. Zhang, Y. Luo, X. Ren, H. Zhao, X. Wang, L. Sun, Ch. Yan, J. Phys. Chem. C 113 (2009) 4413.
- [18] E.W. Barrera, M.C. Pujol, F. Díaz, S.B. Choi, F. Rotermund, K.H. Park, M.S. Jeong, C. Cascales, Nanotechnology 22 (2011) 075205.

UNIVERSITAT ROVIRA I VIRGILI
LANTHANIDE-BASED DIELECTRIC NANOPARTICLES FOR UPCONVERSION LUMINESCENCE
Elixir William Barrera Bello
Dipòsit Legal: T. 450-2013

UNIVERSITAT ROVIRA I VIRGILI
LANTHANIDE-BASED DIELECTRIC NANOPARTICLES FOR UPCONVERSION LUMINESCENCE
Elixir William Barrera Bello
Dipòsit Legal: T. 450-2013